A Rydberg-dressed Magneto Optical Trap

BOUNDS, ALISTAIR,DAVID

A Rydberg-dressed Magneto Optical Trap

Alistair Bounds

A thesis submitted in partial fulfilment
of the requirements for the degree of
Doctor of Philosophy

Department of Physics
Durham University

April 2, 2018

A Rydberg-dressed Magneto Optical Trap

Alistair Bounds

We Rydberg dress a magneto-optical trap of strontium atoms, mixing Rydberg character into atoms as they are cooled and confined. A recently developed tunable high-power narrow-linewidth 319 nm laser is used to excite and characterise triplet Rydberg states in strontium. Off-resonantly dressing a cloud of atoms in a narrow-line MOT operating on the $5s^2\ {}^1S_0 \leftrightarrow 5s5p\ {}^3P_1$ transition, we observe a one-body AC Stark shift on the cloud, which we characterise to identify a regime in which only Rydberg dressed atoms are trapped in the MOT. In this cloud the Rydberg dressed atoms are both trapped and cooled.

Increasing atomic density in the dressed MOT, plasma formation is observed at densities lower than the density necessary for observation of Rydberg dressed atoms. This plasma is caused by a build-up of charges due to spontaneous ionisation of Rydberg atoms, which then DC Stark shift the Rydberg state onto resonance with the coupling laser. The high charge density of the plasma then results in strong Rydberg excitation that causes rapid depletion of atoms. Regimes using optimum Rydberg states and charge-extracting electric fields are identified that may prevent plasma formation, and allow the interacting regime to be reached. Such a regime, with cooling, confinement, and tunable interactions, may form the basis of a quantum simulator for dissipative many-body systems.

Declaration

I confirm that no part of the material offered has previously been submitted by myself for a degree in this or any other University. Where material has been generated through joint work, the work of others has been indicated.

Alistair Bounds
Durham, April 2, 2018

Acknowledgements

I would like to offer my sincerest thanks to all the people that have helped me through my PhD. There are too many people across too many years to mention everyone here but I will do my best. Firstly, I must thank the group that I worked with on the strontium experiment and of all of the people involved I must thank Matt Jones for his guidance, support and friendship. I can't think of anyone with whom I would have developed so much under his supervision and companionship. The strontium group has ebbed and flowed whilst I have been here, but Niamh Jackson has been a rock. Her perserverence against a frustrating research laboratory is inspiring. Dani Boddy and Liz Bridge have done so much to build the lab but also to build the team that use it, and their patience and encouragement have been invaluable. Ryan Hanley and Paul Huillery have been a constant source of energy and enthusiasm and I'm sure they will take the experiment on to new and exciting things. I also have Dan Sadler, Riccardo Faoro and Christophe Vaillant to thank for showing me the ropes and helping me settle into the project.
The wider AtMol group has been a wonderful group to be part of, it is a friendly and welcoming group and whilst everyone in AtMol plays their part in that special mention goes to Chris, Nikola, James and Hannes for their support, both in the lab and outside. FAtMol and the Friday evening seminars have been a welcome source of solace from a disobedient lab, and Ifan gets a special mention for his enthusiasm in rounding up the group on a Friday evening.
I have also been very lucky to be a part of the fantastic St John's community, the MCR being a respite from physics and a source of much joy. Special thanks goes to the resident tutor teams throughout the years and in particular Mark Ogden for his support and friendship.
I must also thank my old physics teacher, Dr Moseley, who inspired my interest in physics with his passion and knowledge.
The European Union and the United Kingdom (EPSRC) funded this work and I owe thanks to both. Hopefully the collaborations that AtMol has developed across Europe and that the strontium project has benefited so much from will continue.
Finally, I must thank my family for their support and love. Thank you.

Contents

List of Figures

Chapter 1

Introduction

The field of quantum technology is growing rapidly, with massive investment on a UK [1], European [2, 3] and global level [4, 5]. There is a booming field of proposed and developing quantum devices for precision measurements of gravity [6, 7], magnetic field [8, 9], microwave electric fields [10, 11], and time-keeping [12–14]. These measurements may enhance our understanding of fundamental constants [15, 16]. Quantum logic gates [17, 18] and quantum annealing [19, 20] are bringing quantum computing closer to fruition [21, 22], and quantum communication [23, 24] and cryptography [25, 26] offer inherently secure means of information transfer.

Quantum devices are not the only product of quantum technology. Quantum mechanics formed the basis for the microcomputer revolution through understanding of semiconductors [27, 28]. Quantum simulation of many-body systems that are too computationally intensive to model classically offers new insight into phenomena with great potential for both developing new technology, such as room temperature superconductors [29], and improving our understanding of the universe, such as modelling Hawking radiation [30].

A many-body quantum simulator requires [31, 32] a quantum system with many degrees of freedom that can be initialised in an approximately known state. There must be engineerable interactions between particles, either between nearest neighbours or on longer lengthscales. Finally, the system must be measurable in a verifiable manner. These systems may be closed, conservative systems, or open systems that interact with a reservoir that results in dissipation within the system.

In addition to quantum simulation, there are novel phases of matter [33], such as supersolid formation [34, 35], and phase transitions [36, 37] that have been theorised and

observed [38] in media with these requirements.

Ultracold atoms [39], ions [40] and molecules [41, 42], superconducting circuits [43, 44] and quantum dots [45] have all been proposed or demonstrated as quantum simulators. We are interested in ultracold neutral atoms due to their widely tunable dimensionality, the high degrees of freedom offered by a three dimensional system, and the scope for nearest neighbour and many-body interactions [46].

Several techniques have been used to introduce interactions to neutral atoms, such as Feshbach resonances [32] and optically mediated interactions [47, 48]. Atoms in Rydberg states, with an electron in a state of high principal quantum number resulting in a very large dipole moment, offer a mechanism to engineer very strong, tunable interactions between neutral atoms [49], and there are numerous proposals for Rydberg atom quantum devices [50], quantum logic gates [51, 52] and quantum simulators [53, 54]. However, whilst Rydberg atom interactions are strong and tunable, atoms in Rydberg states can't be optically trapped and cooled (barring some velocity selective cooling proposals [55, 56]), and have many decay channels to the atomic ground state [57], resulting in high trap loss rates and limited trap lifetimes.

Rydberg-dressed interactions have emerged as another mechanism to control interactions in a many-body system [34, 58]. Rather than populating the Rydberg state and facing the limited lifetime and trapping challenges associated with Rydberg atoms, a fraction of the Rydberg state can be mixed into a ground or low-lying excited state, creating a combined state that we refer to as the dressed state. This controllable Rydberg fraction results in a controllable interaction between dressed state atoms. These interactions are very widely tunable in strength through readily accessible experimental parameters of laser intensity and frequency, and choice of Rydberg state allows control of interaction lengthscale, as well as control of interaction sign and level of anisotropy [59]. A final benefit is that the lifetime of the system is extended by the low fraction of the Rydberg state in the dressed state.

Several interesting and useful manifestations of Rydberg-dressed interactions have been proposed, for example, supersolid formation in Bose-Einstein condensates [34], spin squeezing to suppress the quantum projection noise limit on optical lattice clocks [60], and quantum logic circuits [61]. Entanglement through a Rydberg-dressed spin-flip blockade in a two-atom system [62] and many-body interferometry in a two-dimensional system [63] have been demonstrated, but both demonstrations have been performed on short

timescales, without scope for extension to the long timescales that Rydberg dressing enables and that many quantum simulators and novel phases of matter require. In addition, these interactions occur without confinement of the atoms during dressing and are limited to one or two dimensions and spatially ordered clouds.

1.1 Motivation

The goal of this thesis is to introduce-Rydberg dressed interactions into a cloud of atoms that is both cooled and confined.

Previous observations of Rydberg dressed interactions and attempts to observe Rydberg dressed interactions have been performed in free space in the frozen gas regime or using optical dipole forces to trap atoms [62–65]. In this work we want to include dissipation within the system; we therefore move away from conservative optical dipole trapping to a dissipative trap.

To obtain trapping and cooling we will use a magneto-optical trap (MOT). A MOT drives atoms between two states, so by dressing the excited state of the MOT transition the cooling of the system becomes inherently linked to the interactions that occur within the system. To achieve sufficiently high atomic densities and low temperatures for Rydberg dressed interactions to be significant we will use a narrow-line strontium MOT. The Rydberg dressed interactions we expect to be achievable within our system are comparable in strength to MOT temperatures, comparable in lengthscale to the interparticle separation in a MOT, and give lifetimes that are comparable to the MOT equilibration time (shown in more detail in Chapter 2.6).

Such a system offers a versatile platform as a many-body quantum simulator. Whilst the Rydberg-dressed interactions are inherently linked to the cooling of the cloud, the interaction strength and lengthscale can be controlled through the Rydberg coupling laser power and frequency independently of the MOT beam power and frequency that control the cooling (dissipation) rate and fraction of atoms in the interacting dressed state. The system is three-dimensional, with many degrees of freedom, and the readout of the simulation is readily available through imaging of the cloud. Whilst it is not immediately clear what system we may model with such a quantum simulator, the demonstration of such a tunable quantum simulator may generate interest sufficient to identify simulatable systems.

1.2 Thesis outline

The work in this thesis towards an actively cooled, confined, interacting medium has several stages of progression, and the structure of this thesis maps these stages accordingly:

- First we outline Rydberg dressing and the mechanism of Rydberg-dressed interactions, consider narrow-line MOTs as a platform for Rydberg-dressed interactions, and set out the concept of a Rydberg-dressed MOT in Chapter 2.
- We summarize the experimental apparatus, including modifications to the operation of the experiment made over the course of this work, in Chapter 3.
- In Chapter 4 we present the 319 nm laser source developed to couple to Rydberg states, outline the Rydberg excitation process, and characterise a range of previously unseen Rydberg states that we will dress the MOT with.
- We couple the MOT to the Rydberg state, observing and characterising the non-interacting Rydberg-dressed MOT and identifying a regime in which only Rydberg-dressed atoms are trapped in the MOT in Chapter 5.
- Increasing the ground state density to reach the interacting regime, we observe loss of ground state atoms associated with plasma formation. We study the origins and consequences of the plasma in Chapter 6 and identify regimes in which plasma formation may be avoided or suppressed.
- Finally, in Chapter 7 we conclude the findings of this thesis, and provide an outlook for the experiment.

Chapter 2

Rydberg dressing a MOT

In this chapter we will present the concept of the dressed state and of Rydberg atom interactions, which we draw together to explain the concept of Rydberg dressing. We consider demonstrations of Rydberg dressing in limited dimensions, and the challenges that have prevented the observation of Rydberg-dressed interactions in three dimensions. We then give a brief description of narrow-line MOTs. From this position we will present the concept of a Rydberg-dressed MOT, possible manifestations of Rydberg-dressed interactions in the MOT, and how to circumvent the barriers to observation of Rydberg-dressed interactions in three-dimensional systems.

2.1 The dressed state

In 1955 Autler and Townes observed splitting of a microwave transition in OCS molecules when one of the two levels was strongly coupled to a third level in a process now known as Autler-Townes splitting [66]. The cause of this splitting is that the bare eigenstates of the uncoupled molecular levels were no longer eigenstates of the coupled system. Instead the new eigenstates contained fractions of both the strongly coupled levels, giving rise to a splitting between the new eigenstates.

The dressed state picture is a powerful tool for understanding this splitting, and can be used to explain a host of other effects. Both semiclassical [67] and fully quantized [68] dressed state approaches exist, but the essence is to express a coupled system of bare states and driving photons, then calculate new eigenstates of the coupled system that are comprised of fractions of the bare states, illustrated in Figure 2.1.

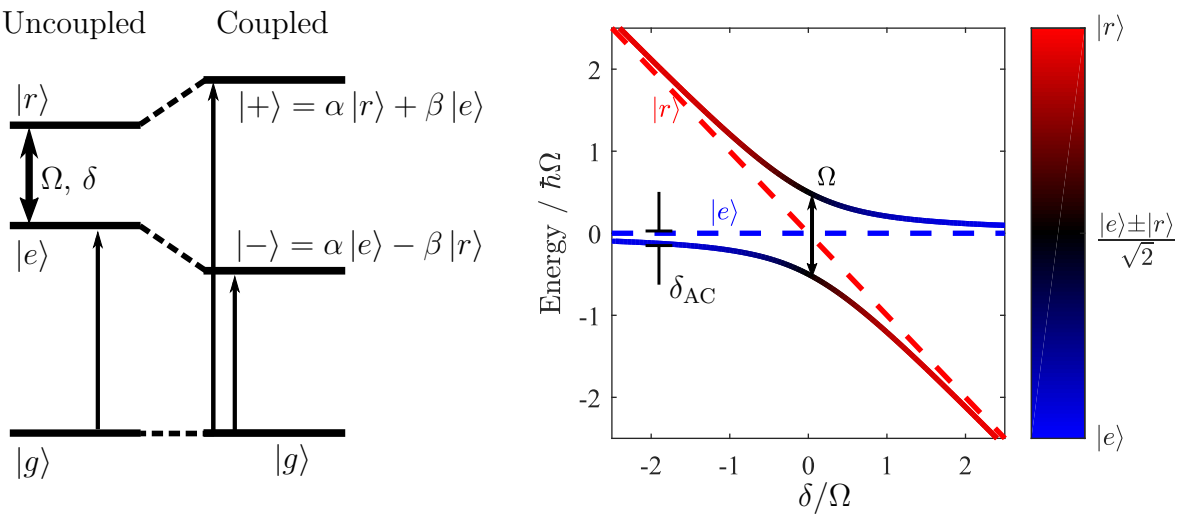

Figure 2.1: The dressed state. Strong coupling between bare states $|e\rangle$ and $|r\rangle$ with coupling light of Rabi frequency Ω and detuned from the transition frequency by δ results in two eigenstates $|+\rangle$ and $|-\rangle$ containing fractions of the two bares states. On the right, the energy of the two dressed states are shown as a function of detuning, the fraction of the bare states (shown as dashed lines) is indicated by colour. For $\delta > \Omega$ we are in the AC Stark shifted regime, on resonance we are in the Autler-Townes regime.

We will consider two eigenstates of an uncoupled system that contains an excited state $|e\rangle$ and a Rydberg state $|r\rangle$. We assume strong coherent coupling between $|e\rangle$ and $|r\rangle$ such that the Rabi frequency Ω, set by the dipole transition strength and the electric field strength, is greater than the inverse of the state lifetime Γ. Using the Rotating Wave Approximation (RWA) the Hamiltonian that describes the system is given by the atom Hamiltonian H_A and the atom-light interaction Hamiltonian H_{AL} [69]:

$$H = H_A + H_{AL} = \hbar \begin{bmatrix} 0 & \Omega/2 \\ \Omega/2 & -\delta \end{bmatrix} ; \tag{2.1}$$

where $\delta = \omega - \omega_0$ is the detuning of the driving field frequency ω from the transition frequency ω_0. This gives the eigenvalues $E_\pm$ and eigenvectors $|+\rangle$ and $|-\rangle$:

$$E_\pm = -\frac{\hbar\delta}{2} \pm \frac{\hbar\sqrt{\Omega^2 + \delta^2}}{2} ; \tag{2.2}$$

$$|+\rangle = \sin\theta\,|e\rangle + \cos\theta\,|r\rangle = \alpha\,|r\rangle + \beta\,|e\rangle \ ; \tag{2.3}$$

$$|-\rangle = \cos\theta\,|e\rangle - \sin\theta\,|r\rangle = \alpha\,|e\rangle - \beta\,|r\rangle \ ; \tag{2.4}$$

$$\tan 2\theta = -\frac{\Omega}{\delta} \ . \tag{2.5}$$

These equations allow us to express both the energy levels of the dressed states and the bare state components of the dressed states. This is illustrated in Figure 2.1. We will also consider how a ground state $|g\rangle$ that may couple to the excited state $|e\rangle$ couples to the two dressed states in the presence of a weak probe beam.

When the coupling laser is exactly on resonance $\alpha = \beta$ and the two dressed states contain equal fractions of the two bare states. The ground state $|g\rangle$ couples equally to the $|e\rangle$ component of the two eigenstates, which are split by $\hbar\Omega/2$ from the undressed states, and separated by $\hbar\Omega$ from each other, shown in Figure 2.1. This is Autler-Townes splitting, shown in Figure 2.2(a), and increases proportionally with Rabi frequency and hence with the square root of coupling beam intensity. The splitting is observed by scanning the probe beam detuning from the bare state $|g\rangle \leftrightarrow |e\rangle$ transition δ_P.

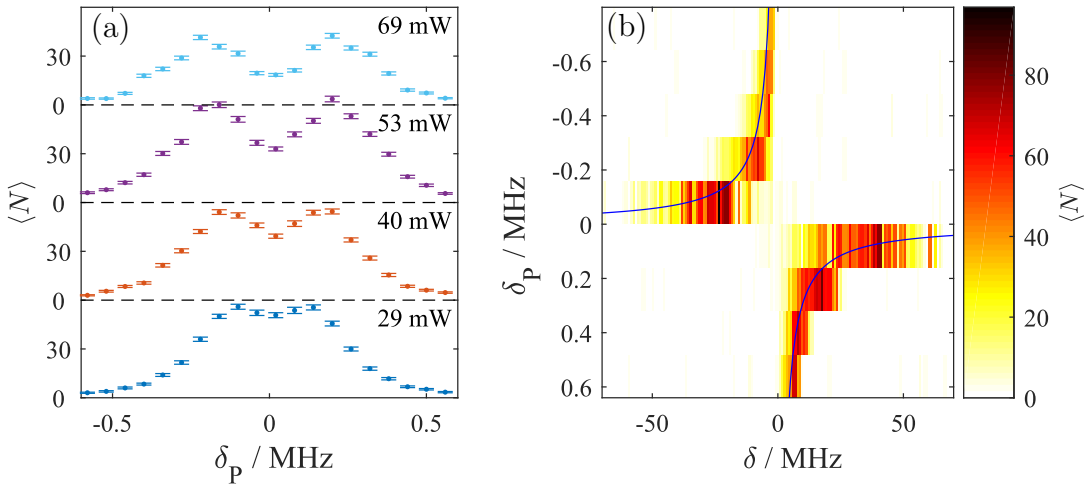

Figure 2.2: Autler-Townes splitting, shown in (a), occurs due to a strong resonant coupling beam resulting in splitting of the dressed states. As we increase the coupling beam power the splitting increases, which we observe by scanning the probe beam δ_P. If the coupling beam is off-resonance by a detuning δ (shown in (b)) the dressed state is AC Stark shifted from the undressed case by $\Omega^2/4\delta$, shown by the blue line. The colourbar indicates ion signal as a measure of Rydberg population. Experimental details are found later in this thesis.

We are interested in the weakly-dressed regime, in which a small fraction of one bare state is mixed into an eigenstate primarily comprised of another bare state. This occurs for small θ, where we can approximate the trigonometric terms ($\cos\theta \approx 1$, $\sin\theta \approx \theta$ and $\tan 2\theta \approx 2\theta$) to get:

$$|e'\rangle \approx |e\rangle - \frac{\Omega}{2\delta}|r\rangle \ . \tag{2.6}$$

Here, we have changed notation from $|+\rangle$ and $|-\rangle$ to $|e'\rangle$ and $|r'\rangle$, where the state $|e'\rangle$ is the state that is predominantly $|e\rangle$ with only a small fraction of $|r\rangle$. The ground state $|g\rangle$ couples strongly to the $|e'\rangle$ due to the large $|e\rangle$ component. The Rydberg fraction of the dressed state $|e'\rangle$ is $f = \beta^2 \approx \Omega^2/4\delta^2$. The dressed state acquires an energy difference with respect to the bare state that is described by Eq. 2.2, which for $\delta \gg \Omega$ can be written as:

$$E_{e'} = \hbar\frac{\Omega^2}{4\delta} \ . \tag{2.7}$$

This shift is known as an AC Stark shift and is shown in Figure 2.2(b). Thus, for coupling with a Rabi frequency that is small compared to the the detuning of the coupling beam, we expect an AC Stark shift that is proportional to the beam intensity and inversely proportional to the beam detuning.

This dressed state picture gives insight into the state mixing that strong coupling light can induce in atoms, without considering interactions between atoms. The motivation of applying this dressed state picture to interacing states is that we can mix small fractions f of a strongly interacting Rydberg state $|r\rangle$ into a non-interacting state $|e\rangle$, to create very controllable, tunable interactions. Before we consider this, however, we will give a brief outline of Rydberg interactions.

2.2 Rydberg atom interactions

Our interest in Rydberg atoms is based on the strong dipole-dipole interactions that they offer. We will first consider the origin of these interactions, and then outline the Rydberg blockade mechanism that results from this.

Origins of Rydberg interactions

The dipole-dipole interactions of Rydberg atoms are well documented in several sources e.g. [49, 70], and are only briefly outlined here. Typically long-range dipole-dipole (also known as van der Waals) and resonant dipole-dipole interactions are considered; both have the same origins. We treat the atoms as hydrogenic i.e. a nucleus of charge $+e$ and an electron of charge $-e$, and assume that the separation of Rydberg atoms is much greater than the nucleus-electron separation.

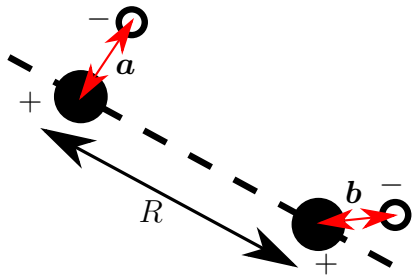

Figure 2.3: Dipole-dipole interaction

First we can express the dipole interaction between the two atoms as [71]:

$$V(R) = \frac{e^2}{R^3}(\hat{\boldsymbol{a}} \cdot \hat{\boldsymbol{b}} - 3a_z b_z) \ ; \tag{2.8}$$

for a quantization axis z defined along the atom axis, and valence electron positions relative to atom A and atom B given by $\boldsymbol{a}$ and $\boldsymbol{b}$. Unit vectors corresponding to these positions are given by $\hat{\boldsymbol{a}}$ and $\hat{\boldsymbol{b}}$, and a_z and b_z represent the electron position in the z direction relative to the positions of atom A and B. Note the R^{-3} dependence, where R is the atomic separation.

This interaction couples the atom pair state $|nl, nl\rangle$ (with binding energy $2E$) to other pair states. For simplicity we consider coupling only to one final pair state $|n_1 l_1, n_2 l_2\rangle$ (with binding energy $E_1 + E_2$):

$$|nl, nl\rangle \rightarrow |n_1 l_1, n_2 l_2\rangle \ . \tag{2.9}$$

The final pair state can be any pair that preserves the angular momentum projection of the initial pair. The initial and final state pairs will have different binding energies, giving rise to an energy defect δ_{12} given by:

$$\delta_{12} = E_1 + E_2 - 2E \ . \tag{2.10}$$

The relative size of this energy defect and the interaction strength $V(R)$ dictates whether we are in the resonant dipole-dipole regime or the van der Waals regime. From the energy defect δ_{12} and the interaction strength $V(R)$ we build the interaction Hamiltonian for the two states $|nl, nl\rangle$ and $|n_1 l_1, n_2, l_2\rangle$:

$$H = \begin{bmatrix} 0 & V(R) \\ V(R) & \delta_{12} \end{bmatrix} \ . \tag{2.11}$$

The eigenvalues of this Hamiltonian are:

$$\Delta_{\pm} = \frac{1}{2}\Big(\delta_{12} \pm \sqrt{\delta_{12}^2 + 4V(R)^2}\Big) \ . \tag{2.12}$$

From this expression we can obtain two regimes. The first is the van der Waals regime, where $\delta_{12}^2 \gg 4V(R)^2$. Under this condition we can Taylor expand to see [a]:

$$\Delta_+ \approx \frac{V(R)^2}{\delta_{12}} = \frac{C_6}{R^6} \ . \tag{2.13}$$

This gives an interaction that decays as R^{-6}, and occurs when the interaction between atoms is much weaker than the energy difference between the pair state and all possible other Rydberg pairs. We introduce the C_6 coefficient, which reflects the energy difference between pair states and may be anisotropic due to angles between the quantisation axis and electron position shown in Equation 2.8. The C_6 coefficient can be positive or negative, indicating whether interaction between the Rydberg atoms is repulsive or attractive.

One eigenstate will comprise primarily of the $|nl, nl\rangle$ state and the other will comprise primarily of the $|n_1 l_1, n_2 l_2\rangle$ state, with very little mixing, so a ground state that only couples to the $|nl, nl\rangle$ state will only couple to one of the two eigenstates. We expect to see a shift in energy of the $|nl, nl\rangle$ state described by C_6/R^6.

The second regime is the resonant dipole-dipole regime, where $\delta_{12}^2 \ll 4V(R)^2$ i.e. the interaction between the atom pair is greater than the energy difference between the two pair states. Taylor expanding, we see:

[a] Here $\delta_{12} < 0$ resulting in repulsive van der Waals interactions, and the eigenvalue Δ_+ corresponds predominantly to the $|nl, nl\rangle$ state. It is trivial to instead consider $\delta_{12} > 0$ and attractive interactions.

$$\Delta_{\pm} \approx \pm|V(R)| = \pm\frac{C_3}{R^3} \ . \tag{2.14}$$

Here the interaction scales as R^{-3} according to the C_3 coefficient, which, as with the C_6 coefficient, reflects anisotropies due to the quantisation axis. This regime typically occurs near Förster resonances, where the excited Rydberg pair is degenerate or nearly degenerate with another Rydberg pair. It also becomes dominant at short separations as $V(R)$ increases. There is strong mixing of both pair states; consequently, a state that couples only to the $|nl, nl\rangle$ state may couple to either of the eigenstates, one of which rises in energy and one of which falls.

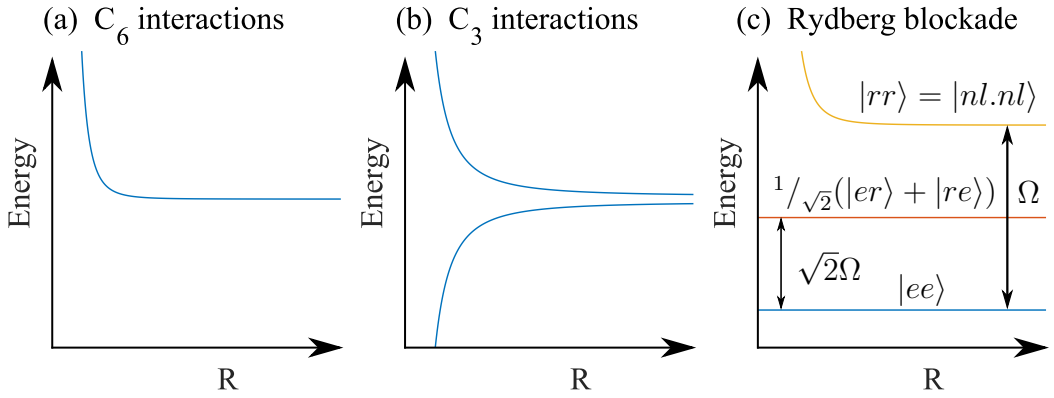

Figure 2.4: Energy level shifts for repulsive C_6 interactions (a) and symmetric C_3 interactions (b). (c) illustrates the Rydberg blockade - at long distances Rabi oscillations between the ground state $|ee\rangle$ and the doubly excited state $|rr\rangle$ occur with the same Rabi frequency as the one-body $|e\rangle \leftrightarrow |r\rangle$ Rabi frequency Ω. At close distances the Rydberg pair state $|rr\rangle$ is off resonance with the coupling laser and Rabi oscillations occur between the ground state $|ee\rangle$ and the intermediate state $^1/_{\sqrt{2}}(|er\rangle + |re\rangle)$ with a $\sqrt{2}$ increase in Rabi frequency.

The difference between the two interactions is illustrated in Figure 2.4(a-b). A key difference between the two is that only resonant dipole-dipole interactions are symmetric - a coupling laser that is detuned from the transition may excite pairs of Rydberg atoms when the interaction shift matches the coupling laser detuning magnitude. In the case of van der Waals interactions, the coupling beam laser detuning must also match the sign of the interaction for pair excitation to occur. As we will see later, this is critical to the ability to off-resonantly dress atoms with Rydberg state.

Rydberg blockade

Both regimes can give rise to one of the most interesting results of Rydberg atoms - Rydberg blockade [72, 73]. Consider the Hamiltonian of a two-atom two-level system, with four possible states $|ee\rangle$, $|er\rangle$, $|re\rangle$ and $|rr\rangle$ and an interaction V_{int} occuring between the two atoms in the doubly excited $|rr\rangle$ state. The $|e\rangle$ state couples to the $|r\rangle$ state through a resonant coupling beam of Rabi frequency Ω, resulting in the Hamiltonian:

$$H = \hbar \begin{bmatrix} 0 & \Omega/2 & \Omega/2 & 0 \\ \Omega/2 & 0 & 0 & \Omega/2 \\ \Omega/2 & 0 & 0 & \Omega/2 \\ 0 & \Omega/2 & \Omega/2 & V_{\text{int}} \end{bmatrix} . \tag{2.15}$$

To simplify this we transform the system to an effective three-level system $|ee\rangle$, $(|er\rangle + |re\rangle)/\sqrt{2}$ and $|rr\rangle$ by noting that the eigenstate $(|er\rangle - |re\rangle)/\sqrt{2}$ has a matrix element of 0 i.e. is not coupled:

$$H = \hbar \begin{bmatrix} 0 & \sqrt{2}\Omega/2 & 0 \\ \sqrt{2}\Omega/2 & 0 & \sqrt{2}\Omega/2 \\ 0 & \sqrt{2}\Omega/2 & V_{\text{int}} \end{bmatrix} . \tag{2.16}$$

If $V_{\text{int}} \ll \Omega$ we can reduce this further to a two-level system and we will see Rabi oscillations between the $|ee\rangle$ and $|rr\rangle$ states with a Rabi frequency of Ω. However, for interactions much stronger than the Rabi frequency the $|rr\rangle$ state becomes far off resonance, and we will observe Rabi oscillations between the $|ee\rangle$ and $(|er\rangle + |re\rangle)/\sqrt{2}$ states with a Rabi frequency $\sqrt{2}\Omega$.

We will therefore see a blockade effect, in which we do not couple to the doubly excited state, which is accompanied by a $\sqrt{2}$ increase in Rabi frequency. This is illustrated in Figure 2.4(c). It is trivial to see that an increase in the number of atoms experiencing strong interactions from 2 to N will result in a $\sqrt{N}$ speed-up in Rabi frequency.

We also define a Rydberg blockade radius to characterise the separation over which atoms will experience this speed-up, defined as the distance at which the Rydberg pair interaction equals the transition width. For van der Waals interactions and a transition width defined by the Rabi frequency this gives a Rydberg blockade radius of:

$$r_{\mathrm{B}} = \sqrt[6]{\frac{|C_6|}{\hbar\Omega}} \ . \tag{2.17}$$

To maximise the interaction strength and minimise the density at which we may observe Rydberg atom interactions, we require large C_6 coefficients.

C_6 coefficients

Having considered the theory of van der Waals interactions, we now consider the C_6 coefficients of the Rydberg states that we may couple the MOT to. The excited state of the narrow-line strontium MOT transition is the $5s5p\ ^3P_1$ state, and we will therefore consider Rydberg states that can couple to from this state, namely the $5sns\ ^3S_1$, $5snd\ ^3D_1$ and $5snd\ ^3D_2$ states, where n is the principal quantum number. The strength of the van der Waals interaction is dependent on angular momentum state and orientation of the interacting Rydberg atoms; averaging over the possible angular momentum states and directions C_6 coefficients are estimated based on [74], shown in Figure 2.5.

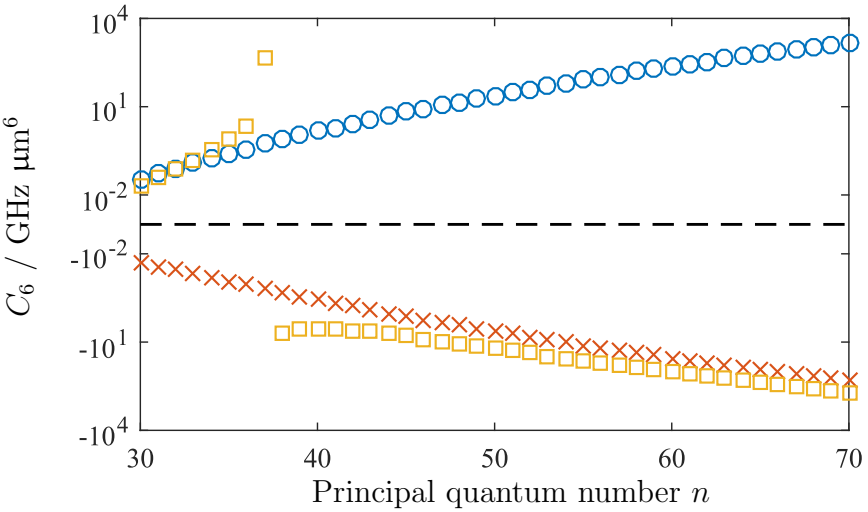

Figure 2.5: Calculated C_6 coefficients for the $5sns\ ^3S_1$ (blue circles), $5snd\ ^3D_1$ (red crosses) and $5snd\ ^3D_2$ (yellow squares) series.

We see repulsive interactions for the $5sns\ ^3S_1$ series, since the C_6 coefficients are positive, attractive interactions for the $5snd\ ^3D_1$ series, and a Förster resonance at $5s37d\ ^3D_2$, below which the interactions are repulsive and above which the interactions are attractive. Förster resonances occur at small quantum defects; we therefore see stronger interactions

at and near the Förster resonance. At $5s37d\ ^3D_2$ we expect to observe resonant dipole-dipole interactions rather than van der Waals interactions.

The approach to Rydberg atom interactions outlined above yields insight into the phenomenon of Rydberg blockade when the coupling beam is resonant and transitions may be strongly driven by coupling light. However, we are interested in the Rydberg dressed regime, in which an off-resonant coupling laser mixes a small fraction of the Rydberg state $|r\rangle$ into the excited state $|e\rangle$.

2.3 Rydberg-dressed interactions

In this section we will consider how Rydberg atom interactions can translate through the dressed state picture to result in interactions between atoms that are primarily in non-interacting states [75, 76]. At large separations and weak interactions, the interaction between two dressed state atoms can be described by the $|rr\rangle$ fraction in the dressed-dressed state $f^2 = (\Omega^2/4\delta^2)^2$ so that the dressed interaction strength is given by $f^2 C_6/r^6$. At small separations, the $|rr\rangle$ fraction of the dressed state pair is suppressed by the strong interactions of the bare state Rydberg pair.

We will first consider a simple Hamiltonian similar to the one used to understand Rydberg blockade, which illustrates the energy shift that results from Rydberg dressed interactions [77]. A more advanced perturbative treatment from [34] then yields information on the interaction strength dependence on separation of atoms. We consider only van der Waals interactions and a coupling beam detuning sign opposite to the van der Waals interaction sign to avoid Rydberg pair excitation.

A simple approach to Rydberg-dressed interactions

In Section 2.1 we showed how the dressed state picture can explain the energy difference between the bare state and the dressed state i.e. the AC Stark shift. We will use the same approach to show the energy difference between the dressed state with Rydberg atom interactions and without Rydberg atom interactions. This treatment was developed in [77].

The AC Stark shift of the non-interacting case will simply be N times the one-body AC Stark shift given in Equation 2.2 where N is the number of interacting dressed state

atoms:

$$E_{N,V\ll\Omega} = \frac{-N\hbar\delta}{2}\left(1 - \sqrt{\frac{\Omega^2}{\delta^2}+1}\right) . \tag{2.18}$$

The AC Stark shift of the strongly interacting case is more complicated, but can be understood from a simplified version of the N-body Hamiltonian. Firstly, we neglect any state with two or more atoms in the Rydberg state, as the strong Rydberg interactions will prevent coupling to this state. This leaves the ground state $|e^N\rangle$ and N singly excited states $|re^{N-1}\rangle$, $|ere^{N-2}\rangle$ etc. We simplify this further to obtain a Hamiltonian in terms of the ground state $|e^N\rangle$ and the fully symmetric state ${}^1/_{\sqrt{N}}(|re^{N-1}\rangle + |ere^{N-2}\rangle + ... + |e^{N-1}r\rangle)$:

$$H = \hbar \begin{bmatrix} 0 & \sqrt{N}\Omega/2 \\ \sqrt{N}\Omega/2 & -\delta \end{bmatrix} ; \tag{2.19}$$

where all other states are not coupled. This is simply expressing Equation 2.16 in the case of N atoms, a coupling beam detuning, and sufficiently strong interactions for multiply excited Rydberg states to not be coupled. Note the $\sqrt{N}$ speed-up due to Rydberg blockade. For $|\delta| \gg \sqrt{N}\Omega/2$ the eigenvalue of the $|e^N\rangle$ state is:

$$E_{N,V\gg\Omega} = \frac{-\hbar\delta}{2}\left(1 - \sqrt{\frac{N\Omega^2}{\delta^2}+1}\right). \tag{2.20}$$

Equations 2.18 and 2.20 describe the AC Stark shift of the $|e^N\rangle$ state for N atoms that are not interacting and that have strong Rydberg interactions respectively. Taking the difference between these two equations by using the assumption that $\sqrt{\frac{N\Omega^2}{\delta^2}} \ll 1$, we get the peak energy shift from the non-interacting to the strongly interacting regime:

$$V_D = |E_{N,V\ll\Omega} - E_{N,V\gg\Omega}| = \hbar\frac{N(N-1)}{2}\frac{\Omega^4}{8\delta^3} . \tag{2.21}$$

This is the Rydberg dressed interaction, emerging due to the $\sqrt{N}$ speed-up in Rabi frequency that occurs due to Rydberg blockade. This interaction displays several interesting features.

Firstly, the dressed interaction strength is only dependent on the coupling beam Rabi frequency, detuning and the number of interacting atoms, not the C_6 coefficient that

characterises the Rydberg state interactions. Once the $|rr\rangle$ fraction of the dressed state pair is suppressed, the energy shift of the dressed state pair becomes flat. This is a major strength - it allows the dressed interaction strength to be tuned through coupling laser Rabi frequency and detuning, which are readily available experimental controls. As we require $\Omega \ll \delta$ to be in the dressed regime we can maximise our interaction strength by increasing both Ω and δ.

Finally, we observe an $N(N-1)$ dependence, where N is the number of atoms with strong Rydberg-Rydberg state interactions. To understand the significance of this number, we must understand the lengthscale of the Rydberg dressed interaction. This requires a more advanced model, where we can't simply treat the Rydberg-Rydberg interaction as much greater or smaller than the Rabi frequency. To do this, we use the results of a perturbative treatment.

A perturbative approach to Rydberg dressed interactions

The treatment outlined above reveals the Rydberg dressed interaction strength as a result of the $\sqrt{N}$ speed-up that Rydberg blockade causes. However, it only considers the regimes of very strong and very weak van der Waals interactions. For small N we can construct and numerically solve the appropriate Hamiltonian. Equation 2.22 shows the same two-atom two-level Hamiltonian as Equation 2.16 but including a coupling beam detuning δ, expressed as a three-level system $|ee\rangle$, $(|er\rangle + |re\rangle)/\sqrt{2}$ and $|rr\rangle$:

$$H = \hbar \begin{bmatrix} 0 & \sqrt{2}\Omega/2 & 0 \\ \sqrt{2}\Omega/2 & -\delta & \sqrt{2}\Omega/2 \\ 0 & \sqrt{2}\Omega/2 & {}^{C_6}/_{r^6} - 2\delta \end{bmatrix} . \tag{2.22}$$

Figure 2.6 shows a numerical calculation of the eigenvalues of this Hamiltonian, which illustrates the Rydberg dressed interaction. However, we prefer a technique that offers more insight and scalability to high N.

In [59] a perturbative treatment is applied to this Hamiltonian. The eigenvalue of the ground state is considered as a series of expansions, subject to $\Omega \ll \delta$. Odd orders of this expansion correspond to an odd number of virtual processes that do not modify the ground state energy. The second order of this perturbative expansion yields the one-body AC Stark shift associated with a two-photon event i.e. the ground state coupling to a singly excited state that couples to the ground state. The fourth order of this

perturbation treatment considers four-photon events, allowing the ground state to couple to a doubly-excited state that couples to the ground state. This yields the Rydberg dressed interaction that we seek:

$$V_D(r) = \frac{\hbar\Omega^4}{8|\delta|^3}\left[1 + \left(\frac{r}{r_D}\right)^6\right]^{-1}. \tag{2.23}$$

The shape of the dressed interaction potential is shown in Figure 2.6 for $\delta = 12$ MHz, $\Omega = 4$ MHz. At large separations $(r/r_D)^6 \gg 1$ we see an interaction energy described by $(\Omega/2\delta)^4 C_6/r^6 = f^2 C_6/r^6$. Thus at large separations, Rydberg dressed interactions follow the Rydberg-Rydberg interaction but reduced by the $|rr\rangle$ fraction of the excited-excited state. At small separations, we see the interaction level off at the value given by Equation 2.21, as expected.

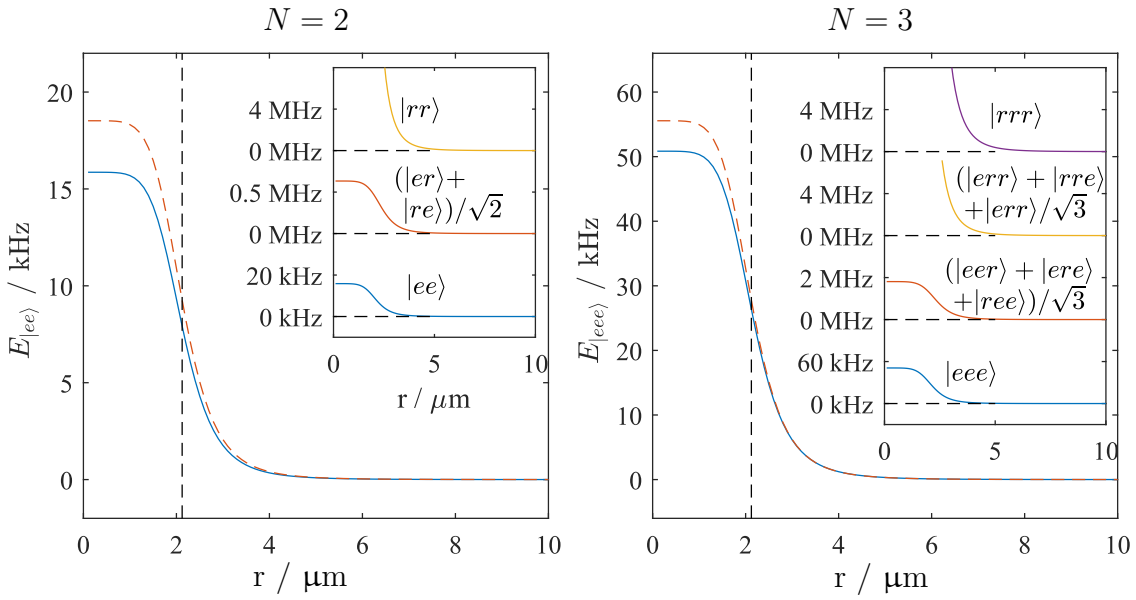

Figure 2.6: Shift of the dressed state as a function of interatomic separation for two (left) and three (right) atom systems and $\delta = -12$ MHz, $\Omega = 4$ MHz. $C_6 = 2.2$ GHz μm^6. The solid blue line shows the lowest eigenvalue of the Hamiltonian 2.22, the dashed orange line shows the perturbative approach described by Equation 2.23, which relies on the assumption $\Omega \ll |\delta|$. The vertical dashed line represents the dressed blockade radius r_D. Inset, all eigenvalues are shown- the labels are deceptive as $|e\rangle$ and $|r\rangle$ are eigenvalues of the uncoupled system only, and are for indicative use only. The one-body AC Stark shift has been subtracted.

In this expression we have defined a dressed blockade radius corresponding to the distance

at which the effective Rabi frequency $\Omega_{\text{eff}} = \sqrt{\Omega^2 + (2\delta)^2} \approx 2|\delta|$ equals the Rydberg-Rydberg interaction C_6/r^6:

$$r_D = \left(\frac{C_6}{2\hbar\delta}\right)^{1/6} . \tag{2.24}$$

Comparing the result of this perturbative treatment to a numerically calculated eigenvalue of Equation 2.22 in Figure 2.6 we see good agreement between the dependence of the interaction on separation, although there is a constant scaling between the two values due to the limited accuracy of the approximation $\delta \gg \Omega$. In the case of the numerical solution of the full Hamiltonian we have subtracted the one-body AC Stark shift.

This perturbative treatment can be extended to the many-body case, subject to the validity of the perturbative treatment, which requires that $\sqrt{N}\Omega \ll 2\delta$. Here, we must be careful of our use of a single value r to express distance between dressed state atoms - as there are many atoms there will be many distances between them. A thorough treatment is given in [59]; we will consider the two cases shown in Figure 2.7.

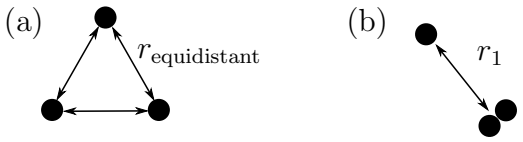

Figure 2.7: An illustration of the separation of dressed state atoms. Left, we consider all atoms being equidistant. Right, we consider a single dressed state at a distance r_1 from other dressed state atoms.

First we consider the number of atoms per dressed blockade sphere, which can be calculated from the dressed blockade radius r_D and the dressed state density ρ_D:

$$N = \frac{4}{3}\pi r_D^3 \rho_D . \tag{2.25}$$

When $N > 1$ we expect Rydberg dressed interactions to emerge.

If we consider the case of a collection of N atoms all separated from every other atom by a distance $r_{\text{equidistant}}$ the perturbative treatment yields [59]:

$$V_D(r_{\text{equidistant}}) = \frac{N(N-1)}{2}\frac{\Omega^4}{8|\delta|^3}\left[1 + \left(\frac{r_{\text{equidistant}}}{r_D}\right)^6\right]^{-1} . \tag{2.26}$$

In this case we go from all atoms within the blockade radius at $r_{\text{equidistant}} \ll r_D$ to no atoms within the dressed blockade radius at $r_{\text{equidistant}} \gg r_D$. The factor of $N(N-1)/2$ is the total number of pairs that can be made from N atoms, and returns the two atom case given in Equation 2.23 when $N = 2$. This expression also yields the interaction strength given using the simple approach of Equation 2.21.

Next we consider a cluster of $N-1$ atoms occupying the same position and the N^{th} atom at a distance r_1 from the cluster:

$$V_D(r_1) = (N-1)\frac{\Omega^4}{8|\delta|^3}\left[1 + \left(\frac{r_1}{r_D}\right)^6\right]^{-1}. \tag{2.27}$$

In this case we go from N atoms within the dressed blockade radius to $N-1$ atoms in the dressed blockade radius as r_1 increases, reducing the number of pairs by $N-1$. Again, the two-atom case is recovered for $N = 2$.

As with the two-atom case, we compare the results of Equation 2.27 with a numerically calculated dressed interaction from the three-atom two-level Hamiltonian, again with the one-body AC Stark shift subtracted. This is shown in Figure 2.6. We see good agreement subject to a scaling due to the limited accuracy of the approximation $\sqrt{N}\Omega \ll 2\delta$.

Rydberg dressed interactions

In this section we have shown how the Rydberg blockade can translate through the dressed state picture to introduce interactions in ground or excited states. A key point to note from Equation 2.23 is the high level of control offered by Rydberg dressed interactions. The maximum strength of the interactions is given by $\Omega^4/8|\delta|^3$, both easily controllable parameters through laser power and frequency, and the interaction lengthscale is given by $(C_6/2\delta)^{1/6}$. C_6 coefficients scale with principal quantum number as n^{11}, allowing wide tunability of interaction lengthscale.

The versatility of these interactions have led to a boom in theoretical predictions concerning potential applications of Rydberg dressing, for example, formation of supersolids [34] [78], enhanced metrology [60] and quantum computing [61, 79]. Experimental progress is much slower.

2.4 State of the art Rydberg dressing

In optical tweezers, with only two atoms, Rydberg-dressed interactions have been observed and used to entangle atoms in a Bell state, although outside of the usually taken condition $\Omega \ll \delta$ [62]. In a two-dimensional lattice spin-spin correlation measurements have shown Rydberg dressed interactions and demonstrated the tunability and anisotropy of Rydberg dressed interactions, subject to post filtering to eliminate a fast avalanche-like loss process on some shots [63].

Both these systems use limited dimensionality and highly controlled systems to control the form of the interactions. In addition, neither observe, nor expect to observe, atomic motion attributable to the Rydberg dressed interaction, due to the short timescales of the experiment. A key strength of Rydberg dressing is the extended lifetime of the system obtained by mixing small fractions of the Rydberg state into non-interacting states, which has not been demonstrated yet [77].

Moving away from this regime, to the three-dimensional, disordered case, work towards Rydberg dressed interactions has faced heavy trap loss [64, 65]. This has largely been attributed to Rydberg atoms being driven by blackbody radiation to neighbouring Rydberg states. These states exhibit symmetric resonant dipole-dipole interactions, which can facilitate enhanced Rydberg excitation when off-resonantly coupling to the Rydberg state. This is a problem that must be avoided or overcome.

From these studies we can place our work on a Rydberg dressed MOT in perspective. We must be able to avoid the resonant dipole-dipole loss mechanisms that prevent the observation of loss in other systems.

All of these techniques have been attempts to dress the ground state. In the case of one-photon dressing, this requires using $l = 1$ Rydberg states as the dressing state, which results in anisotropy in the interactions. Two-photon dressing allows a choice of $l = 0$ or $l = 2$ Rydberg states, but typically with a lower effective Rabi frequency, reducing the Rydberg dressed interaction strength. Dressing an excited state allows a wider range of coupling states and strong one-photon coupling.

Finally, all of the experiments above have used atoms trapped using optical dipole forces. This presents a limitation in seeing continued cooling of the trapped atoms, as optical dipole trapping is conservative, making it difficult to combine trapping, cooling and Rydberg dressed interactions,

From this work we can conclude that whilst Rydberg dressed interactions are observable, there are many challenges to be overcome. An ideal system would:

- Use one-photon dressing to maximise the dressing Rabi frequency;
- Operate over a sufficiently long timescale with sufficiently strong interactions for a change in cloud dynamics to be observable;
- Include a dissipative cooling process to allow a change in cloud temperature;
- Avoid rapid loss due to resonant dipole-dipole interactions that occur at high density;
- Extend the previous observations of Rydberg dressed interactions to three dimensional disordered systems.

Having considered the theory of Rydberg dressed interactions, and some of the experimentally observed barriers to seeing Rydberg dressed interactions, we now provide an introduction to narrow-line MOTs. This will allow us to present the concept of a Rydberg dressed MOT.

2.5 Narrow-line MOTs

In broadline MOTs, transition linewidths are several orders of magnitude larger than the Doppler shift due to a single photon recoil, and the temperature will largely be set by the transition width, excluding sup-Doppler cooling techniques. In this section we will describe how narrow-line MOTs differ from broadline MOTs, and how these differences make narrow-line MOTs an ideal platform for the observation of Rydberg dressed interactions.

Narrow-line consequences and regimes

The narrow transition width condition $\Gamma \sim \omega_R$ states that the transition linewidth $\Gamma = 2\pi \times 7.4$ kHz is comparable to the photon recoil frequency shift $\omega_R = \hbar k^2/m$, where $k = 2\pi/\lambda$ is the photon wavenumber and m is the atomic mass. The first consequence of this is that **single photon recoil can dominate the MOT dynamics**, with a single photon

recoil sufficient to take the atom off resonance with the MOT light. Consequently, the cloud temperature may be dominated by the single photon recoil temperature, allowing us to reach cloud temperatures as low as 400 nK [80].

The narrowness of the transition also means that a small magnetic field can take the MOT light off resonance. The MOT light can thus be made to scatter only at a particular magnetic field, creating a resonant ring, making the **MOT position very sensitive to magnetic field gradient and MOT beam detuning**. We can reach cloud sizes as small as 20 μm $1/e^2$ radius in the vertical direction and 50 μm $1/e^2$ radius in the horizontal direction. This shell-like structure is observed in Figure 2.8.

A consequence of the low scattering rate is the reduced light force - photons can be scattered at a maximum rate of $\Gamma/2$. In the case of the narrow strontium transiton this limits the maximum scattering force to ~ 16 times that of gravity, and **gravity can no longer be considered negligible to atom dynamics**, particularly where the detuning of the MOT beams is greater than the power-broadened linewidth. Figure 2.8(b-d) shows atoms sagging under gravity to near the bottom of the resonance shell, but being trapped slightly above the resonance position, where scattering matches gravity. We often use a more intense vertical red MOT beam to compensate the effect of gravity, with a ratio of 3:1:1 in the vertical and horizontal directions.

The low scattering rate also increases the radiation pressure limit - in broad line MOTs scattered photons create a force that pushes away from the densest region of the MOT, limiting the trap density. With a reduced scattering rate, **the maximum MOT density is higher** [80]. We can reach densities as high as 2×10^{12} cm^{-3}.

Typically when considering narrow-line MOTs three regimes are considered based on the relative strength of MOT beam detuning δ_{MOT}, power-broadened linewidth Γ_E and single photon recoil frequency shift [81]:

- **Regime I**: $\delta_{\mathrm{MOT}} > \Gamma_E$ - the resonant ring regime, in which atoms predominantly interact with the vertically upward-pointing MOT beam, sagging under gravity to a point where the Zeeman shift matches the MOT beam detuning. This is shown in Figure 2.8(b-d).
- **Regime II**: $\Gamma_E \gtrsim \delta_{\mathrm{MOT}}$ - the standard Doppler regime, in which atoms can scatter from all MOT beams and cooling is dominated by the velocity of the atoms, closest to standard Doppler theory. The scattering force follows a dispersive shape and the

effect of gravity is small, illustrated in Figure 2.8(a).

- **Regime III**: $s \approx 1$ - the quantum regime, in which single photon recoils dominate trap dynamics, and the temperature is limited by the photon recoil limit. The sensitivity to detuning is similar to Regime I.

Figure 2.8 shows the detuning dependence of a MOT for $s = I/I_{\mathrm{SAT}} = 18$ (6) in the vertical (horizontal) beams. This illustrates the detuning dependence of the MOT position and also the transition from Regime II at $\delta_{\mathrm{MOT}} = -50$ kHz to Regime I at $\delta_{\mathrm{MOT}} = -150$ kHz.

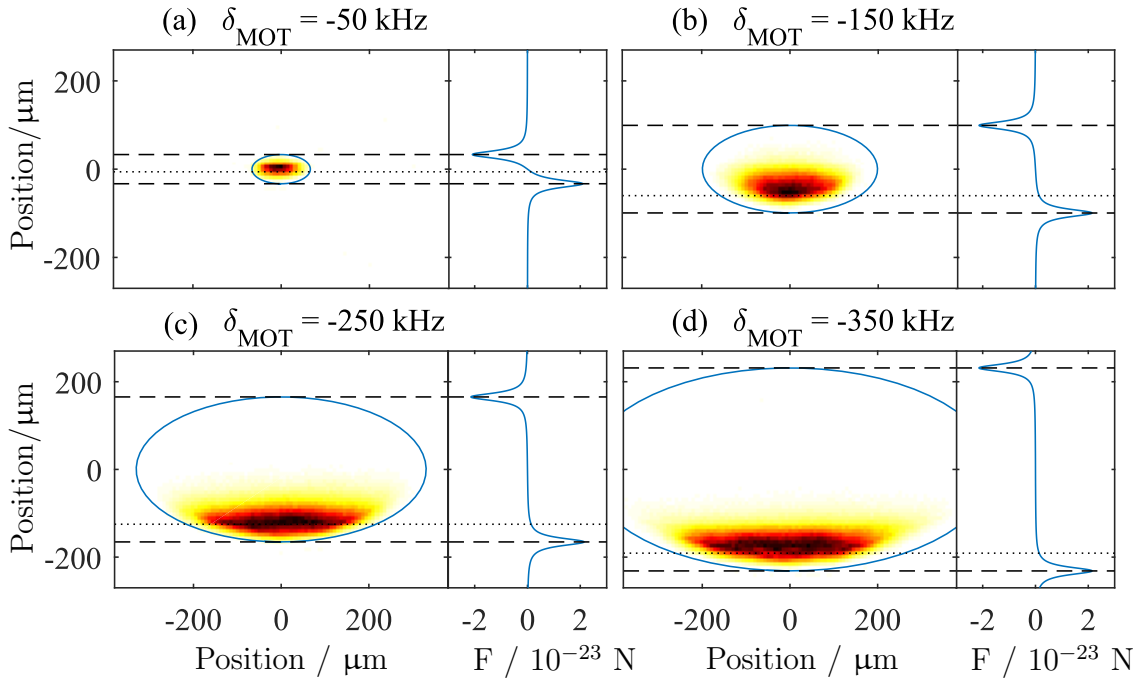

Figure 2.8: MOT images and vertical scattering force (right) for four different MOT beam detunings. The resonant ellipse is shown in blue; the position of maximum scattering force in the vertical direction is shown by dashed lines, and equilibrium with gravity is shown as a dotted line.

Another novel regime that can occur for blue-detuned MOT or probe light and narrow transitions is momentum space crystals, demonstrated in Appendix B. These further demonstrate the sensitivity of the cloud to small changes in MOT or probe beam detuning, with changes of 20 kHz being detectable from images of momentum space crystals.

Resonance curves

A key feature of Regime I and III MOTs is the resonance curves that they can be described by. When the MOT beam detuning is large compared to the power broadened linewidth scattering will only occur for a thin resonance shell where the Zeeman shift of the $5s5p\ ^3P_1\ m_J = -1$ state matches the MOT beam detuning δ_{MOT}:

$$\delta_{\mathrm{MOT}} = m_J g_J \mu_B \frac{\mathrm{d}\boldsymbol{B}}{\mathrm{d}\boldsymbol{z}} \cdot \boldsymbol{z}_{\mathrm{res}} \ ; \tag{2.28}$$

Here $m_J = -1$ is the magnetic sublevel of the MOT transition, $g_J = 1.5$ is the Lande g factor and $\mu_B = 1.4$ MHz/G is the Bohr magneton. $\frac{\mathrm{d}\boldsymbol{B}}{\mathrm{d}\boldsymbol{z}}$ is the magnetic quadrupole field gradient, typically 8 G/cm in the vertical direction and half this in the horizontal directions, and $\boldsymbol{z}_{\mathrm{res}}$ is the resonant ellipse at which the Zeeman shift matches the MOT beam detuning.

Changing the detuning of the MOT beams causes this resonance condition to form at a different position, and widens the bowl that the atoms sit at the bottom of, illustrated in Figure 2.8(b-d), but does not change the cloud temperature. The temperature depends purely on the MOT beam power. This is shown in Figure 2.9(d). Another consequence of MOT beam power is that the cloud position will change slightly, as the MOT forms not at the position of maximum scattering, but at the position where scattering compensates gravity, resulting in the offset between the cloud position and the resonance curves observed in Figure 2.8(b-d).

MOT modelling

Whilst the resonant ellipses that describe the cloud position are useful, they don't provide insight into the cloud dynamics. To understand these dynamics a narrow-line MOT model has been developed by R. Hanley and P. Huillery [82]. This model has three components:

- Propagating the position and velocity of atoms based on gravity and scattering events, requiring;
- Calculating the probability of scattering events for all six beams and three transitions, calculated from the steady state optical Bloch equations, requiring;

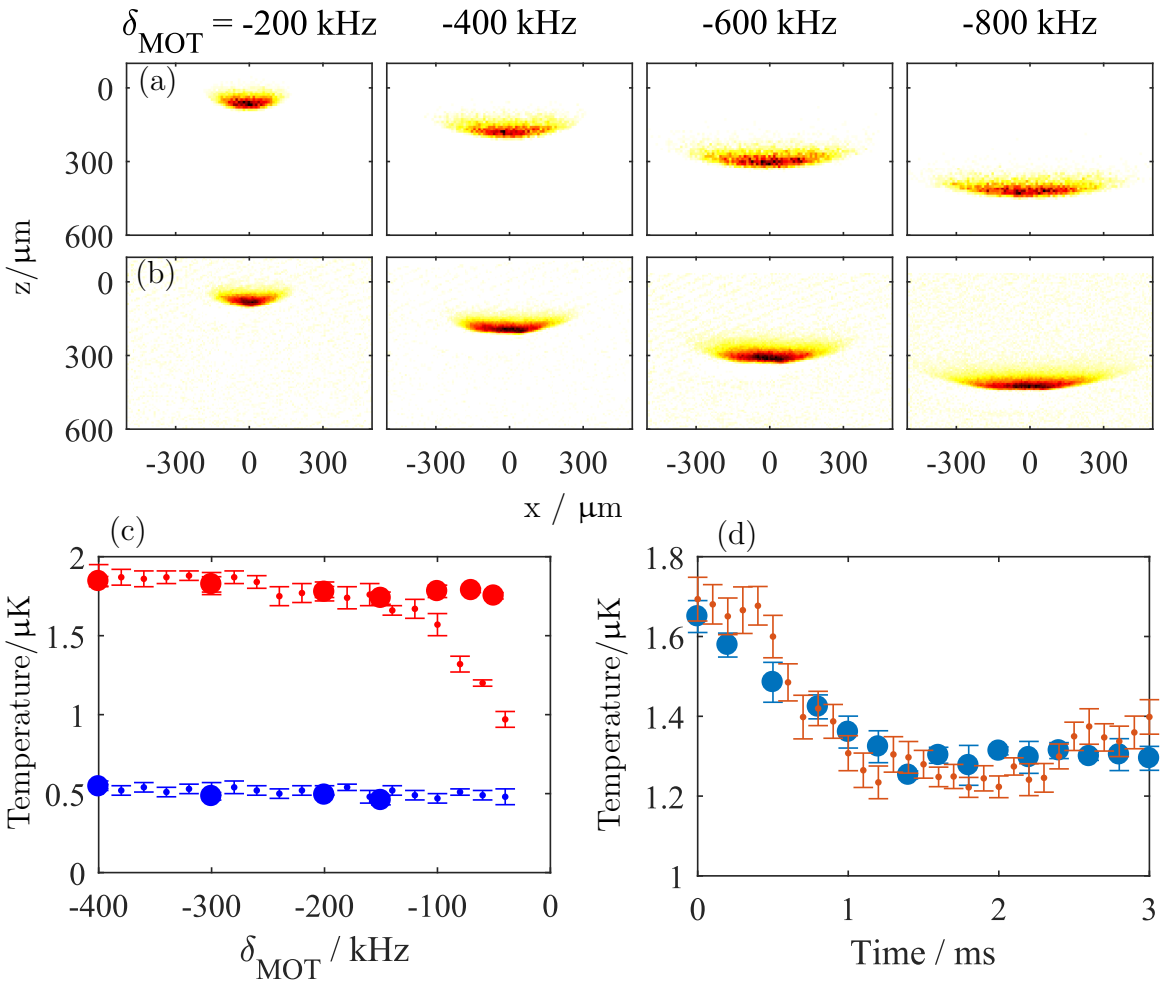

Figure 2.9: The Monte-Carlo MOT model presented in [82] can accurately reproduce the cloud shape and size, temperature and cooling and heating rates for Regime I and III MOTs. Row (a) shows model data for a range of coupling beam detunings, compared to experimental data in row (b). (c) shows model temperatures (dots) compared to experimental data (filled circles) for MOT beam intensities of $s = 1.9$ (blue) and $s = 60$ (red). We see good agreement for Regime I and III MOTs, but the model breaks down for Regime II MOTs (high power and small MOT beam detunings) as the scattering rates are no longer independent. We also observe good agreement to the cloud cooling rate, shown in (d) by introducing a step-change in MOT beam intensity from $s = 31$ to $s = 14$.

- Calculating the effective polarisation of each MOT beam in the atomic reference frame.

This model reproduces the cloud shape, temperature and cooling rate, illustrated in Figure 2.9, for Regime I and III MOTs. The probability of scattering light from the MOT beams is calculated independently for all MOT beams and all Zeeman sublevels, a treatment that breaks down in regimes where the Zeeman shift is small compared to the transition width or where the MOT beam detuning is small compared to the Zeeman shift. Consequently, the model breaks down in Regime II MOTs, where atoms interact with all the MOT beams. However, when working with Regime I and III MOTs the model yields excellent agreement with the data. This model is extended to the Rydberg dressed MOT in Section 5.2 by replacing the two-level optical Bloch equations with three-level optical Bloch equations to provide insight into the Rydberg dressed MOT.

From this model we can also predict the fraction of atoms in the excited state. In Regime I and III MOTs this is $\sim$ 5 - 10% for typical parameters, this is comparable to simple estimates based on the relative strength of single photon recoil, the force of gravity and the mean atomic speed. In Regime II MOTs we expect half of the atoms to be in the excited state and half in the ground state.

A MOT for Rydberg dressing

An ideal MOT for Rydberg dressing would have:

- The low temperatures associated with Regime III;
- The high detuning sensitivities of Regimes I and III;
- The high densities and trap lifetimes associated with Regimes I and II;
- The high excited state fractions associated with Regime II.

Clearly, no single regime is universally better for Rydberg dressing. We have other requirements; we want a MOT that is small compared to the Rydberg dressing laser beam, and a MOT beam detuning that is large compared to the frequency noise of the 689 nm laser. The nature of the Rydberg dressed interaction that we wish to see will also influence our choice of MOT regime, which we consider in the next section.

2.6 A Rydberg dressed MOT

The goal of this thesis is to observe tunable, controllable interactions between atoms in an ultracold cooled and confined atomic cloud. The mechanism we choose to do this is to introduce Rydberg dressed interactions into a magneto-optical trap. In this section we will present the concept of a Rydberg dressed MOT, outline the viability of such a system and describe some potential manifestations of Rydberg dressed interactions within the trap.

In this thesis we describe the process of coupling the $5s5p\ ^3P_1$ state to a Rydberg state whilst sustaining the magneto-optical trap that operates on the $5s^2\ ^1S_0 \leftrightarrow 5s5p\ ^3P_1$ transition. By doing this, we mix Rydberg character into the MOT, introducing the potential for atoms in the Rydberg dressed state, which primarily comprises of the $5s5p\ ^3P_1$ state, to interact with neighbouring Rydberg dressed state atoms, illustrated in Figure 2.10.

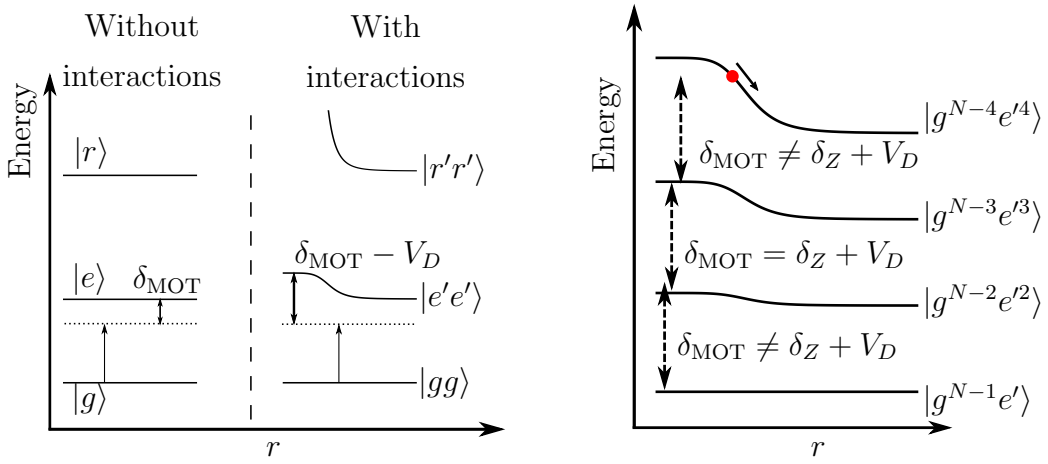

Figure 2.10: A Rydberg dressed MOT - by mixing Rydberg character into the MOT we introduce interactions into the excited state of the MOT transition, illustrated on the left. The MOT beam detuning from the dressed state δ_{MOT} will become density-dependent. This may manifest in several ways illustrated on the right, for example a repulsive force between atoms at a given separation, illustrated by the red point, or a density-dependent position where the position at which the MOT beams are resonant reflects both the Zeeman shift of the $5s5p\ ^3P_1\ m_J = -1$ state δ_Z and the Rydberg dressed interaction V_D.

For these interactions to be observable they must be comparable in strength to the cloud temperature, and the dressed blockade radius must be comparable to the average dressed state separation.

Viability

To compare the strength and lengthscale of Rydberg dressed interactions and the properties of narrow-line MOTs we must know the Rabi frequency that we can achieve for different Rydberg states (detailed in Chapter 4), and the C_6 coefficients for these states (shown in Figure 2.11). Both are strongly dependent on the Rydberg state principal quantum number n, Rabi frequency scaling as $n^{-3/2}$ and C_6 scaling as n^{11}. From the excited state of the MOT transition we can couple to the $5sns\ ^3S_1$, $5snd\ ^3D_1$ and $5snd\ ^3D_2$ series. These couplings all use one-photon dressing to obtain large Rabi frequencies.

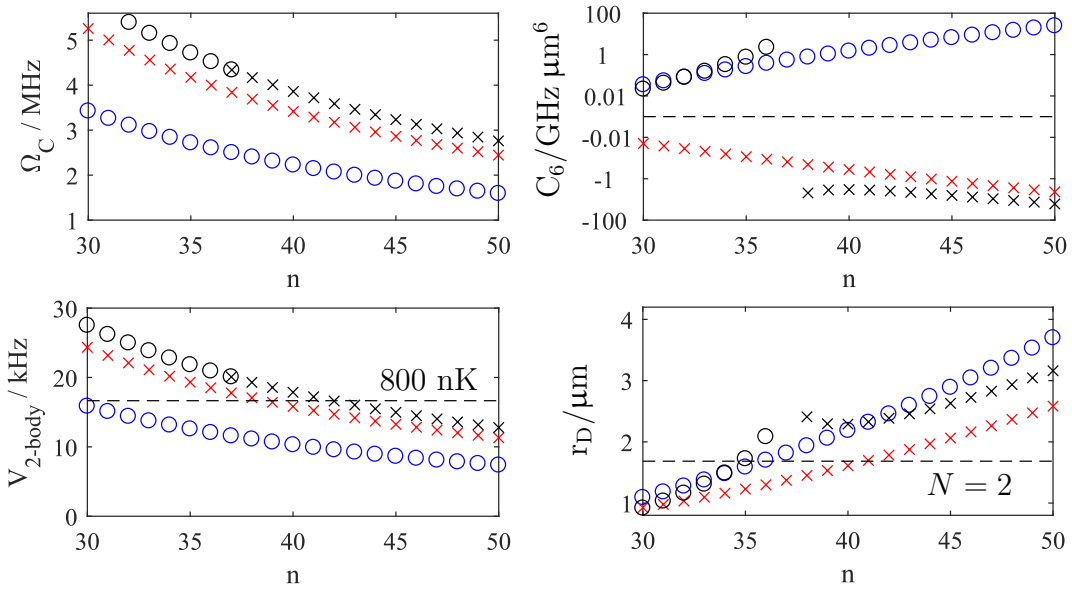

Figure 2.11: Scaling with principal quantum number n of Rydberg dressing parameters. Three series are shown, $5sns\ ^3S_1$ (blue), $5snd\ ^3D_1$ (red) and $5snd\ ^3D_2$ (black). Attractive states are shown as crosses, repulsive states as rings. The falling Rabi frequency with rising principal quantum number results in a falling two-body interaction (calculated for a detuning of three times the Rabi frequency), whilst the rising C_6 coefficient results in a rising dressed blockade radius. A Förster resonance at $5s37d\ ^3D_2$ results in a very large C_6 coefficient (not shown), and both attractive and repulsive interactions.

Setting $\Delta = 3\Omega$, we can calculate the Rydberg dressed blockade radius and the two-body interaction strength. We compare these to a typical cloud temperature of 0.8 μK and a dressed state density of 10^{11} cm^{-3}, estimated from a cloud density of 10^{12} cm^{-3} and a 10% fraction in the excited state. At this density, two atoms per dressed blockade sphere occurs at a dressed blockade radius of $r_D = 1.7$ μm. These values are indicated by dashed

lines on Figure 2.11.

We can clearly see that for $35 \lesssim n \lesssim 40$ there are Rydberg states for which we can achieve two-body dressed interaction strengths comparable to the cloud temperature and densities sufficient to reach two dressed state atoms per dressed blockade sphere, showing the comparable strength of Rydberg dressed interactions to the properties of the MOT.

This considers only two-body Rydberg dressed interactions. We can go further than this, calculating the number of atoms per dressed blockade sphere N as a function of principal quantum number, and calculating a many-body dressed interaction from this. Here, we must be careful what many-body interaction we use, the full $N(N-1)/2$ interaction given by Equation 2.26 or the $N-1$ interaction given by Equation 2.27. These interactions are illustrated in Figure 2.12. The full interaction potential of $N(N-1)/2$ times the two-body interaction is accumulated over a series of excitations from the $|g^N\rangle$ state. An individual scattering event will experience $N-1$ times the two-body interaction strength. We are interested in the shift that a single scattering event will result in.

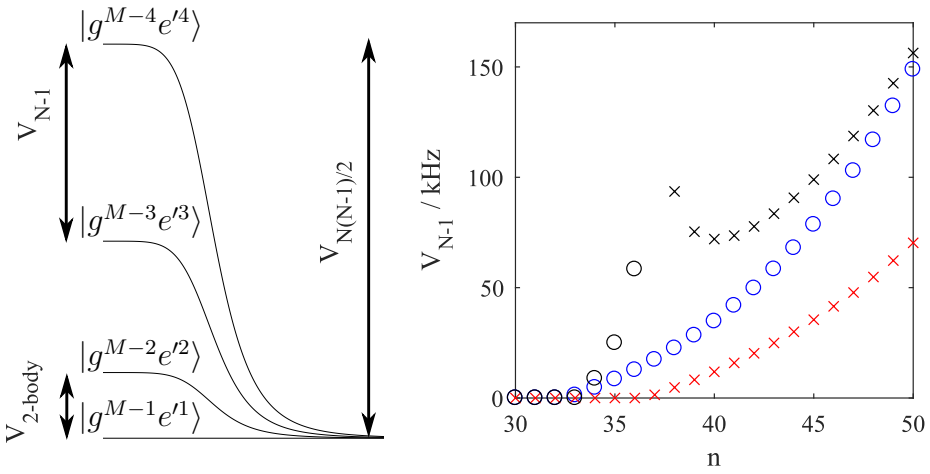

Figure 2.12: Many-body interactions in the Rydberg dressed MOT. If there are M atoms per dressed blockade sphere and N of these atoms are in the dressed state $|e'\rangle$ the interaction shift experienced by the $\mathrm{N^{th}}$ excitation (labelled $\mathrm{V_{N-1}}$) will be $N-1$ times that of the two-body interaction $\mathrm{V_{2-body}}$. The rapidly increasing dressed blockade radius with principal quantum number results in strong many-body interactions with rising principal quantum number, shown on the right for a dressed state density of 10^{11} cm^{-3}. As before blue, red and black correspond to the $5sns\ ^3S_1$, $5snd\ ^3D_1$ and $5snd\ ^3D_2$ states, crosses indicate attractive Rydberg-dressed interactions and circles indicate repulsive Rydberg-dressed interactions.

We see in Figure 2.12 that although the Rabi frequency falls with rising principal quantum number, the rise in C_6 coefficient more than compensates, allowing many-body interactions that are far greater than the cloud temperature. As N increases, the approximation that $\sqrt{\frac{N\Omega^2}{\delta^2}} \ll 1$ will break down, reducing the interaction strength compared to that shown in Figure 2.12.

Typically Rydberg dressing experiments are limited by the Rydberg state lifetime τ_{R} and the Rydberg fraction in the dressed state f as atoms excited to the Rydberg state are unlikely to decay to the ground state on the timescale of the experiment. This limits the trap lifetime to τ_{R}/f. As only ∼10% of the atoms in the MOT are in the dressed state, loss due to Rydberg excitation limits the dressing experiment to $\tau_{\mathrm{R}}/(f \times 0.1)$. For typical Rydberg state lifetimes of 10-50 µs and a coupling beam detuning of three times the Rabi frequency we expect a trap lifetime of 3.6-18 ms. This is orders of magnitude larger than previous dressing experiments [62, 63], and is also large compared to the equilibration time of the cloud [81].

We can conclude from this study that:

- The densities we can reach are sufficient to reach the two-body case at $n \sim 35$ and the many-body case above this.
- The Rydberg dressed interaction strength we can expect to achieve is comparable to the cloud temperature in the two-body case below $n \lesssim 40$, and significantly larger in the many-body case for $n \gtrsim 35$.
- The trap lifetime is sufficient for Rydberg-dressed interactions to modify the cloud dynamics before excessive loss occurs.

We next consider how interactions may modify the cloud dynamics.

Signatures of interactions

Whilst in previous experiments Rydberg dressing was observed through measurement of atomic states we intend to observe a modification in cloud dynamics due to Rydberg dressed interactions. We consider two mechanisms through which interactions may modify the dynamics; a modification of the scattering rate, and the conversion between kinetic energy, potential energy and photon energy.

Narrow-line MOTs are very sensitive to MOT-beam frequency, with small detuning changes having a direct effect on the position and shape of the MOT. An 8 G/cm magnetic field gradient corresponds to a Zeeman shift gradient of -1.7 kHz/μm on the $5s5p\ ^3P_1\ m_J = -1$ state, so a Rydberg dressed interaction shift of 20 kHz may result in the MOT forming in a position where the Zeeman shift is 20 kHz different from the non-interacting case, resulting in a cloud movement of 12 μm. We typically work with MOTs with a $1/e^2$ radius of ∼30 μm, so this is a significant shift. A many-body shift of ∼50 kHz may cause the cloud position to shift by a full cloud width. We may therefore expect the cloud position to become density dependent. This is illustrated in Figure 2.10.

Alternatively, given that the two-body dressed interaction strength can reach gradients of ∼10 kHz/μm, greater than the magnetic field gradient, we may see a rearranging of the cloud position distribution. The scattering rate varies across the cloud due to the Zeeman shift. A density-dependent scattering rate may compensate the Zeeman shift, resulting in a density-profile across the cloud that is set by the Zeeman shift. This is illustrated in Figure 2.13 for attractively interacting Rydberg dressed interactions that result in a falling dressed state energy with rising density.

A more localised version of this would be a suppression of scattering close to atoms in the Rydberg dressed state for repulsively interacting Rydberg dressed atoms. It isn't obvious whether this repulsion between Rydberg dressed atoms would reduce the density of the MOT - a reduced scattering rate at high density may result in dense clusters of atoms forming. Alternatively, for attractive dressed atom pairs, we may observe stronger scattering by close pairs, which could result in a flat-topping of density, as close atom pairs experience a stronger scattering force, repelling them.

As well as a modification of scattering due to interactions, there may be a direct force between dressed state atoms. The time that this force is active over is limited by the excited state lifetime of 22 μs, at a temperature of 0.8 μK atoms move ∼ 0.3 μm in this time, resulting in a 3 kHz change in potential energy for a 10 kHz/μm two-body interaction potential gradient. This energy may then be released through spontaneous emission as atoms decay from the dressed state to the ground state, creating a dissipative effect that may give rise to heating or cooling. Whilst a 3 kHz shift may be too small to be observed, in the many-body case this conversion of potential energy may rise by a factor of $N - 1$.

For repulsively interacting dressed pairs we may expect stronger scattering from pairs at

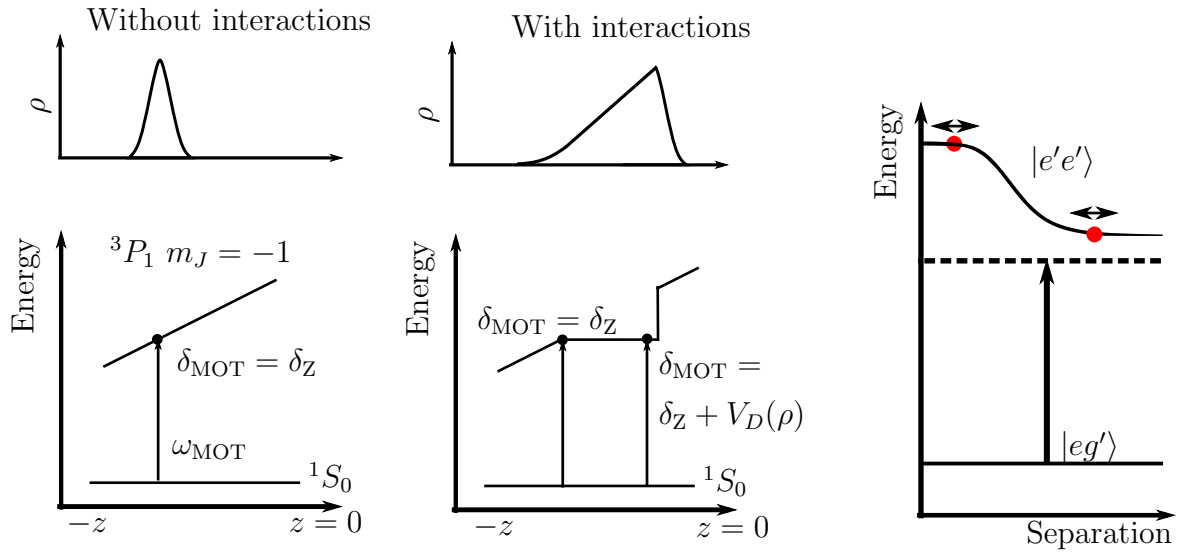

Figure 2.13: Without interactions (left), the MOT forms around the position at which the MOT beam detuning from the dressed state δ_{MOT} matches the Zeeman shift δ_Z of the $5s5p\,^3P_1\ m_J = -1$ state. With interactions, this energy level becomes density-dependent. We may observe a density ρ that maps onto the Zeeman shift, modifying the cloud shape (centre). Alternatively we may see a reduction in scattering from close pairs of atoms (right) for repulsive Rydberg dressed interactions.

a distance where this interaction is weaker given the red-detuned MOT beams. Should the atoms move closer during this time, a fraction of the kinetic energy of the pair will be converted to potential energy, which will then be removed by the photon following decay to the ground state by one of the two atoms. Given the stronger scattering by distant pairs, we may expect an additional cooling force from scattered light resulting in a lower cloud temperature in the dressed MOT. The higher probability of the MOT light exciting pairs of atoms that will experience cooling, rather than heating, is similar to Sisyphus cooling [83], although in this case the modification of scattering probability originates in the interaction rather than the polarisation of the cooling light.

We can thus hypothesise many mechanisms through which Rydberg dressed interactions may affect the cloud. Many of these mechanisms are many-body and non-trivial to solve, we therefore haven't attempted to further quantify these effects, but we note that the Rydberg dressed interaction potential we expect to achieve may exceed both the cloud temperature and the Zeeman shift across the cloud, and that the gradient of this interaction potential may exceed the Zeeman shift gradient. We may expect changes

to the cloud position, density profile, and velocity distribution, which will be density dependent and tunable through Rydberg state, coupling beam intensity and coupling beam detuning.

Summary

In this chapter we have outlined the dressed state picture and Rydberg atom interactions, which we bring together to understand Rydberg dressed interactions. These interactions have been observed in highly controlled systems in reduced dimensions, but have not been observed in three dimensions, on long timescales, or in actively cooled gases.

We have outlined narrow-line MOT dynamics, and presented the concept of a Rydberg dressed MOT. The predicted interaction strength, lengthscale and timescale of Rydberg dressed interactions are comparable to the properties of strontium narrow-line MOTs, which suggest that we may expect to observe both two-body and many-body interactions within the Rydberg dressed MOT. Several possible consequences of these interactions, which may modify the cloud position, density profile and velocity profile, are considered.

Finally, we consider the requirements of a Rydberg dressed MOT. To observe Rydberg dressed interactions in a Rydberg dressed MOT we first require:

- **A cold, dense MOT** - we need a MOT with excited state densities of around 10^{11} cm^{-3} to reach the interacting regime, and temperatures on the order of 1 μK for the effect of interactions to be observable;
- **Coupling to Rydberg states** - we need a laser capable of providing strong coupling from the excited state of the MOT to a range of Rydberg transitions, and we need to characterise the Rydberg states that we will couple to;
- **Dressed MOT characterisation** - coupling the MOT to a Rydberg state will induce a one-body AC Stark shift, modifying the operation of the MOT. We need to characterise these changes to understand the effect of the one-body AC Stark shift.

Once these requirements are met we can examine the characterised Rydberg dressed MOT to identify suitable parameter regimes for the observation of Rydberg dressed interactions.

Chapter 3

The cold strontium experiment

To Rydberg dress a narrow-line MOT we must obtain small, dense narrow-line MOTs and characterise the Rydberg states that we will dress the MOT with. This chapter describes the experimental apparatus, steps to increase the density of the narrow-line MOT, and the diagnostic tools that we have to characterise Rydberg states and the ground state population. This chapter will:

- Briefly describe the experimental set-up, with emphasis on changes made during the course of this work.
- Summarise the steps taken to increase the density of the narrow-line red MOT.
- Document the imaging and ion detection techniques that we use for Rydberg state characterisation and studying the Rydberg dressed MOT.

Having done this, we will characterise Rydberg states, documented in Chapter 4, which will allow us to Rydberg dress the narrow-line MOT, documented in Chapter 5.

3.1 Experimental apparatus

The experimental apparatus can loosely be broken into three categories; the vacuum system; the laser systems; and the control program, all with assorted supporting equipment such as electronics. We consider the apparatus in that order. More details on the experimental apparatus can be found in [84–87]; this section offers an outline and details of significant changes to the apparatus made during the course of this work.

3.1.1 Vacuum chamber

The main vacuum chamber is illustrated in Figure 3.1. An oven heated to ∼700 K produces a collimated beam of atomic strontium that passes through a Zeeman slowing stage, provided by a set of coils that generate a magnetic 'Zeeman' field, which is permanently on, and a counterpropagating 461 nm Zeeman beam.

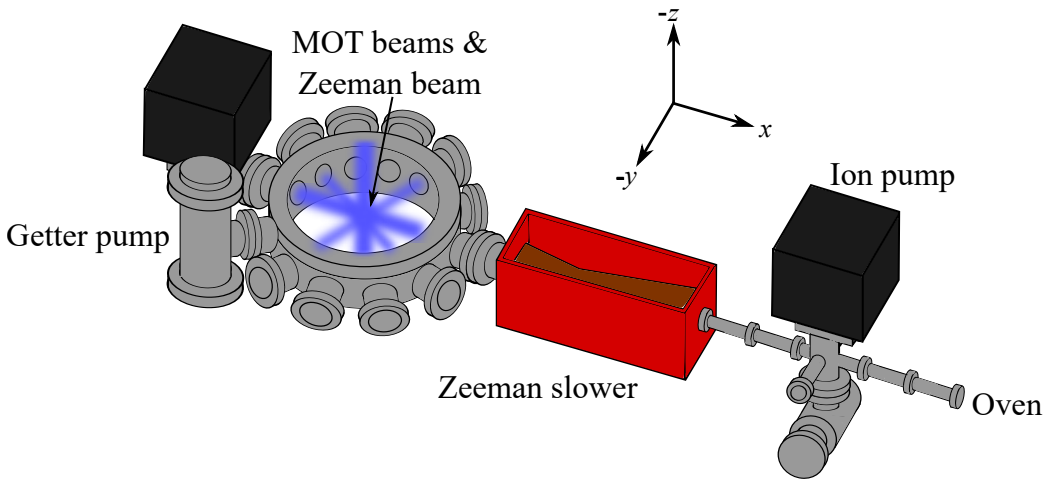

Figure 3.1: Strontium atoms from an oven are decelerated as they pass through a Zeeman slower. They can then be trapped in a blue MOT. Taken from [86].

The main chamber contains a pair of in-vacuum copper coils that can produce a magnetic quadrupole field gradient of up to 25 G/cm without the need (or the capability) for water cooling. A set of four pairs of electrodes in a split-ring configuration allow application of uniform electric fields during Rydberg excitation and steering of ions towards a micro channel plate (MCP).

The chamber has twelve horizontal DN40 ports housing eight viewports; four for MOT beams; two for an imaging camera and an imaging beam; and two for spectroscopy beams. The other four horizontal ports are for the atom beam, the MCP, a getter pump and a cross that is connected to the Zeeman viewport, an ion pump and a valve. On the vertical axis, the MOT beam is aligned 3° off axis, allowing spectroscopy beams to be aligned on the vertical axis. Electrical connections to the electrodes and MOT coils are made through feedthroughs on the top of the chamber.

External to the vacuum chamber, a 'quantisation coil' sits beneath the vacuum chamber, allowing uniform magnetic fields to be applied to the chamber. Due to the very narrow

transitions we can now observe, and the ability to rapidly repeat Rydberg excitations, we have observed that this quantisation coil may induce eddy currents, most likely in the copper gasket that sits between the quantisation coil and the excitation region. More details are given in Appendix C.

Three pairs of external coils are wrapped around the vacuum chamber to apply a magnetic field to compensate the Earth's magnetic field and any stray field. These are also used for shifting the effective quadrupole field centre, shifting the MOT position through the spectroscopy beams; hence they are referred to as shim coils.

The most significant changes on previous generations largely relate to the viewport through which the Zeeman laser beam passes. As the oven is directed towards this viewport we expect that atoms may be deposited on the glass, where they can chemically bond, causing the viewport to become opaque. Whilst this was not observed previously, following vacuum maintenance work documented in [87] where the Zeeman viewport was replaced with an anti-reflection coated viewport, we have observed significant build-up of strontium on the viewport, causing attenuation of the Zeeman laser beam and a lower blue MOT loading rate. As the blue MOT transition is not closed, the atom number that we can trap in the blue MOT is proportional to the loading rate until the radiation pressure limit is reached, so attenuation of the Zeeman beam causes a reduced atom number in the blue MOT. Several techniques to address this issue will be presented in this chapter.

3.1.2 Laser systems

Several laser systems are necessary for this experiment, although only one will receive any significant attention in this thesis, the Rydberg coupling laser described in Chapter 4. Most of the wavelengths used for this experiment are demonstrated in Figure 3.2.

The primary transition in strontium is the $5s^2\ {}^1S_0 \leftrightarrow 5s5p\ {}^1P_1$ transition at 461 nm. We use this transition for Zeeman deceleration ($\sim$ 40 mW), the first stage of MOT cooling ($\sim$ 10 mW) and imaging the cloud ($\sim$ 2 mW). We produce up to 300 mW of 461 nm light from a commercial Toptica DL100-TA-SHG system, which is frequency stabilised using modulation transfer spectroscopy [88]. A new strontium beam machine has been developed to perform this locking, documented in [89], but for the purposes of locking the 461 nm laser there is no difference to the previous locking cell [90].

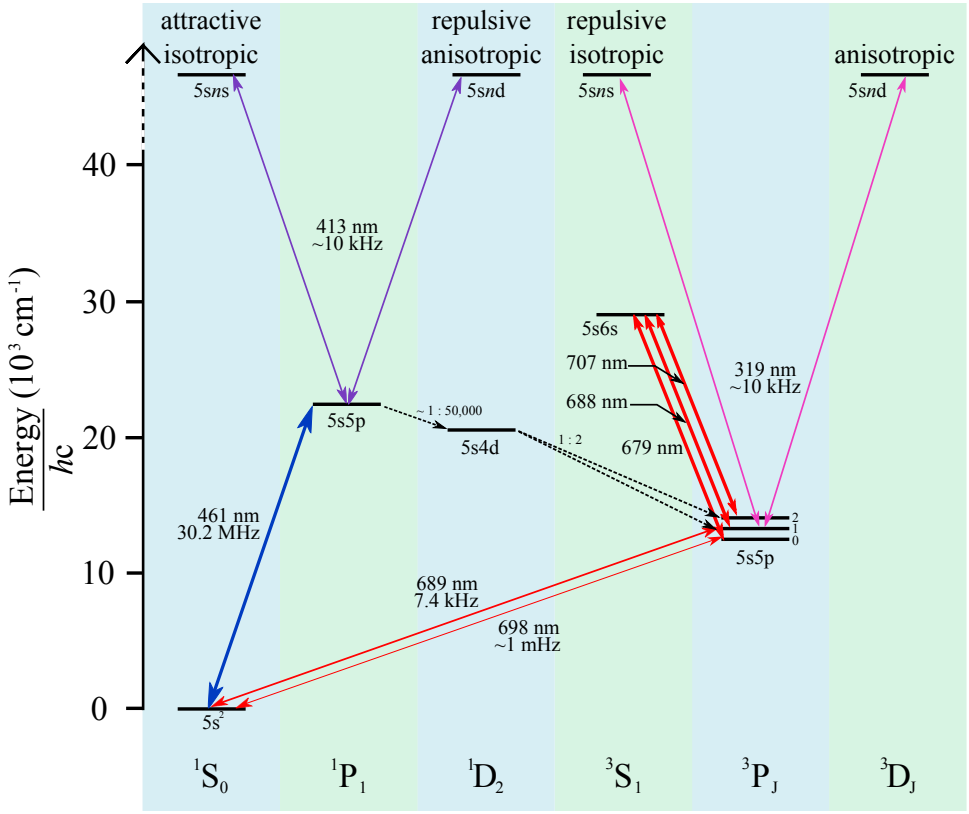

Figure 3.2: Strontium atomic energy levels. Imaging and primary cooling occur on the $5s^2\ {}^1S_0 \leftrightarrow 5s5p\ {}^1P_1$ transition, which is not a closed transition, resulting in the use of repump lasers at 707 nm and 679 nm lasers to prevent loss to the metastable $5s5p\ {}^3P_{0,2}$ states during cooling. Secondary cooling uses the $5s^2\ {}^1S_0 \leftrightarrow 5s5p\ {}^3P_1$ transition. We couple the $5s5p\ {}^3P_1$ state to Rydberg states using a 319 nm laser. Taken from [86].

Initially, the light out of the laser was immediately coupled into a polarisation maintaining fibre, allowing drift in the laser output direction to be corrected without requiring significant alignment, but resulting in immediate fibre coupling losses of $\sim 45\%$. Due to attenuation of the Zeeman beam on the strontium coated viewport, we now pick off the Zeeman beam before the fibre, allowing us to compensate Zeeman viewport losses with reduced fibre coupling loss. All 461nm beams (Zeeman, MOT and probe) are controlled with AOMs; in addition, the Zeeman beam and the MOT beam have mechanical shutters to eliminate light leakage, which was found to heat the red MOT.

The second stage of cooling is performed on the $5s^2\ {}^1S_0 \leftrightarrow 5s5p\ {}^3P_1$ transition using 689 nm light. Due to the narrow ($\Gamma/2\pi = 7.4$ kHz) line, action must be taken to ensure the laser has a narrow linewidth, on the order of the transition linewidth. To do this,

we use an ECDL master laser at 689 nm that is stabilised to high-finesse cavity, which is itself stabilised to a modulated fluorescence signal from a strontium beam machine. This master laser also injects a slave laser to produce sufficient power for the MOT beams (~ 10 mW).

The high-finesse cavity developed in [86] for frequency stabilising the 689 nm laser uses mirrors mounted on two piezo-electric transducers to stabilise the length of the cavity. The piezos have different stroke lengths, allowing broad scanning using the 'large' piezo and precision locking using the 'small' piezo, although the smaller piezo initially did not function due to a loose connection. This connection has since been fixed. A consequence of stabilising the length of the cavity using the small piezo is that the drift range that the circuit can correct for is small; to compensate this a low noise integrator feeds back to the large piezo voltage from the voltage of the small piezo. In addition, the large piezo was found to show hysteresis, particularly at low voltages (< 80 V), possibly due to the absense of a pre-load. When the large piezo voltage is below 80 V a high drift rate results in increased frequency noise on the 689 nm laser. The piezo is driven by a Thorlabs 150 V driver; the output of the driver is connected in series with a 50 V battery pack to reach the 200 V rating of the piezo and to avoid regions demonstrating hysteresis. The two issues of limited drift range and hysteresis are independent of each other.

The other change to the 689 nm laser set-up is picking off a probe beam from the zeroth order of the MOT AOM, which we control with a second double-passed AOM, producing up to 3 mW of probe light. As a result we can't use the 689 nm probe beam and the red MOT light simultaneously.

At the vacuum chamber the blue MOT and red MOT beams are collimated and overlapped using a dichroic mirror.

During loading of the blue MOT atoms have a small probability of decaying to the $5s5p\ ^3P_{1,2}$ states. Whilst the $5s5p\ ^3P_1$ state decays to the ground state quickly enough to be retrapped the $5s5p\ ^3P_2$ state is metastable, introducing a source of loss to the cloud. Previously, this has not been a problem and we could reach the radiation pressure limit in the blue MOT. However, attenuation of the Zeeman beam through the Zeeman viewport reduces the blue MOT loading rate and therefore the achievable blue MOT atom number, making it necessary to implement repumps to prevent loss to the metastable state.

Several repumping techniques may be employed to address this [91]; for reasons of cost and convenience of laser sources we use ECDL repumps at 707 nm and 679 nm. The

707 nm light drives atoms from the $5s5p\ ^3P_2$ state to the $5s6s\ ^3S_1$ state, which can decay into any of the $5s5p\ ^3P_{0,1,2}$ states. We use 679 nm light to drive atoms from the $5s5p\ ^3P_0$ back to the $5s6s\ ^3S_1$ state, thus depopulating both metastable states. The repump lasers are frequency stabilised to a wavemeter, and are controlled using a shutter rather than an AOM as precise time control of the repump beams is not necessary. The repump lasers have been implemented in previous versions of the experiment, but are only necessary now. Both beams enter the chamber via a multimode optical fibre through a MOT viewport.

A 408 nm laser is used to autoionise Rydberg atoms; this laser is not frequency stabilised as the autoionising transitions that we utilise are typically on the order of GHz wide. This laser is an ECDL with pulses controlled using a single-pass AOM.

The Toptica DL100-TA-SHG 413 nm laser used in previous experiments is not used in the context of this thesis. Instead Rydberg excitation from the $5s5p\ ^3P_1$ state uses 319 nm light, detailed in Chapter 4.

All laser beams reach the vacuum chamber via steering optics after optical fibres, apart from the 461 nm Zeeman beam and the 319 nm beam, which passes from the doubling cavity through a shutter and an AOM to the vacuum chamber. This laser is considered in Section 4.1.

3.1.3 Experimental control

The experiment has always been controlled using a field programmable gate array (FPGA) programmed through LabVIEW, but early in the start of this thesis both the FPGA card and the code have been replaced. The replacement, Durham Experimental Terminal (DExTer), was developed by Tim Wiles [92] and modified by David Szwer before being implemented in the strontium group. The essence of the program is the same; a sequence of digital TTL outputs and analog voltage outputs with deterministic time-steps. The digital TTL outputs are used to trigger AOMs, pulse generators, electronics etc; the analog voltage outputs are used to set MOSFET current levels, generate electric fields, scan laser powers and frequencies etc. The program also includes communication with other devices e.g. arbitrary function generators, cameras etc. Communication with these devices is performed outside of the well-controlled timing sequence.

The new program has improved the timing resolution from 2 µs to 25 ns, offers 96 digital

arrays, of which we typically need up to 20, and eight analog outputs scanning from -10 V to +10 V with 16-bit resolution. These analog outputs can be ramped linearly between two voltages. It offers the facility to repeat sections of the sequence, which is particularly useful for performing multiple Rydberg excitations within a single MOT, which will be considered later. It also offers much more versatility for adding new devices controlled from the main computer rather than the FPGA card (e.g. passing values to function generators) to the control program, and easier user interface.

The program can vary parameters across a two-dimensional parameter-space, with the functionality to perform immediate repeats of experimental sequences under identical conditions and full repeats of every experimental sequence run. The full repeats can be done in a linear, alternating or random order. Typically we use a random order to reduce the effect of laser power drift, but in the case of the UV laser frequency, which can't be scanned in large steps, we use alternating repeats. Parameters that can be scanned are analog voltages, timesteps, or values passed to instruments controlled by DExTer, for example AOM frequencies or drive powers.

To increase the transfer efficiency between the blue MOT and the broadband red MOT we have developed a new MOT coil driver. Previously the current through the coils was set by a circuit that could pass two levels of current, which would set the quadrupole magnetic field gradient necessary for the blue MOT and the red MOT. This circuit has now been replaced, allowing the current through the coils to be varied linearly in response to a voltage applied to the circuit. Combined with the computer control system described above, this allows us to ramp the magnetic field gradient, increasing the transfer efficiency from the blue MOT to the red MOT. This circuit is documented in Appendix A.

Previously a 'pushing' electric field from two electrodes was used to direct ions towards an MCP in the vacuum chamber and four other electrodes were used to generate uniform electric fields. Following changes in internal electric field described in [87], it is now necessary to apply a voltage to 5 of the 8 electrodes to guide the ions towards the MCP. We therefore require some of the electrodes to both generate uniform electric fields and apply ion steering electric fields. As the steering electric fields and uniform electric fields are generated by different sources (pulse generators and the experimental control program respectively) we have designed and implemented an electrode switching circuit. This allows us to switch the connection on all the electrodes with a switching time of ~ 1 μs and a voltage range of $\pm$ 10 V, allowing electric fields in the horizontal direction of up to $\pm$ 3.5 V/cm. This allows us to generate uniform electric fields during Rydberg

excitation and ion steering electric fields during autoionisation. A $\sim$ 50 mV difference between the pulse generator ground and the chamber ground results in a stray field of $\sim$ 18 mV/cm at the position of the MOT when the electrodes are connected to the pulse generator.

3.2 Optimising the red MOT performance

In all of the above work the red MOT light is assumed to be monochromatic. In practice the MOT operates in stages, shown in Figure 3.3. First the blue MOT is loaded. Then a broadband MOT uses 689 nm red light that is -2.3 MHz detuned from resonance and modulated with $\pm$ 2 MHz of sidebands of 50 kHz separation - this artificial broadening of the light is chosen to match the Doppler profile of the blue MOT, increasing the fraction of atoms transferred from the blue MOT to the broadband MOT [93]. Details of this technique are provided in [86]. Depending on the experiment, this MOT is either used as a platform for Rydberg excitation, or a third stage of cooling using single frequency red MOT light is used, usually obtaining a smaller, colder, denser MOT.

We will consider two aspects of the MOTs that we generate. Firstly, we outline some techniques to increase the transfer efficiency between stages of the MOT. Secondly, we consider a technique to turn the MOT off and on in quick succession, allowing us to perform multiple Rydberg excitations within a single MOT.

Transfer efficiency enhancement

An ideal MOT for Rydberg dressing is small, cold and dense, requiring small MOT beam detuning, low MOT beam power, and having high transfer efficiency between MOT stages. Optimum transfer efficiency occurs for large MOT beam detuning and high MOT beam power. We therefore require a transition from optimum transfer parameters to optimum Rydberg-dressed MOT parameters. This also compensates the previously noted effect of Zeeman beam attenuation. We have implemented three new changes to the MOT to increase our transfer efficiency and change the red MOT parameters from optimum transfer efficiency to optimum dressing parameters; all are illustrated in Figure 3.3.

The first change is the introduction of a rampable magnetic quadrupole field, explained in Section 3.1.1 and documented in Appendix A. The transfer from blue MOT to broadband MOT requires the velocity distribution of the cloud to match the frequency profile of

the broadband MOT light and the position of the atoms in the blue MOT to match the resonance curve of the red MOT light. Using a lower magnetic field during initial cooling of the broadband MOT increases the size of the resonance curve, resulting in lower confinement but a higher transfer efficiency to the broadband MOT. Smoothly increasing the magnetic field gradient, we combine the high transfer efficiency obtained at low magnetic field gradients and the high confinement of high magnetic field gradients. Typically, we perform 50 ms of cooling at a low magnetic field of 3 G/cm before linearly ramping the magnetic field to 8 G/cm over 50-100 ms. Magnetic field gradient ramps were implemented previously [86] using pulse width modulation but the pulse width modulation technique was found to increase the cloud temperature.

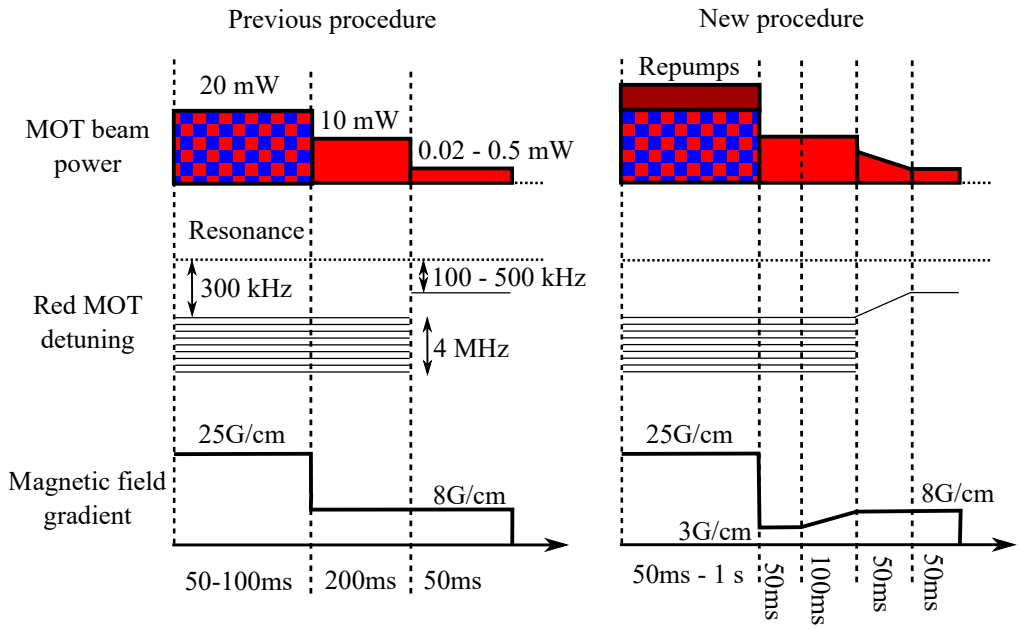

Figure 3.3: Left - the previous MOT loading procedure detailed in [86, 87]. Right - the new MOT procedure, with the addition of repump lasers, a magnetic quadrupole field gradient ramp, and single frequency red MOT power and frequency ramps. These modifications allow control of the final single frequency red MOT parameters without sacrificing transfer efficiency. They are also required to compensate attenuation of the Zeeman laser beam on the strontium coated Zeeman viewport.

The second change is the use of a frequency ramp when moving from broadband MOT to single frequency MOT. Simply stepping from a large MOT beam detuning to a small MOT beam detuning results in atoms outside of the smaller resonance curve being lost. Several groups ramp the red MOT beam detuning and sideband separation from large to

small [80, 94] to maximise the transfer from the broadband stage to the single frequency stage of the narrow-line MOT, requiring complicated arbitrary function generation. We exploit the property that, for a broadband MOT that has been trapped for sufficiently long for cooling to be complete, the position of the atoms is dominated by the sideband closest to resonance [81]. Thus by choosing a single frequency red MOT beam detuning of $\delta_{\mathrm{MOT}} = -300$ kHz, the resonance curve of the MOT encompasses the whole cloud, and we obtain a high transfer efficiency into the single frequency red MOT. We can then linearly sweep the initial single frequency red MOT beam detuning to a smaller MOT beam detuning for greater confinement of the cloud.

The final modification is the use of a power ramp in the single frequency MOT stage. High single-frequency MOT beam power typically increases transfer efficiency from the broadband stage but we frequently want low MOT beam power for Rydberg dressing experiments. We use a voltage variable attenuator to reduce the MOT beam power as we scan the MOT beam frequency to increase transfer efficiency without sacrificing low final MOT beam powers. This technique is particularly beneficial when used with the MOT beam frequency ramp.

The exact times used in these sequences are dependent on the final MOT parameters but common values are given in Figure 3.3. The increase in transfer efficiency also depends on final MOT beam parameters, all can offer at least a factor of two gain in transfer efficiency in some regimes. As these ramping techniques were implemented to transition to optimum red MOT dressing parameters, a detailed study of the increase in transfer efficiency that these techniques cause has not been performed. We can reach the single frequency red MOT radiation pressure limit of $\sim 2 \times 10^{12}$ cm^{-3} with these techniques. As we show in Chapter 6, in the future we may attempt to optimise these ramping techniques to reach the radiation pressure limit at lower MOT beam powers.

Retrapping

To perform Rydberg spectroscopy we excite Rydberg atoms from the cloud and detect the ions generated from the Rydberg atoms. We must turn off the MOT laser beams and quadrupole field to do this. Previously, the experiment control program and the oscilloscope read time limited us to performing a single Rydberg excitation per MOT. This is no longer true due to the new control program documented in Section 3.1.3 and a new oscilloscope documented in Section 3.3.2. We have now implemented a retrapping

technique that turns the trap off, performs a Rydberg excitation, and turns the trap back on, allowing us to perform up to 100 Rydberg excitations within each MOT, drastically increasing our data-taking rate.

It takes ~ 400 μs for the MOT quadrupole field to decay to a sufficiently low point as to not affect the Rydberg excitation. Combined with the Rydberg excitation time and the time taken for the field to turn back on, this corresponds to ~ 1 ms when the MOT is not trapping the cloud between Rydberg excitations. We typically run the MOT for 3 ms between Rydberg excitation to sustain cooling and trapping, in the broadband MOT we typically observe cloud depletion of less than 20% due to trap leakage over the course of 100 excitations, and otherwise no change between the first excitation and the last.

In low MOT beam power single frequency MOTs this is not the case. In the 1 ms when atoms are not trapped atoms move due to their thermal motion, resulting in a changed Zeeman shift. At 1 μK and 8 G/cm, this Zeeman shift will be 29 kHz if this motion is in the vertical direction. The atoms will also acquire a Doppler shift of 13 kHz as they accelerate due to gravity. The total shift in transition frequency in the 1 ms when the atoms are not confined may therefore exceed the transition linewidth, resulting in atoms not being retrapped. As a result, this retrapping technique does not work at low MOT beam powers. At high MOT beam powers where the line is power broadened to significantly greater than this, we can perform ~ 10 retrapping repeats of the cloud with less than 20% depletion[a].

We have attempted rapid repeated Rydberg excitation in low power MOTs without retrapping between excitations, but as shown in Appendix C eddy currents caused by the quantisation coil result in a varying magnetic field that affects the Rydberg excitation.

This retrapping technique has drastically increased our data-taking rate when performing Rydberg state characterisation.

3.3 Experimental readout

To observe MOTs and characterise Rydberg states we have two diagnostics - imaging and ion detection. We briefly outline these two diagnostics here.

[a]MOT beam powers used in the single frequency red MOT are typically one to three orders of magnitude less than those used in the broadband red MOT, so even high power single frequency red MOTs have less power than the broadband red MOT, reducing the number of repeats possible.

3.3.1 Imaging techniques

We image the cloud to obtain both the atom number and the atomic position distribution. Typically the cloud spatial profile is Gaussian, and can be described by a vertical and horizontal width and position. If the cloud is radially symmetric around the vertical axis, as we typically assume it is, we can estimate the width of the cloud in the imaging axis to be equal to the width of the cloud on the horizontal axis perpendicular to the imaging axis. From the atom number and cloud widths we calculate a density.

We primarily use absorption imaging using a 461 nm probe beam to image the MOT. We use a PCO PixelFly QE camera with a magnification of 0.8 and a 1.4 µs resonant 461 nm laser pulse, with $1/e^2$ radius of 2.5 mm and a power of up to 2 mW corresponding to a peak intensity of $s \approx 0.5$.

Initially in the experiment we used fluorescence imaging using the 461 nm MOT beams but the high density of the single frequency red MOT inhibits the use of fluorescence imaging - the cloud is optically thick, so only atoms in the outer shell of the cloud are imaged through fluorescence imaging. To partially suppress this we implemented absorption imaging, measuring the optical depth of the cloud. The use of a smaller probe beam allows us to reach higher intensities, and allows us to clearly detect optically thick clouds through the absence of probe light on the camera [87].

Whilst this imaging technique makes it clear when the cloud is optically thick, it does not eliminate the problem. When the cloud is optically thick and so little of the light reaches the camera as to be indistinguishable from noise, we can't measure the true optical depth of the cloud. To address the problem of optically thick clouds we use two techniques. We can ballistically expand the cloud, leaving it to fall and expand as it does. This allows us to accurately image the atom number but sacrifices information on the cloud width and position.

Alternatively, when we are confident that the cloud has a Gaussian spatial profile, we can fit a Gaussian distribution to the wings of the cloud, where the cloud is not optically thick. This technique is developed and presented in [87]. By comparing the atom number of an optically thick cloud to a ballistically expanded cloud taken under the same conditions we can be confident that this technique is effective in reproducing the atom number. This technique is only valid for clouds that have a Gaussian spatial profile and are radially symmetric.

3.3.2 Ion detection

Ionised Rydberg atoms are detected using an MCP inside the vacuum chamber. The MCP cathode is held at -2 kV, allowing the detection of positively charged particles by the MCP. A metal mesh grid in front of the MCP at -20 V shields the MOT region from this voltage and draws positively charged particles towards the MCP. In addition, after Rydberg excitation and ionisation, a pulsed 'steering electric field' pushes ions towards the MCP. When ions hit the MCP they create a voltage spike lasting $\sim$ 5 ns, which is detected on an oscilloscope by observing the number of times the MCP voltage crosses a threshold, illustrated in Figure 3.4. The threshold is set to avoid 'ringing', when the oscillation in voltage due to a single ion causes the voltage to pass the threshold more than once.

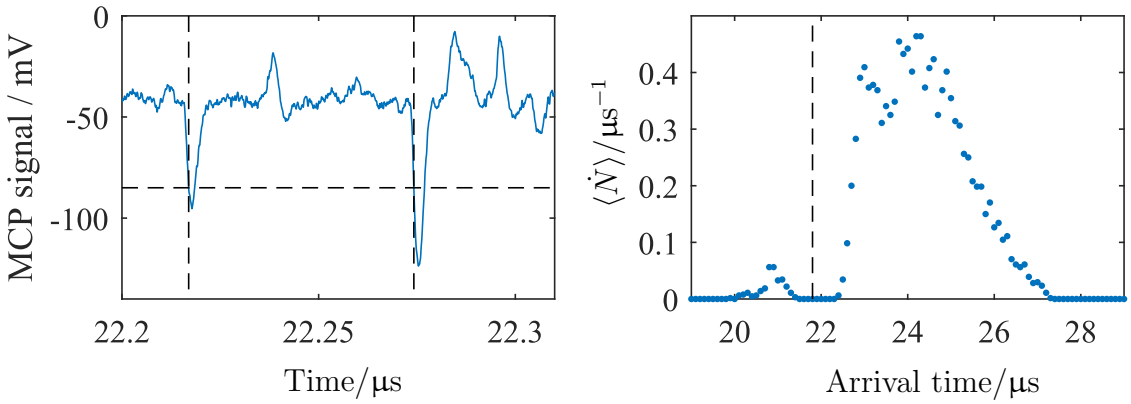

Figure 3.4: When ions hit the MCP they create a voltage spike, shown on the left. The number of times a threshold (black horizontal dashes) is passed and the time at which the threshold is crossed (black vertical dashes) are recorded, generating an ion number and ion arrival times. This allows us to determine an ion detection rate $\langle \dot{N} \rangle$ illustrated on the right in addition to an ion number. By starting the ion steering electric field before autoionising the Rydberg population we can distinguish between spontaneously ionised Rydberg atoms that arrive first (before the vertical line), and autoionised Rydberg atoms that arrive later (after the vertical line).

Previously, we used a Tektronix DPO4054 oscilloscope, which recorded only the number of times that this threshold was crossed. In the course of this work we replaced this oscilloscope with a LeCroy 610Zi oscilloscope, which has allowed us to make two changes. Firstly, the large memory of the oscilloscope allows us to store several scans and then analyse them. This allows us to perform multiple (up to 100) Rydberg excitations,

separated by $\sim$ 3 ms of trapping, and then analyse and observe the results of all 100 excitations independently.

By increasing the number of Rydberg excitations per MOT we drastically increase our data-taking rate but we must still take sufficient repeats to suppress both atom number fluctuation and the Poissonian nature of the Rydberg excitation.

Secondly, we can record the time at which each ion is detected, illustrated in Figure 3.4. Turning on the ion steering electric field before autoionising the Rydberg population with the 408 nm laser, we can use the ion arrival time to distinguish between Rydberg atoms that spontaneously ionise and those that are autoionised, also shown in Figure 3.4. Ions that have spontaneously ionised when the ion steering field is turned on will be immediately accelerated towards the MCP. Rydberg atoms that are autoionised will only be accelerated towards the MCP after they have been autoionised. Spontaneously ionised Rydberg atoms will therefore reach the MCP before the autoionised Rydberg atoms.

The biggest advantage to this time-resolved ion detection is clear from Chapter 6 - it allows us to observe real-time ion creation rates in the Rydberg-dressed MOT, which offers a powerful diagnostic of the loss processes in the Rydberg-dressed MOT.

Detection efficiencies

As detailed in [85] the peak detection efficiency is limited by the threshold at which an ion is observed, resulting in ions hitting the MCP having a 60% chance of being recorded. In addition, the grid in front of the MCP has an open area of 37%, we therefore expect a maximum detection efficiency of 22%. This is the probability of an ion at the centre of the vacuum chamber reaching the MCP and being recorded by the oscilloscope under the presence of steering electric fields.

In Chapter 6 we compare the ions detected from the cloud to the number of atoms lost from the cloud. To do this we must estimate the detection efficiency in the cloud under the conditions being used. We do not use an ion steering electric field during these experiments. Typically, when performing Rydberg excitation and ionisation under identical conditions with and without ion steering electric fields we observe a factor of $\sim$ 5 increase in detection efficiency when using ion steering electric fields.

Additionally, it is necessary to reduce the time-resolution that the oscilloscope operates at to observe ion signals over the length of the dressing experiments ($\sim$ 10 ms) compared to

when we observe ions following Rydberg excitation (~ 10 μs). Reducing the oscilloscope time-resolution to 10 ns, we observe a factor of two reduction in detector efficiency, which is consistent with ion spikes that last ~ 5 ns.

These two factors combine to reduce the estimated detection efficiency to $\sim 2\%$ for data taken without ion steering electric fields in Chapter 6. This is not a precise estimate, but will allow us to calculate a ballpark conversion rate from atom numbers to total ion numbers. In cases where we dress for longer times we may reduce the oscilloscope time-resolution further, further reducing the ion detection efficiency. At large charge densities Coulomb repulsion will also reduce the detection efficiency and high ion detection rates will cause detector saturation.

Detector saturation

A key property we must understand is the mechanisms that can saturate our ion detection. Saturation of Rydberg population is a crucial diagnostic, and we must be able to distinguish between the effects that can come about due to saturation of Rydberg excitation and saturation due to ion detection. We consider two saturation mechanisms that may affect the probability of ions reaching the MCP and the probability of ions being detected when they reach the MCP. Both are presented in [87].

The first effect is Coulomb repulsion of ions. At low ion densities the electric field due to neighbouring charges is negligible and ions can be steered by the ion steering electric field. At high charge densities, ions can repel each other, expanding as they are propelled towards the MCP. This is expected to become an issue for detected ion numbers > 60 per shot in a MOT of 40 μm $1/e^2$ radius [87]. A technique implemented to suppress this is to turn on the ion steering field before autoionising the Rydberg atoms. This reduces the peak ion density, reducing the charge repulsion as well as allowing us to distinguish between spontaneously ionised Rydberg atoms and autoionised Rydberg atoms. When performing Rydberg excitations we tailor our Rydberg excitation rate to avoid reaching the Coulomb repulsion regime; however, when observing massive ion detection rates in Chapter 6 it is likely that Coulomb repulsion will reduce the probability of ions being detected.

The second effect is due to the method that we use for counting ions. Voltage spikes caused by ions last ~ 5 ns, so if an ion arrives within ~ 5 ns of another ion, it will not be recorded as the MCP voltage will not have dropped back below the detector threshold.

To avoid this occuring we must ensure that there is a very low probability of two ions arriving within 5 ns of each other. In addition, ringing of the MCP may modify the probability of an ion being detected immediately after the MCP voltage drops below the detector. As explained in [87] this saturation becomes significant for ion counts of ~ 60 for ions arriving spread over ~ 2 μs i.e. a detection rate of 30 ions/μs.

In cases where the detection efficiency is reduced due to the oscilloscope time-resolution settings, the detection rate at which saturation occurs will be proportionally reduced i.e. if we reduce the detection efficiency by a factor of two, we expect detector saturation to become significant at a detection rate of 15 ions/μs.

In Appendix D we consider the role that atom number fluctuations and detector saturation have on the ion statistics.

Experimental summary

In this chapter we first described the experimental apparatus. The most significant changes made during the course of this thesis has been a series of steps necessary to increase the transfer efficiency to compensate attenuation of the Zeeman laser beam on the Zeeman viewport due to a build-up of strontium on the viewport. We have also implemented techniques to control the final stage of the single frequency red MOT without sacrificing high transfer efficiency into the final stage MOT. A new control program has been implemented, offering more versatility and allowing sections of experimental sequences to be rapidly repeated.

We outline the two diagnostics of the experiment. We use absorption imaging to obtain ground state atom numbers and atomic distributions, and we use ion detection as a measure of the Rydberg population. We present estimates of the detector efficiency and the threshold at which detector saturation becomes significant. Two improvements to the ion detection method have been implemented, the use of repeated Rydberg excitation within the cloud to improve the data-taking rate, and the recording of ion arrival times, which allows us to distinguish between spontaneously ionised and autoionised Rydberg atoms and provides a measure of the ion production rate within the experiment.

Having described the experiment and reached densities in the narrow-line MOT that are high enough to reach the Rydberg dressed interactions regime, we can now identify and characterise the Rydberg states with which we will Rydberg dress the MOT.

Chapter 4

Rydberg state characterisation

A key requirement of the Rydberg-dressed MOT is the coupling to and characterisation of Rydberg states that we will dress with. Previous spectroscopy on these triplet states is very limited [95–99], due to the difficulties of UV laser spectroscopy and the narrow widths of the transitions, and several of the states that we have observed have never been observed before. This chapter will:

- Describe the laser system used to observe the Rydberg states, documented in [100].
- Describe techniques used for first observation of the states and characterise our excitation methods and sequences.
- Thoroughly characterise these states.

To characterise the states we need to know the state energy and coupling strength, to assess the dressed state fractions that we can achieve in the Rydberg dressed MOT. We need to know the state sensitivity to electric and magnetic field, and the state lifetime. This will provide a better understanding of the loss mechanisms within our system. Finally, we observe autoionisation spectra for the Rydberg states. Previous Rydberg dressing experiments described in Section 2.4 have been limited by state transfer, which we can diagnose through autoionisation.

4.1 Rydberg excitation laser

A major challenge in this work was the development of a suitable laser source for coupling to Rydberg states from the $5s5p\ ^3P_1$ state. The laser needs to meet several criteria:

- Operate in the ultraviolet at ~ 319 nm;
- Be tunable across a range of Rydberg states;
- Be narrow linewidth, on the order of 10 kHz, to coherently drive narrow transitions;
- Produce high power, on the order of 100 mW, to allow high Rabi frequencies necessary for off resonant Rydberg dressing.

In addition, the research group has interest in Rydberg excitation from the metastable $5s5p\ ^3P_0$ state, requiring laser light ~ 317 nm. However, although the laser system described here has this capability, this has not been tested or used and is not considered in this thesis. A laser capable of meeting these requirements has been developed by E. M. Bridge, and is documented in [100], so is only briefly outlined here, and illustrated in Figure 4.1. The laser consists of two infrared lasers, which are amplified and frequency summed to produce red light. This light is then frequency doubled to produce UV light.

Two seed lasers, an ECDL with operation from 1549-1565 nm (referred to as the 1550 nm laser) and a fibre laser at 1079 nm, both with 10 mW outputs, feed two fibre amplifiers outputting 5 W and 10 W of infrared light respectively. The amplified beams make a single pass through a periodically-poled stoichiometric lithium tantalate (PPSLT) crystal that produces up to 1.8 W of red light at ~ 638 nm. A high power fibre, with a coupling efficiency of ~ 70 %, transmits most of this light into a frequency doubling cavity that initially produced more than 200 mW of UV light at 319 nm.

To stabilise the laser frequency and to narrow the laser linewidth ~ 1 mW of 638 nm light is coupled to a high-finesse transfer cavity that is actively stabilised to the $5s^2\ ^1S_0 \leftrightarrow 5s5p\ ^3P_1$ transition (described in Section [86]). To obtain tunability, we frequency shift the 638 nm light into two equally shifted carrier bands by a variable shift of up to the free spectral range of the transfer cavity (1.5 GHz). To lock the laser to the cavity using Pound-Drever-Hall (PDH) locking [101] we add sidebands to both carrier bands at ± 10 MHz. Both the frequency shift and the sideband modulation is provided by a wideband EOM. This provides both frequency stability and linewidth narrowing, with

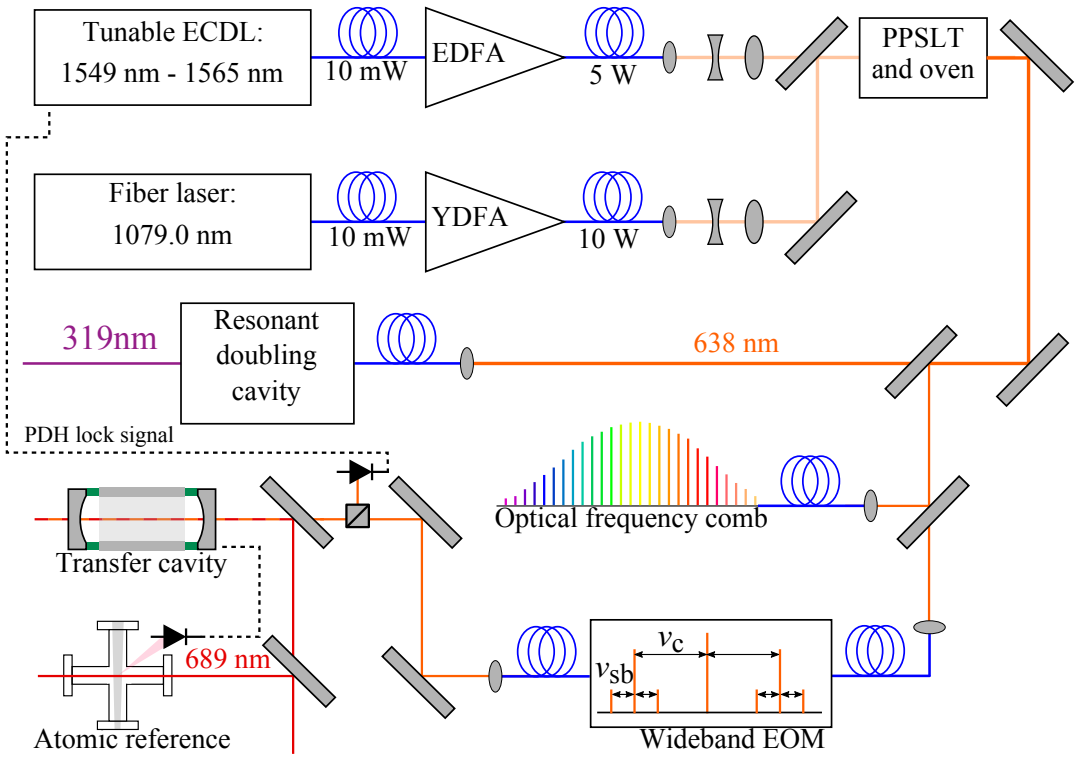

Figure 4.1: Schematic of the 319 nm laser, adapted from [100]. Two seed lasers are amplified and frequency summed to produce 638 nm light. Most of the 638 nm light is passed to a frequency doubler to produce 319 nm light, $\sim$ 1 mW of the 638 nm light is used to generate an error signal that is fed back to one of the seed lasers.

a longterm frequency stability $<$ 35 kHz in the UV. When well optimised, the 638 nm locking electronics can correct for step shifts of up to 2 MHz on the 638 nm light, allowing us to shift the UV frequency in steps of up to 4 MHz (as the 319 nm light is doubled from the 638 nm light) without unlocking from the cavity. As there are two carrier sidebands either side of the main frequency, and multiple possible cavity modes, occasionally these modes will overlap, causing the 638 nm to lock to the wrong mode, careful choice of appropriately spaced cavity modes avoids this.

Of the four Rydberg laser criteria considered, UV operation and power are obtained through the use of fibre amplifiers and non-linear crystals. Tunability is given by the large tuning range of the 1549-1565 nm ECDL. Frequency stability and narrow linewidth is given by the high-finesse cavity lock. A final merit of this laser system, which has not been utilised for the work considered in this thesis, is a 638 nm pickoff beam that goes to an optical frequency comb [102], allowing high-precision frequency measurements to be

made.

Since [100] has been published some additional features and challenges of the laser system have been observed:

- Transmission fluctuations in the high power fibre at maximum power;
- Degradation of the frequency doubling crystal performance over time;
- Very weak sidebands (at least two orders of magnitude smaller than the main frequency) on the UV light at ± 20 MHz originating from the sidebands used to stabilise the frequency doubling cavity.

The transmission fluctuations and degredation of the frequency doubling performance limit our reliable UV output power to 80 mW.

The sidebands are so weak as to be neglected in most cases unless we are operating ± 20 MHz from resonance. More detail is given in Appendix E.

This laser meets all the criteria set out at the start of this section, and has been used to characterise the Rydberg states with which we will Rydberg dress the MOT.

4.2 Exploratory Rydberg spectroscopy

Extensive Rydberg spectroscopy has been performed on strontium in the past 40 years but this has largely focussed on singlet Rydberg states and low principal quantum number triplet Rydberg states accessible through one-photon excitation from the metastable $5s5p\ ^3P_{0,1,2}$ states [95–98, 103–106]. Detailed characterisations of highly excited triplet Rydberg states are less frequent, although it is a growing field e.g. [99]. We must therefore perform exploratory spectroscopy to first observe triplet series Rydberg states.

When this strontium project began an exploratory Rydberg spectroscopy technique was developed, in which a blue MOT was continuously loaded, driving population to the $5s5p\ ^1P_1$ state, and a $\sim$ 413 nm coupling laser was shone onto the MOT and scanned in frequency. When on resonance, the Rydberg state is populated and a fraction of the Rydberg atoms ionise and are detected by the MCP.

In the case of triplet Rydberg states the process is similar, but as we drive atoms to the Rydberg state from the $5s5p\ ^3P_1$ intermediate state, we must use a 689 nm, red MOT.

The low scattering rate of this transition inhibits loading atoms directly into a red MOT; instead we load a blue MOT in $\sim$ 50 ms, transfer to a broadband red MOT with a lifetime $>$ 1 s, then shine the UV coupling laser onto the red MOT. We scan the coupling laser frequency by scanning the piezo voltage of the 1550 nm ECDL; on resonance we observe massive depletion, which is detected through imaging the cloud, and we observe the 638 nm laser frequency on a wavemeter. We do not lock the 638 nm to the high finesse cavity for these experiments.

This depletion can be observed in realtime through imaging the red MOT. This is challenging due to the low scattering rate of the $5s^2\ {}^1S_0 \leftrightarrow 5s5p\ {}^3P_1$ transition but by increasing the imaging time to 50 ms/frame, we can video the MOT, observing high depletion on resonance shown in Figure 4.2. However, the camera video frames can't be accurately synchronised with the laser frequency, and the time resolution of this technique is poor. It is a useful technique for first observation of Rydberg states.

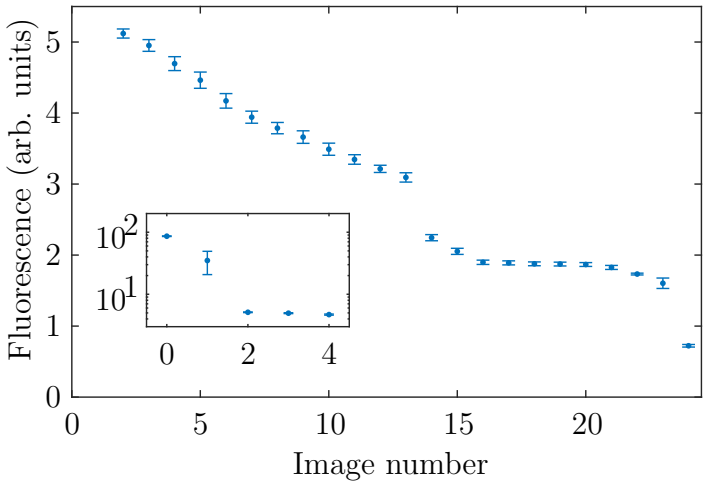

Figure 4.2: Fluorescence from the $5s5p\ {}^3P_1$ state detected on the camera during exploratory spectroscopy. Images are $\sim$ 50 ms apart, and the coupling laser was scanned around 3GHz during this time. Two resonances occur, around the 14^{th} and 24^{th} images. Inset, a massive spike in fluorescence that saturates the camera indicates the loading of the blue MOT, which is used to synchronise the scan start point.

A more sensitive probe of Rydberg excitation is to scan the coupling laser whilst recording the ion detection rate on an oscilloscope. When on resonance, we see high ion detection rates on the MCP, illustrated in Figure 4.3. By applying a small electric field of $\sim$ 1 V/cm we allow excitation to otherwise forbidden states. From the transition frequency,

the energy difference between neighbouring states, and the electric field sensitivity we can identify the observed Rydberg states, although this becomes harder at very high n where the density of states is higher.

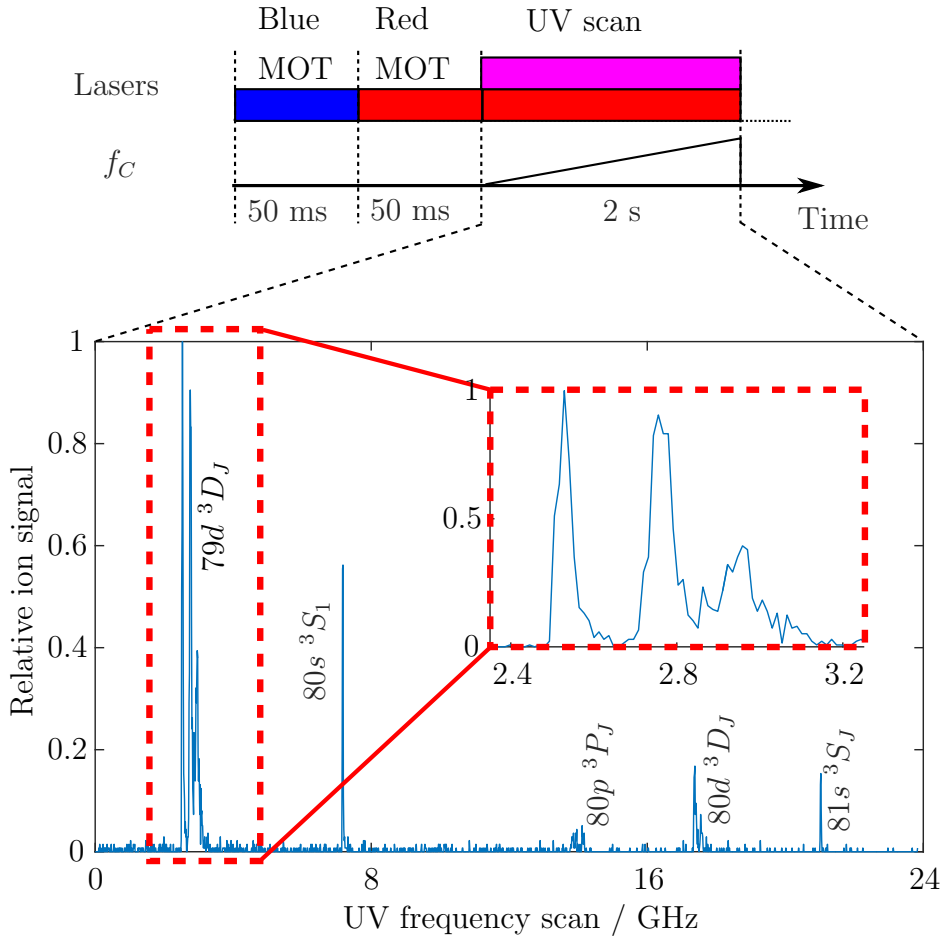

Figure 4.3: An exploratory UV frequency scan in a red MOT, at $n \sim 80$. A small electric field allows excitation to otherwise forbidden states. Inset is a zoom on the $5s79d\ ^3D_J$ states and the timing sequence is illustrated above, showing the laser frequency f_C scan. The laser frequency is shown from ~ 941.616 THz.

This technique is much more sensitive than imaging depletion, allowing better time-resolution and the observation of multiple transitions.

This frequency sweep method has several limitations. The observed signal strengths will be a combination of coupling strength, atom number in the MOT, and density dependent excitation and ionisation effects etc, so we can't use the observed signals as a measure of transition strength. The UV laser frequency can drift, and the wavemeter used to

calibrate the frequency scan has a relative accuracy of 40 MHz and an absolute accuracy of 3 GHz, which is poor compared to the absolute accuracy we can reach when the laser is locked to the high-finesse cavity and an optical frequency comb beat measurement is taken. In addition the linearity of the laser scan with time is not guaranteed, depending on the behaviour of the piezo in the 1550 nm seed laser. The coupling laser power is derived from a frequency doubling cavity stabilised using PDH locking, so scanning the frequency too quickly can reduce the final UV power if the locking feedback is not sufficient to correct for change in frequency.

We thus need a second stage of state characterisation. For this, we must lock the coupling laser to the high-finesse cavity.

4.3 Frequency stabilised excitation

To thoroughly characterise the Rydberg states we lock the 638 nm light that is used to generate 319 nm light to the high-finesse cavity as described in Section 4.1. With both the 689 nm probe and the 319 nm coupling laser frequency stabilised, and a typical cloud temperature of $1 - 20$ μK (sufficient to suppress Doppler broadening and operate in the frozen gas regime) we can perform very high precision spectroscopy.

4.3.1 Typical excitation techniques and sequences

Several excitation techniques are available to us. We can shelve atoms in the $5s5p\ ^3P_1$ state and use a one-photon excitation from this state, a technique that exploits the 22 μs lifetime of this state. We can use a two-photon excitation, driving directly from the ground state, either with both lasers on resonance, or both lasers equally and oppositely off-resonant. These two excitations are shown in Figure 4.4.

One-photon excitation from atoms shelved in the $5s5p\ ^3P_1$ state offers several interesting features, including the use of Rabi or Ramsey pulses to control the excitation fraction. In particular, it allows us to eliminate two-photon effects, such as AC Stark shifts, and measure transition frequencies independently of the other transition. We use 689 nm light to populate the $5s5p\ ^3P_1$ state, turn the 689 nm light off, then turn the 319 nm light on to populate the Rydberg state. We use this technique to measure precise frequencies, distinguish between two-photon excitation and control the intermediate state population.

Two-photon excitation offers different advantages, such as electromagnetically induced transparency (EIT) [107, 108], coherent population trapping (CPT) [109] and two-photon off-resonant excitation to populate the Rydberg state without populating the intermediate state. We use two-photon excitation, shining both excitation lasers on simultaneously, to measure the Rydberg coupling Rabi frequency using Autler-Townes splitting.

We can also use stimulated Raman adiabatic passage (STIRAP) [110]. In many ways our set-up is ideally suited to STIRAP, given the high Rabi frequencies (∼MHz) that we can achieve on both transitions and the long lifetimes (∼10 µs) of both excited states. Future work may utilise these advantages, but as a spectroscopic tool we only need a small fraction of the cloud excited to the Rydberg state. In fact, a high excitation fraction would cause problems, due to both the resulting strong Rydberg-Rydberg interactions, and the high depletion of the cloud that we would see, limiting the number of excitations we can do in each MOT.

In this work we have used both two-photon excitation from the ground state and one-photon excitation from atoms shelved in the $5s5p\ ^3P_1$ state to populate the Rydberg state.

The excitation sequence depends on whether we use one-photon or two-photon excitation sequences, shown in Figure 4.4. After MOT formation the MOT laser beams and fields are turned off and a quantisation magnetic field is turned on. After 400 µs (sufficient for the magnetic fields to stabilise) the Rydberg excitation is performed. This excitation will consist of either simultaneous or consecutive 689 nm and 319 nm laser pulses for two-photon or one-photon excitation. Excitation pulses are typically 5-30 µs, long enough to limit Fourier broadening and obtain detectable Rydberg population but not long enough for significant blackbody transfer to other Rydberg states.

A 408 nm autoionising laser beam then ionises the Rydberg population with near-unity ionisation probability and a steering electric field pushes ions towards the MCP. Turning on the steering field before the autoionising laser we widen the ion arrival time spread, increasing the MCP saturation limit, and can distinguish between spontaneously ionised Rydberg atoms and autoionised Rydberg atoms from arrival time, as explained in Section 3.3.2.

Naturally, care must be taken to ensure that if an electric or magnetic field is switched on or off then the field has stabilised before the laser pulses are applied, and that the different laser pulse switching times are considered, to ensure correct ordering of excitation pulses.

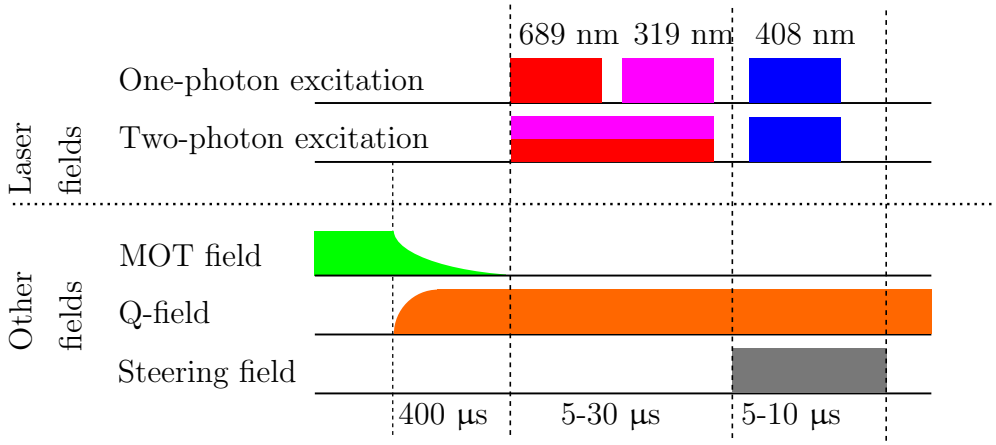

Figure 4.4: Typical excitation sequences. We perform either one-photon excitation to the Rydberg state from atoms shelved in the $5s5p\ ^3P_1$ state or two-photon excitation from the ground state, before autoionising the atoms with the 408 nm beam, which are pushed by an ion steering electric field towards the MCP. Before excitation, we turn the MOT quadrupole field off and turn a uniform magnetic quantisation field of 2-3 G on.

As discussed in Section 3.2 after Rydberg excitation and detection we can turn the trap back on for 3 ms to maintain trapping and cooling. We then turn the trap off again, allowing for multiple Rydberg excitations to be performed in each MOT. In broadband MOTs this allows up to 100 excitations/MOT and in high-power single-frequency red MOTs this allows up to 10 excitations/MOT. In low power single frequency red MOTs this technique is not effective in retrapping the cloud. Consecutive excitations (excitations 100 μs after the previous excitation without retrapping) can be used, but these incur problems due to eddy currents induced in a copper gasket between the quantisation coil and the cloud, resulting in a magnetic field that is dependent in the time that the quantisation coil has been turned on for. Detail of these eddy currents are presented in Appendix C.

4.3.2 Zeeman resolved excitation

Initial spectroscopy was performed using the red MOT beams to drive the lower transition without an applied magnetic or electric field. This resulted in split features, due to stray magnetic and electric fields that split and shifted the states. An example of this is shown in Fig. 4.5(a), scanning the probe beam frequency across resonance with the coupling beam resonant with the $5s80s\ ^3S_1$ state. The MOT light drives to all three $5s5p\ ^3P_1$

magnetic sublevels, all of which couple to the Rydberg state.

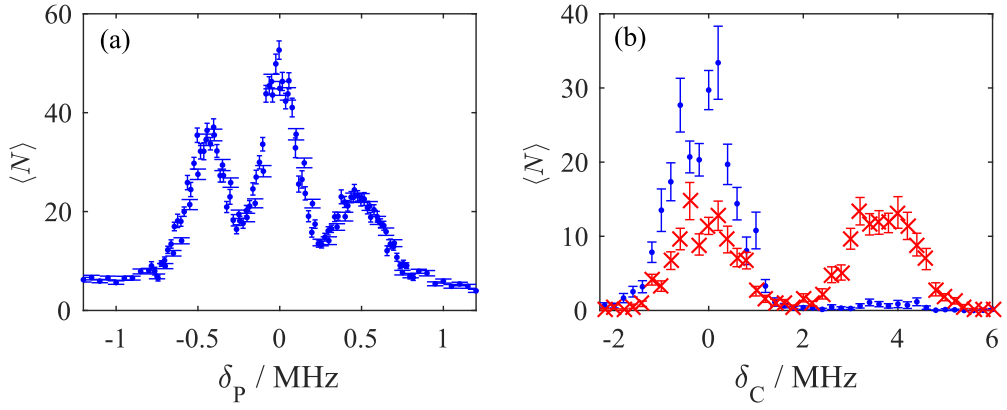

Figure 4.5: (a) Scanning the probe laser detuning δ_P without a quantisation field and using the 689 nm MOT beams as the probe beam. A stray magnetic field splits the intermediate state magnetic sublevels and all are driven by the MOT beams. (b) Effect of coupling beam detuning δ_C and polarisation with a vertical quantisation field of 2-3 G, driving from the $5s5p\ ^3P_1\ m_J = -1$ state. Blue points show vertically polarised coupling light, red points show a combination of vertically and horizontally polarised light. We see wider features scanning the coupling beam than scanning the probe beam.

The relative amplitude of the three features is influenced by the polarisation of the MOT beams and the coupling beam relative to the stray magnetic field and the coupling beam detuning from the possible transitions.

To better distinguish between the magnetic sublevels we apply a vertical quantisation field of 2-3 G, sufficient to cause Zeeman splitting greater than the expected Autler-Townes splitting.

To control the polarisation of the probe light we switch to using a single probe beam, typically mounted on the vertical axis. By defining a quantisation field we are able to control which m_J state we drive using the frequency and polarisation of the driving lasers, illustrated in Figure 4.5(b). Here, we drive to the $5s37s\ ^3S_1$ state via the $5s5p\ ^3P_1\ m_J = -1$ using two coupling beam polarisations. Blue dots indicate vertically polarised light that drives only to the $5s37s\ ^3S_1\ m_J = -1$ state, red crosses are a combination of vertical and horizontal polarisation, the horizontally polarised light can partially drive σ^+ transitions to the $5s37s\ ^3S_1\ m_J = 0$ state.

It is possible if one of the driving lasers is slightly off-resonance and both lasers are on simultaneously to observe both one-photon excitation from the $5s5p\ ^3P_1$ state and two-

photon excitation from the ground state in a single spectrum. These are easily distinguished; one-photon transition amplitudes (frequencies) are much more (less) dependent on the fixed laser beam frequency than two-photon transitions.

Unless otherwise stated, spectroscopy is performed on the $5s^2\ {}^1S_0 \leftrightarrow 5s5p\ {}^3P_1\ m_J = -1 \leftrightarrow 5snl\ {}^3l_1\ m_J = -1$ transition in the presence of a 2-3 G quantisation field in the z-axis with a vertically polarised coupling beam propagating horizontally and a circularly polarised probe beam propagating vertically.

A key point to note is the narrow widths that we can observe on these transitions, with FWHMs scanning the coupling laser as small as 350 kHz observed, and narrower lines when scanning the probe laser. Previously the narrowest features measured in this experiment have been an order of magnitude greater than this for both probe and coupling beam frequency scans due to the larger (30 MHz) width of the intermediate transition when coupling to singlet Rydberg states. In future, the research group intends to perform precision spectroscopy on these Rydberg states in conjunction with an optical frequency comb.

4.4 Rydberg state properties

Having characterised the Rydberg laser and excitation method, we can characterise Rydberg states. To do this we will measure the Rabi frequency, state lifetime, sensitivity to electric fields, and autoionisation spectra. All of these properties are relevant to our attempts to Rydberg dress a MOT, and we will characterise the Rydberg states with which we intend to Rydberg dress the MOT.

4.4.1 Autler-Townes splitting

A critical part of observing Rydberg dressing is obtaining a high Rabi frequency on the Rydberg transition. We measure the Rabi frequency of the coupling beam using Autler-Townes splitting, this is sometimes challenging for coupling beams of comparable size to the cloud.

We have measured Autler-Townes splitting in the broadband MOT using two coupling beam sizes and in the single frequency MOT using a single beam size.

Autler-Townes splitting in a broadband MOT

We observe Autler-Townes splitting using two-photon excitation with a resonant coupling beam and varying the probe beam frequency, shown in Figure 4.6. As we increase the coupling beam intensity we see the resonance feature split into two distinct features, the separation of which is the Rabi frequency that we couple to the Rydberg state with.

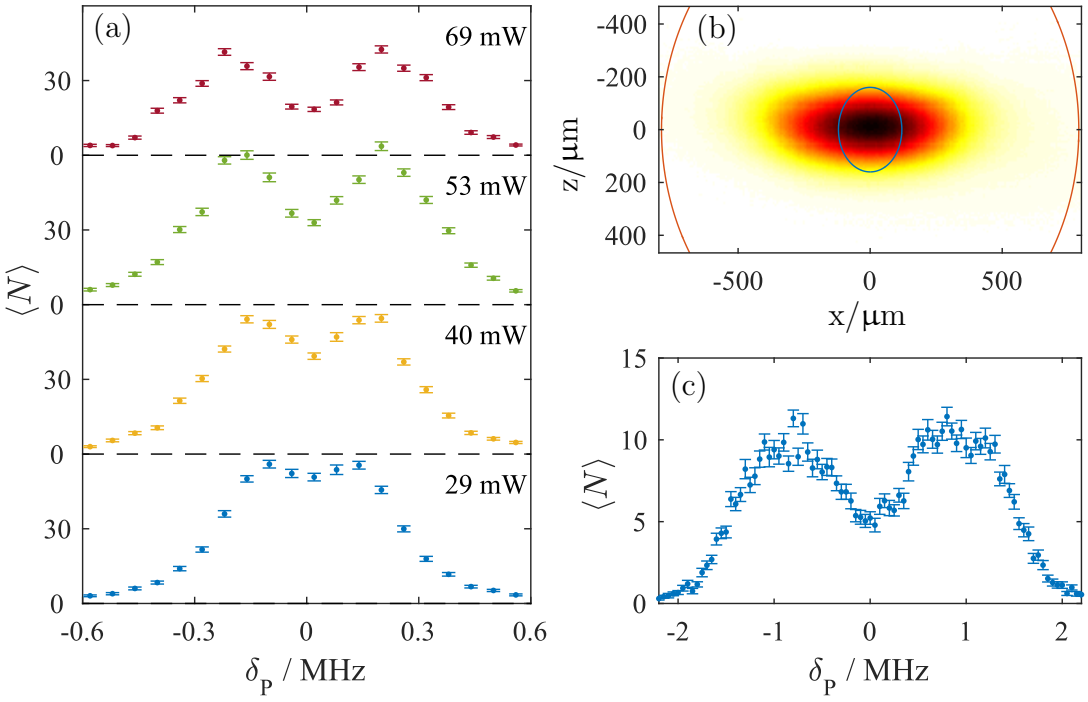

Figure 4.6: Autler-Townes splitting in a broadband MOT with a large (a) and a small (c) coupling beam with respect to the cloud. Focussing the coupling beam gives higher Rabi frequencies, illustrated through the increased splitting, but also blurs the features out due to the range of Rabi frequencies experienced by the cloud. (b) shows an averaged fluorescence image of the cloud, the red ring indicates the size of the large coupling beam and the blue ring indicates the size of the small coupling beam - both are $1/e^2$ radii.

In the broadband MOT we can see splitting of up to 400 kHz at full coupling beam power at the $5s37s\ ^3S_1$ state. This is not sufficient for Rydberg dressing experiments, as to obtain a dressed interaction of 20 kHz with this Rabi frequency we would need a maximum coupling beam detuning of 580 kHz, where we would not be in the $\Omega_C \ll \delta_C$ regime.

To increase the Rabi frequency we focus the coupling beam to around a fifth of its previous

size, expecting a rise in peak intensity of 5^2 and a rise in peak Rabi frequency of 5. The broadband MOT typically has a $1/e^2$ horizontal radius of 420 μm and vertical radius of 150 μm. By comparison, the coupling beam before focussing has a $1/e^2$ horizontal and vertical radius of 790 μm and 930 μm. The focussing lens is outside the vacuum chamber, so measuring the exact size of the coupling beam at the position of the atoms is challenging.

Initially, we attempted to see Autler-Townes splitting in the broadband MOT with the focussed coupling laser beam. This had some success, shown in Figure 4.6(c), as we observe a power dependent splitting, but the features are not as resolved as we would like. The peaks are more separated than those in Figure 4.6(a) but are also much more broad, with less dip in the centre than we would expect extrapolating from the previous data. This is due to averaging over a range of Rabi frequencies due to using an atom cloud that is larger than the coupling beam; to avoid this we switch to using a smaller, single frequency MOT.

Autler-Townes splitting in a single frequency MOT

To avoid this averaging effect we use a single frequency MOT that is much smaller (65 μm by 140 μm $1/e^2$ radii) than the expected coupling beam size, eliminating the averaging effect and allowing us to see well resolved Autler-Townes peaks. Figure 4.7 shows Autler-Townes spectra taken coupling to the $5s36d\ ^3D_1\ m_J = -1$ state, where we expect a larger Rabi frequency due to the larger dipole matrix element [74].

The peaks are much more separated due to the higher intensity of the focussed coupling beam and stronger coupling of the $5s36d\ ^3D_1$ state than the $5s37s\ ^3S_1$ state, allowing us to reach Rabi frequencies of 4 MHz. This is sufficient to off-resonantly Rydberg dress the MOT with - a 4 MHz Rabi frequency and a detuning of 12 MHz gives rise to a two-body dressed interaction strength of 18 kHz (Equation 2.21), comparable to the cloud temperature. The averaging effect observed in the broadband MOT is largely suppressed, allowing us to be confident that all of the atoms experience strong coupling to the Rydberg state.

We also observe a central feature that occurs in a similar position to the unsplit feature. Close inspection suggests that this is due to weakly confined atoms that are not trapped at the quadrupole field centre. We are using a high MOT beam power of 500 μW and a MOT beam detuning of -120 kHz to reach such a small tightly confined MOT that

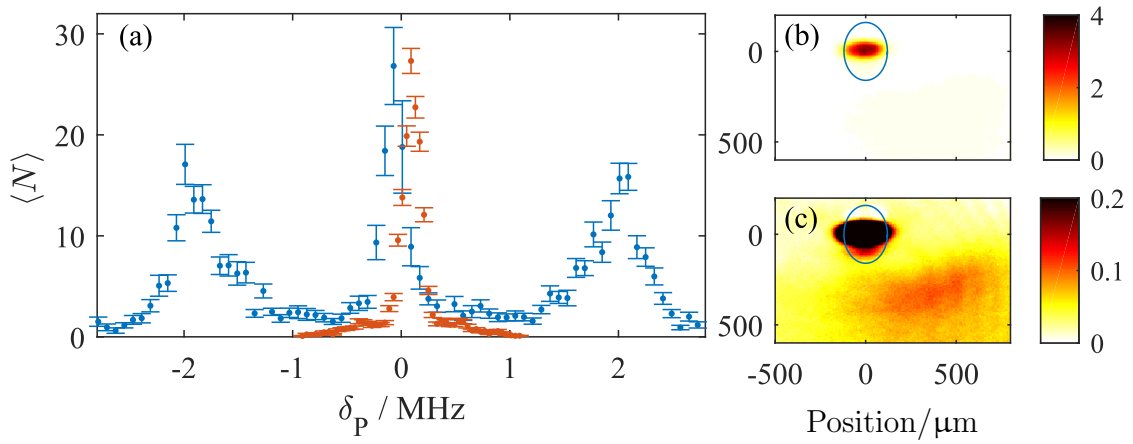

Figure 4.7: Autler-Townes splitting in a retrapped single frequency MOT. (a) Ion signals for high (blue, 50 mW) and low (orange, 200 μW, rescaled for comparison) coupling beam powers. At high coupling power Autler-Townes splitting is observed, as well as a third central peak caused by trap leakage illustrated in the optical depth images (b) and (c). The same cloud is shown with a different colorbar, allowing atoms trapped far from the quadrupole field centre to be observed.

can be retrapped, under these conditions atoms are observed leaking from the cloud. We believe that these atoms are being retrapped by leaked broadband red MOT light. Far from the focus of the coupling beam, they can still be excited to Rydberg states but will not be Autler-Townes split. The rate of atoms leaking from the trap is slightly density dependent, making this appear to be an effect of Rydberg atom interactions, but it is observed well below the blockade density for this state.

Coupling beam profile from Autler-Townes splitting

We can move the MOT position by changing the current in the external shim coils, moving the cloud through the coupling beam and taking Autler-Townes spectra at different positions. This allows us to measure the beam size and ensure accurate alignment of the atoms in the coupling beam. Figure 4.8 shows the ion signal as a function of both cloud vertical position and probe beam detuning. We can clearly see splitting, as well as a position dependent shift, which is caused by the changing magnetic field due to the shim coils. The splitting is poorly resolved as the cloud was a similar size to the coupling beam width.

From the splitting dependence on position, we estimate the coupling beam $1/e^2$ radii

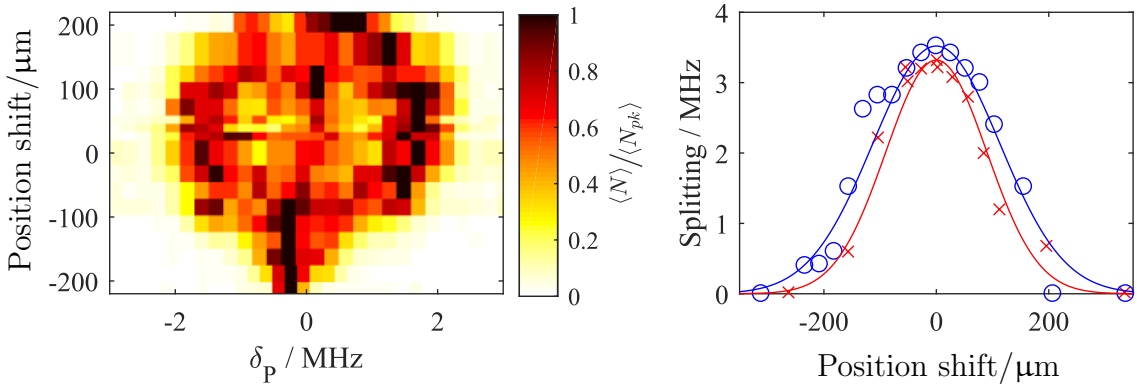

Figure 4.8: Moving the MOT and scanning the probe beam detuning for a high power coupling beam, we observe position dependent Autler-Townes splitting on the left (colour indicates the ion number over the peak ion number). This is heavily blurred due to the comparable cloud size and coupling beam size, but by plotting the separation of the two peaks (shown on the right) we can fit the width of the coupling beam. Blue (orange) rings indicate Autler-Townes splitting as a function of vertical (horizontal) position.

as 160 μm and 120 μm in the vertical and horizontal direction. These numbers are comparable to those estimated from the increase in Rabi frequency due to focussing the coupling beam of 160 μm and 130 μm.

In future, an optical dipole trap will be implemented; this will allow the quantisation field to be on for long enough for eddy currents to decay, allowing consecutive excitations. Dipole traps can be switched off and on rapidly without the need for a 400 μs MOT coil switching time, allowing for easy recapture. It will also allow for a smaller trap size, reducing the averaging effect. The techniques described are sufficient for estimating Rabi frequency for our purposes; a particular strength of these techniques is that any observation of blurring of Autler-Townes splitting due to cloud size provides information on the distribution of Rabi frequencies that the atoms experience.

Rabi frequencies

Rabi frequency scales with the square root of beam intensity. From the data presented we have calculated the coupling strength as a function of coupling beam intensity to be $\Omega_{37s}/\sqrt{I} = 190\pm30$ kHz$/\sqrt{\text{W/cm}^2}$ for the $5s5p\ ^3P_1\ m_J = -1 \leftrightarrow 5s37s\ ^3S_1\ m_J = -1$ transition and $\Omega_{36d}/\sqrt{I} = 290\pm30$ kHz$/\sqrt{\text{W/cm}^2}$ for the $5s5p\ ^3P_1\ m_J = -1 \leftrightarrow 5s36d\ ^3D_1\ m_J = -1$ transition. Uncertainties are dominated by the precision of our

coupling beam width measurements and, for the s-state, the position averaging of the relative MOT and coupling beam size. These values are sufficient for Rydberg dressing experiments as shown in Chapter 2.6.

A thorough comparison between these measurements and predicted values is not the focus of this thesis, but we do compare our measured Rabi frequency to the predicted Rabi frequency achievable coupling to the $5s37s\ ^3S_1$ state. Using the oscillator strengths set out in [74] we expect a total coupling strength of 920 kHz/$\sqrt{\mathrm{W/cm^2}}$ on the $5s5p\ ^3P_1 \leftrightarrow 5s37s\ ^3S_1$ transition, giving a predicted coupling strength of 150 kHz/$\sqrt{\mathrm{W/cm^2}}$ on the $5s5p\ ^3P_1\ m_J = -1 \leftrightarrow 5s37s\ ^3S_1\ m_J = -1$ transition. Given the paucity and limited accuracy of the spectroscopic data that [74] is based on, and the accuracy of our measurements, we consider a 21% difference between theory and experiment to be very reasonable.

4.4.2 DC Stark sensitivity

The Rydberg dressed MOT will have a sensitivity to electric field due to the admixture of Rydberg character into the MOT, as shown in Section 5.5. In addition, the role of charged particles in the dressed MOT is critical to the losses from the dressed MOT, shown in Chapter 6. We therefore require an understanding of the static polarisability, α_0, of the bare Rydberg states.

The large dipole moments of Rydberg atoms make them very sensitive to electric fields, which mix nearby Rydberg states together [111, 112]. For small electric fields F we expect the DC Stark shift of Rydberg states δ_{DC} to scale with F^2 according to the scalar polarisability of the Rydberg state α_0:

$$\delta_{\mathrm{DC}} = -\alpha_0 F^2. \tag{4.1}$$

Figure 4.9 shows a Stark map for the $5s36d\ ^3D_1$ state, taken by scanning the coupling beam laser over resonance for a range of electric fields. Two $|m_J|$ sublevels are observed, both increasing in energy with electric field, but at different rates. By fitting to the feature centres (shown as solid lines in Figure 4.9) we can calculate Rydberg state polarisability. This has been done for both sublevels for the $5s36d\ ^3D_1$ and $5s37s\ ^3S_1$ Rydberg states that we Rydberg dress the MOT with in Chapter 5. The fitted static polarisabilities are shown in Table 4.1.

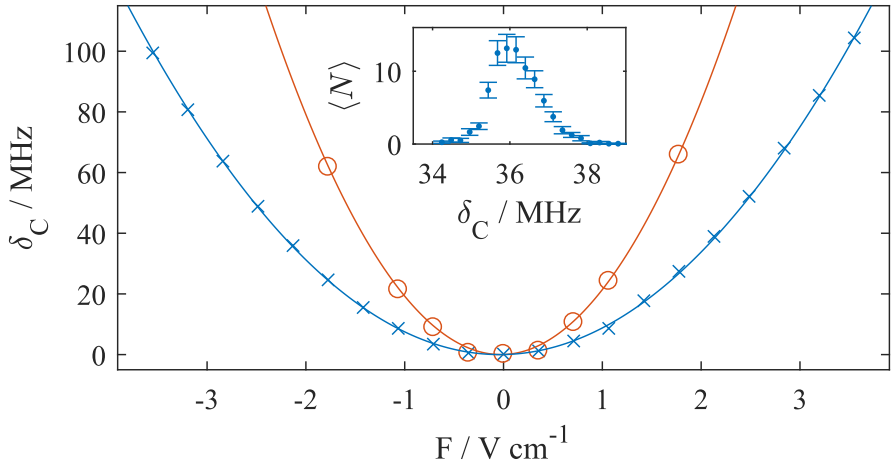

Figure 4.9: A Stark map of the $5s36d\ ^3D_1$ state. The inset shows an example scan at an electric field of -2.13 V/cm coupling to the $5s36d\ ^3D_1$ $|m_J| = 1$ state, by combining several scans we can observe the DC Stark shift of the Rydberg state. Fits to the $|m_J| = 1$ and $|m_J| = 0$ states are shown in blue and orange.

The data was taken with one-photon excitation to eliminate possible two-photon effects, using two consecutive 689 nm and 319 nm pulses of 8 µs separated by 1 µs. No quantisation coil was used, as the electric field is used to define a quantisation axis.

Two electric field pulses are required for this experiment, the first a uniform field during which excitation takes place, and the second an ion steering field to direct ions towards the MCP. The uniform electric field was supplied directly from the FPGA card analog output voltage; the ground of the analog output is not the same as the ground of the vacuum chamber, resulting in an offset of around 100 mV in electric field ground that causes an asymmetry around the field centre in Figure 4.9. Two voltages of ± V are applied to two opposite pairs of electrodes, resulting in a horizontal electric field perpendicular to the MCP. We obtain an electric field of 0.355 V/cm per ± V applied to the electrode pairs [85].

The static polarisabilities given in Table 4.1 are consistent with Stark maps generated from predicted and measured Rydberg energy levels, although precise measurements of static polarisability will require more attention to the cancellation of stray electric field for small applied fields.

We will use the static polarisabilities measured here to understand the dressed MOT sensitivity to electric field, and also understand the role of charged particles in the dressed

State	α_0 / MHz / (V/cm)^2
$5s37s\ ^3S_1\ \|m_J\| = 0$	1.4 ± 0.1
$5s37s\ ^3S_1\ \|m_J\| = 1$	1.4 ± 0.1
$5s36d\ ^3D_1\ \|m_J\| = 0$	-20 ± 1
$5s36d\ ^3D_1\ \|m_J\| = 1$	-8.1 ± 0.4

Table 4.1: Rydberg state static polarisability. For small electric fields, polarisability scales with F^2, and scales with principal quantum number as n^7. The dominant source of error is the electric field calibration.

MOT. As shown in Chapter 6, the Rydberg state response to electric field may be critical to the ability to observe Rydberg dressed interactions without prohibitive loss.

4.4.3 State lifetime

Rydberg state atoms may be resonantly transferred through blackbody radiation to several states and have many decay channels, including to metastable states, making it unlikely that atoms in the Rydberg state will decay to the ground state on the timescale of dressing experiments. As a result the dressed MOT lifetime will depend on the Rydberg state lifetime. To measure the lifetime of the Rydberg state we excite atoms to the Rydberg state and then leave a variable delay before using the 408 nm laser to autoionise any surviving Rydberg atoms, shown in Figure 4.10. We can distinguish between spontaneously ionised ions and autoionised Rydberg atoms from their arrival times at the MCP, allowing us to remove the spontaneous ion signal to get a true measure of Rydberg population.

Coupling to the $5s36d\ ^3D_1$ Rydberg state, we observe double-exponential decays in ion signal, in which Rydberg atoms decay into other, longer-lived Rydberg atoms. This is shown in Figure 4.10, which shows the detected ions against delay time t with two fits, a single exponential $N(t) = N_{\mathrm{pk}}\mathrm{e}^{-t/\tau}$ and a double exponential $N(t) = N_1\mathrm{e}^{-t/\tau_1} + N_2\mathrm{e}^{-t/\tau_2}$. We see far better agreement to the double exponential, yielding lifetimes of $\tau_1 = 11.8 \pm 1.1$ µs and $\tau_2 = 63 \pm 13$ µs. We use excitation pulses that are short compared to the Rydberg state lifetime to limit transfer to other states during excitation.

Coupling to the $5s37s\ ^3S_1$ Rydberg state, we observe a lifetime of $\tau = 35 \pm 3$ µs and don't observe a clear double exponential. This could be due to reduced transfer to other

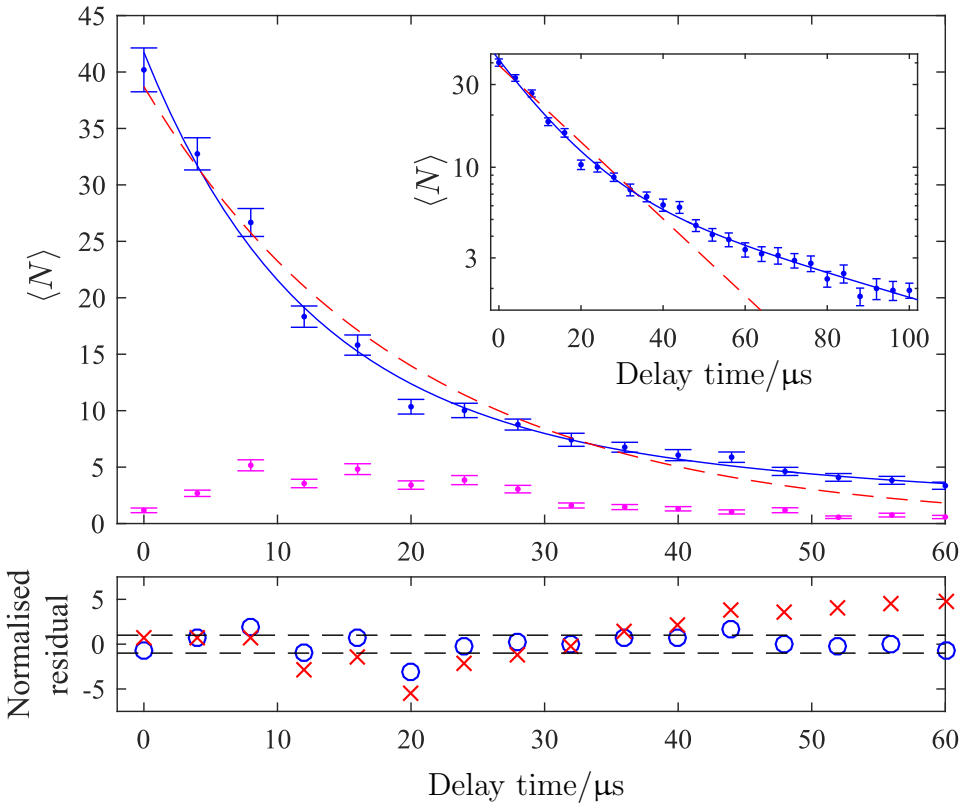

Figure 4.10: Lifetime of the $5s36d\ ^3D_1$ Rydberg state. Blue points are autoionised Rydberg atoms, purple points are spontaneously ionised Rydberg atoms, distinguished from arrival time on the MCP. Fitting a single lifetime (red dashes) yields a poor fit, a double exponential (solid blue) yields a better fit, indicating decay to longer lived Rydberg states. This is more obvious from the inset, for which the change in lifetime is more obvious.

states, but could also be due to the comparable lifetime of the $5s37s\ ^3S_1$ state to the states that are transferred to. A $5s38s\ ^3S_1$ state lifetime of 20 ± 1 μs is measured in [99], measured using state selective field ionisation, suggesting that there is state transfer that is not obvious from our lifetime measurement technique when the initial state and the transfer states have comparable lifetimes.

To better understand this we can use autoionisation as a probe of the Rydberg population - if Rydberg atoms transfer to nearby Rydberg states with different lifetimes they will also have different probabilities of autoionising.

4.4.4 Autoionisation spectroscopy

A merit of using a divalent atom is the presence of a second valence electron that allows for autotionisation [113]. Many processes, such as blackbody radiation, radiative decay, collisions, facilitated growth and plasma formation may transfer Rydberg atoms into new states and autoionisation may be a powerful tool for diagnosing Rydberg population in the Rydberg dressed MOT.

Exciting the inner valence electron of a Rydberg atom can lead to very rapid ionisation of the Rydberg atom and the high ionisation rate results in very broad autoionising spectra. The ionisation rate is dependent on the overlap of the Rydberg electron wavefunction and the inner valence electron wavefunction, with higher n states having narrower autoionising spectra, and high l states typically having negligible autoionisation.

The data in Figure 4.11 were taken by exciting atoms to the Rydberg state, then ionising the Rydberg atoms before applying an ion steering electric field. We autoionise the Rydberg atoms before applying the ion steering electric field, to avoid mixing additional Rydberg state into the Rydberg atoms being ionised, as this may modify the observed spectra. We also observe the ion signal without the autoionising laser and subtract this spontaneous ionisation from the autoionisation signal. Care must be taken when taking these spectra to avoid depleting the Rydberg population with the autoionising laser.

Two spectra are shown in Figure 4.11 for the $5s37s\ ^3S_1$ and $5s37p\ ^3P_1$ Rydberg states. We clearly see a frequency shift of several GHz between the two Rydberg states. The lower plot of Figure 4.11 illustates autoionisation as a diagnostic of state transfer. Measuring the spectra of the $5s37s\ ^3S_1$ state with a delay between excitation and ionisation, we can see an autoionisation laser frequency dependent lifetime - when the autoionising laser is strongly resonant with the $5s37p\ ^3P_1$ state and not the driven $5s37s\ ^3S_1$ state we predominantly ionise Rydberg atoms in the p series that are populated through decay and transfer from the driven $5s37s\ ^3S_1$ state, and measure the longer lifetime of the p-state Rydberg atoms. Autoionisation is expected to be stronger for the p states than the s states as there is more overlab between the two orbitals of the electrons for p-state Rydberg atoms.

From these data we can be confident that the lifetime measurement technique we use in Section 4.4.3 will measure the Rydberg population in both the $5s37s\ ^3S_1$ state and neighbouring $5snp\ ^3P_1$ Rydberg states. This is the likely cause of the discrepancy between our Rydberg state lifetime measurement and the Rydberg state lifetime observed in [99].

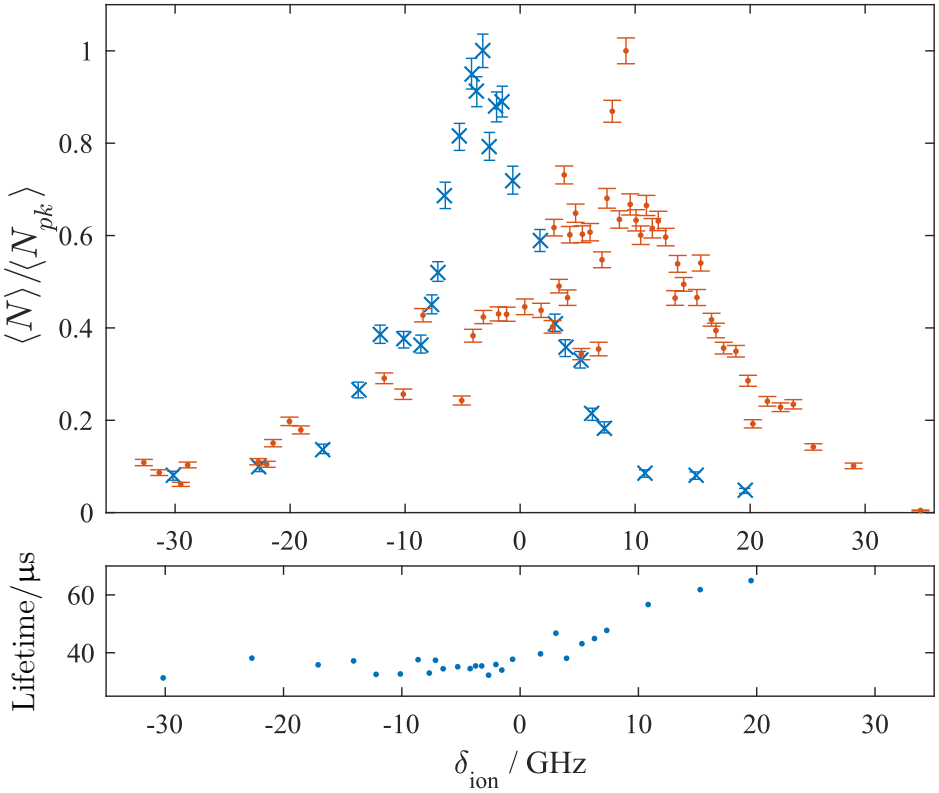

Figure 4.11: Autoionising spectra for the $5s37s\ ^3S_1$ (blue crosses) and $5s37p\ ^3P_1$ (orange dots) Rydberg states. We can readily distinguish between the two Rydberg states from their autoionising spectra. Also shown is the lifetime of the Rydberg population, measured as a function of autoionising laser detuning. The longer lifetime nearer resonance with the $5s37p\ ^3P_1$ state implies that $5s37s\ ^3S_1$ Rydberg atoms are decaying to the $5snp\ ^3P_J$ series.

When there is a large difference in lifetime between the state that we couple to and the states that are transferred to we can observe this in the exponential, as shown in Figure 4.10 but when these lifetimes are comparable we require a more careful technique to measure Rydberg state lifetimes, for example, state selective field ionisation.

The detuning axis of Figure 4.11 is from the ion line $4p^65s\ ^2S_{1/2} \leftrightarrow 4p^65p\ ^2P_{3/2}$ ion transition at 734.99 THz [114]. Excitation to the $5s37p\ ^3P_1$ is possible by applying a weak electric field during the coupling pulse; this mixes a small amount of s- and d-states into the p-state, allowing excitation from the $5s5p\ ^3P_1$ intermediate state.

In practice these experiments are time-consuming and challenging - the autoionising laser must be scanned over several tens of GHz and frequently modehops to a multimode posi-

tion when being scanned. The laser must be scanned by hand, making these experiments difficult to automate, and fitting the spectra requires knowledge of the autoionisation spectra of nearby Rydberg states. A possible enhancement of this autoionisation spectroscopy technique is the use of ion arrival times - the rate of Rydberg population depletion under the autoionising laser depends on the autoionisation cross section and the Rydberg state lifetime, both of which are strongly state dependent. Consequently, different Rydberg states will deplete in the presence of the autoionising laser at different rates, which can be observed from the ion arrival times. This could drastically reduce the time needed to diagnose the Rydberg population by avoiding the need to scan the laser frequency. This technique may be tested at a later point.

In the future, we may attempt to fit the autoionising spectra using multichannel quantum defect theory (MQDT) [113]. A this stage, we have measured spectra allowing us to potentially diagnose the Rydberg population in the Rydberg dressed MOT.

4.5 Summary

In this chapter we have described the laser that we will use to Rydberg dress the MOT, and have characterised several previously unseen Rydberg states.

The 319 nm coupling laser can reliably produce up to 80 mW of coupling light with a frequency stability of $\sim$ 35 kHz. Ideally we will avoid operating at $\pm$ 20 MHz from resonance, due to a very small amount of frequency modulated 638 nm light from the doubling cavity being summed with unmodulated light.

We have observed several previously unmeasured Rydberg states, typically identifying states from ion signals or MOT depletion when the coupling laser is on resonance. Thorough characterisation is performed when both probe and coupling laser are frequency stabilised, and involves measurement of coupling Rabi frequency, state lifetime, static polarisability and autoionisation spectra. We have thoroughly characterised the $5s37s\,^3S_1$ and $5s36d\ ^3D_1$ Rydberg states. Most challenging of this characterisation is the observation of Autler-Townes spectra to measure Rabi frequency, due to the comparable size of the coupling beam and the atom cloud, and difficulties in performing multiple excitations within a single frequency MOT.

The research group intend to enhance and extend this characterisation to a range of Rydberg series in conjunction with an optical frequency comb to perform very high resolution

spectroscopy of previously unobserved Rydberg series in strontium with unprecedented precision. Doing this in an optical dipole trap will allow easier trap switching and smaller traps.

Having characterised several Rydberg states we can now Rydberg dress the MOT.

Chapter 5

A Rydberg Dressed MOT

Having described Rydberg dressing and the experiment in Chapters 2 and 3 and characterised several Rydberg states in Chapter 4, we now bring these together to demonstrate a Rydberg dressed MOT. The first half of this chapter will:

- Describe some initial experiments to observe the AC Stark shift due to the coupling laser on the cloud shape.
- Introduce a simple AC Stark shifted resonance model to understand the cloud shape and develop the Monte-Carlo MOT model described in Section 2.5 to include coupling to the Rydberg state.
- Identify an appropriate MOT regime for Rydberg dressing, in which only Rydberg dressed atoms are trapped in the MOT.

Having identified a regime in which atoms remain both trapped and coupled to the Rydberg state, we can characterise the Rydberg dressed MOT. The second half of this chapter will:

- Demonstrate the Rydberg character of the cloud through sensitivity to electric field.
- Study the cloud dynamics and demonstrate sustained cooling of the cloud.
- Study the lifetime of the trapped cloud, which we want to be comparable or longer than the equilibration time of the cloud.

This dressed MOT characterisation will both demonstrate the viability of a Rydberg dressed MOT and the challenges that must be overcome to observe Rydberg dressed interactions in a Rydberg dressed MOT.

5.1 Adding Rydberg character to the MOT

A single coupling laser beam is required to mix Rydberg character into the excited state of the single frequency red MOT transition. The Rydberg fraction of the dressed state, subject to $\Omega \ll \delta$ is then given by Equation 2.6. This fraction can give rise to Rydberg dressed interactions, but the first effect we observe is an AC Stark shift given by Equation 2.7. Initial Rydberg dressing experiments were performed on the $5s37s\ ^3S_1$ and $5s36d\ ^3D_1$ Rydberg states, with achievable Rabi frequencies of 2.5 MHz and 4 MHz respectively.

The first step towards characterising the Rydberg dressed MOT is looking at the effect of the AC Stark shift on the spatial distribution of the cloud.

5.1.1 Initial experiments

Initial Rydberg dressing experiments were performed by shining the coupling laser onto a single frequency red MOT for a range of coupling beam detunings and dressing times, shown in Figure 5.1. The first observation, even before considering the shape of the MOT, is that the trap continues to operate. After 5 ms of dressing we still observe atoms when the coupling beam is red- and blue-detuned. The $5sns\ ^3S_1$ Rydberg series exhibits repulsive interactions, and we might expect a blue-detuned coupling laser to excite pairs of Rydberg atoms, leading to heavy depletion, but at initial densities of 10^{11} cm^{-3}, we don't see this.

When the coupling beam is red-detuned from resonance we observe a dimple protruding into the MOT, shown in the top two lines of Figure 5.1. Atoms within this dimple are not trapped and fall under gravity. When blue-detuned (bottom two rows of Figure 5.1), we see a dimple outside of the MOT, into which atoms flow. On resonance we see heavy loss due to Rydberg excitation, shown in the third row of Figure 5.1.

The cause of this dimple is illustrated in Figure 5.2. The red-detuned coupling beam results in an AC Stark shift that reduces the MOT beam detuning from the dressed

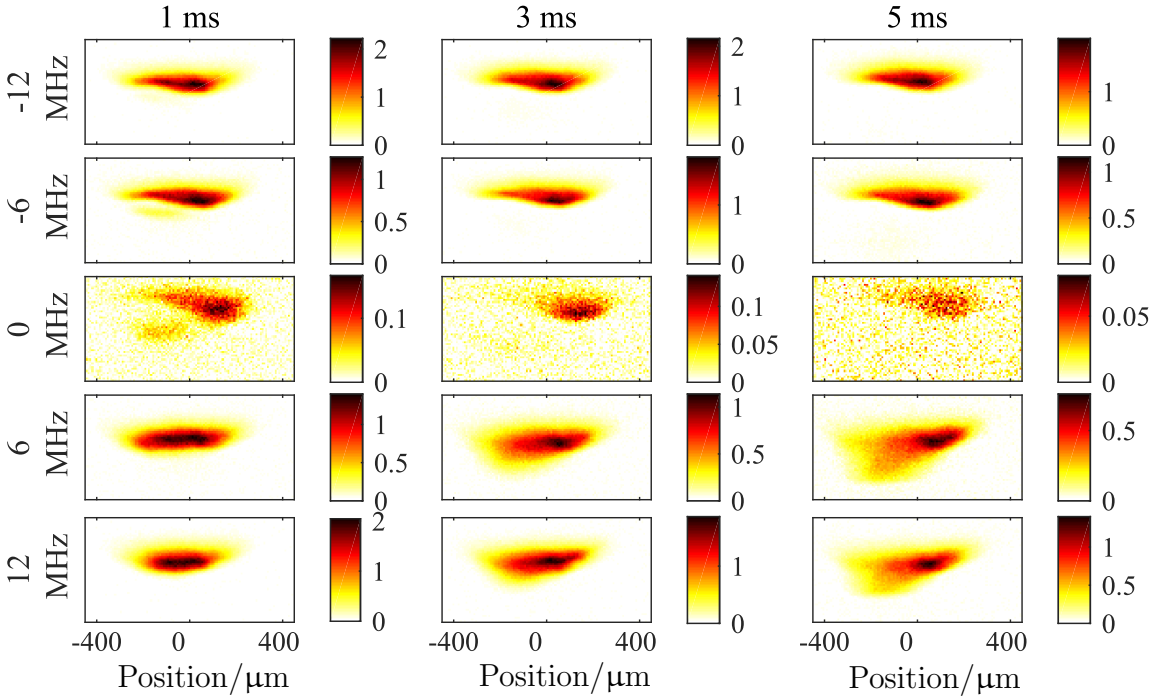

Figure 5.1: Dressing a MOT with $5s37s\ ^3S_1$ Rydberg character, using $\Omega = 2.5$ MHz, $\delta_{\mathrm{MOT}} = -400$ kHz and $\mathrm{P_{MOT}} = 150$ μW for different dressing times (left to right) and coupling beam detunings (top to bottom). The scale shows cloud optical depth, averaged over two repeats. The single frequency red MOT is held for 50 ms for cooling to complete before the coupling laser is turned on.

state. MOT beam resonance with the dressed state then occurs for a smaller Zeeman shift, closer to the quadrupole field centre. The reverse is true for blue-detuned coupling - MOT beam resonance with the dressed state occurs further from the quadrupole field centre, creating a dimple into which atoms can flow.

The effect observed in Figure 5.1 is spatially asymmetric, suggesting the coupling beam is not perfectly aligned onto the cloud centre. As the cloud is larger than the coupling beam the AC Stark shift only affects part of the cloud.

A two-stage dressed MOT

To better understand the effect that the AC Stark shift has we have developed a two-stage MOT detuning scan, shown in Figure 5.3. We form a single frequency red MOT at $\delta_{\mathrm{MOT}} = -350$ kHz and $\mathrm{P_{MOT}} = 90$ μW, which we then dress with $5s37s\ ^3S_1$ Rydberg character using $\Omega = 2.5$ MHz, $\delta_C =$ -6 MHz. Being red-detuned, we expect a dimple to

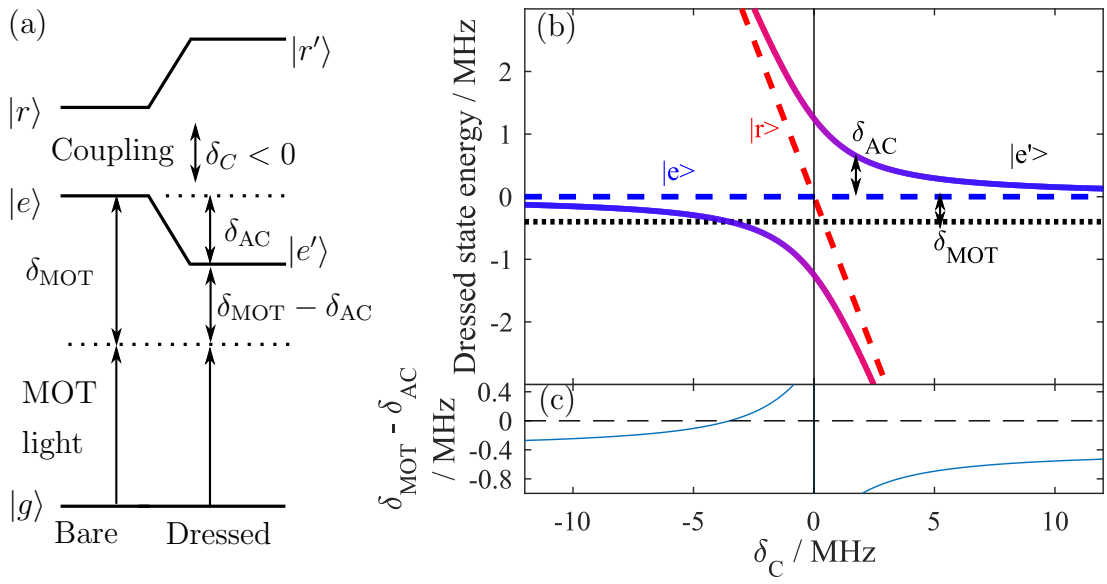

Figure 5.2: (a) When the coupling beam δ_C is red-detuned it reduces the energy of the dressed state $|e'\rangle$ below the bare state $|e\rangle$, effectively reducing the MOT beam detuning magnitude, illustrated on the left. The smaller effective MOT beam detuning results in resonance occuring for a smaller Zeeman shift, closer to the quadrupole field centre. (b) shows the dependence on the coupling beam detuning δ_C - when the coupling beam is blue-detuned the dressed state $|e'\rangle$ is shifted higher in energy than the bare state $|e\rangle$, and resonance occurs for a larger Zeeman shift. The colour of the dressed state indicates the fraction of $|e\rangle$ (blue) and $|r\rangle$ (red) in the dressed state and the black dotted line indicates the MOT beam detuning. (c) shows the effective MOT beam detuning $\delta_{MOT} - \delta_{AC}$ from the dressed state $|e'\rangle$.

protrude into the cloud. When the coupling laser is turned on the MOT beam detuning δ_{MOT} is changed. This was repeated with and without the coupling laser, for 10 ms of dressing.

In the bare state case (Figure 5.3(a-e)), as the MOT beam frequency moves further from resonance the cloud gets larger and moves lower, retaining the ellipse outline set by the quadrupole field as we expect. When the coupling beam is on (Figure 5.3(f-j)) we see very different MOT shapes - as the MOT beam detuning increases the cloud gets larger but also splits into two clouds that form either side of the dimple due to the coupling beam. We also see a fraction of the cloud that is not trapped and falls under gravity, seen in Figure 5.3(f).

Making a composite image from all the MOT images at different MOT beam detunings,

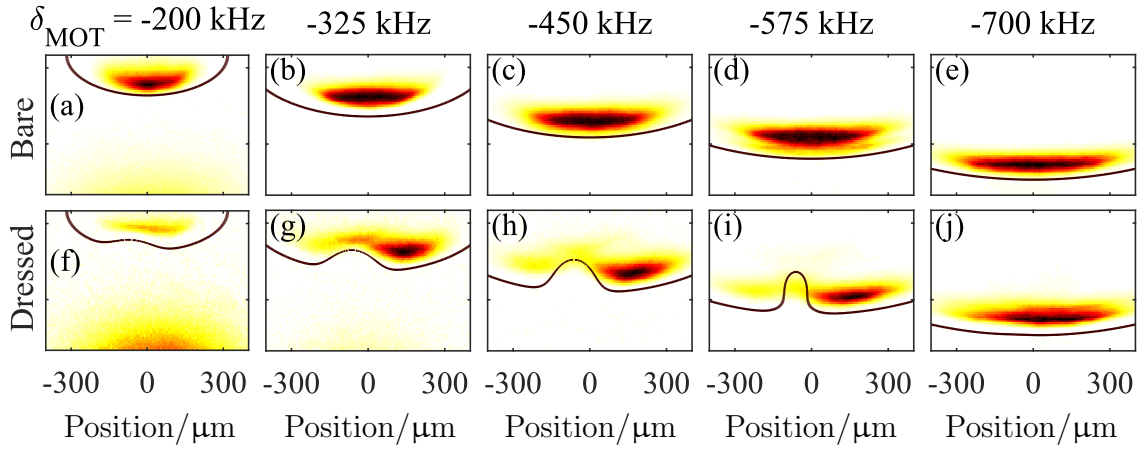

Figure 5.3: Stepping the MOT detuning to a new value (row a-e), we see the MOT form in a new position. Adding the red-detuned coupling laser to this (row f-j) modifies the cloud shape - the cloud flows under gravity to either side of the coupling beam dimple. Taken with $\delta_C = -6$ MHz, $\Omega = 2.5$ MHz. Predicted resonance curves described in Section 5.1.2 are overlaid.

we can map out the shape of the dimple that protrudes into the MOT. This is shown in Figure 5.4, and offers a very striking representation of the effect of the coupling beam. Rather than atoms simply sagging to the lowest point of a resonance ellipse set by the quadrupole field, the resonance condition is met either side of the coupling beam, and above the coupling beam. Atoms sag under gravity to the lowest positions on the resonance curve, either side of the coupling beam. As the coupling beam is slightly off-centre, the atoms preferentially fall to the right of the coupling beam. The effect does not appear to be significantly blurred by the 30° angle between the coupling beam and the imaging axis.

5.1.2 An AC Stark shifted resonance model

In Figure 5.3 we overlay a modified resonance curve on the data that accounts for the AC Stark shift. This section will use the dressed state picture and the MOT resonance curves from Chapter 2 to calculate these resonance curves. To do this we will consider when the MOT beams are resonant with the dressed state $|e'\rangle$ rather than the bare state $|e\rangle$.

We first consider how the energy of the dressed state $|e'\rangle$ is shifted by the AC Stark shift

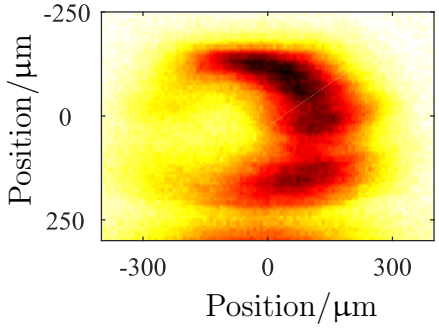

Figure 5.4: A composite image from the data in Figure 5.3, made using a range of MOT beam detunings to visualise the effect of the coupling beam.

from the bare state $|e\rangle$, and the position dependence of this shift.

In Chapter 2 we demonstrated that the AC Stark shift of the dressed state $|e'\rangle$ compared to the bare state $|e\rangle$ is given by $\delta_{\mathrm{AC}} = -\frac{\delta_C}{2} \pm \frac{\sqrt{\delta_C^2+\Omega_C^2}}{2}$, where δ_C is the coupling beam detuning and Ω_C is the coupling beam Rabi frequency. The coupling beam intensity is Gaussian, $I(x,z) = I_0 \exp\left(-\frac{2(x-x_0)^2}{\omega_x^2} - \frac{2(z-z_0)^2}{\omega_z^2}\right)$, where I_0 is the peak intensity, $\omega_{x,z}$ is the $1/\mathrm{e}^2$ radius in the horizontal and vertical direction, and x_0 and z_0 describes the coupling beam position. The Rabi frequency is proportional to the square root of intensity, so $\Omega_C^2(x,z) = \Omega_C^2(x_0,z_0) \exp\left(-\frac{2(x-x_0)^2}{\omega_x^2} - \frac{2(z-z_0)^2}{\omega_z^2}\right)$.

From this we obtain an expression for the AC Stark shift of the dressed state $|e'\rangle$ that reflects the intensity profile of the coupling beam, which can be simplified when $\Omega_C \ll \delta_C$:

$$\delta_{\mathrm{AC}} = -\frac{\delta_C}{2} \pm \frac{\sqrt{\delta_C^2 + \Omega_C^2 \exp\left(-\frac{2(x-x_0)^2}{\omega_x^2} - \frac{2(z-z_0)^2}{\omega_z^2}\right)}}{2} \approx \frac{\Omega_C^2}{4\delta_C} \exp\left(-\frac{2(x-x_0)^2}{\omega_x^2} - \frac{2(z-z_0)^2}{\omega_z^2}\right). \tag{5.1}$$

This is simply introducing a position dependent term to the AC Stark shift to reflect the coupling beam intensity profile. The AC Stark shift is shown in Figure 5.5(b) for the parameters used in Figure 5.3.

This treatment assumes that the Rabi frequency position dependence is purely dependent on the coupling beam intensity. In practice, the angle between the magnetic field and the coupling beam polarisation will influence what transitions are coupled and the effective Rabi frequency, but at this point we consider only Regime I MOTs, where the magnetic field is primarily vertical. This matches the coupling beam polarisation axis and the configuration under which the Rabi frequency was measured. In Appendix F we consider

the effect of magnetic field direction variation.

Having considered the AC Stark shift that the dressed state experiences we now consider when the MOT beams are resonant with the dressed state. The atoms will be trapped where the MOT beams are resonant.

In Chapter 2.5 we did this by equating the MOT beam detuning from the bare state δ_{MOT} to the Zeeman shift $m_J g_J \mu_B \frac{\mathrm{d}\boldsymbol{B}}{\mathrm{d}\boldsymbol{z}} \cdot \boldsymbol{z}$, shown in Figure 2.8. Now we are interested in the dressed state $|e'\rangle$ so we replace the MOT beam detuning from the bare state δ_{MOT} with the MOT beam detuning from the dressed state $\delta_{\mathrm{MOT}} - \delta_{\mathrm{AC}}$ to obtain:

$$\delta_{\mathrm{MOT}} - \delta_{\mathrm{AC}} = m_J g_J \mu_B \frac{\mathrm{d}\boldsymbol{B}}{\mathrm{d}\boldsymbol{z}} \cdot \boldsymbol{z} \ , \tag{5.2}$$

The MOT beam detuning δ_{MOT} is constant, the Zeeman shift and AC Stark shift are shown in Figure 5.5(a-b). We can numerically solve this to obtain a curve on the $x - z$ plane where the MOT beams are resonant with the dressed state, shown in Figure 5.5(c). Included in this calculation is an offset on the 689 nm frequency due to an offset on the laser lock point, which has been estimated based from the MOT shape. Parameters used in this calculation were chosed to match experimental parameters and are: $\Omega_C = 2.4$ MHz, $\delta_C = 6$ MHz, $\omega_x = 120$ µm, $\omega_z = 160$ µm, $x_0 = 60$ µm, $z_0 = 250$ µm, dB/dz = 7.2 G/cm, and a 689 nm laser lockpoint offset of -40 kHz.

In Figure 5.3(d-h) we see good agreement between the resonance curve and the cloud shape, subject to the vertical offset due to the cloud forming above the resonance curve. The largest limitation is the two-dimensional nature of this model. The imaging axis is at 30° to the coupling beam propagation axis, so the position offset will not be constant across the imaged plane. As a result, the position of the dimple will be dependent on the depth of the plane being imaged, resulting in a blurring of the dimple across the image. The larger the MOT, the stronger this effect will be; this is particularly apparent in Figure 5.5(g).

Whilst the agreement between the model and the data is good, there is a position offset between the resonance curve and the cloud. We expect the cloud to be positioned slightly above the resonance curve, where the scattering force is equal to gravity, rather than where scattering is strongest [115]. This is observed in Figure 2.8 in the undressed MOT; by calculating when the scattering force is equal to gravity we identify the true cloud position. We extend this treatment to the dressed MOT in Figure 5.6 for a range of coupling beam positions and detunings.

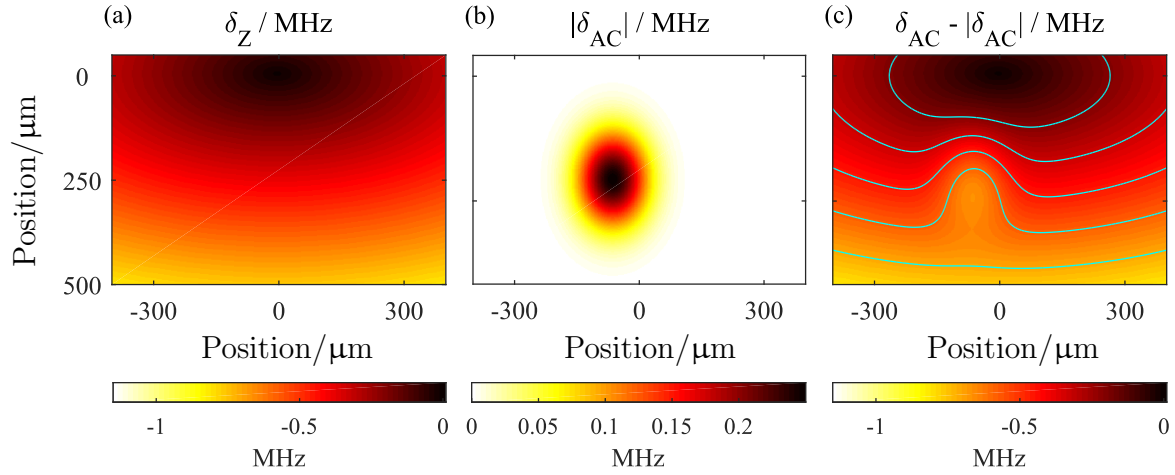

Figure 5.5: Modelling the AC Stark shift due to the coupling beam. (a) and (b) show the Zeeman shift and the AC Stark shift of the $5s5p\ ^3P_1\ m_J = -1$ state through a plane perpendicular to the coupling beam through the quadrupole centre. (c) shows the combined effect; overlaid are contour plots for the detunings used in in the data. These contours are compared to data in Figure 5.3.

The data in Figure 5.6 show four coupling beam detunings and three MOT positions, labelled high, medium and low. Moving the cloud with the shim coils is equivalent to moving the coupling beam and the images are corrected for the cloud movement to illustrate the effect of coupling beam position.

Having accounted for the relative strength of scattering and gravity we see excellent agreement between data and the model. We can see the dimple becoming more pronounced both as the coupling laser frequency nears resonance, and as the coupling laser alignment on the cloud is improved.

Two ellipses at which the scattering force equals gravity are observed, an inner curve and an outer curve. Atoms outside these curves are lost, atoms inside the outer curve will be pushed to the inner curve, where a stable equilibrium between gravity and scattering is reached. This is particularly apparent for the -6 MHz detuned case - at high alignment, the lower curve encompasses the entire position of the undressed cloud, consequently all of the atoms remain trapped. At the lowest alignment, the outer resonance curve is shifted above the position of part of the undressed cloud. Atoms that are below this curve when dressing is initiated are not trapped and are observed falling under gravity. This model therefore provides insight both into the cloud shape and the recapture fraction.

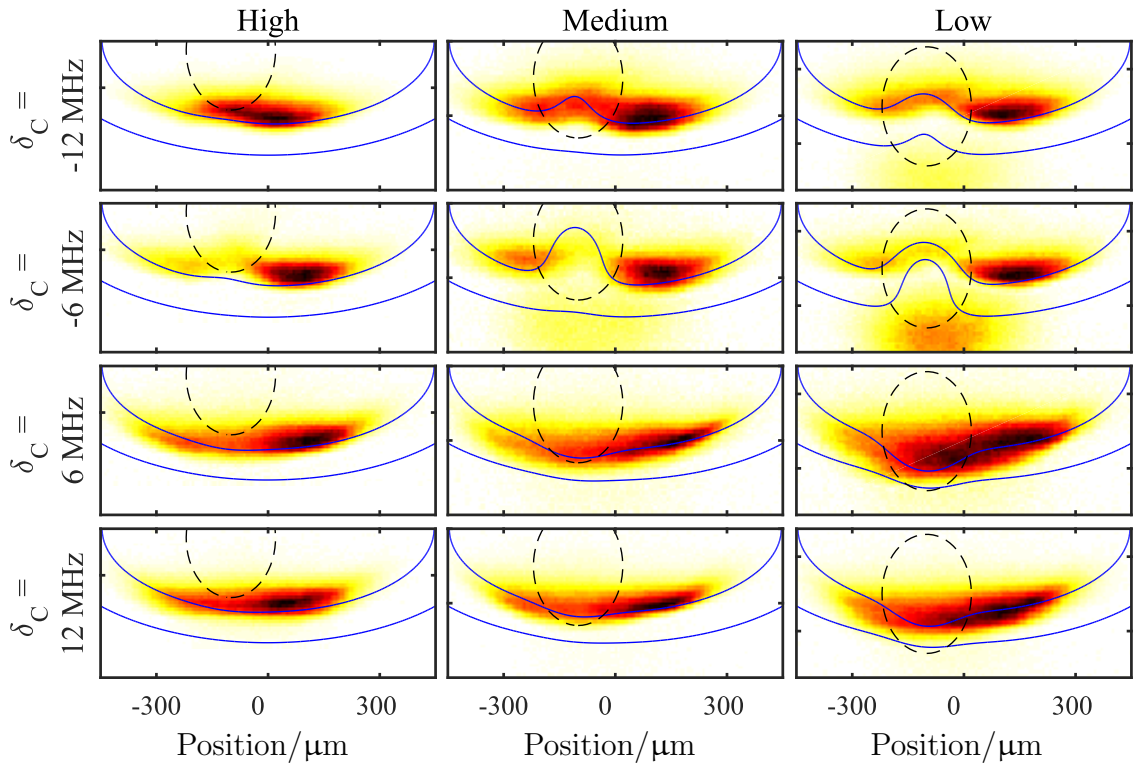

Figure 5.6: Rydberg dressed MOTs for four coupling beam detunings and three coupling beam positions. The dashed black line indicates the modelled position of the coupling beam and the solid blue lines indicate positions where the scattering force magnitude is equal to gravity, which occurs above and below the position of strongest scattering. Taken with $\delta_{\mathrm{MOT}} = -400$ kHz, $\mathrm{P}_{\mathrm{MOT}} = 90$ μW and 5 ms of dressing with $\Omega_C = 2.4$ MHz. The modelled coupling beam includes a position offset from the quadrupole centre of $x_0 = 100$ μm and $z_0 = 25$ μm (high), 100 μm (medium) and 175 μm (low).

This technique is only suited to Regime I and III MOTs as it neglects the direction of scattering. It also does not account for different MOT beam power ratios in the vertical and horizontal MOT beams, and considers only a single $x - z$ plane. We use an imaging axis that is at 30° angle from the coupling beam axis. Given these limitations, the success of this model is very satisfactory.

5.2 Monte-Carlo modelling of the MOT

The AC Stark shift model offers insight on the outline of the cloud shape and even on the recapture fraction, but does not provide insight into the cloud dynamics, such as atom

temperature, settling time and trap lifetime. To understand these properties we extend the Monte-Carlo MOT model described in Section 2.5 and documented in [82] to the dressed MOT case.

The underlying principle of the model is the same, that the probability of being found in an excited state is calculated for each atom as a function of position, weighted by a timestep to generate a probability of scattering a photon, compared to a random number that 'decides' whether a scattering event occurs, and the position and momentum of the atom updated accordingly. To modify this another level is added to the OBEs, coupled through the coupling laser, to make a three-level system with a position-dependent Rabi frequency. However, as the Rydberg transition is not closed, we expect most Rydberg atoms that are excited to decay to long-lived or metastable states, and thus not be trapped. Atoms excited to Rydberg states are therefore removed from the model, introducing an additional source of loss.

For the sake of simplicity the Rydberg state is included as a single level that all intermediate states can couple to. In reality, the Rydberg state comprises of three magnetic sublevels and the coupling strength to these sublevels will be dependent on the relative coupling beam polarisation and local magnetic field. In Regime I and III MOTs the atoms sag to the bottom of the resonance curve and predominantly experience a vertical magnetic field, allowing us to neglect these effects. The Zeeman shift of the Rydberg state is small compared to the detuning of the coupling beam, so is neglected.

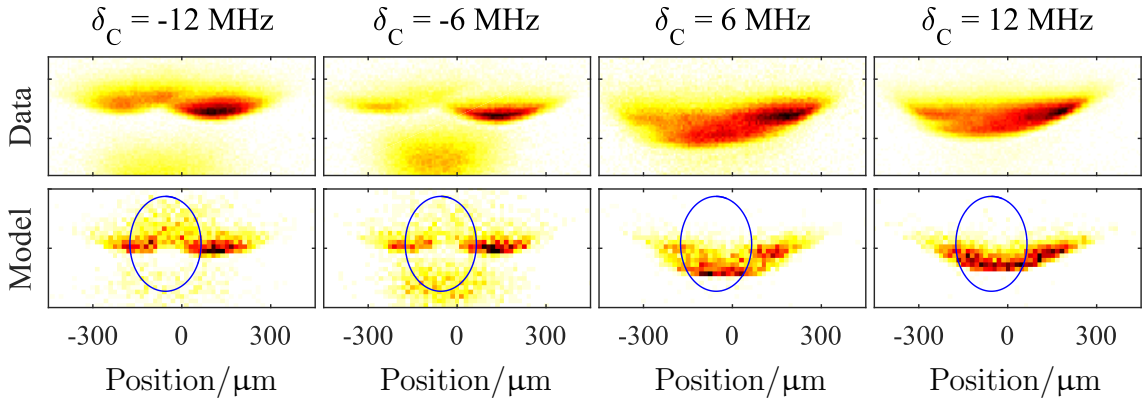

Figure 5.7: Comparison of data and dressed MOT model results. We see very good agreement between the data and the model, particularly given the uncertainty in experimental parameters such as MOT beam detuning and coupling beam position.

Figure 5.7 shows the resulting shape of the MOT model to simulate the data from the

'Low' dataset in Figure 5.6. We see very good agreement between the model and data.

A key strength of the model is that it can predict the dressed MOT dynamics. Later in this chapter we measure cloud temperatures, which we compare to predictions taken using this model.

As in the undressed case the model breaks down for Regime II MOTs. In addition, modelling of the small clouds associated with Regime II MOTs is very sensitive to uncertainty in experimental parameters such as coupling beam position and MOT beam detuning and the fractional uncertainty in these parameters rises.

We now have a very good understanding of the effect of AC Stark shift on the cloud. The next stage towards Rydberg dressed interactions in a Rydberg dressed MOT is for all of the atoms to experience strong coupling to the Rydberg state. This requires us to use a cloud that is smaller than the coupling beam.

5.3 Smaller MOTs, stronger coupling

In Figure 5.6 the cloud is larger than the coupling beam, so only a small fraction of the cloud experiences strong coupling to the Rydberg state. If most atoms experience a low coupling Rabi frequency we will not observe Rydberg dressed interactions.

To address this we must use smaller MOT beam detunings to reduce the cloud size. The breakdown of the MOT model for small clouds therefore poses a problem. In this section we present dressed MOT data using a smaller MOT beam detuning to reduce the size of the cloud to less than that of the coupling beam. We also develop the resonance curves considered above to better account for the small MOT size.

Dressing a smaller MOT

Figure 5.8 shows a single frequency MOT of $\delta_{\mathrm{MOT}} = -140$ kHz, $\mathrm{P_{MOT}} = 30$ μW split in a power ratio of 3:1:1 in the vertical and two horizontal directions dressed for 10 ms. The cloud is similar in size to the coupling beam in the horizontal direction, and is substantially smaller in the vertical direction. We also move to dressing the MOT with the $5s36d\ ^3D_1$ Rydberg state, allowing us to Rydberg dress with a higher Rabi frequency of $\Omega_C/2\pi = 3.7$ MHz, for a range of δ_C. Overlaid is a modified resonance curve that is described later.

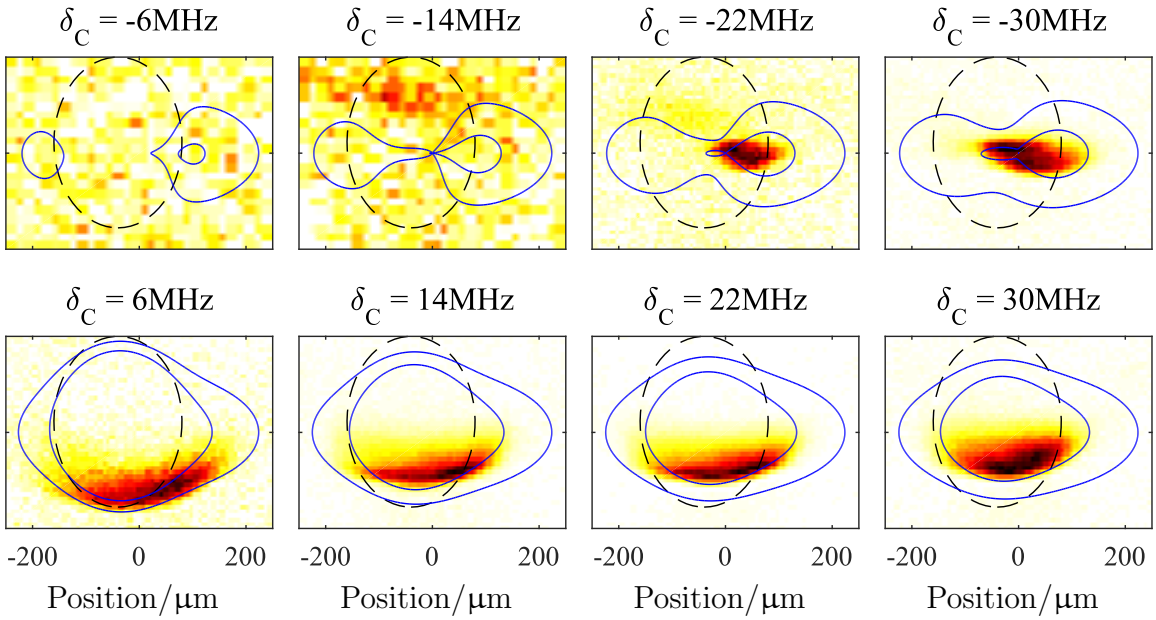

Figure 5.8: Single frequency MOTs dressed for 10 ms with a Rabi frequency of 3.7 MHz. Pixels in the images for $\delta_C = -6$ MHz and $\delta_C = -14$ MHz have been binned in 2 by 2 cells to improve the signal-to-noise ratio. The dashed black line indicates the coupling beam position, the solid blue lines indicate the modelled gravity-matched scattering force reflecting the angle between coupling beam polarisation and local magnetic field.

The smaller MOT beam detuning clearly results in a cloud that is smaller than the coupling beam. However, the cloud still experiences poor coupling to the Rydberg state. When the coupling beam is blue-detuned, atoms sag to the bottom of the coupling beam. When the coupling beam is red-detuned for small detunings, the dimple created by the coupling beam is larger than the cloud and the MOT is destroyed. We will consider techniques to rectify these issues, but first we consider the resonance curves that describe the smaller dressed MOT.

We had success reproducing the dressed MOT cloud shape using a simple resonance model given by Equations 5.1 and 5.2. We want to repeat this for the smaller MOT, but for smaller clouds, the approximation that all atoms experience a similar magnetic field breaks down - the magnetic field direction is no longer primarily vertical. We previously calculated the AC Stark shift in Equation 5.1 by assuming a Rabi frequency proportional to the square root of intensity, with no consideration of driven transitions, in this section we consider what transitions the coupling light can drive.

When the cloud sags under gravity and predominantly interacts with a vertical mag-

netic field, the vertical coupling beam polarisation and the quantisation axis align, and the coupling light drives π transitions. All of the coupling light can couple to the $5snl\ ^3l_1\ m_J = -1$ state.

When atoms are in the wings of a Regime II cloud and experience a horizontal magnetic field, the coupling light can be considered as a combination of left-hand and right-hand circularly (LHC+RHC) polarised light that may drive $\sigma^{\pm}$ transitions. From the $5s5p\ ^3P_1\ m_J = -1$ intermediate state only transitions to the $5snl\ ^3l_1\ m_J = 0$ state can then be driven, so only one component of the LHC + RHC polarised light may drive the transition. Consequently the coupling is weaker as less of the light couples the states.

Treating the the coupling light as a combination of parallel and perpendicular polarisation to the quadrupole magnetic field, and treating the coupling to the two Rydberg states as independent, the AC Stark shift can be approximated as:

$$\delta_{\mathrm{AC}} = \frac{\Omega_C^2 \exp\left(-\frac{2x^2}{\omega_x^2} - \frac{2z^2}{\omega_z^2}\right)\left[1 - \frac{r^2}{r^2+4z^2}/2\right]}{4\delta_C}\ , \tag{5.3}$$

where $\Omega_C \ll \delta_C$ and $r^2 = x^2 + y^2$ is the horizontal position from the quadrupole centre. The vertical position from the quadrupole centre is z, so the term ${}^{r^2}/_{r^2+4z^2}$ reflects the component of the coupling light that is polarised orthogonal to the magnetic quadrupole field. The derivation of this expression is given in Appendix F.

In the two-dimensional case, we set $y = 0$ so that $r = x$. The exponential term accounts for the coupling beam intensity profile as in Equation 5.1, the term in the square bracket accounts for the weaker coupling strength when the coupling beam polarisation and the quantisation axis are not aligned.

This treatment considers only the shift of the $5s5p\ ^3P_1\ m_J = -1$ level, and assumes the sublevels are defined only by the local magnetic field. This approach breaks down in some regimes, either where a second quantisation field is present, as will be considered in Section 5.5, or where the coupling light drives π and σ^+ transitions with similar strengths. Appendix F demonstrates a six-level Hamiltonian solution (considering the three magnetic sublevels of the $5s5p\ ^3P_1$ state and the Rydberg state) and considers multiple planes of resonance, which more accurately replicate the cloud shape, but which requires numerical solution. We will therefore typically use Equation 5.3 and Equation 5.2 to reproduce the cloud shape.

In Figure 5.8 we overlay the resonance curves, matched to where the scattering force

is equal in magnitude to gravity, over the data. As in Chapter 2.5, we use a model MOT beam power ratio of 1:1:1 in the vertical and horizontal directions, compared to experimental parameters of 3:1:1, as it is simpler to calculate the scattering strength for a constant power in all beams.

This modified resonance condition shows good agreement to the experimental data taken with a smaller MOT, shown in Figure 5.8, although the agreement is not as good as in Regime I MOTs (Figure 5.6). This is partly because of the limited validity of this approach for small magnetic fields, as explained above. We expect these limitations to predominantly affect the fit close to the quadrupole field zero. There are several other factors.

Firstly, as the atoms can interact simultaneously with several MOT beams rather than a single MOT beam being dominant this model is not particularly effective even in the undressed regime. This is particularly true when the coupling beam is red-detuned, resulting in a smaller cloud.

Secondly, the resonance condition only shows when the Zeeman shift and AC Stark shift match the MOT beam detuning, but if the resonance ring does not encompass the quadrupole field zero, the scattering force will not be from all six MOT beams, so there will not be a restoring force in every direction. Consequently, the trap may not be sealed.

As explained previously, we are using a two-dimensional model to compare to a three-dimensional system. The effects of this are exacerbated by the 30° angle between the coupling beam axis and the imaging axis. Whilst using a smaller MOT reduces the effect of the imaging axis angle, the added dependence on r, which varies through the imaged axis, reduces the effectiveness of the two-dimensional model. In Appendix F multiple planes are considered, yielding better agreement between the observed and predicted cloud shape, but with less intuitive insight.

Appropriate coupling beam parameters

As shown above, we can couple the MOT to a Rydberg state and for large clouds we reproduce the MOT outline through a simple AC Stark shifted resonance model. Smaller MOTs pose a greater challenge to reproduce the shape outline, but we see reasonable success modifying this simple model by considering the coupling beam polarisation and good agreement using a six-level Hamiltonian and considering multiple resonance curves at different imaging depths.

An optimum Rydberg dressed MOT regime involves atoms being confined to the coupling beam region; as is apparent from Figure 5.8 this is challenging whether red- or blue-detuned. We consider several techniques for keeping atoms in the coupling beam in Section 5.4; before we do this we must identify appropriate coupling beam parameters.

To obtain strong two-body interaction strengths (given by $\Omega^4/8\delta_C^3$) we want large coupling beam Rabi frequencies and detunings. For achievable Rabi frequencies of 4 MHz coupling to the $5s36d\ ^3D_1$ state and a detuning of +12 MHz we expect a two-body dressed interaction strength of 19 kHz from Equation 2.21. This is comparable to the cloud temperature and will be used for the next stage of the experiment.

5.4 Keeping atoms in the coupling beam

The motivation for reducing the MOT size in the previous section was to confine the atoms to a region of strong coupling. However, as shown in Figure 5.8, reducing the MOT beam detuning alone is not enough to keep atoms in the coupling beam. We see the cloud either sagging to a position below the peak coupling beam intensity (when blue-detuned), or simply failing to trap (when red-detuned) for the desired coupling beam detunings. Several approaches have been considered to address this:

- Increasing the magnetic field gradient to more tightly confine the cloud to the coupling beam region.
- Using a larger coupling beam width, reducing the peak AC Stark shift and AC Stark shift gradient but sacrificing Rabi frequency and thus interaction strength.
- Smoothly increasing the coupling beam intensity over time. Whilst this does not change the final resonance condition it avoids a step-change in resonance condition, allowing atoms to reach a new equilibrium rather than falling under gravity.
- Changing the MOT beam detuning when the coupling beam is turned on, to compensate the AC Stark shift.

We prefer to keep our choice of Rydberg state based on the achievable coupling strength and interaction strength. However, we do note that going to higher n will reduce our coupling strength, reducing the perturbation due to the AC Stark shift, but also increasing

the interaction length scale, allowing us to move beyond the two-body dressed interactions case.

The most effective technique that we have used to keep atoms in the coupling beam when using blue-detuned coupling light is to compensate the AC Stark shift by changing the MOT beam detuning when we turn the coupling laser on. This is shown in Figure 5.9. Parameters used are the same as in Figure 5.8 but with a shorter dressing time of 5 ms and a coupling beam detuning fixed at +12 MHz. We change the MOT beam detuning by a compensation amount δ_{COMP}, if we undercompensate the cloud still moves lower and if we overcompensate the cloud will move and a fraction of the cloud will fall under gravity and be lost from the trap.

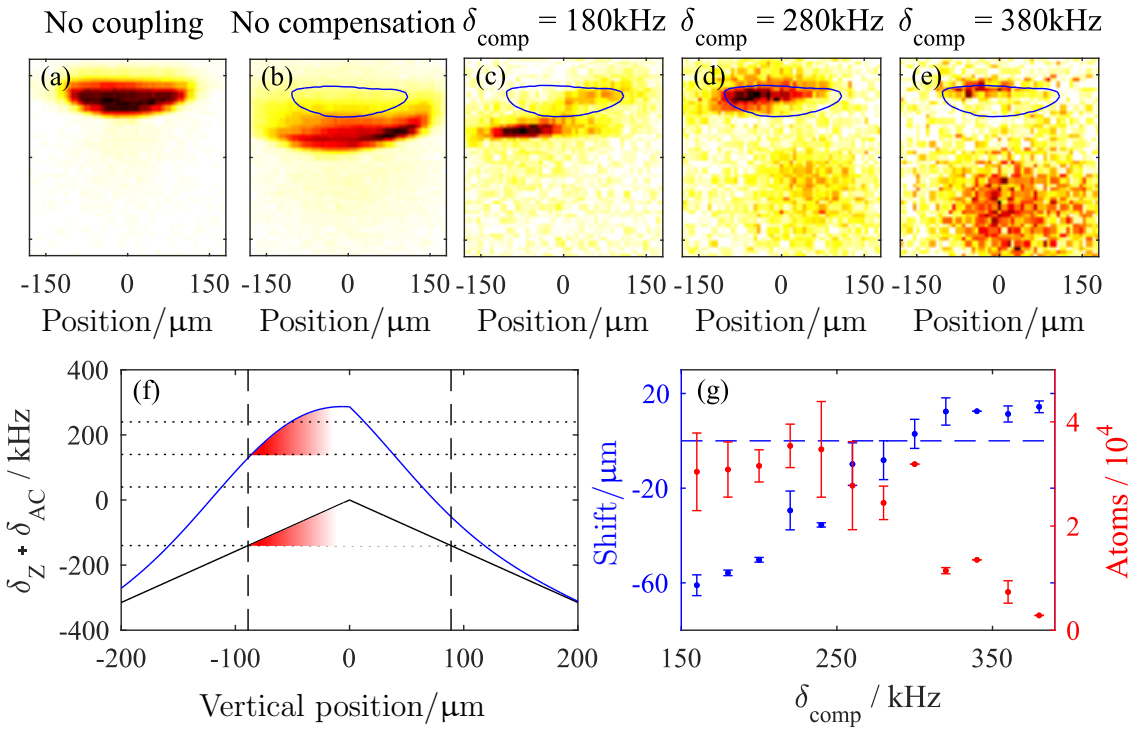

Figure 5.9: The dressed MOT (b) forms at a lower position than the undressed MOT (a). Changing the MOT beam detuning (c-e) when coupling reduces the position shift but excessively large changes result in atom loss. (g) shows the cloud movement (blue) and the atom number (red). The dashed line indicates the initial cloud vertical position. (f) shows the Zeeman shift (black, solid) and the combined Zeeman shift and AC Stark shift (blue) as a function of vertical position. Dotted lines indicate the four δ_{MOT} used in (b-e), dashed lines indicate resonance for the undressed case. The shaded red areas illustrate the cloud position for the undressed MOT and the optimally compensated MOT.

This has been done with an initial MOT beam detuning of $\delta_{\mathrm{MOT}} = -140$ kHz. What is particularly interesting about this is that optimum compensation occurs at $\delta_{\mathrm{COMP}} = +280$ kHz i.e. the compensated MOT is blue-detuned by +140 kHz from the bare state. Consequently, the trap can only work in the presence of the coupling laser, and only traps Rydberg dressed atoms.

A peak Rabi frequency of 3.7 MHz and a coupling beam detuning of +12 MHz gives rise to a peak AC Stark shift of 280 kHz, which matches the observed optimum compensation. Using this compensation technique we can successfully trap atoms at the centre of the coupling beam, where coupling is strongest. We will refer to MOTs formed using this technique as 'compensated MOTs'.

In addition to reduced cloud movement and atom loss, compensation of the AC Stark shift minimises the perturbation to the MOT dynamics - the more the resonance condition changes between the dressed and the undressed MOT, the longer it will take for the cloud to reach a new equilibrium. Reducing the initial perturbation of the cloud when we begin dressing will make it easier to eliminate effects due to atoms reaching a new equilibrium position that may make the effect of Rydberg dressed interactions less clear. Cloud dynamics are considered more later in this chapter.

This technique is effective at keeping atoms trapped at the quadrupole field centre for blue-detuned dressing experiments, but is less effective when red-detuned, as illustrated in Figure 5.10. When blue-detuned the Zeeman shift and AC Stark shift both cause the $5s5p\,{}^3P_1\ m_J = -1$ state to fall in energy with increasing distance from the quadrupole and coupling beam centre, referred to as the trap centre. This means that there will always be a MOT beam detuning for which the cloud can form at the trap centre, illustrated in Figure 5.10(a).

When red-detuned the Zeeman shift and AC Stark shift compete, shifting the $5s5p\,{}^3P_1\ m_J = -1$ state down and up in energy respectively. The two effects both have different gradients in the vertical and horizontal direction, the Zeeman shift because of the nature of the quadrupole field and the AC Stark shift because of the ellipticity of the coupling beam spatial profile. We can therefore identify three possibilities when coupling with red-detuned light:

- In regions where the AC Stark shift gradient is stronger than the Zeeman shift gradient in both vertical and horizontal directions, the $5s5p\ {}^3P_1\ m_J = -1$ state energy rises with distance from the trap centre and the MOT cannot form.

- In regions where the Zeeman shift gradient is stronger than the AC Stark shift gradient in the vertical direction but not in the horizontal direction, atoms will be trapped in the wings of the MOT rather than at the trap centre, illustrated in Figure 5.10(b).

- Where the Zeeman shift gradient is stronger than the AC Stark shift gradient in both directions, the trap can form in the centre of the coupling beam.

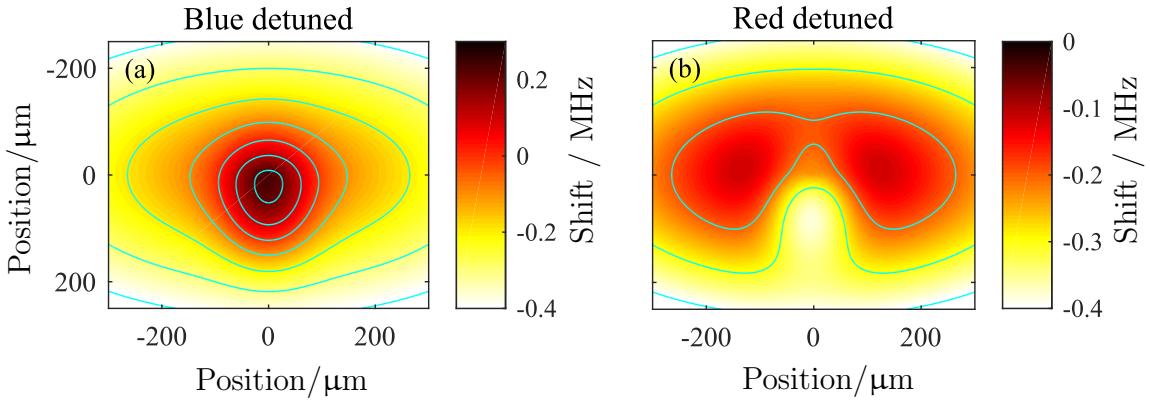

Figure 5.10: Combined Zeeman and AC Stark shift for red- and blue-detuned Rydberg coupling of $|\delta_C| = 12$ MHz, $\Omega_C = 4$ MHz, with resonance contours overlaid.

To compensate the AC Stark shift due to red-detuned coupling light, we must ensure that the Zeeman shift gradient is stronger than the AC Stark shift gradient in both the vertical and horizontal directions at the trap centre. This may involve increasing the quadrupole field strength, defocussing the coupling beam, using a lower Rabi frequency, coupling to a higher principal quantum number Rydberg state, or a combination of these techniques. There are also more novel techniques we can attempt, such as using a spatial light modulator to control the coupling beam spatial profile, or retroreflection of the coupling beam with a position offset to reduce the AC Stark shift gradient.

These techniques are being investigated as part of the ongoing work on Rydberg dressed MOTs in this group; however, this thesis will focus on compensated MOTs that are dressed with blue-detuned coupling light. Our ability to compensate the AC Stark shift caused by Rydberg dressing of the MOT allows us to keep atoms trapped at the centre of the coupling beam, where the Rydberg-mixed fraction is strongest, and reduces the equilibration time of the cloud by reducing the initial perturbation of the cloud when we couple the cloud to the Rydberg state.

In the above sections we have demonstrated techniques for coupling the MOT to the Rydberg state. We understand the role of the AC Stark shift in modifying the spatial distribution of the cloud, and we can confine atoms to regions of strong Rydberg coupling. A full characterisation of the Rydberg dressed MOT will demonstrate the Rydberg character of the MOT, study the cloud dynamics, observing the cloud velocity and velocity distribution and measure loss from the Rydberg dressed MOT.

5.5 An electric field sensitive MOT

Our goal in Rydberg dressing a MOT is to introduce Rydberg interactions to the MOT. However, even in the non-interacting case we have introduced Rydberg character into the MOT. To demonstrate that we have made a MOT with Rydberg character, we observe the dressed MOT sensitivity to electric fields, a property that the dressed MOT acquires due to the high polarisability of Rydberg atoms.

Figure 5.11 shows the Rydberg dressed MOT for a range of electric field strengths and a coupling beam detuning from the unshifted Rydberg state of +50 MHz. We see a very striking dependence of cloud shape, position, and trap viability on the electric field that is not observed in the undressed MOT. We see that we can make the MOT form either side of the coupling beam (e.g. Figure 5.11(e-f), at the coupling beam centre (Figure 5.11(k-l)) or below the coupling beam centre (Figure 5.11(c)). To the best of our knowledge, this is the first magneto-optical trap that demonstrates sensitivity to electric fields.

To understand the shape of the MOT and how it depends on the electric field, we consider the Stark map of the bare Rydberg states $5s36d\ ^3D_1\ |m_J| = 0$ and $5s36d\ ^3D_1\ |m_J| = 1$, shown in Figure 5.12(a). Resonance with a Rydberg state will occur at two electric fields, resulting in the MOT being destroyed, but we clearly see that different regions of the MOT have different sensitivities to the two different Rydberg states. To understand this, we consider the AC Stark shift that the $5s5p\ ^3P_1\ m_J = 0$ and $5s5p\ ^3P_1\ m_J = \pm 1$ states will experience. The coupling beam polarisation is orthogonal to the electric field, so drives $\sigma^{\pm}$ transitions. As a result the $5s5p\ ^3P_1\ m_J = 0$ and $5s5p\ ^3P_1\ m_J = \pm 1$ states will be AC Stark shifted when the coupling beam is near resonance with the $5s36d\ ^3D_1\ |m_J| = \pm 1$ and $5s36d\ ^3D_1\ |m_J| = 0$ states respectively.

Figure 5.12(a) shows the AC Stark shift that the $5s5p\ ^3P_1\ m_J = 0, \pm 1$ state experiences as defined in the electric field basis (dashed lines). However, the MOT transition is defined

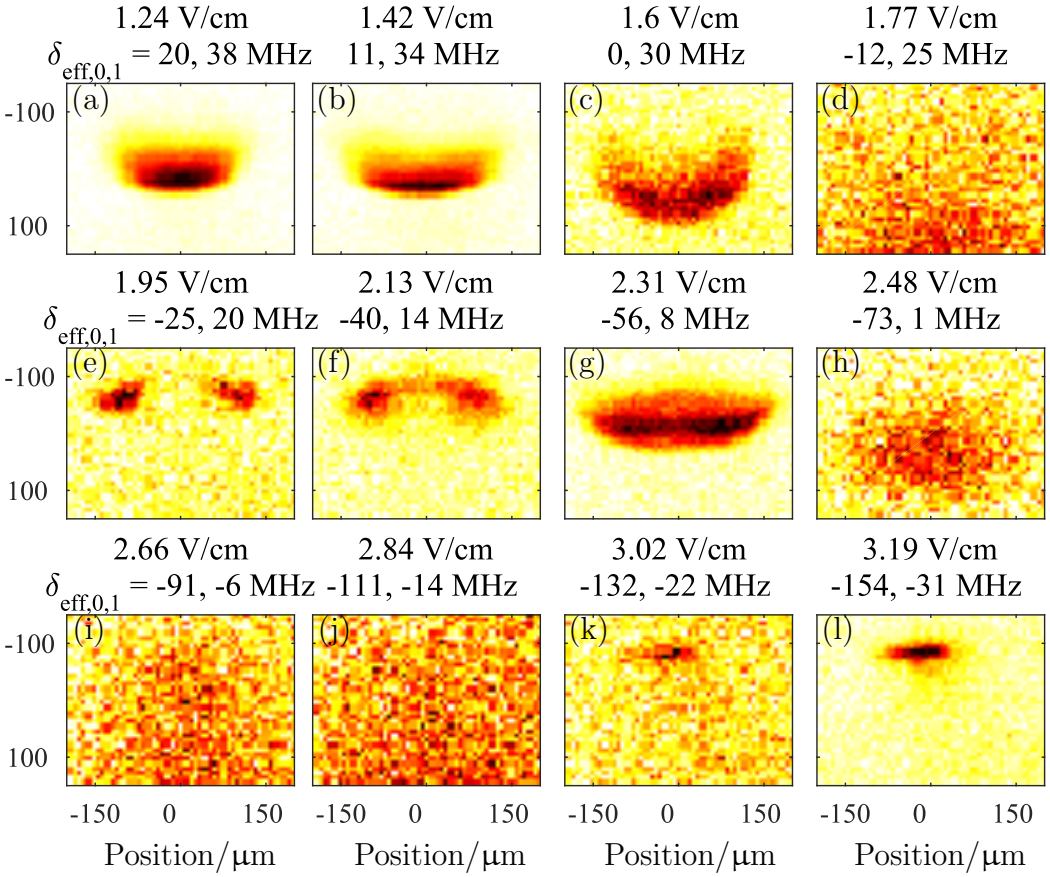

Figure 5.11: A MOT dressed with $5s36d\ ^3D_1$ Rydberg character for 10 ms under the presence of an electric field applied along the imaging axis. Taken with $\delta_C = 50$ MHz, the effective detuning from the electric-field-shifted Rydberg sublevels is indicated above the images.

in the magnetic field basis. We must therefore rotate the angular momentum projection of the upper state of the MOT transition from the magnetic field basis into the electric field basis.

We define the magnetic field basis as m_{mag} and the electric field basis as m_{el}. Treating the MOT light as only driving to the $5s5p\ ^3P_1\ m_J = -1$ state, we only ever populate the $m_{\mathrm{mag}} = \{1, 0, 0\}$ state, where $m_{\mathrm{mag}} = \{1, 0, 0\}$, $\{0, 1, 0\}$ and $\{0, 0, 1\}$ correspond to the $5s5p\ ^3P_1\ m_J = -1$, 0 and +1 states. The two bases are related by the rotation matrix:

$$R(\beta) = \begin{pmatrix} 1/2(1+\cos(\beta)) & -\sin(\beta)/\sqrt{2} & 1/2(1-\cos(\beta)) \\ \sin(\beta)/\sqrt{2} & \cos(\beta) & -\sin(\beta)/\sqrt{2} \\ 1/2(1-\cos(\beta)) & \sin(\beta)/\sqrt{2} & 1/2(1+\cos(\beta)) \end{pmatrix}. \tag{5.4}$$

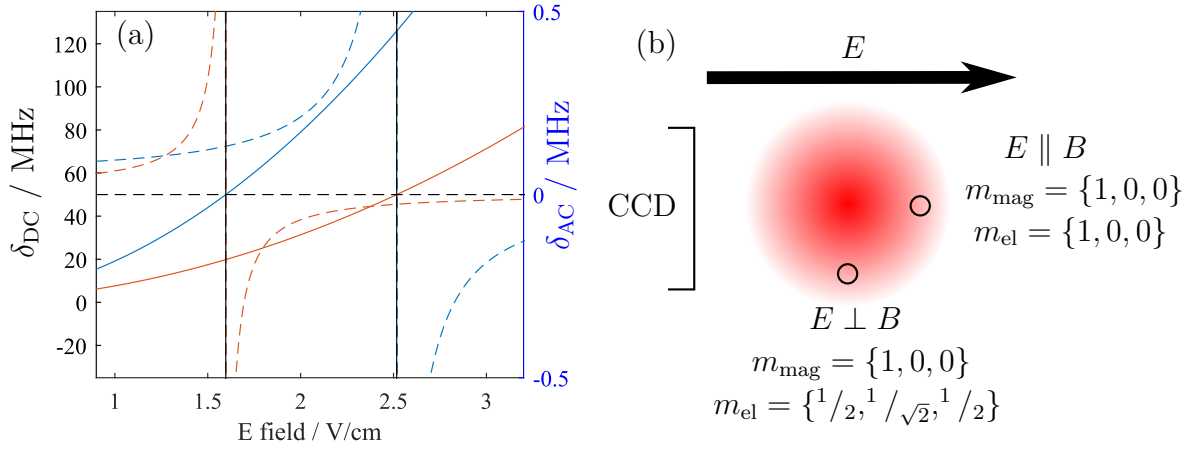

Figure 5.12: The $5s36d\ ^3D_1\ |m_J| = 0$ (blue, solid) and $5s36d\ ^3D_1\ |m_J| = 1$ (orange, solid) Rydberg states rise in energy at different rates in response to an electric field (left axis). The $5s5p\ ^3P_1\ m_J = 0$ (blue, dashed) and $5s5p\ ^3P_1\ m_J = \pm 1$ (orange, dashed), defined in the electric field basis therefore experience different AC Stark shifts as a function of electric field (right axis). On the right, the relationship between $5s5p\ ^3P_1$ sublevel in the electric field basis and magnetic field basis as a function of position is shown.

Here β is the angle between the magnetic and electric field directions. Where the electric and magnetic field are parallel ($E \parallel B$), the $5s5p\ ^3P_1$ sublevel remains the same in both bases. Where the electric and magnetic field are orthogonal ($E \perp B$) the magnetic sublevel $m_{mag} = \{1, 0, 0\}$ is translated into the electric sublevel $m_{el} = \{{}^{1}/_{2}, {}^{1}/_{\sqrt{2}}, {}^{1}/_{2}\}$. This is illustrated in Figure 5.12(b).

From the AC Stark shift of the $5s5p\ ^3P_1$ states in the electric field basis, and the relationship between the magnetic field basis and electric field basis as a function of the angle between the electric field and the magnetic field, we can now express the AC Stark shift that different regions of the MOT experience. This is shown in Table 5.1

Table 5.1 gives the excited state of the MOT transition in both bases for $\beta = 0°$ and $\beta = 90°$, as well as the effective coupling strength for both transitions given the coupling beam polarisation. Note that this treatment utilises the equal coupling strengths of all allowed Rydberg transitions; different weightings must be applied if coupling to the $5snd\ ^3D_2$ state, where the different sublevel transitions have different transition strengths.

This approach is effective in explaining many of the features of the electrically sensitive MOT shown in Figure 5.11. When near resonance with the $5s36d\ ^3D_1\ |m_J| = 0$ state, the strongest AC Stark shift will occur where $E \parallel B$, which occurs in line with the quadrupole

Quantisation axes	$E \parallel B$	$E \perp B$
m_{mag}	$\{1, 0, 0\}$	$\{1, 0, 0\}$
m_{el}	$\{1, 0, 0\}$	$\{^1/_2, ^1/_{\sqrt{2}}, ^1/_2\}$
Coupling to $5s36d\ ^3D_1\ \lvert m_J\rvert = 0$	0.5	0.25
Coupling to $5s36d\ ^3D_1\ \lvert m_J\rvert = 1$	0	0.5

Table 5.1: Rydberg state coupling due to a vertically polarised coupling beam, a horizontal electric field, and two magnetic field directions. m_{mag} is the excited state of the MOT transition, defined in the magnetic field basis, m_{el} is the excited state of the MOT transition, defined in the electric field basis. Coupling strength is given relative to the peak coupling strength of the $5s5p\ ^3P_1\ m_J = -1$ to $5s36d\ ^3D_1\ m_J = -1$ transition measured in the absence of an electric field.

field centre as imaged. Consequently, we expect atoms to drop out of this region due to the strong AC Stark shift when blue-detuned, as seen in Figure 5.11(c), and the MOT to form either side of this region when red-detuned, as seen in Figure 5.11(e-f).

When near resonance with the $5s36d\ ^3D_1\ |m_J| = 1$ state we expect no coupling directly in line with the quadrupole field zero, and strong coupling in the cloud wings. When blue-detuned, we therefore see a wide spread of atom positions (Figure 5.11(h)) corresponding to a wide spread of AC Stark shifts, and when red-detuned we see the cloud preferentially form in line with the quadrupole field zero, where the AC Stark shift is smallest (Figure 5.11(k-l)).

Electric fields between 1.7 V/cm and 2.6 V/cm are of particular interest, as the coupling beam is effectively red-detuned from the $5s36d\ ^3D_1\ |m_J| = 0$ transition and blue-detuned from the $5s36d\ ^3D_1\ |m_J| = 1$ transition. Due to the coupling dependence on β it may be possible to construct a MOT that predominantly experiences blue-detuned coupling from one Rydberg state sublevel for regions of high β, whilst predominantly experiencing red-detuned coupling from the other Rydberg state sublevel in regions of low β, or vice versa, depending on choice of coupling beam polarisation. However, whilst interesting, this regime is not a useful platform for the observation of Rydberg dressed interactions - to observe Rydberg dressed interactions the coupling laser frequency must not excite pairs of Rydberg atoms, which is not possible if there is a resonance above and below the laser frequency.

Further study of the MOT may involve alternate electric field axes and coupling beam

polarisations - a coupling beam polarisation that is linear and aligned with the electric field axis would only allow coupling via π transitions, thus not allowing coupling to the $5s36d\ ^3D_1\ |m_J| = 0$ state. Use of the $5snd\ ^3D_2$ Rydberg series would increase the sublevels available to couple to and change the coupling strengths of transitions between sublevels.

These experiments demonstrate the Rydberg character of the cloud. In addition, as we will show in Chapter 6, the presence of an electric field may modify the loss mechanisms in a Rydberg dressed MOT, requiring an understanding of the effect of electric field on cloud shape.

Having demonstrated the Rydberg character of the dressed MOT, we return to Rydberg dressed MOTs in the absense of electric fields.

5.6 Laser cooling of Rydberg dressed atoms

Our goal is to create a Rydberg dressed MOT that exhibits trapping, cooling and Rydberg dressed interactions. We have thoroughly characterised the trapping and the Rydberg character of the cloud in previous sections. In this section we characterise the cooling rate of the Rydberg dressed MOT. To do this we characterise both the cloud mean velocity and the velocity distribution of the cloud - typically the mean velocity of a steady state cloud will be zero, but the initial perturbation of the cloud by the coupling laser may result in a non-zero mean velocity e.g. [116].

We will first demonstrate that the cloud follows a Maxwellian velocity distribution, which allows us to express the velocity distribution as a cloud temperature. The cloud mean velocity resulting from the initial perturbation will also be measured. We will then compare these experimental results to the Rydberg dressed MOT model.

Cloud ballistic expansion

To observe the velocity distribution of the cloud, we perform a ballistic expansion, turning off all laser beams and fields for a variable time up to 5 ms, during which the cloud expands and falls, then image the cloud. The final position distribution of the cloud becomes a convolution of initial position distribution and velocity distribution. If the initial position distribution is Gaussian and described by the standard deviation $\sigma_x(0)$,

and the velocity distribution is Maxwellian and described by the temperature T_x, the final position distribution $\sigma_x(t)$ follows [117]:

$$\sigma_x(t) = \sqrt{\sigma_x^2(0) + \frac{k_B T_x}{m} t^2} \ . \tag{5.5}$$

Figure 5.13 shows a MOT that has been dressed for 2 ms and expanded for 1 ms, 3 ms and 5 ms. Vertical slices through the centre of the cloud agree well with a Gaussian fit, allowing us to treat the cloud using Maxwellian statistics.

In the horizontal direction, we are very sensitive to which part of the cloud is fitted to - initially the densest slice of the cloud (which is what we fit to) is not the widest part of the cloud, but as the cloud expands the densest part of the cloud becomes the widest part of the cloud. Consequently, we can't fit to the densest part of the cloud in the horizontal direction. Instead we sum the columns of the image and fit to a summed horizontal cloud profile.

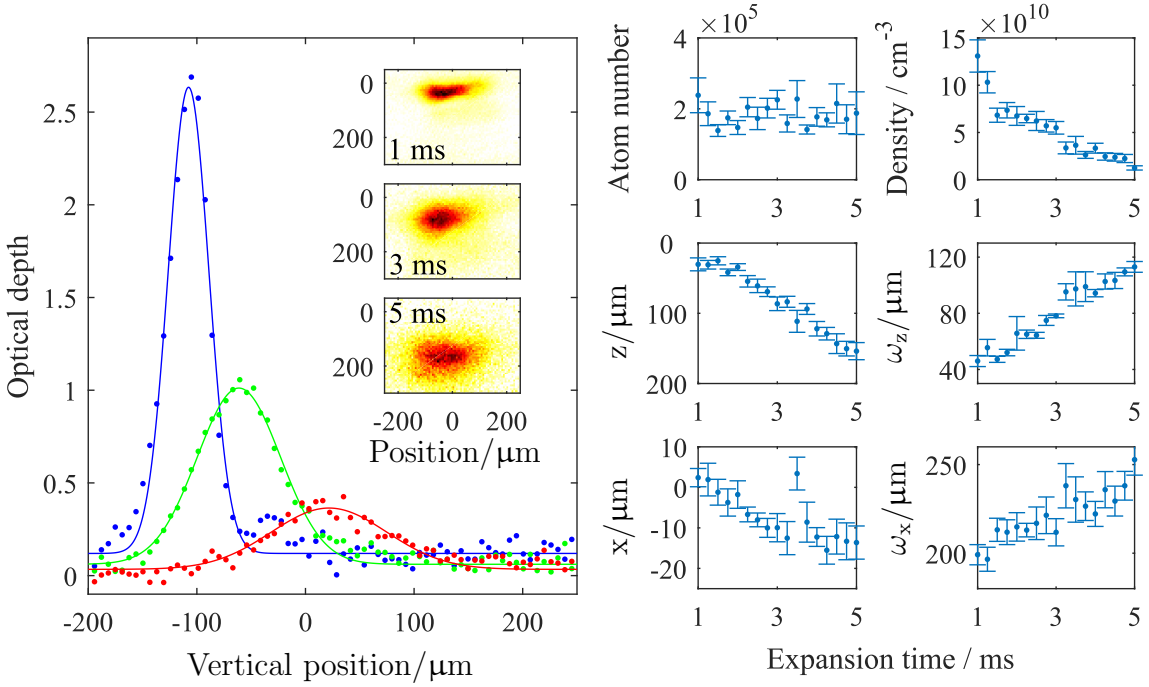

Figure 5.13: Ballistically expanding a MOT dressed for 2 ms, we see freefall and expansion (inset images). Plotting vertical slices through the densest region of the cloud for expansion times of 1 ms (blue), 3 ms (green) and 5 ms (red), we see good agreement to Gaussian fits. From the fits we obtain peak column density, cloud position (from an arbitrary constant) and cloud width, from which we calculate density and atom number.

The cloud is dressed with $\Omega = 3.7$ MHz of coupling light that is detuned +12 MHz from the $5s36d\ ^3D_1$, and then expanded for up to 5 ms. The optimum MOT beam compensation of +190 kHz is less than the previously observed +280 kHz, suggesting a slight misalignment of the coupling beam from the centre of the cloud.

Having verified the Maxwellian nature of the dressed cloud we obtain cloud positions, widths and peak density from the fits[a]. We calculate atom number from the peak density and the cloud widths. We see no change in atom number with expansion time, which gives confidence in the fitting. To reduce the effect of the initial size, and also to reduce the problems of fitting to an optically thick cloud, we only consider datasets that have been expanded for 1 ms or longer for vertical fitting and 2 ms or longer for horizontal fitting.

Cloud temperature and velocity

Using Equation 5.5 we can fit a temperature to the width of the cloud as a function of expansion time, shown in the top line of Figure 5.14. The fractional change in cloud size with expansion time is small in the horizontal direction, resulting in large uncertainties in the cloud horizontal temperature, however the trend is clear.

We observe initial heating in both the vertical and horizontal direction, followed by cooling. This is expected; when the resonant position changes there will be heating as the atoms reach the new resonant position, followed by cooling once the position is reached. That the cloud then returns to its initial temperature demonstrates that there is sustained cooling in the MOT. This is a key finding; we believe this is the first demonstration of sustained trapping and cooling of atoms with measurable Rydberg character. We see a vertical cooling time on the order of 3 ms.

The cooling rate is faster in the vertical direction as the atoms predominantly interact with the vertical MOT beam and experience an effective damping force due to gravity.

In addition to the cloud temperature, we can observe cloud movement with expansion

[a]When fitting the cloud shape we assume rotational symmetry. Whilst common practice with most MOTs, we break the rotational symmetry of the MOT when dressing. When the cloud is larger than the coupling beam this treatment is not appropriate but in this case the cloud is smaller than the coupling beam, and as we will show later by modelling the cloud temperature, this treatment is reasonable. In addition, the imaging axis and the coupling beam axis, being neither parallel nor orthogonal, are effectively blurred.

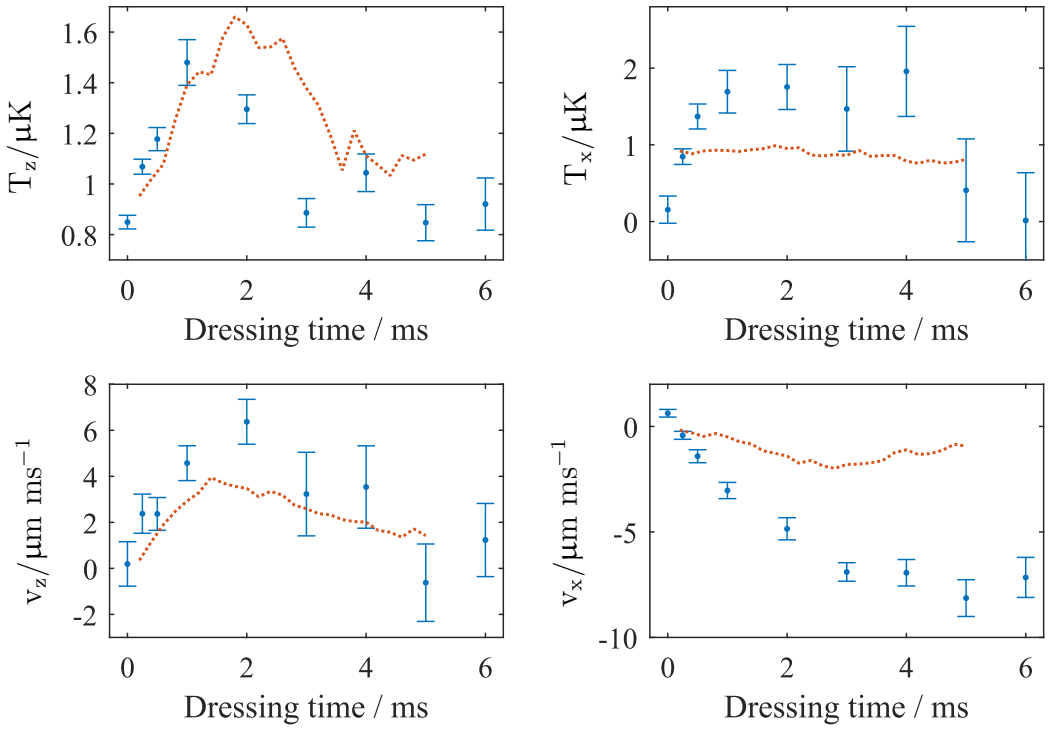

Figure 5.14: Cloud temperature (top) and mean velocity (bottom) in the vertical (left) and horizontal (right) direction. The orange line is the results of a Monte-Carlo model simulation.

time, in both the vertical and horizontal direction. Vertical movement during expansion is expected to follow a parabola as the cloud freefalls under gravity, but horizontal movement is not expected. We attribute this movement to the misalignment of the coupling beam from the cloud centre, which results in a net cloud velocity causing the cloud to move sideways as it falls. Fitting a parabola ($z(t) = z_{\text{init}} + v_z t + 0.5gt^2$) to the cloud movement in the vertical direction and a linear fit ($x(t) = x_{\text{init}} + v_x t$) to cloud movement in the horizontal direction as the cloud expands and falls, we can measure the cloud velocity in the vertical and horizontal direction, shown in the bottom line of Figure 5.14.

The vertical velocity rises for ~ 2 ms. This velocity is downwards, suggesting the equilibrium dressed MOT position is below that of the dressed MOT. Comparing the position of the MOT before and after dressing, we observe a shift of ~ 15 μm downwards in the dressed MOT, which corresponds to the area under the curve of ~ 15 μm for the vertical velocity against time graph in Figure 5.14. The vertical velocity of the cloud therefore corresponds to the cloud moving to the new equilibrium position, and returns to zero once the cloud has reached the new equilibrium position. As a comparison to the data,

1 ms of freefall will give rise to a mean vertical velocity of 9.81 μm/ms. This is larger than the observed velocity as the vertical MOT beam opposes the freefall of atoms.

The velocity in the horizontal direction does not return to zero - we see the cloud fall sideways for all dressing times greater than 0 ms. We also observe the equilibrium position of the cloud move by $\sim$ 35 μm from the undressed case to the dressed case after 5 ms. We attribute this to the coupling beam alignment, which is not centred on the cloud. The different AC Stark shift on one side of the cloud to the other may result in stronger scattering from one direction than the other, resulting in a net force on the cloud. As the mean velocity is calculated based on the change of the fitted mean position of the cloud with expansion time, it is susceptible to changes in cloud shape and this technique may overstate the cloud velocity. It is also possible that attenuation of the retroreflected MOT beams or imperfect polarisation of the MOT beams results in a net force on the cloud that modifies the perturbation of the cloud when the coupling laser is turned on.

Modelling the cloud temperature

In Section 2.5 we show that the Monte-Carlo MOT model can reproduce the cloud temperature and the cooling rate of the MOT and in Section 5.2 we describe how the Rydberg state can be added to the MOT model. We now use this model to simulate the cloud temperature. We show the results of a simulation of the experiment compared to experimental data in Figure 5.14 showing both cloud temperature and mean velocity.

Given the complexity of the system the results of this simulation show good qualitative agreement. The large uncertainty on coupling beam position and challenges of fitting in the horizontal direction make exact agreement hard to obtain for temperature and mean velocity in the vertical and horizontal direction. We can optimise for any of these four observables individually but it is too computationally intensive to thoroughly fit all four observables.

From the Monte-Carlo MOT model we can study the dependence of the initial temperature on the parameter space. We observe that the initial perturbation of the cloud that results in cloud movement and heating can be minimised through optimum compensation. Small misalignments of the coupling beam from the cloud centre also modify the optimum compensation that we must apply to reduce initial heating. We consistently see that trapped atoms continue to be cooled in the dressed MOT.

The poor temperature agreement in the horizontal direction is likely to be due to the

challenges of fitting to an optically thick cloud that only expands by a small fraction of its width during the expansion time. The difference in cloud movement is similarly attributed to the changing shape of the cloud as it expands as discussed previously. The cloud velocity from the MOT model is taken as the mean velocity of all atoms rather than by fitting the changing position of the cloud during freefall so is less susceptible to changing cloud shape.

The model is calculated with $\Omega = 3.7$ MHz, $\delta_C = 12$ MHz, $\delta_{\mathrm{MOT}} = -140$ kHz before dressing begins and $\delta_{\mathrm{MOT}} = +50$ kHz during dressing and $\mathrm{P_{MOT}}$ =20 μW. The coupling beam misalignment is given by $x_0 = -80$ μm, $z_0 = +10$ μm. Small changes in coupling beam Rabi frequency can have drastic effects on the cloud heating rate, as the AC Stark shift due to coupling changes the resonance condition.

Cloud dynamics

In this section we have thoroughly characterised the cloud dynamics. When we begin dressing we perturb the cloud, causing initial heating in both directions. Cooling of the cloud continues, returning the cloud temperature to the initial temperature. This is believed to be the first observed laser cooling of atoms with Rydberg character. The initial perturbation also results in a net velocity of the cloud. Both the heating and the net velocity can be reduced through optimum alignment of the coupling beam onto the cloud and optimum compensation of the AC Stark shift of the cloud.

In previous sections we thoroughly demonstrated that the dressed MOT continues to trap Rydberg dressed atoms. In this section we have shown that the cloud continues to cool Rydberg dressed atoms. Our goal is to observe Rydberg dressed interactions in a system containing both confinement and cooling and with a trap lifetime longer than the equilibration time of the cloud. Having shown confinement and cooling, and measured the vertical cooling time of the cloud to be on the order of 3 ms, we now measure the cloud lifetime.

5.7 Dressed MOT lifetime

The $5s^2\ {}^1S_0 \leftrightarrow 5s5p\ {}^3P_1$ transition used for the narrow-line red MOT is closed, allowing long trap lifetimes of seconds to be obtained in the broadband MOT for high MOT beam powers. In low power single frequency MOTs, we typically reach trap lifetimes of tens

to hundreds of milliseconds, limited by several processes such as collisions, laser jitter, and atoms passing through the resonant region without scattering sufficient photons to be retrapped.

However, the Rydberg laser introduces a new loss mechanism to the cloud - atoms excited to the Rydberg state have several decay paths to the ground state, many through longlived or metastable intermediate states, and we therefore expect most atoms excited to the Rydberg state not to decay to the ground state on the timescale of the experiment. Most atoms excited to the Rydberg state are therefore lost both from the trap and from the images.

In this section we measure the trap lifetime - we want a cloud lifetime that is long compared to the 3 ms equilibration time of the cloud measured in Section 5.6.

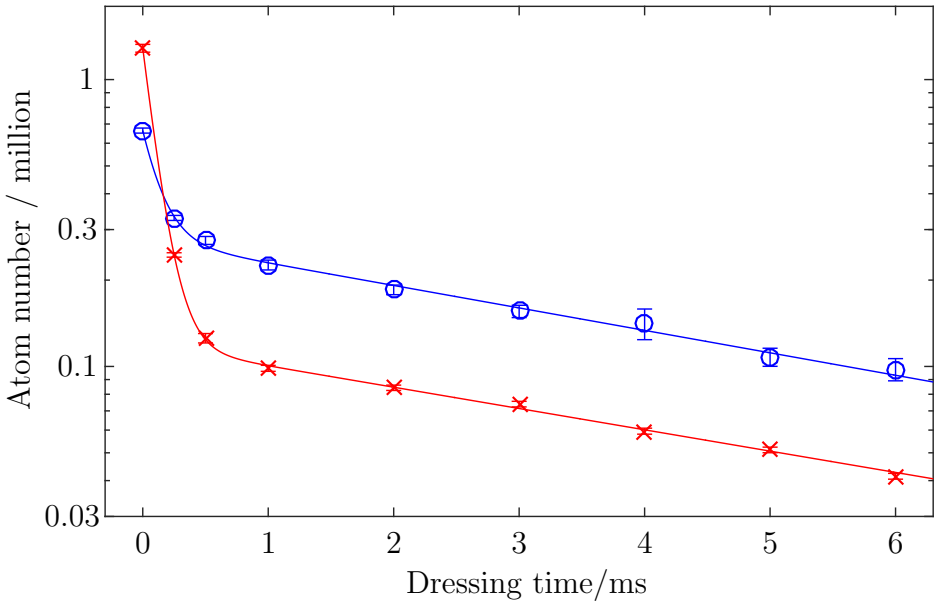

Figure 5.15: Dressed MOT lifetime. We see rapid loss in the first ~ 300 μs, followed by a steady decay. Two datasets are shown with MOT beam powers of 20 μW (blue rings) and 40 μW (red crosses), both fitted with a double exponential. At higher MOT beam power we obtain a higher initial density and atom number but see a faster rapid decay that terminates at a lower atom number.

To avoid problems with calculating atom numbers from optically thick clouds we ballistically expand the cloud before imaging, using the same data that we have from Section 5.6. We note that the atom number remains constant during expansion, shown in Figure 5.13, allowing us to average the atom number across all ballistic expansion times.

Figure 5.15 shows atom number as a function of dressing time for the dataset given in Figure 5.14, and a second dataset using a higher MOT beam power of 40 μW, rather than 20 μW. We see a very rapid decay in atom number in the first ∼ 300 μs, followed by a slower exponential decay. This rapid decay is fatal to our attempts to see Rydberg dressed interactions in these two datasets as it reduces the cloud density to below the interacting regime. This is shown in Figure 5.16 - the interparticle spacing of dressed state atoms is comparable to the dressed interaction lengthscale when dressing begins, but the catastrophic loss that occurs within the first millisecond of dressing increases the interparticle separation to much greater than the interaction lengthscale.

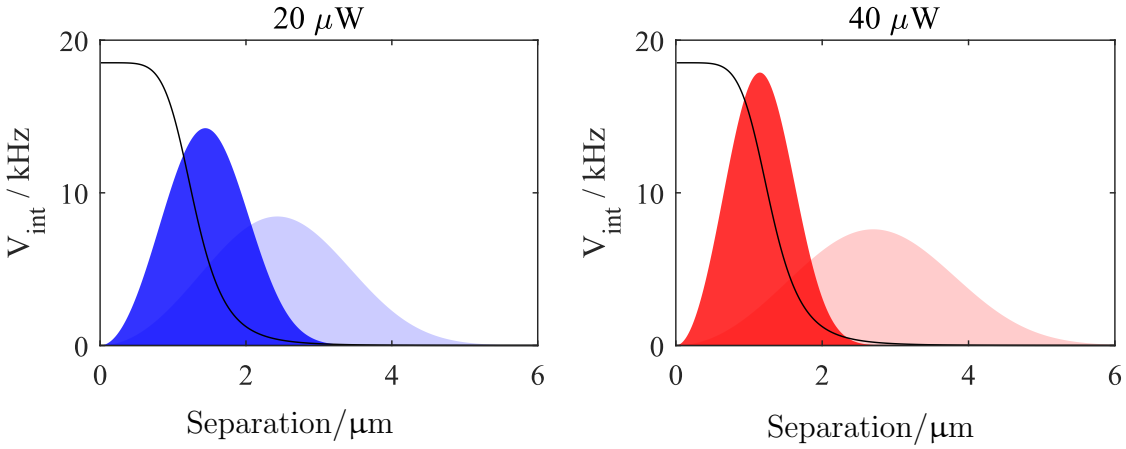

Figure 5.16: Intermediate state nearest neighbour distribution before dressing (dark shading) and after 1 ms of dressing (light shading) for two MOT beam powers of 20 μW (left) and 40 μW (right), based on a 5% intermediate state fraction. Also shown is the two-body interaction potential. In both cases, the rapid loss process shown in Figure 5.15 drastically reduces the expected interaction strength.

The nature of the rapid decay is not obvious. We see good agreement fitting a double exponential decay of atom number $((a_1 \exp(-t/\tau_1) + a_2 \exp(-t/\tau_2)))$. The fit results are shown in Table 5.2. At higher MOT beam power and higher initial density, the rapid loss occurs slightly faster and saturates at a much lower atom number - around 90% of the initial atom population is lost to this rapid loss process. Clearly, any observation of Rydberg dressed interactions in the dressed MOT will require us to eliminate this effect. Before we can do this we must understand what this rapid loss process is. This investigation is presented in Chapter 6.

The slow loss τ_2 is expected to be one-body losses such as atoms leaking from the trap or being excited to Rydberg states. The Monte-Carlo dressed MOT model predicts a cloud

Fit parameter	20 μW	40 μW
a_1	$3.9 \pm 0.1 \times 10^5$	$1.17 \pm 0.03 \times 10^6$
τ_1 / ms	0.15 ± 0.01	0.11 ± 0.01
a_2	$2.7 \pm 0.1 \times 10^5$	$1.19 \pm 0.02 \times 10^5$
τ_2 / ms	5.5 ± 0.4	5.9 ± 0.2

Table 5.2: Dressed MOT lifetimes, fitted to a double exponential for two MOT beam powers and initial densities. After the rapid loss the dressed MOT lifetime is reasonable, but we must eliminate the rapid loss process if we are to see Rydberg dressed interactions in the Rydberg dressed MOT.

lifetime of 9 ms, limited by atoms passing through the resonant region without scattering sufficient photons to remain trapped; given that this model does not include several loss mechanisms, such as collisions with hot atoms, laser frequency noise etc., we consider the two values of 5.5 ± 0.2 ms and 9 ms to be in reasonable agreement.

A second trap lifetime estimate calculated from the Rydberg fraction of the excited state ($\Omega^2/4\delta^2$), the Rydberg state lifetime (11 μs) and the estimated excited state fraction (5%) corresponds to a predicted lifetime of 8 ms, which again is in reasonable agreement with the observed lifetime. This lifetime does not account for the falling Rabi frequency far from the coupling beam centre, or other MOT loss mechanisms.

The observed lifetime of 5.5 ± 0.2 ms is longer than the 3 ms equilibration time of the cloud, and is long enough for the effects of Rydberg dressed interactions to manifest themselves, but only if we can eliminate the rapid loss that depletes the cloud.

Summary

In this chapter we have demonstrated a Rydberg dressed MOT, creating a system in which only Rydberg dressed atoms are trapped. This is the first demonstration of sustained trapping and cooling of atoms with observable Rydberg character.

If we can reach the density necessary for Rydberg dressed interactions to occur we will have a versatile and tunable platform for quantum simulation of dissipative many-body systems. However, rapid loss that occurs at high density prevents us from reaching this regime.

We have thoroughly studied the effect of AC Stark shift on the MOT, observing that for large MOT beam detunings we can simply consider the AC Stark shift as dependent on coupling beam intensity but for small MOTs that experience a range of magnetic field directions, the polarisation of the coupling beam relative to the magnetic field must be considered. This sensitivity to polarisation is particularly apparent when applying an electric field to the dressed MOT, which shows a striking sensitivity to both the magnitude of the electric field and the direction of the electric field relative to the magnetic field. We believe this to be the first demonstration of a MOT that is sensitive to electric fields.

When we initially couple the cloud to the Rydberg state we create a perturbation that causes heating of the cloud as the cloud settles into the new potential. This heating may be associated with a mean cloud velocity if the coupling beam alignment and AC Stark shift compensation is not optimal. However, the MOT continues to cool the Rydberg dressed atoms and the cloud returns to its initial temperature within 3 ms. The cloud lifetime at low density is longer than this time, allowing the Rydberg dressed MOT to be used as a many-body quantum simulator, but only if the rapid loss process observed in Figure 5.15 can be suppressed. The investigation of this loss process forms the basis of Chapter 6.

Chapter 6

Losses in a Rydberg dressed MOT

In Chapter 5 we characterised a Rydberg dressed MOT with respect to cloud shape, cloud dynamics and trap lifetime, using imaging of ground state atoms. We would like to increase the density in the Rydberg dressed MOT to the Rydberg dressed interaction regime, but a rapid loss process shown in Figure 5.15 limits the cloud density to below the interacting regime. In this chapter we will study this loss process using time-resolved ion detection, allowing us to attribute this loss process to the formation of a plasma. To do this we will:

- Present data on the ion signals detected in dressing experiments, identifying signatures and stages of plasma formation.
- Provide an outline of ultracold plasma physics.
- Present some Rydberg dressing experiments studying the different stages of the plasma.
- Identify a range of solutions to eliminate the plasma.

From the study of the plasma, we will present regimes in which we expect to avoid the formation of a plasma, allowing us to identify regimes in which we may observe Rydberg dressed interactions in a Rydberg dressed MOT.

Aspects of this analysis were performed after datataking was completed, so at times hypotheses have been tested against data taken for other purposes, rather than more direct experiments.

6.1 Ion signals from the Rydberg dressed MOT

A key tool to study the loss mechanism in the dressed MOT is to observe the ions generated during dressing. In this section we will describe the ion signals that we observe whilst Rydberg dressing the MOT, identify four stages within the ion signals, and show that these stages are consistent with the formation of an ultracold neutral plasma that causes accelerated atom loss from the trap.

Figure 6.1 shows ion signal from the dressed MOT presented in Section 5.6. We detect without autoionisation or steering electric fields.

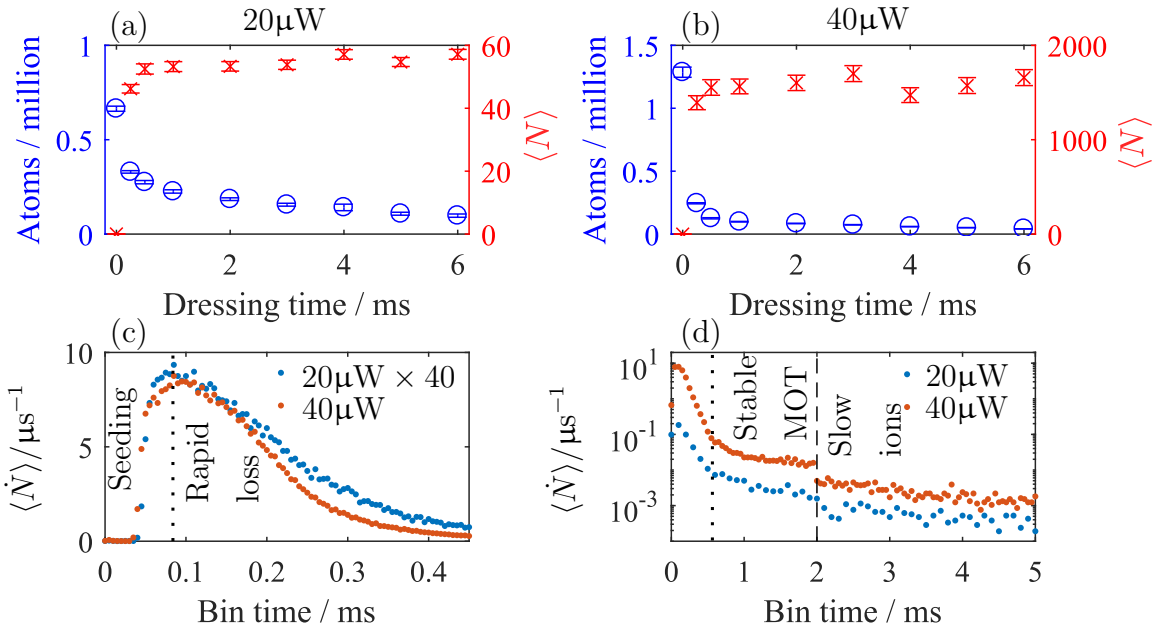

Figure 6.1: Atom number (blue circles) and ion number (red crosses) from the dressed MOT as a function of total dressing time for $P_{MOT} = 20$ μW (a) and $P_{MOT} = 40$ μW (b). We see massive ion signals on a similar timescale to the atom loss. By binning the ion arrival times we measure an ion detection rate as a function of bin time, observing a very sharp rise in detection rate followed by a rapid fall shown in (c), and a second, slower fall after the initial drop in atom number shown in (d). Ions continue to be detected after the dressing is turned off, indicated by the vertical dashed line.

We observe a mean ion signal of $\langle N \rangle \approx 1,600$ in Figure 6.1(b), which is enormous by the standards of this experiment, where we typically tailor Rydberg excitations to keep ion detection below ~ 50. Clearly, the rapid loss observed in Figure 5.15(a-b) is associated with a massive ion signal. From an estimated detection efficiency of $< 2\%$ (described in

Section 3.3.2) this suggests that at least 5% of the ground state atoms are converted to ions within the first 500 μs of dressing.

As we observe up to 90% of the atoms being lost from the images and on the order of 5% of the atoms being ionised the high loss rate must therefore be dominated by loss to atomic states that are dark to detection through imaging. The $5s^2\ {}^1S_0 \leftrightarrow 5s5p\ {}^3P_1$ transition is closed, so for loss to dark states to occur, atoms must be excited to a Rydberg state.

From the arrival times of the ions we observe an ion detection rate $\langle \dot{\mathrm{N}} \rangle$ explained in Section 3.3.2. This time-resolution is a major strength of this work as it gives us a real-time indication of the processes occuring in the Rydberg dressed MOT, and allows us to observe processes over several orders of magnitude in ion detection rate. From the ion detection rates we can identify four stages within the ion signals, shown in Figure 6.1(c-d).

Ions are first detected $\sim$ 40 μs after dressing begins, and the ion detection rate rises sharply for $\sim$ 20 μs, shown in Figure 6.1(c). This initial delay and rise we will refer to as the **'seeding stage'**.

The ion signal then falls for a few hundred microseconds, seen in Figure 6.1(c-d). This fall time is largely exponential and occurs with the same timescale as the loss in atom number. We therefore refer to this stage as the **'rapid loss stage'**. The peak ion detection rates of $\langle \dot{\mathrm{N}} \rangle \sim 8/\mu\mathrm{s}$ are consistent with an ion production rate of $\sim 400/\mu\mathrm{s}$ (see detection efficiencies outlined in Section 3.3.2), which suggests that a sufficient accumulation of ions in the cloud occurs to pass the plasma threshold, described in Section 6.2.

On a longer timescale ions continue to be observed whilst the coupling laser is on, shown in Figure 6.1(d). The ion decay rate here is also exponential, although with a different timescale to the decay in atom number after the rapid loss is complete. We refer to this stage as the **'stable MOT stage'**.

Even when the coupling laser is turned off, ion detection does not completely stop, although there is a drop in ion detection rate and a change in decay rate. This is shown in Figure 6.1(d) and is referred to as the **'slow ions stage'**. The ions that appear after the coupling laser is turned off can't be attributed to the Rydberg state that we couple to, due to the massive difference in 11 μs lifetime of $5s36d\ {}^3D_1$ Rydberg atoms and the ion detection decay lifetime, which is on the order of milliseconds. Long-lived Rydberg state atoms are a characteristic feature of ultracold Rydberg plasmas, populated through

Rydberg-electron collisions and three-body ion-electron recombinations (considered more in Section 6.2).

The conversion of a significant fraction of the cloud to ions [118], the large overall ion signal [119], and the longlived ion signal [120, 121] after the coupling laser is off are all characteristic features of plasmas. Another signature of Rydberg cloud to plasma formation is a threshold with atom number [118], which we investigate by varying both the ground state density and the MOT beam power.

Figure 6.2(a) shows the ion signal as a function of initial atom number for a range of MOT beam powers after 5 ms of dressing, using the same coupling parameters as in Figure 6.1. There is clearly a threshold of ∼0.6 million atoms at which ion signals start being observed, this threshold appears to be dependent on MOT beam power.

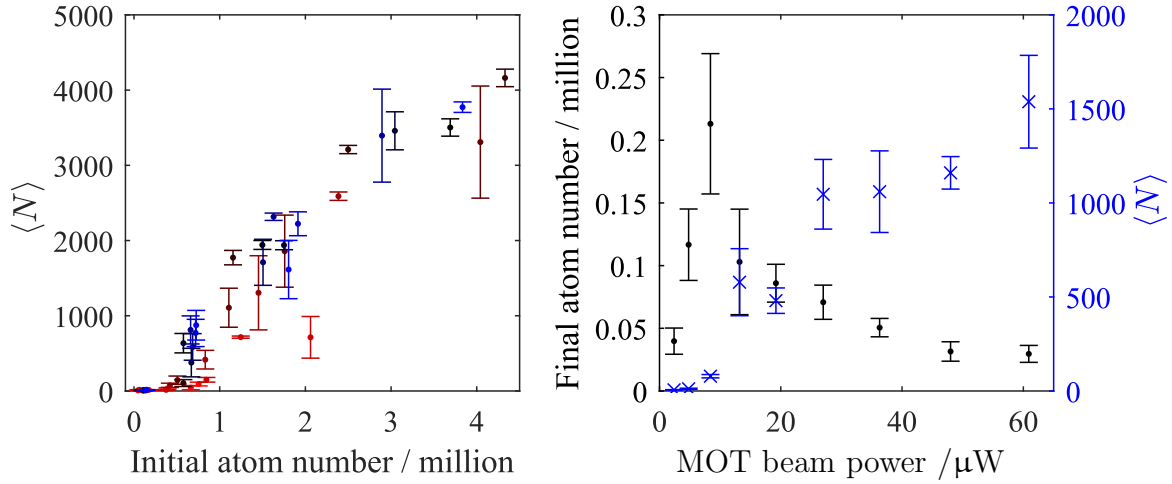

Figure 6.2: (a) Ions detected as a function of initial atom number, for a range of MOT beam powers from 16 μW (red) to 300 μW (blue). There is clearly a threshold density, which is dependent on MOT beam power. (b) Increasing the red MOT beam power increases the transfer efficiency into the MOT, but also increases the rapid loss. Varying the red MOT beam power formed after loading a blue MOT to the radiation pressure limit, we identify 9 μW as the MOT beam power that supports the highest atom number without plasma formation.

This initial study suggests that the loss process is dependent on density and MOT beam power, and associated with a significant fraction of the population being converted to ions. From the rate of ion production we expect the ions in the cloud to exceed the plasma threshold (considered more in Section 6.2). There is a clear threshold in ion signal with

atom number. Finally, ions are detected well after the coupling laser is turned off. From these findings we conclude that there is plasma formation within the Rydberg dressed MOT.

To identify the maximum density that we can achieve without plasma formation we load a blue MOT to the radiation pressure limit, then transfer this via a broadband red MOT to a single frequency red MOT for a range of single frequency red MOT beam powers, before dressing the MOT for 5 ms with compensation of the AC Stark shift. The resulting atom numbers and ion signals are shown in Figure 6.2(b). The highest atom number occurs at a MOT beam power of 9 μW, above this power plasma formation reduces the density of the cloud, below this power transfer efficiency into the undressed MOT is prohibitively low.

The peak ground state density that we can obtain after 5 ms of dressing is 1.3×10^{11} cm^{-3}. For a dressed state fraction of 10% (based on the MOT model), this corresponds to a dressed state Wigner-Seitz radius of 2.6 μm. This is double the dressed blockade radius of 1.3 μm at the $5s36d\ ^3D_1$ Rydberg state. Clearly, the plasma occurs before we reach the Rydberg dressed interaction regime.

To understand and eliminate the plasma, we must perform a detailed study of the plasma. Before we do this, we provide a brief overview of ultracold neutral plasmas.

6.2 Ultracold plasmas

There are several studies and reviews of ultracold plasma physics (e.g. [122, 123]) and Rydberg-plasma systems (e.g. [124]), which we do not seek to replicate in this work. We will provide a brief overview of ultracold plasmas, describing what they are and the evolution of Rydberg gases to plasmas, and we will identify some experiments that are very relevant for our system. This will allow us to identify suitable experiments to investigate plasma formation.

Plasma formation

Ultracold neutral and quasi-neutral plasmas have been formed and studied since 1999 [125], commonly by photoionising laser cooled atoms. Conservation of momentum results in the energy difference between the photoionising photon and the ionisation potential

being largely transferred to the electron, resulting in hot electrons that rapidly disperse leaving a cluster of cold ions. If the Coulomb potential of the cold ions exceeds the kinetic energy of the electrons the electrons are bound to the cloud, resulting in a plasma.

For a plasma to form the Coulomb potential of the cold ions must be sufficient to bind electrons to the cloud. Rydberg atoms may ionise through many mechanisms, but typically the electron kinetic energy is on the order of the binding energy of the Rydberg state [126]. At $n = 36$, this is ~ 3 THz.

The binding energy of the ions for a single electron is given by [84]:

$$U_i = \sqrt{\frac{2}{\pi}} \frac{N_i e^2}{4\pi\epsilon_0 r} \ , \tag{6.1}$$

where r is the electron distance from the N_i ions. For a typical cloud length of 50 μm the ion binding energy matches the electron kinetic energy for $N_i = 670$. If the cloud contains 670 ions we therefore expect a plasma to occur. Given the very high electron speeds and the very small cloud sizes, we expect untrapped electrons to clear the cloud very quickly (on the order of ns).

We can make a rough estimate of the atom number required to reach the plasma threshold in the one-body case by considering the Rydberg fraction, the ionisation rate and the stray electric field. It is not trivial to calculate an expected Rydberg fraction as the detuning of the MOT beams varies across the cloud and we are in the AC Stark shifted regime, but a simple estimate based on 10% of the atoms being in the dressed state (based on the MOT model) and a Rydberg fraction of $\Omega_C^2/4\delta_C^2$ in the dressed state suggests we expect a Rydberg fraction of around 0.28%.

We can make a rough estimate from the ionisation rate and the stray electric field as to the atom number required to reach the plasma threshold, based on one-body excitation and ionisation. A stray electric field of 20 mV/cm (documented in Section 3.1.3) will remove a singly ionised stationary strontium ion from a 50 μm cloud in 6.7 μs. From Figure 4.10 we estimate probability of spontaneous ionisation of $5s36d\ ^3D_1$ state atoms to be ~ 0.2. From the Rydberg state lifetime of 11 μs, we can therefore estimate that for every Rydberg atom in the cloud, there will be a $0.2 \times 6.7/11 \approx 0.13$ ions in the cloud. Given the Rydberg fraction of 0.28% we expect 3.6×10^{-4} ions per atom in the cloud.

To reach 670 ions in the cloud, we therefore require ~ 1.8 million atoms in the cloud. These are rough estimates, but clearly the predicted plasma threshold is substantially

more than the plasma threshold of $\sim 600,000$ observed in Figure 6.2(b). This suggests there must be an enhancement of Rydberg excitation or ionisation in the dressed MOT.

A key property of plasmas is the ability of the bound electrons to redistribute to shield the plasma from the effect of an applied electric field [127]. This redistribution marks the divide between individual responses of charged particles and collective behaviour and is described by the Debye screening length λ_{D}. When the ion temperature is much lower than the electron temperature the Debye wavelength is given by $\lambda_{\mathrm{D}} = \sqrt{\epsilon_0 k_B T_{\mathrm{e}}/e^2 n_{\mathrm{e}}}$ where T_{e} and n_{e} are the electron temperature and density [128]. For an electron kinetic energy of 3 THz and a charge density corresponding to 670 electrons in a 50 μm cloud (all typical values), we obtain a Debye length of 7.4 μm, much less than the size of the cloud.

A Debye length that is smaller than the cloud but larger than the interparticle separation is a significant result. It suggests that whilst the cloud will be shielded from externally applied electric fields, electrons in the plasma will not be sufficient to shield the atoms in the cloud from the ions in the plasma. Atoms in the cloud will experience large variation in electric fields.

Another key measure of ultracold plasmas is whether they are strongly coupled i.e. whether the Coulomb potential energy between ions is larger than the kinetic energy of the plasma [128]. This has a significant effect on the evolution of the plasma. From estimates of the electron energy and the Coulomb repulsion of ions we expect not to be in the strongly coupled regime.

Plasma evolution

Typically during ultracold plasma formation the ion temperature is initially dominated by the pre-ionisation atom temperature and the electron temperature depends on the ionisation process. Electron gas pressure [128] or disorder induced heating between ions [129] then results in expansion of the cloud of ions [130, 131] reaching ion expansion velocities on the order of 40 m/s [128]. As the cloud expands, the Coulomb potential falls, and previously trapped electrons can escape.

As the plasma expands three-body recombinations can occur, which populate high angular momentum Rydberg states [121]. The three-body recombination typically consists of a single ion and two electrons, and is therefore very dependent on both electron density and electron energy [132]. This is not the only process that can populate high angu-

lar momentum Rydberg states; if Rydberg atoms are present in the cloud before plasma formation these can be redistributed to high angular momentum states through Rydberg-electron collisions [133]. These long-lived Rydberg atoms are responsible for the 'slow ion stage' shown in Figure 6.1(d).

Rydberg gas evolution to plasma

There has been a lot of interest in the evolution of clouds of Rydberg atoms into ultracold neutral plasmas given the potential to create strongly coupled plasmas i.e. with Coulomb interaction strengths that significantly exceed the kinetic energy of the charged particles [118]. In addition, Rydberg blockade can lead to structure in the Rydberg spatial distribution, which may reduce the effect of disorder induced heating [129].

Experiments have studied several ionisation mechanisms for Rydberg atoms, studying the effect of blackbody radiation [134], Penning ionisation between Rydberg atoms [135, 136] and ground or intermediate state atoms [137], collisions with hot Rydberg atoms [126] and many-body ionisation processes [119]. All of these may influence the 'seeding stage' of the plasma.

The key feature of Rydberg plasma formation is an avalanche ionisation process that occurs when the ions pass the plasma threshold. At this point, electrons are bound to the cloud and Rydberg-electron collisions rapidly ionise the Rydberg population, resulting in more ions and electrons [118]. In addition to ionising collisions, collisions between Rydberg atoms and electrons can transfer Rydberg atoms to long-lived high angular momentum Rydberg states with long lifetimes and high probability of ionising due to blackbody radiation[120].

Of particular interest to us is the work of [137], [138] and [139]. Whereas in most of the experiments referenced above, in which a Rydberg population is excited and then left to evolve without coupling lasers present, in these cases resonant coupling to the Rydberg state is sustained during plasma formation, allowing continuous Rydberg excitation in the plasma. In [137] an ultracold gas of Rb is excited to the Rydberg state in the strongly blockaded regime. As Rydberg atoms ionise through blackbody radiation and collisions the ion number in the cloud grows until the plasma threshold is reached. At this point the Rydberg population experiences strong ionisation through collisions with electrons, breaking the Rydberg blockade and resulting in strong excitation to the Rydberg state.

In [138] the effect of three body recombinations is considered and found to partially limit

the plasma by removing electrons and ions from the system. In [139] the effect of ion blockade is considered as a broadening of the Rydberg line and a reduction in the Rydberg excitation rate - in this case the Rydberg excitation rate is reduced by the presence of the plasma through ion blockade, rather than in [137] where ionisation breaks the Rydberg blockade, enhancing Rydberg excitation.

From the above work we conclude that van der Waals interactions and Coulomb interactions are the likely processes that may modify plasma seeding and Rydberg excitation in the plasma. Figure 6.3 shows the energy level shift of a $5s36d\ ^3D_1$ state atom as a function of distance from another $5s36d\ ^3D_1$ state atom and an ion.

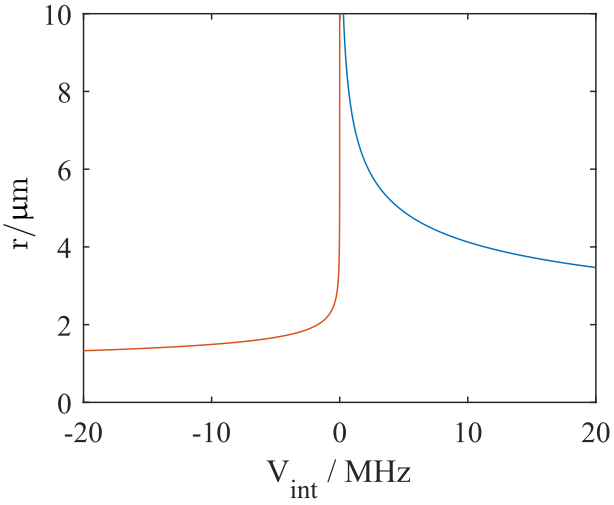

Figure 6.3: Energy shift of the $5s36d\ ^3D_1$ Rydberg state in response to the the DC Stark shift due to an ion (blue) and the van der Waals shift of another atom in the $5s36d\ ^3D_1$ Rydberg state (orange), averaged over m_J states.

To study these processes of van der Waals and Coulomb interactions we will vary the coupling beam detuning (equivalent to the x-axis of Figure 6.3) and the ground state density (equivalent to the y-axis of Figure 6.3). There are two key questions we must answer in this plasma study. Firstly, we must understand why we observe a plasma threshold that is so much lower than the predicted plasma threshold. Secondly, we must understand why the Rydberg excitation rate is so much higher in the plasma than after the plasma disperses.

6.3 Seeding the plasma

In Figure 6.1 we identify a seeding stage in the plasma formation, consisting of a delay of ~ 40 μs followed by a sharp rise in ion detection rate lasting ~ 20 μs. In Figure 6.3 we show that coupling beam detuning and atomic density are the natural parameters to study this process.

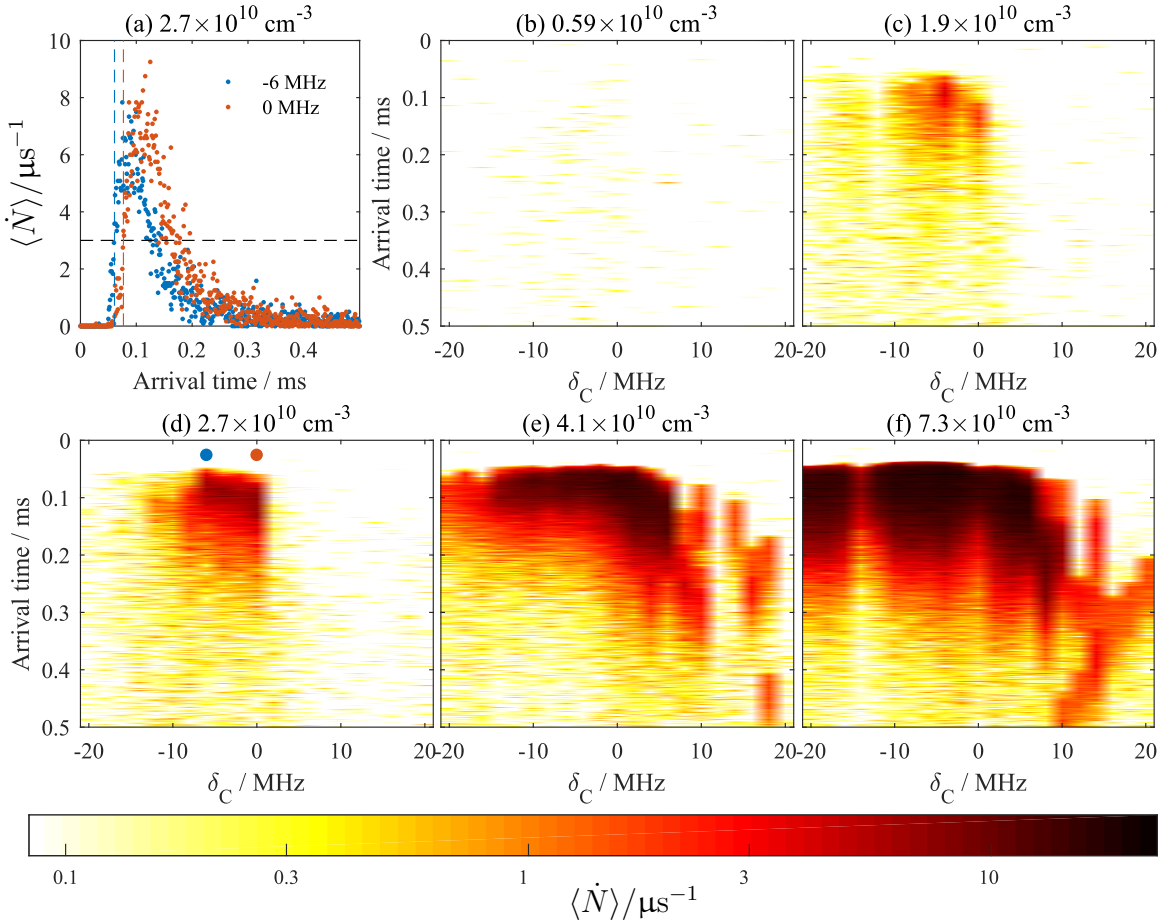

Figure 6.4: (a) Ion detection rate as a function of arrival time from when the coupling begins, for two coupling beam detunings indicated by dots in (d). Taking a series of coupling beam detunings, we create colourmaps of ion detection rate against time and coupling beam detuning, shown for different densities (b-f). We can also measure a seeding time from when a threshold is crossed, indicated by the dashed lines in (a).

Figure 6.4 shows ion detection rates for a series of dressing experiments. Figure 6.4(a) illustrates the ion detection rate as a function of arrival time at two coupling beam detunings. Repeating this for a wide range of coupling beam detunings we build up a colourmap of the ion detection rate against arrival time and coupling beam detuning.

This is then repeated for a range of densities to build a thorough picture of the parameter space in which the plasma exists.

This offers a very striking visualisation of the ion signals from the dressed MOT. Starting from low density (Figure 6.4(b)), we see very few ions, and the ions that we do see have little structure in their arrival times. Increasing the density we see a rise in ion detection rate on resonance and for small red-detunings consistent with van der Waals enhanced Rydberg excitation (Figure 6.4(c-d)). Increasing the density further (Figure 6.4(e-f)) the broadening of the feature to the red-detuned side continues, and ions appear earliest when red-detuned rather than on resonance. In addition, strong ion signals are observed when blue-detuned with large variation in seeding time. As well as large variation in seeding time these ion signals are highly super-Poissonian. This is shown in Appendix G. The ion signals when red-detuned are also super-Poissonian until MCP detector saturation occurs. Super-Poissonian ion detection is consistent with Rydberg or Coulomb anti-blockade and Rydberg density dependent ionisation.

A drop in detection rate at $\delta_C = -12$ MHz and -14 MHz in Figure 6.4(c) and (f) corresponds to the 689 nm laser unlocking from the cavity and the MOT being lost for some of the shots. Between 12 and 20 repeats were taken for each detuning (more repeats at lower densities), the ion detection rates are the mean of all repeats. The MOT beam detuning is $\delta_{\mathrm{MOT}} = -210$ kHz, resulting in a cloud that is larger than the coupling beam, and the MOT power is 500 μW. This high MOT beam power results in plasma formation at relatively low ground state densities.

In Appendix G we demonstrate that reducing the cloud size and MOT beam power increases the density at which plasma formation occurs. This is consistent with a reduced Rydberg fraction and an increased plasma charge density threshold. Ionising collisions between Rydberg atoms and excited state atoms may also be reduced.

6.3.1 Van der Waals interactions

We expect van der Waals interactions to increase the Rydberg excitation rate when the coupling beam is red-detuned from the $5s36d\,^3D_1$ state due to the attractive van der Waals interactions of this state. This is illustrated in Figure 6.5 - when a ground or excited state atom is at a distance from a Rydberg atom where the van der Waals interaction shift matches the coupling beam detuning there will be a strong enhancement of Rydberg excitation rate.

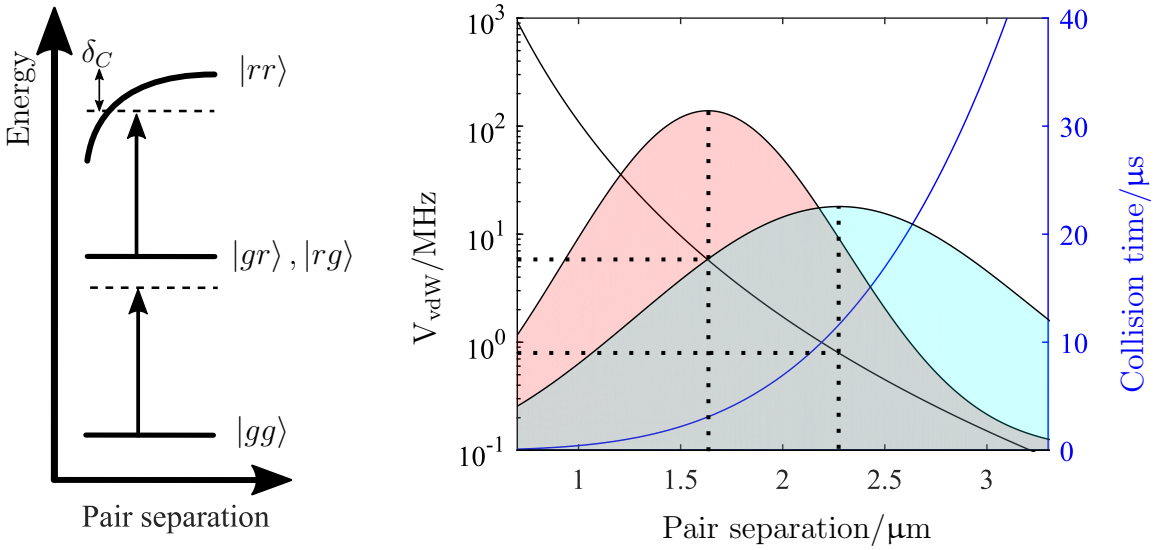

Figure 6.5: Ground or excited state atoms may be excited in the presence of a Rydberg atom when the van der Waals interaction strength equals the coupling beam detuning (left). We can estimate the range of interaction strengths the atoms will experience by overlaying the van der Waals interaction strength of the $5s36d\ ^3D_1$ state (black line) and the intermediate state interparticle distributions (shown for ground state densities of 7.3×10^{10} cm^{-3} (pink) and 2.7×10^{10} cm^{-3} (light blue)). Also shown is the time taken for the attractive van der Waals interactions to result in collisions of Rydberg atoms.

From the atomic density we can estimate an interparticle separation for the ground or intermediate state, and calculate the most probable interparticle separation, shown in Figure 6.5. In Regime II MOTs half of the population occupies the intermediate state, which will experience stronger one-photon coupling to the Rydberg state than the two-photon coupling of ground state atoms to the Rydberg state. We will therefore consider the intermediate state particle density.

To compare the density-dependent van der Waals interaction shift illustrated in Figure 6.5 to the density-dependent seeding of the plasma observed in Figure 6.4 we measure a seeding time, defined as the first point at which $\langle \dot{\mathrm{N}} \rangle > 3\langle \mathrm{N} \rangle / \mu\mathrm{s}$ [a]. This is illustrated in Figure 6.4(a). This seeding time is a measure of when the ion detection rate begins to rise (as the rise does not begin as soon as the coupling laser is turned on) and includes a

[a]We reduce the bin size to 200 ns to improve our time-resolution at the expense of greater noise on the ion detection rate. A threshold of $\langle \dot{\mathrm{N}} \rangle > 3/\mu\mathrm{s}$ is the lowest threshold at which we avoid 'false seeding' measurements, where the noise exceeds this threshold.

$\sim$ 35 µs delay between when the ions are created and when the ions reach the detector, we subtract this delay and invert to get a seeding rate, shown in Figure 6.6. [b]

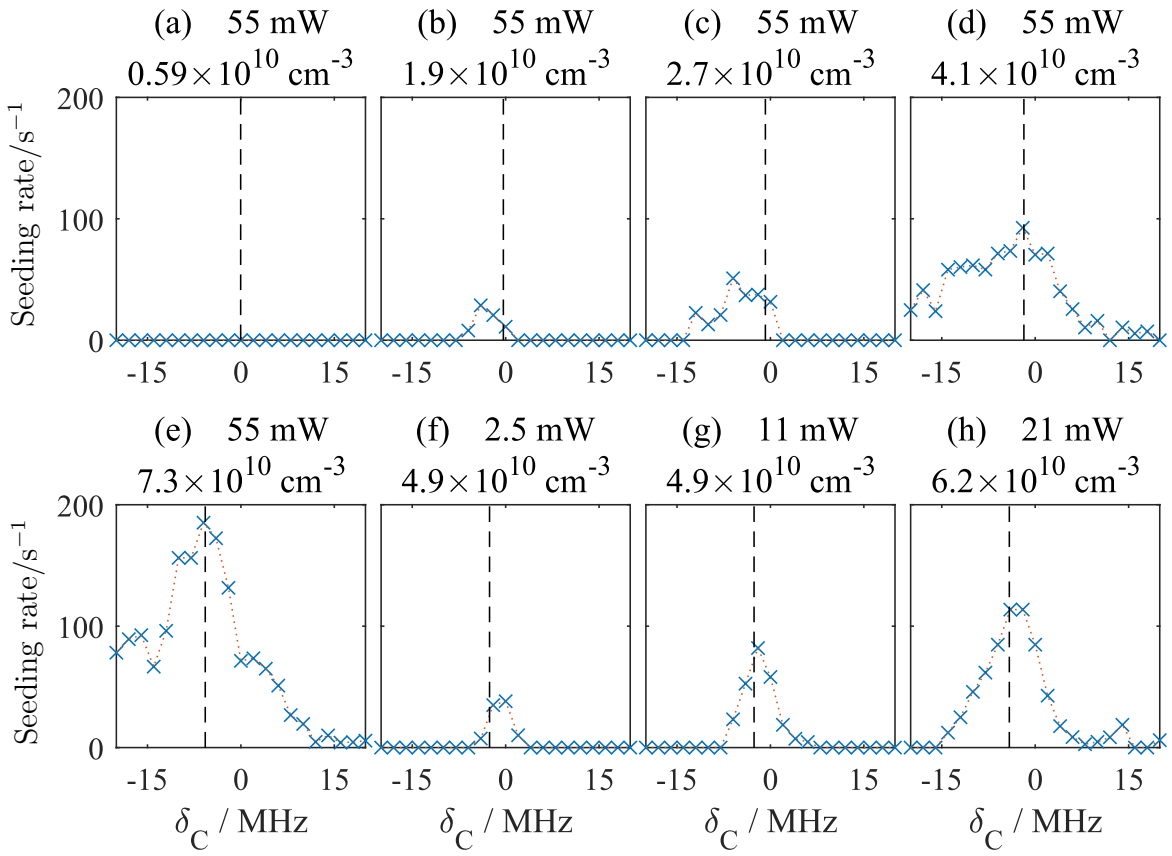

Figure 6.6: The ion detection seeding rate (blue crosses and dotted line) and the most probable van der Waals interaction strength (dashed black vertical line), calculated from the density. We see good agreement between the most probable interaction strength and the highest seeding rate. Penning ionisation and Rydberg excitation from the ground state may both increase the seeding rate at larger red-detunings, and one-body excitation in the low power regime is expected to draw the peak seeding rate closer to resonance.

We can clearly see a broadening and a shift to the red-detuned side of resonance with increasing density and a broadening with increasing coupling beam power from the data given in Appendix G. Particularly at high densities greater than 2.7×10^{10} cm^{-3} and powers greater than 2.5 mW we see good agreement between the most probable interaction strength and the peak seeding rate. We therefore conclude that van der Waals

[b] Also included in this Figure is seeding rates for different coupling beam intensities. The raw data from which this is taken are shown in Appendix G.

interactions therefore play a major role in Rydberg atom excitation at high densities and powers when the coupling beam is red-detuned.

A final effect of van der Waals interactions we must consider is illustrated on the right hand axis of Figure 6.5. The $5s36d\ ^3D_1$ Rydberg state exhibits attractive van der Waals interactions, so a pair of Rydberg atoms will draw themselves together and ionise (collisional ionisation). The greater the coupling beam red-detuning, the closer the pair of Rydberg atoms will be, and the faster the pair will collide [136]. The collision times shown in Figure 6.5 have been estimated from the C_6 coefficients, from which an interatomic force can be calculated. Consequently, Rydberg atom pairs have a higher ionisation probability when excited with red-detuned coupling light. This gives rise to a seeding rate shift to the red-detuned side of resonance and a Rydberg-density-dependent ionisation mechanism that may give rise to super-Poissonian ion statistics. We observe lower spontaneous ionisation on the van der Waals anti-blockade side of resonance for repulsive van der Waals interactions at the $5s37s\ ^3S_1$ state in Appendix G.

In the analysis presented in this section we have shown that the van der Waals interaction shift is comparable to the shift observed in the seeding rate of the plasma. In addition, van der Waals interactions are consistent with the super-Poissonian ion signals that we observe. We are therefore confident that van der Waals interactions are responsible for rapid seeding of Rydberg excitation when the coupling beam is red-detuned. Later in the section we will present further data whilst coupling to the $5s37s\ ^3S_1$ state where the van der Waals interaction is repulsive, corroborating this interpretation of the data. Before doing this, we will consider the role that we expect ions to have on Rydberg excitation.

6.3.2 Charges in the cloud

In Figure 6.3, we identify van der Waals interactions and Coulomb interactions as likely causes for enhancement of Rydberg excitation. In Figure 6.4 we clearly observe very different seeding times, variation in seeding time, and different seeding density thresholds when the coupling beam is red-detuned to blue-detuned. This is consistent with different seeding mechanisms either side of resonance. Having shown the role that van der Waals interactions play, we now consider the role that ions play.

We can consider the DC Stark shift that a Rydberg state will experience as a function of distance from an ion. This is shown in Figure 6.7 - at a detuning dependent 'Coulomb anti-blockade' distance the DC Stark shift will match the coupling beam detuning and

we will see a strong enhancement of Rydberg excitation rate. As we will show in this section, for relevant experimental parameters, this anti-blockade radius is comparable to the separation of atoms from ions. As with the Rydberg anti-blockade, this excitation enhancement will result in super-Poissonian ion statistics.

In Figure 6.7 we quantify the effect of the Coulomb anti-blockade on the Rydberg fraction. We have estimated the fraction of atoms in the Rydberg state P_{Ryd} using the two-level optical Bloch equations to avoid the challenges of modelling a varying MOT beam detuning across the cloud i.e.

$$P_{\mathrm{Ryd}}(r) = P_{\mathrm{E}} \frac{1}{2} \frac{\Omega^2}{\Omega^2 + 2(\delta_{\mathrm{C}} - \delta_{\mathrm{DC}})^2} \ . \tag{6.2}$$

Here P_{E} is the fraction of atoms in the excited state, which in a Regime II MOT is $^1/_2$. δ_{C} and δ_{DC} are the coupling beam detuning from the unshifted state and the DC Stark shift of the Rydberg state and Ω is the one-photon coupling to the Rydberg state from the excited state. This two-level treatment treats half of the atoms as completely uncoupled from this two-level system (i.e. in a ground state that plays no further part in Rydberg excitation) and the other half as occupying a two-level system of the excited state and the Rydberg state. This will understate the Rydberg fraction, but is sufficient to test whether ions in the cloud may strongly modify the Rydberg excitation rate.

To estimate the effect that ions have on the cloud we weight the charge-modified Rydberg fraction $P_{\mathrm{Ryd}}(r)$ given by Equation 6.2 and shown in Figure 6.7 by the probability of finding an atom in a shell of thickness δr and radius r:

$$P_{\mathrm{Ryd}} \approx \frac{\int_0^{r_{\mathrm{ion}}} P_{\mathrm{Ryd}}(r) \times 4\pi r^2 \delta r}{^4/_3 \pi r_{\mathrm{ion}}^3} \ . \tag{6.3}$$

The limit of this integral is the ion Wigner Seitz radius r_{ion}, requiring us to estimate the ion density. In Section 6.2 we estimate that with one-body Rydberg excitation and ionisation we have 3.6×10^{-4} ions per atom in the cloud for a Regime I MOT and a coupling beam detuning of $\delta_C = +12$ MHz. In a Regime II MOT this rises to 1.8×10^{-3} ions per atom as half of the atoms are in the excited state, rather than 10%.

From Figure 6.4 we observe plasma formation, evidenced by very large ion signals, in 3 of 12 shots for an atomic density of 7.3×10^{10} cm^{-3} and $\delta_C = +12$ MHz. We will consider the effect of Coulomb anti-blockade at this density. In the one-body excitation and ionisation case a density of 7.3×10^{10} cm^{-3} corresponds to an ion density of 1.3×10^8 cm^{-3} and an

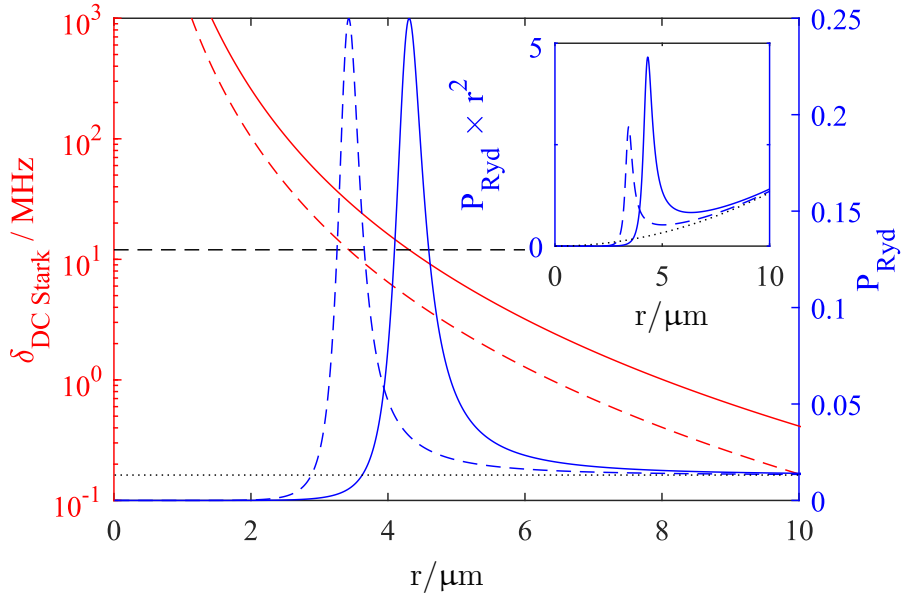

Figure 6.7: DC Stark shift (red) of the $5s36d\ ^3D_1$ Rydberg state for the $|m_J| = 0$ (solid) and $|m_J| = 1$ (dashed) sublevels, and Rydberg state fraction (blue) for a two-level system with coupling beam detuning of +12 MHz (dashed black line) that has been DC Stark shifted, as a function of distance r from an ion. The black dotted line indicates the unshifted fraction. The fraction of atoms that experiences this shift is proportional to r^2, illustrated in the inset.

ion Wigner-Seitz radius of $r_{\text{ion}} = 12$ μm.

Numerically solving Equation 6.3 for an ion Wigner-Seitz radius of $r_{\text{ion}} = 12$ μm we predict a Rydberg fraction of 1.8%, compared to the one-body case of 1.3%. This estimate is an average of the two Rydberg sublevels. As a first order approximation we therefore expect an increase in Rydberg excitation rate on the order of 35% in response to ions in the cloud. This is a significant increase in the Rydberg excitation rate, and suggests that charges in the cloud will increase the Rydberg excitation rate when the coupling laser is blue-detuned.

This is a first iteration - as charges increase the Rydberg fraction, the rising Rydberg fraction will increase the charge density. Iteratively recalculating the ion Wigner-Seitz radius r_{ion} we observe convergence within ~ 5 iterations, reaching a Rydberg fraction of 2.0%. We therefore expect ions in the cloud to increase the Rydberg excitation rate by a factor of ∼50%.

This factor is very dependent on the ionisation probability and the ion extraction time

that set the ratio of ions per Rydberg atom in the steady state. For example, if this ratio is doubled (i.e. a higher ionisation probability or atoms remaining in the cloud for longer) this technique predicts the Rydberg fraction will rise to 3.5%, a 165% increase on the one-body case. Recalling that there is approximately a factor of three between the estimated plasma threshold based on one-body Rydberg excitation and the observed plasma threshold in Figure 6.2(a), ion enhanced Rydberg excitation may be a very significant factor in the seeding of the plasma.

This technique is meant only to estimate whether the role of ions in the cloud is significant to the Rydberg excitation rate prior to plasma formation. It has several limitations, most significantly, it does not consider two-photon excitation, it averages over the effect of MOT beam detuning and it does not consider collisional ionisation processes. All of these effects mean that this approach will understate the increase in Rydberg excitation rate due to ions in the cloud. However, it is sufficient to show that ions from spontaneously ionised Rydberg atoms have the potential to significantly increase the Rydberg excitation rate when the coupling beam is tuned to the Coulomb anti-blockade side of resonance.

6.3.3 Variation of Rydberg state

From these analyses we believe van der Waals interactions and Coulomb interactions may both enhance the Rydberg excitation rate. The natural test of this is to vary the Rydberg state that we couple to. We have coupled the MOT to both the $5s36d\ ^3D_1$ state (at which all of the data in this chapter to this point has been taken), which has attractive van der Waals pair interactions and a negative polarisability, and also to the $5s37s\ ^3S_1$ state, which has repulsive van der Waals pair interactions and a positive polarisability. This makes a comparison between the two a valuable technique for testing hypotheses involving van der Waals and Coulomb interactions.

Whilst coupling to the $5s37s\ ^3S_1$ state we used autoionisation after dressing to probe the spontaneous ion and Rydberg population, rather than the continuous detection technique used whilst coupling to the $5s36d\ ^3D_1$ state. Whilst this prevents a direct comparison between the two states, the use of autoionisation offers significant insight. In particular, the ability to distinguish between spontaneously ionised atoms and autoionised atoms described in Section 3.3.2 allows us to observe the relationship between ion population and Rydberg population.

In Figure 6.8 we present ion signals, separated by arrival time to distinguish between spon-

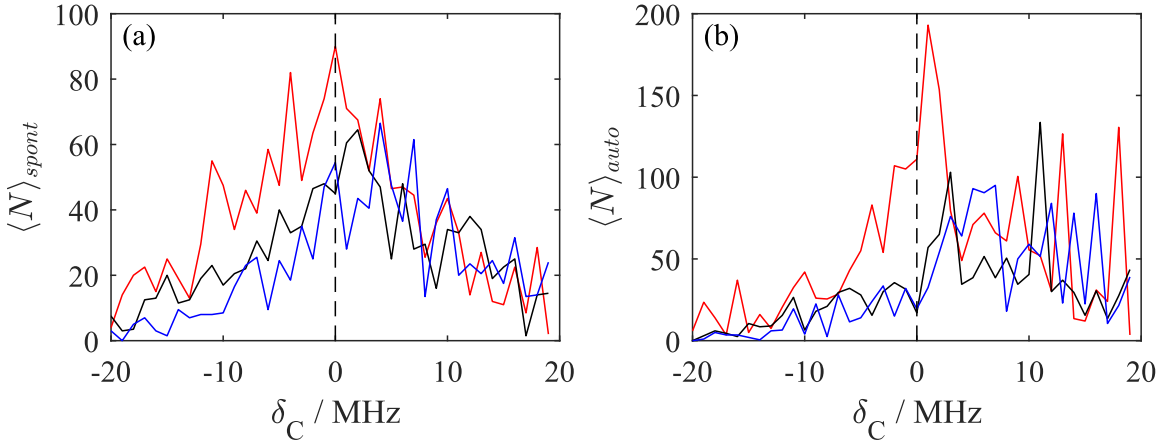

Figure 6.8: Coupling the cloud to the $5s37s\ ^3S_1$ state and performing autoionising laser pulses with steering electric fields after dressing, we can distinguish between spontaneously ionised Rydberg atoms (a) and autoionised Rydberg atoms (b). We dress the cloud for 1 ms (red), 3 ms (black) and 5 ms (blue).

taneously ionised Rydberg atoms and autoionised Rydberg atoms, taken whilst coupling to the $5s37s\ ^3S_1$ Rydberg state for varied dressing times and coupling beam detunings. This is the same dataset that was shown in Figure 5.1.

We see a strong shift to the red-detuned side of resonance in spontaneous ion signal after 1 ms of dressing relative to longer dressing times. This is consistent with a plasma formation increasing both Rydberg excitation and ionisation rate on the Coulomb anti-blockade side of resonance, which for the positive polarisability of the $5s37s\ ^3S_1$ state is red-detuned. This dies away quickly, due to the short timescale of plasma formation.

In contrast the autoionised ion signals show a clear shift to the blue-detuned side of resonance. We attribute this to van der Waals enhanced excitation - a +12 MHz interaction shift corresponds to a pair separation of 1.9 μm for the doubly excited $5s37s\ ^3S_1$ state, whilst the ground state density of 10^{11} cm^{-3} corresponds to a ground state Wigner Seitz radius of 1.3 μm (the excited state Wigner-Seitz radius is greater than this). We don't observe a rapid decay in signal except on resonance, which is expected given that we only see strong depletion on resonance (discussed in Section 5.1.1).

Notably the spontaneous ion signal and the autoionised ion signal do not match each other even after the plasma formation, with the autoionised ion signal stronger than the spontaneously ionised ion signal when blue-detuned and vice versa when red-detuned. Recalling from Figure 6.5 that attractive van der Waals interactions may lead to strong

ionisation of pair states, we note that this is not the case for the repulsive van der Waals interactions of the $5s37s\ ^3S_1$ state. In Appendix G we show further evidence of collisional ionisation occuring for the $5s36d\ ^3D_1$ state but not for the $5s37s\ ^3S_1$ state through the use of coupling beam intensity ramps.

Only two repeats are taken at each coupling beam detuning, the average of which is shown, limiting our analysis to a qualitative study. However, the signals shown in Figure 6.8 are fully consistent with the hypothesis that both van der Waals interactions and Coulomb interactions can strongly enhance the Rydberg excitation rate on the van der Waals anti-blockade and Coulomb anti-blockade side of resonance.

Seeding processes

In this section we have estimated the most probable van der Waals interaction strength for a range of atomic densities and found the shift resulting from van der Waals interactions to be consistent with enhanced excitation rates for a range of densities and coupling beam powers. We also observe strong spontaneous ionisation on the van der Waals anti-blockade side of resonance for the attractive van der Waals interactions of the $5s36d\ ^3D_1$ state, which is not observed for the repulsive van der Waals interactions of the $5s37s\ ^3S_1$ state, consistent with Penning ionisation for attractive van der Waals interactions.

We have also estimated the Coulomb interactions that we expect from ionised Rydberg atoms in the cloud and found the effect to be significant at the densities at which we observe plasma formation.

We are therefore confident that both van der Waals interactions and Coulomb interactions can result in a drastically increased Rydberg excitation rate compared to the one-body, off-resonant case. In turn, this increased Rydberg excitation rate results in a greater ion population in the cloud, which then results in plasma formation. When the Rydberg state that we dress with exhibits attractive van der Waals interactions there is an additional collisional ionisation mechanism. There may be other effects that modify the ionisation rate, but these are beyond the scope of this study.

Having shown the effect of interactions in the seeding of the plasma, we must now consider why the plasma increases the Rydberg excitation rate.

6.4 Rapid loss during plasma formation

As shown in Figure 6.1, we observe massive loss from the MOT whilst the plasma exists. We have studied the plasma seeding mechanisms of van der Waals interactions and Coulomb interactions, we now consider why the Rydberg excitation rate is so high in the plasma. We will focus this study on the regime that we expect to observe Rydberg dressed interactions in. For the $5s36d\ ^3D_1$ Rydberg state, this occurs at $\delta_C = +12$ MHz, where Coulomb interactions are the natural candidate for enhancing the Rydberg excitation rate.

In this section we will estimate the charge density in the cloud and show that charges in the cloud are sufficient to drastically increase the Rydberg excitation rate in the cloud. We then compare the predicted loss rate that results from Coulomb enhanced Rydberg excitation to observed ion detection rates and atom loss rates.

6.4.1 Charges in the plasma

As we have discussed previously, we expect a plasma to occur when the number of ions in the cloud passes a threshold at which electrons are bound to the cloud. Electron pressure or Coulomb repulsion will cause plasma expansion, reducing the charge density, and Rydberg excitation and ionisation will increase the charge density. Whilst the Rydberg excitation and ionisation rate is sufficient to compensate plasma expansion, the plasma will continue to exist.

Given the unknown plasma expansion rate, the modified excitation rate within the cloud, and the dependence of collisional ionisation on the electron density and temperature, it is not trivial to calculate a charge density. Neither is it obvious what the mean electric field experienced by atoms in the plasma will be. Overall, the net charge of the cloud is limited to the plasma threshold and electrons can shield the electric field produced by ions over the Debye length of ~ 7 μm [127], but the mean interparticle separation is much less than this.

Having established that a quantitative calculation of the distribution of electric fields within the plasma is too complex for this work, we instead make some simple estimates of the charges in the cloud at the point the plasma is seeded.

A cloud of 50 μm containing 670 ions (the plasma threshold) corresponds to a charge

density of 2×10^9 cm^{-3} and an ion Wigner-Seitz radius of 4.9 μm. As we see from Figure 6.7 this is close to the 4.3 μm Coulomb anti-blockade radius at $\delta_C = 12$ MHz for the $5s36d\ ^3D_1\ |m_J| = 0$ state, so we expect a strong enhancement of Rydberg excitation. Calculating the Rydberg fraction of the excited state using Equation 6.3 for an ion Wigner-Seitz radius of 4.9 μm we expect the Rydberg fraction of the excited state to rise to 6.3%, compared to 1.3% based on one-body Rydberg excitation and ionisation in a Regime II MOT. This suggests that charges in the plasma will give rise to a very large increase in Rydberg excitation rate.

Given the Rydberg state lifetime of 11 μs and the negligible probability of decay to the ground state on the timescale of the MOT, a 6.3% Rydberg state fraction suggests a cloud lifetime of ~ 170 μs, considering only atom loss due to Rydberg excitation within the plasma. This is comparable to the lifetimes measured in Section 5.7, although these lifetimes are taken in Regime I MOTs.

Once the Rydberg excitation rate in the plasma falls below that necessary to sustain the charge density against plasma expansion the plasma will disperse, leaving the MOT with a largely one-body lifetime as measured in Section 5.7.

As previously discussed this treatment only considers Rydberg excitation from the excited state, as to include two-photon excitation from the ground state is challenging given the varying detuning and polarisation of the MOT beams. It is therefore better suited to MOTs with high excited state fractions and will overstate the cloud lifetime.

6.4.2 Plasma lifetime

Having shown that the charge density of the plasma is sufficient to drastically increase the Rydberg excitation rate and cause rapid depletion, we now compare the atom loss rate to the ion detection rate. Figure 6.9 shows both the atom number and the ion detection rate for a Regime II MOT, taken with $\delta_{\mathrm{MOT}} = -140$ kHz, $\mathrm{P_{MOT}} = 230$ μW. We observe strong correlation between the atom number and the ion detection rate, confirming that Rydberg excitation is responsible for the loss and that ionisation in the plasma results in the ion signal that we observe.

The data are taken for three initial atom numbers. We see that the final atom number of $\sim 3 \times 10^4$ is largely independent of the initial atom number. This is expected - the cloud will be depleted through Rydberg excitation to the density at which Rydberg excitation

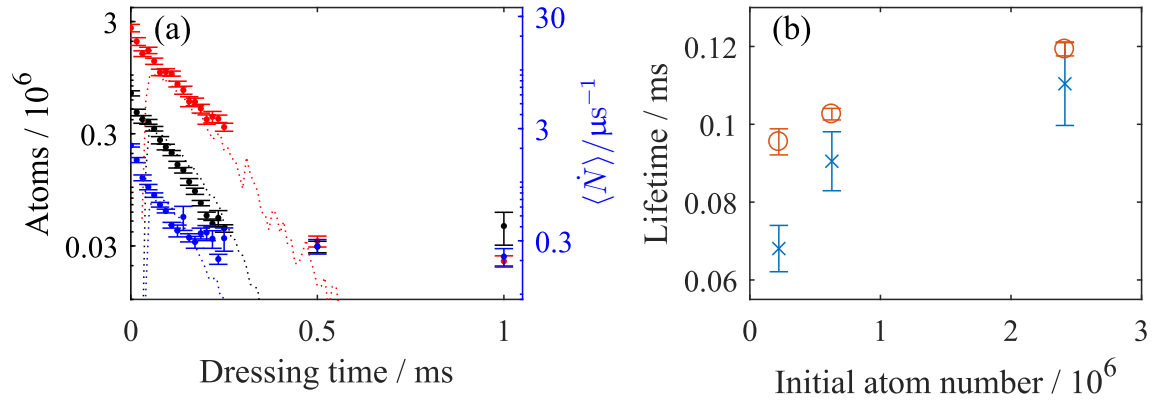

Figure 6.9: (a) Atom number (points, left axis) and ion detection rate (dotted line, right axis) for three initial atom numbers, indicated by colour. We see matching rapid decay in atom number and ion detection rate until the plasma terminates. (b) Fitting an exponential decay to the fall in atom number (blue crosses) and ion detection rate (orange circles), we see a lifetime that rises with initial atom number.

is no longer sufficient to sustain the plasma.

The most surprising feature of Figure 6.9 is the dependence of the lifetime on the initial atom number - higher initial atom numbers result in a slower decay in atom number and ion detection rate. It is not clear why this is the case. Several mechanisms are discussed in Appendix H, but a full study of this effect is beyond the scope of this work. We note that a constant Rydberg excitation rate within the plasma is predicted in [139] due to a plasma feedback mechanism in which Coulomb blockade limits the Rydberg excitation rate to the rate at which ions leave the plasma. If the charge density varies across the plasma the Coulomb blockade may not be complete across the cloud, resulting in an exponential decay in atom number in the wings of the cloud and a linear decay in atom number at the centre of the cloud. As the cloud must be ballistically expanded before imaging to avoid optical depth problems we can't observe this from the cloud images.

The plasma lifetime is quantified by fitting an exponential decay to the ion detection rate after 80 µs of dressing and for $\langle \dot{N} \rangle > 0.1/\mu s$. We see plasma lifetimes that are lower than the $\sim$ 150 µs predicted by Equation 6.3 and the plasma threshold, but not incomparable. The model does not consider the role of electrons, which may suppress the Coulomb blockade that occurs at very small distances (< 3 µm) from ions shown in Figure 6.7, nor does it consider two-photon excitation from the ground state. Both of these effects may increase the Rydberg excitation rate.

From this simple model of ions in the cloud we are confident that the charge density in the plasma is responsible for DC Stark shifting the Rydberg state onto resonance with the coupling laser, resulting in strong Rydberg excitation and loss of atoms from the trap. To observe Rydberg dressed interactions in the MOT we must avoid the enhanced Rydberg excitation that occurs in the plasma.

6.5 Stable dressed MOT

In the previous sections we have studied the processes that result in plasma formation, and that result in massive loss of trapped atoms during plasma formation. When the depletion results in Rydberg excitation and ionisation being less than the ion loss rate, the plasma will cease and both ions and electrons will disperse. At this point we have the Rydberg dressed MOT that we set out to observe, but at too low a density to observe Rydberg dressed interactions; the 'stable dressed MOT' in Figure 6.1(d).

Surprisingly, the rate at which the ion detection rate decays during the stable dressed MOT stage (a lifetime of $\sim$ 2.5 ms), shown in Figure 6.1(d) is different to the rate at which the atom number decays (a lifetime of $\sim$ 5.5 ms).

A second surprising feature of these data is that the ion detection rate is an order of magnitude higher for the data taken at $P_{MOT} = 40$ μW than at $P_{MOT} = 20$ μW, despite the atom number being a factor of two lower by the time the plasma finishes. These two effects combined suggest that the ions detected in the stable dressed MOT stage are attributable to something other than Rydberg excitation of atoms trapped in the MOT.

To quantify this effect we will use the ion detection rate from the stable MOT measured after 1 ms of dressing, $\langle \dot{N}_{1ms} \rangle$. We compare this ion detection rate to the ground state atom number in the stable dressed MOT measured after 1 ms of dressing, S_{1ms}, the initial atom number measured before dressing, S_{0ms}, and the product of the two, $S_{0ms} \times S_{1ms}$, to look for correlations between ion detection rate and atom number. This is shown in Figure 6.10. We do this for two MOT beam powers and three initial atom numbers.

We see poor correlation between the ion detection rate in the stable MOT and the atom number in the stable MOT, confirming the that the ion detection rate from the stable dressed MOT is not attributable to the atoms in the dressed MOT. We see much better correlation between the ion detection rate in the stable dressed MOT and both the initial atom number and the atom number product.

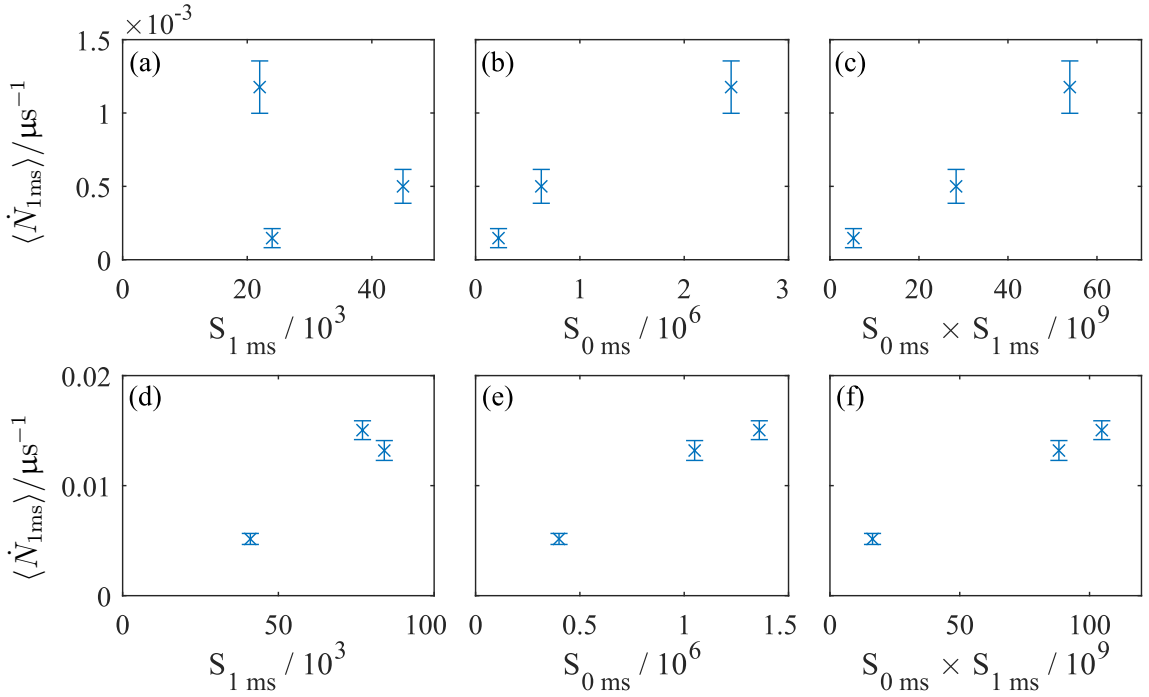

Figure 6.10: Ion detection rate after 1 ms of dressing for P_{MOT} = 230 μW (a-c) and 80 μW (d-f), plotted against the atom number after 1 ms of dressing (a, d), the initial atom number (b,e), and the product of the two (c,f).

The correlation with initial atom number suggests this signal is related to atoms lost during the plasma. This can't simply be spontaneous ionisation of long-lived Rydberg atoms as the ion detection rate drops when the coupling laser is turned off. We attribute the signal to magnetically trapped metastable $5s5p\ ^3P_2$ state atoms populated by atoms decaying from Rydberg states. These atoms may photoionise due to the coupling laser, in which case the ion detection rate should be proportional to the atoms lost in the plasma, or they may collide with Rydberg atoms resulting in ionisation, in which case the ion detection rate should be proportional to the product of the atoms lost in the plasma and the atoms remaining after 1 ms.

For the magnetic field gradient we expect a magnetic trap gradient of 0.16 μK/μm [140] for $5s5p\ ^3P_2\ m_J = +2$ state atoms. This trap depth is sufficient to confine atoms close to the quadrupole field centre, suggesting that Rydberg atoms that decay to the $5s5p\ ^3P_2\ m_J = +1, +2$ state may be trapped near the magnetic quadrupole centre.

The coupling laser is of high enough energy to drive atoms in the $5s5p\ ^3P_2$ state into the continuum, photoionising the atoms. It is not trivial to calculate the photoionisation

cross-section for the $5s5p\ ^3P_2$ state, which is dependent on the excess photon energy (the difference between the photon energy and the binding energy) of ∼9 THz for this state. [141] measures the photoionisation cross-section of the $5s5p\ ^3P_1$ state to be ∼11 Mb = 11×10^{-18} cm^2 for excess energies on this scale. If we treat this as the same for the $5s5p\ ^3P_2$ state, we can estimate a photoionisation rate for our coupling beam intensity. The photoionisation rate is given by [142]:

$$R(\omega) = \frac{I\sigma_\omega}{\hbar\omega} \ . \tag{6.4}$$

A peak coupling beam intensity of 180 W/cm^2, and a photon frequency of 940 THz corresponds to a photoionisation rate of ~ 2.9 ms^{-1} and a lifetime of ~ 300 µs, rising to 2.2 ms at the $1/e^2$ radius of the coupling beam. These numbers are consistent with the observed ion detection rate decay times of ~ 2 ms in the stable dressed MOT.

We have not attempted to calculate the probability of collisional ionsation of Rydberg atoms due to collisions with metastable atoms, but we note that [137], [138] and [139] all consider ionising collisions between Rydberg atoms and excited state atoms in modelling plasma seeding. If the ion detection rate in the stable MOT was due to collisions we may expect the ion detection rate to decay with the same rate as the atom number, ~ 5 ms, although if metastable state atoms are being lost from the trap, the detection rate may fall faster than this.

From this analysis it appears likely that some atoms excited to Rydberg states decay to magnetically trapped metastable states that can then be photoionised or result in collisional ionisation. This is a reasonable expectation of the system - we know that a large fraction of the cloud is lost to dark states, and only a small fraction of the lost atoms are converted to ions. Some atoms will be lost to long-lived Rydberg states, but we still expect a significant fraction of the dark state atoms to decay to metastable or longlived lowlying states, some of which can be magnetically trapped.

This effect could explain the large delay in seeding time observed in Figure 6.4 when the coupling beam is blue-detuned from the $5s36d\ ^3D_1$ state. If a reservoir of atoms is accumulated in the metastable state that may increase the ion production rate, either through collisions or photoionisation, the probability of seeding the plasma may rise with dressing time.

Regardless of the mechanism, the increased ion production rate due to metastable magnetically trapped atoms is not desirable as it increases the probability of plasma formation

and prevents us from studying the ions generated from the stable dressed MOT. Future experiments may use the 707 nm repump laser to depopulate the metastable state.

6.6 Slow ions

The final observed stage of the plasma is the ions that are detected well after the coupling laser has turned off, observed in Figure 6.1(d). Ultracold neutral plasmas can create long-lived high angular momentum Rydberg states through three-body recombination of ions and electrons and Rydberg-electron collisions [121, 133].

These longlived Rydberg atoms act as a probe of the plasma dynamics - the probability of recombination and collision are related to the electron density and the Rydberg atom density. If the feedback mechanism proposed in [139], in which Coulomb blockade limits the Rydberg excitation rate to the rate at which ions leave the cloud, occurs, we expect evidence of this to be apparent from the longlived Rydberg population.

Figure 6.11(a) shows the ion detection rate in the slow ion tail stage for two dressing times. Fitting an exponential to the slow ions we observe a lifetime and an initial ion detection rate from the y-intercept, shown in Figure 6.11(b-c). This has been repeated for a range of dressing times and initial atom numbers.

We see that the fitted peak ion detection rate, shown in Figure 6.11(c) rises until the plasma ceases. This rise is largely linear for the first 200 μs, which is consistent with a plasma charge density that is largely constant with time.

The rise is also fairly constant with initial atom number - there is an order of magnitude between the lowest ground state density (blue, 0.4 million atoms) and the highest ground state density (red, 3.6 million atoms), but there is never more than a factor of two between the ions in the tail until the plasma terminates. This is true apart from the first datapoint of 10 μs of dressing, at which point the plasma has not seeded at the lowest ground state density. This suggests the charge density within the plasma is largely independent of both ground state atom number and dressing time, consistent with the feedback mechanism proposed in [139].

The combination of a density dependent plasma lifetime and the largely density independent and linearly increasing number of long-lived Rydberg atoms populated during plasma formation are consistent with the feedback mechanism proposed in [139] but the data shown above is not sufficient to rule out all other possibilities. Further study may

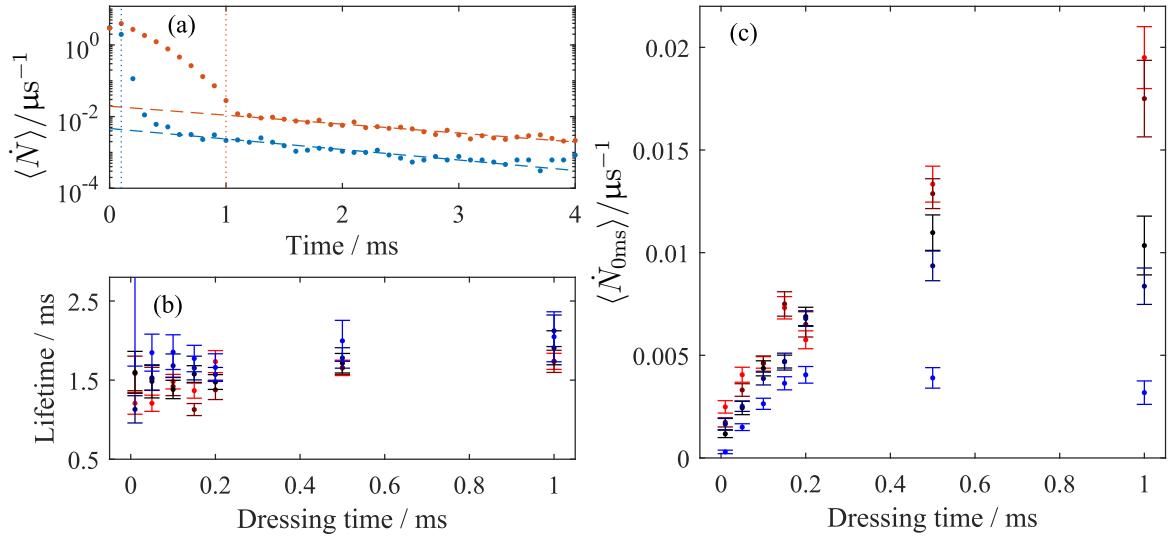

Figure 6.11: (a) Ion signals for a coupling laser turned off after 100 µs (blue) and 1 ms (orange) and an initial atom number of 3 million. We observe an exponential decay in ion detection rate after the coupling laser has turned off. Fitting to this (dashed lines), we obtain a lifetime (b) and an initial ion detection rate (c) as a function of the dressing time and the initial atom number. Colours indicate initial atom number, 0.4, 1.0, 1.4, 3.0 and 3.6 million atoms corresponding to blue, dark blue, black, brown and red respectively. Taken with $\delta_{\mathrm{MOT}} = -140$ kHz, $\mathrm{P}_{\mathrm{MOT}} = 80$ µW.

allow us to conclude the mechanisms that give rise to these phenomena.

The lifetime of the slow ions is consistently on the order of 1.5 ms, and may increase with dressing time, but we do not have the resolution to determine this with the available data. This lifetime may be a reflection of the range of lifetimes that will be populated through collisions and recombinations, alternatively, it could be an artefact of the dispersion of long-lived Rydberg atoms, which are not confined and may be much hotter than the trapped atoms.

We have not observed any increase in ion detection in response to the autoionising 408 nm laser during this stage, but for high angular momentum Rydberg states there is very little orbital overlap between the Rydberg state electron and the excited state of the second valence electron and we don't expect the ∼GHz broadening of the autoionising transition that occurs when coupling to low angular momentum states. A closer study using more careful autoionisation and/or field ionisation may reveal the range of principal quantum numbers and angular momentums states that the longlived Rydberg atoms have.

The ions detected after the coupling laser is turned off are a useful tool for studying the processes that occur during plasma formation. The data from these slow ions are consistent with a process that limits the Rydberg excitation rate to a constant level, regardless of ground state density, until the plasma disperses. This may be related to the density dependent plasma lifetimes observed in Figure 6.9.

Plasma results

So far in this chapter we have shown that during the rapid loss of trapped atoms we observe the formation of an ultracold neutral plasma. Studying the plasma dependence on coupling beam detuning, atomic density, and Rydberg state, we observe facilitated growth in Rydberg population due to both van der Waals and Coulomb interactions.

Within the plasma the high charge density DC Stark shifts the Rydberg state onto resonance with the coupling beam, resulting in strong Rydberg excitation and rapid loss of trapped atoms. Within the plasma, Rydberg atoms may be ionised, decay to metastable states, or be transferred to longlived Rydberg states. Signatures of all of these processes have been observed.

Having studied and understood the processes that give rise to plasma formation and evolution, we can now identify regimes in which plasma formation may be eliminated or suppressed.

6.7 Eliminating plasma-induced loss

To reach the Rydberg dressed interacting regime we must eliminate the plasma. We will consider three approaches to this. First, we describe how optimum choice of Rydberg state may avoid the Coulomb anti-blockade. Secondly, we consider the effect of an ion extracting electric field. Finally, we consider some techniques to increase the plasma threshold to the point that we can observe Rydberg dressed interactions.

The research group is now investigating these techniques, but a full study of these regimes is beyond the scope of this thesis.

6.7.1 Rydberg state selection

As explained in Section 2.3 the coupling laser must be detuned to the van der Waals blockade side of resonance to be in the Rydberg dressed regime. This results in the coupling beam being detuned to the Coulomb anti-blockade side of resonance for both the $5sns\ ^3S_1$ and $5snd\ ^3D_1$ Rydberg series, illustrated in Figure 6.12. This results in heavy loss of atoms during plasma formation. In the $5snd\ ^3D_2$ Rydberg series a Förster resonance at $5s37d\ ^3D_2$ results in repulsive van der Waals interactions below $n = 37$ and attractive van der Waals interactions above $n = 37$ in this Rydberg series. Consequently, in the $5sn_{<37}d\ ^3D_2$ series the van der Waals blockade and the Coulomb blockade occur on the same side of resonance, allowing us to Rydberg dress with red-detuned coupling light and avoid both van der Waals and Coulomb enhanced Rydberg excitation.

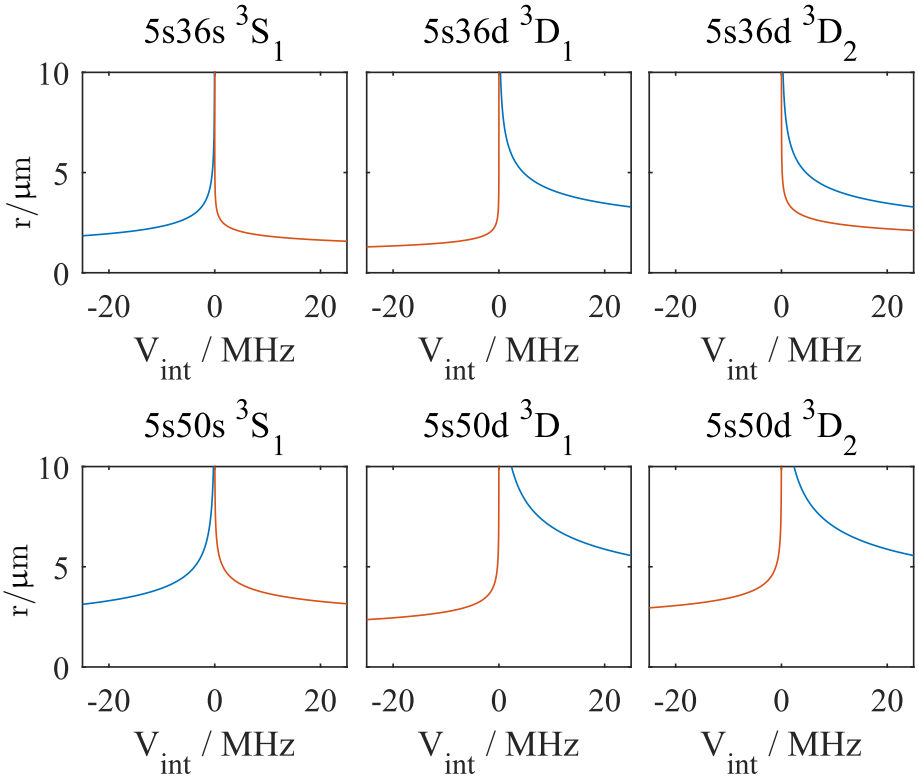

Figure 6.12: DC Stark shifts (blue) and van der Waals shifts (orange) for the three Rydberg series that we can strongly couple to from the $5s5p\ ^3P_1$ state at two principal quantum numbers. For the $5s\ n_{<37}d\ ^3D_2$ Rydberg series, the Coulomb anti-blockade and the van der Waals anti-blockade both occur on the blue-detuned side of resonance.

Given that the C_6 coefficients rise near a Förster resonance, the $5s36d\ ^3D_2$ state is the

most promising state for the observation of Rydberg dressing. For a predicted peak Rabi frequency of 4 MHz and a coupling beam detuning of $\delta_C = -12$ MHz we expect a two-body, dressed interaction potential of 18 kHz, corresponding to a cloud temperature of 0.9 μK. The predicted C_6 coefficient of 2.2 GHz μm^6 corresponds to a dressed blockade radius of 2.1 μm. For a typical atomic density of 10^{12} cm^{-3} and excited state fraction of 10% we can therefore expect up to 4 dressed atoms per dressed blockade sphere and a many-body interaction up to 6 times greater than the two-body interaction of 18 kHz.

These values compare very favourably to the temperatures and densities we can achieve in the Rydberg dressed MOT. In Section 5.4 we showed that compensating the AC Stark shift of the dressed state caused by a non-uniform coupling beam is challenging when coupling with red-detuned light, but an upgrade to the 319 nm coupling laser has increased the laser output power, allowing us to use a larger more uniform coupling beam to make it easier to compensate the resulting AC Stark shift on the MOT. In addition, the polarisation dependence of the coupling beam considered in Section 5.4 will be reduced by coupling to a $J = 2$ Rydberg state, as illustrated by Equation F.6 in Appendix F.

This is not the only route to Rydberg dressed interactions. We can attempt to observe Rydberg dressed interactions in a MOT dressed with a higher principal quantum number. As shown in Figure 2.12, the reduction in two-body Rydberg dressed interaction due to a lower Rabi frequency is more than compensated by the rise in dressed blockade radius, allowing us to reach the many-body interacting regime. The large C_6 coefficients and lower polarisabilities of the $5sns\ ^3S_1$ Rydberg series offer more promise than the d-state Rydberg series at high principal quantum number. However, the rising polarisability of Rydberg atoms with principal quantum number, a falling electron kinetic energy with principal quantum number and a coupling beam detuning that must fall with falling Rabi frequency to maintain a reasonable Rydberg dressed interaction strength, mean that the density at which the plasma terminates will fall sharply as the principal quantum number of the Rydberg state that we couple to rises.

The most promising path to observing Rydberg dressed interactions in the MOT is therefore Rydberg dressing the MOT with the $5s36d\ ^3D_2$ state. We expect to avoid plasma formation by avoiding the Coulomb anti-blockade and, in addition, the repulsive van der Waals interactions should reduce the collisional ionisation rate. We expect a two-body dressed interaction strength comparable to the cloud temperature, and up to 4 dressed state atoms per dressed blockade sphere.

6.7.2 Charge-extracting electric field

Another technique to prevent plasma formation is to apply an electric field to remove ions that result from spontaneously ionised Rydberg atoms and photoionised metastable state atoms. Plasma formation occurs when the number of ions in the cloud passes a threshold at which the Coulomb potential of the ions is greater than the kinetic energy of the electrons. The longer ions remain in the cloud, the more likely it is that this threshold will be reached.

Currently we rely on a stray electric field that we estimate as ~ 20 mV/cm to remove ions from the cloud. We can apply electric fields of up to 3.5 V/cm from the experimental control program, which will extract ions from the cloud in ~ 0.5 μs, rather than ~ 7 μs, potentially increasing the density that we can reach by a factor of 14. However, as we show in Section 5.5, applying an electric field causes significant perturbation to the cloud shape. This may inhibit the compensation of the AC Stark shift of the coupling beam. It may also reduce the coupling strength that the cloud experiences, as the Rabi frequency may be effectively split across transitions.

These issues are not insurmountable. A vertically applied electric field and a Regime I MOT, in which atoms experience a primarily vertical magnetic field, will ensure that both electric and magnetic field quantisation axes are the same. Use of a vertically polarised coupling beam will ensure maximum coupling strength.

A strength of this charge-extracting electric field technique is that it is applicable to a range of Rydberg states, rather than limiting the regime for which Rydberg dressed interactions can be observed to a single Rydberg state.

6.7.3 Increasing the plasma threshold

There are several techniques to increase the density at which plasma formation occurs. We can reduce the cloud size - the charge density at which plasma formation occurs is proportional to r_{MOT}^{-2}, so using a smaller MOT beam detuning and a larger magnetic field gradient may increase the density that we can reach before plasma formation occurs. Currently, the stability of the high-finesse cavity that we use to frequency stabilise the 689 nm laser limits the frequency stability of the laser to ~ 30 kHz, but the next generation of this experiment will have a new high-finesse cavity that will allow us to improve the frequency stability of the laser, potentially allowing us to work with MOT beam detunings

much closer to resonance.

We can also optimise the transfer efficiency into the single frequency red MOT. The density at which plasma formation occurs is dependent on MOT beam power - if we increase the transfer efficiency into the single frequency MOT we can use a lower MOT beam power, reaching a higher density without plasma formation occuring. We can increase the transfer efficiency by optimising the ramps in the magnetic field gradient and MOT beam power discussed in Section 3.2 and we may be able to use shelving of atoms in the $5s5p\ ^3P_2$ magnetically trapped metastable state to avoid the radiation pressure that limits the blue MOT density. We must be confident of recovering these atoms from the metastable state to avoid photoionisation or collisional ionisation.

We can also use repump lasers during Rydberg dressing to remove atoms from the metastable magnetically trapped $5s5p\ ^3P_2$ state. A build-up of atoms in this state may result in an additional source of ions, increasing the probability of plasma formation.

With a higher plasma threshold, filtering of results may allow us to remove shots in which plasma formation occurs, similar to the technique used to avoid resonant dipole-dipole seeding shown in [63].

A combination of these techniques, possibly in conjunction with optimum Rydberg state selection and ion extracting electric field, may allow us to observe Rydberg dressed interactions within the cloud without plasma formation.

6.8 Summary of plasma losses

In this chapter we set out to identify the cause of the catastrophic loss in atom number observed in the Rydberg dressed MOT whilst off-resonantly coupling to the $5s36d\ ^3D_1$ state. Through time-resolved ion detection we have observed $\sim 5\%$ of the ground state population being converted to ions on the same timescale of the loss in atom number, a clear threshold with ground state density, and sustained ion detection after the coupling laser is turned. From these results we conclude that this loss is associated with the formation of an ultracold neutral plasma.

Studying the regime in which this plasma exists we observe facilitated growth in Rydberg population that may be facilitated either by van der Waals interactions when red-detuned from the $5s36d\ ^3D_1$ or, at higher ground state density, by Coulomb interactions when blue-detuned. When coupling to the $5s37s\ ^3S_1$ state, for which the van der Waals and

Coulomb interactions occur with opposite signs to the $5s36d\ ^3D_1$ state, we still observe signatures of facilitated growth, but the repulsive van der Waals interactions do not result in high ionisation rates of pairs of Rydberg atoms observed whilst coupling to the $5s36d\ ^3D_1$ state.

The ions resulting from collisions and spontaneous ionisation are sufficient to bind electrons to the cloud, resulting in plasma formation. Within the plasma, charges DC Stark shift the $5s36d\ ^3D_1$ Rydberg state onto resonance with the blue-detuned coupling beam, resulting in a very strong enhancement of the Rydberg excitation rate. It is this enhancement that results in rapid depletion of ground state atoms. This is the first time this effect has been observed.

Curiously, the lifetime of the plasma rises with ground state density. Several mechanisms for this have been hypothesised in Appendix H, particularly the feedback mechanism between Rydberg excitation and plasma expansion proposed in [139], but it is an open question as to why this occurs. During the plasma formation, Rydberg atoms can decay to the metastable and magnetically trapped $5s5p\ ^3P_2$ state, which may either photoionise or collide with Rydberg atoms, resulting in ionisation. This decay to metastable magnetically trapped states is something that may create an additional ion production mechanism, potentially increasing the probability of plasma formation. We also observe long lived high angular momentum Rydberg states that spontaneously ionise with high probability and are detected after the coupling laser is turned off. These act as a probe of the processes occuring during plasma formation, and imply a charge density in the cloud that is largely constant with dressing time and ground state density, consistent with a feedback mechanism between plasma expansion and Rydberg excitation.

A combination of the different probes of the plasma processes (time-resolved spontaneous ionisation and autoionisation of Rydberg atoms, photoionisation/collisional ionisation of magnetically trapped metastable state atoms, spontaneous ionisation of long-lived high angular momentum state Rydberg atoms and ground state atom imaging) may allow us to thoroughly diagnose the mechanism through which the plasma lifetime rises with ground state density. However, for the purposes of a Rydberg dressed MOT, it is sufficient to conclude that where charges in the cloud result in Coulomb anti-blockade, plasma formation can result in massive depletion of ground state atoms.

Having considered a range of possible techniques to reach the Rydberg dressed interactions regime without plasma formation causing prohibitive loss, we believe that coupling

to the $5s36d\ ^3D_2$ state offers the greatest promise. Here we avoid the Coulomb anti-blockade that results in prohibitive loss, and expect up to four dressed atoms per dressed blockade sphere and interactions of up to six times greater than the cloud temperature.

Another promising route is the application of ion-extracting electric fields. There may be complications in such a system due to the combination of electric and magnetic fields and coupling beam polarisation, but appropriate choice of electric field axes and coupling beam polarisations should allow these complications to be addressed. This technique would be applicable across a range of Rydberg states.

Finally, there are techniques concerning the MOT itself. Reducing the MOT size and MOT beam power may both increase the density at which plasma formation occurs. Increasing the magnetic field gradient may have a similar effect. Removing magnetically trapped metastable state atoms may reduce the ionisation rate, reducing the probability of reaching the plasma threshold.

Chapter 7

Conclusion and outlook

This thesis presents Rydberg dressing in a narrow-line strontium MOT. This has required the development of a 319 nm laser, Rydberg spectroscopy on triplet Rydberg states, and a detailed characterisation of dressed MOT dynamics, allowing us to demonstrate sustained trapping and cooling of Rydberg dressed atoms. At high atom densities plasma formation causes loss of atoms, preventing observation of Rydberg dressed interactions.

In Chapter 2 we provide an introduction to Rydberg dressing. Mixing of Rydberg character into ground or excited 'dressed' states allows highly tunable interactions to be induced in the dressed state and has been demonstrated in one- and two-dimensional systems. By dressing the excited state of the narrow-line MOT transition we may combine the trapping and cooling of the MOT with the tunable interactions of Rydberg dressing. The interaction strengths are comparable to the cloud temperature and the interaction lengthscale is comparable to the dressed state separation. Such a system offers a versatile platform as a quantum simulator of dissipative many-body systems.

In Chapter 3 we describe the experimental apparatus, with emphasis on the changes made during the course of the experiment. The most significant changes relate to techniques to increase the transfer efficiency into the single frequency red MOT, and the ability to perform multiple Rydberg excitations per MOT with measurement of ion arrival times.

The 319 nm laser is presented in Chapter 4. This laser system is widely tunable across Rydberg states, generates up to 80 mW, and has a frequency stability of < 35 kHz. Using this laser, we have thoroughly characterised several Rydberg states, measuring Rabi frequencies, polarisabilities, Rydberg state lifetimes and autoionisation-cross sections. These Rydberg states are previously unstudied, and future work may involve a systematic

measurement of Rydberg state properties.

Coupling the MOT to the Rydberg state for a range of MOT beam and coupling beam parameters, we have thoroughly characterised the AC Stark shift of the $5s5p\ ^3P_1$ state due to dressing. This is shown in Chapter 5. To compensate the AC Stark shift of the MOT, we change the MOT beam detuning when we begin dressing to create a MOT that only traps Rydberg dressed atoms. This trap experiences initial heating when the coupling laser is turned on, before returning to its initial temperature. We believe this to be the first demonstration of trapping and cooling of atoms with Rydberg character. The Rydberg character of the trap is demonstrated by applying an electric field to the trap, observing changes in the cloud shape and position that are dependent on the electric field strength and direction; in this we also believe this to be the first MOT that is sensitive to electric field.

Increasing the dressed state density to reach the Rydberg dressed interactions regime, we observe formation of an ultracold neutral plasma due to build-up of charges from ionised Rydberg atoms. Within the plasma the high charge density results in a DC Stark shift that brings the Rydberg state onto resonance with the coupling laser, resulting in strong excitation to the Rydberg state and heavy depletion of ground state atoms. We believe that this enhancement of Rydberg excitation due to plasma formation has not been previously observed. This loss mechanism limits the Rydberg dressed MOT to a regime in which Rydberg dressed interactions are not observed, and may pose a barrier to observing Rydberg dressed interactions in large three-dimensional many-body systems. This is shown in Chapter 6.

The diagnostic of time-resolved spontaneous ion detection allows observation of multiple signatures of plasma formation, including rapid excitation and ionisation of Rydberg atoms, photoionisation/collisional ionisation of atoms that decay to metastable states and spontaneous ionisation of high angular momentum Rydberg states populated during plasma formation. In conjunction with autoionisation as a probe of Rydberg state and imaging of ground state atoms, we have established the tools to thoroughly study Coulomb enhanced Rydberg excitation within a plasma.

Curiously, the lifetime of the plasma and the cloud are dependent on the ground state density. This may be evidence of a limited Rydberg excitation rate due to the charge density. Further evidence of a Coulomb blockade effect within the plasma is observed through study of the longlived high angular momentum state Rydberg atoms, the population of

which increases largely linearly with dressing time in the plasma and independently of the ground state density, suggesting a constant charge density within the plasma. However, we do not identify the cause of this density dependent lifetime.

Having identified that DC Stark shifts due to ions in the cloud are responsible for the rapid decay in atom number we consider several mechanisms to avoid plasma formation. Appropriate choice of Rydberg state, specifically the $5s36d\ ^3D_2$ state with repulsive van der Waals interactions and a negative polarisability, may allow Rydberg dressing using red-detuned coupling light to avoid both the van der Waals anti-blockade and the Coulomb anti-blockade with two-body interaction strengths comparable to the cloud temperature and up to four dressed state atoms per dressed blockade sphere. Alternatively, the use of an ion extracting electric field may prevent ions accumulating in the cloud.

Outlook

From this work we have identified the regime in which Rydberg dressed interactions in a MOT may be observed, and work towards Rydberg dressed interactions in a Rydberg dressed MOT is ongoing. Optimum choice of Rydberg state has allowed the avoidance of plasma formation, but at the expense of weaker confinement of the cloud. A series of improvements to the 319 nm laser power, the 689 nm laser frequency stability and imaging of optically thick clouds may allow this weaker confinement to be overcome and Rydberg dressed interactions to be observed in the Rydberg dressed MOT.

The research group will also continue work on high precision Rydberg spectroscopy. Previous studies of singlet Rydberg state energy levels face challenges due to one-photon excitation being limited to Rydberg p-state series, and two-photon excitation being limited by the intermediate state linewidth. Two-photon excitation to Rydberg states via the narrow $5s^2\ ^1S_0 \leftrightarrow 5s5p\ ^3P_1$ transition allow very narrow spectra to be measured. In combination with a femtosecond optical frequency comb we believe we can measure Rydberg state energy levels with absolute accuracy on the order of kHz. A systematic study of Rydberg states across a wide range of principal quantum number will allow a detailed study of the quantum defects in strontium; the unprecedented precision with which this can be performed may allow strontium to become the workhorse of studies of quantum defects. Stark maps and autoionisation spectra of these Rydberg series may also enhance this study.

The rate at which this spectroscopy can be performed will be drastically accelerated with the addition of a dipole trap, which can be switched on and off much faster than the magneto-optical trap.

Dipole trapping of the cloud offers further benefits, and the next generation of the experiment contains lenses inside the vacuum chamber, allowing optical tweezers to be implemented. The Ti:Sapphire laser used for the dipole trap can cover magic wavelengths for both the $5s^2\ {}^1S_0 \leftrightarrow 5s5p\ {}^3P_1$ and the $5s^2\ {}^1S_0 \leftrightarrow 5s5p\ {}^3P_0$ transition, allowing trapping of longlived atoms that can be one-photon Rydberg dressed. This opens the potential of performing spin-squeezing proposed in [60] in a scaled up system.

The use of a divalent atom in optical tweezers opens several opportunities, for example, dipole trapping of a strontium Rydberg atom. By exciting one electron to a Rydberg state and using the AC polarisability of the atom due to the second valence electron we may optically trap Rydberg atoms.

We may also explore the potential for charge- and excitation-hopping in a single tweezer of atoms by exciting or photoionising an atom via singlet transitions in the presence of triplet state Rydberg atoms, which can then be probed through state- and position-dependent autoionisation.

Appendix A

Electronics

The new MOT coil circuit allows the current through the MOT coil to be set by two internal trimpots or an externally applied voltage, allowing the current through the coil to be smoothly ramped to increase the transfer efficiency between the blue MOT and the broadband red MOT. The circuit has been largely successful, although a small offset that occurs between the circuit ground and the power supply ground results in a short (< 1 ms) delay in the MOT coil turning on if it has been off for more than a few milliseconds. This delay is negligible given the typical blue MOT loading times (> 40 ms). The previous circuit had the same issue, but with the opposite polarity, resulting in the coil never fully turning off (always passing ~ 5 mA, compared to a typical running current of $0.8 - 2.5$A).

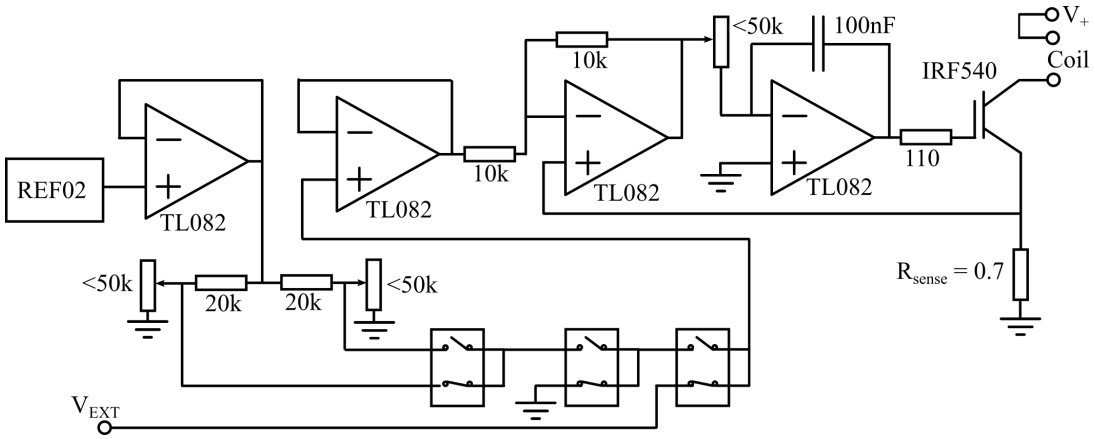

Figure A.1: The MOT coil circuit.

Appendix B

Momentum space crystals

A novel feature of the narrow transition is the existence of momentum-space crystals [81]. If the MOT beams are blue-detuned, rather than cool the atoms they can accelerate the atoms away from the centre of the cloud. This only occurs if the MOT beam frequency is close enough to the Doppler shifted resonance of an atom for an initial scattering event to occur, and every scattering after this results in a Doppler shift that increases the probability of further scattering. This effect saturates once the Doppler shift significantly exceeds the MOT beam detuning; at this point scattering is suppressed. It is therefore possible to choose a MOT beam detuning slightly greater than the cloud temperature, such that a fraction of the atoms will scatter from each MOT beam, and a fraction of the slowest atoms will not scatter. The atoms that scatter photons will be accelerated into discrete velocity classes set by the MOT beam detuning and power, these velocity classes then expand in a face-centred cubic crystal formation.

This has been demonstrated in [81] in three dimensions. In Figure B.1 we demonstrate one-dimensional momentum-space crystals. We use a retroreflected probe beam with a $1/e^2$ radius of 0.5 mm and a power of 1.6 μW, corresponding to a peak intensity of 130 I_{SAT} and a power broadened linewidth of 80 kHz. Despite this relatively large linewidth, we can observe changes in the cloud due to changes in laser frequency of 20 kHz. This offers a very visual representation of the effect of narrow transitions on cloud dynamics, and confirms that frequency shifts of 20 kHz, comparable to the expected cloud interaction strength, are resolvable in the cloud.

The detuning is taken from the $5s5p\ ^3P_1\ m_J = +1$ transition in the presence of a 2.5 G uniform magnetic field provided by the quantisation coil. The probe beam is mounted

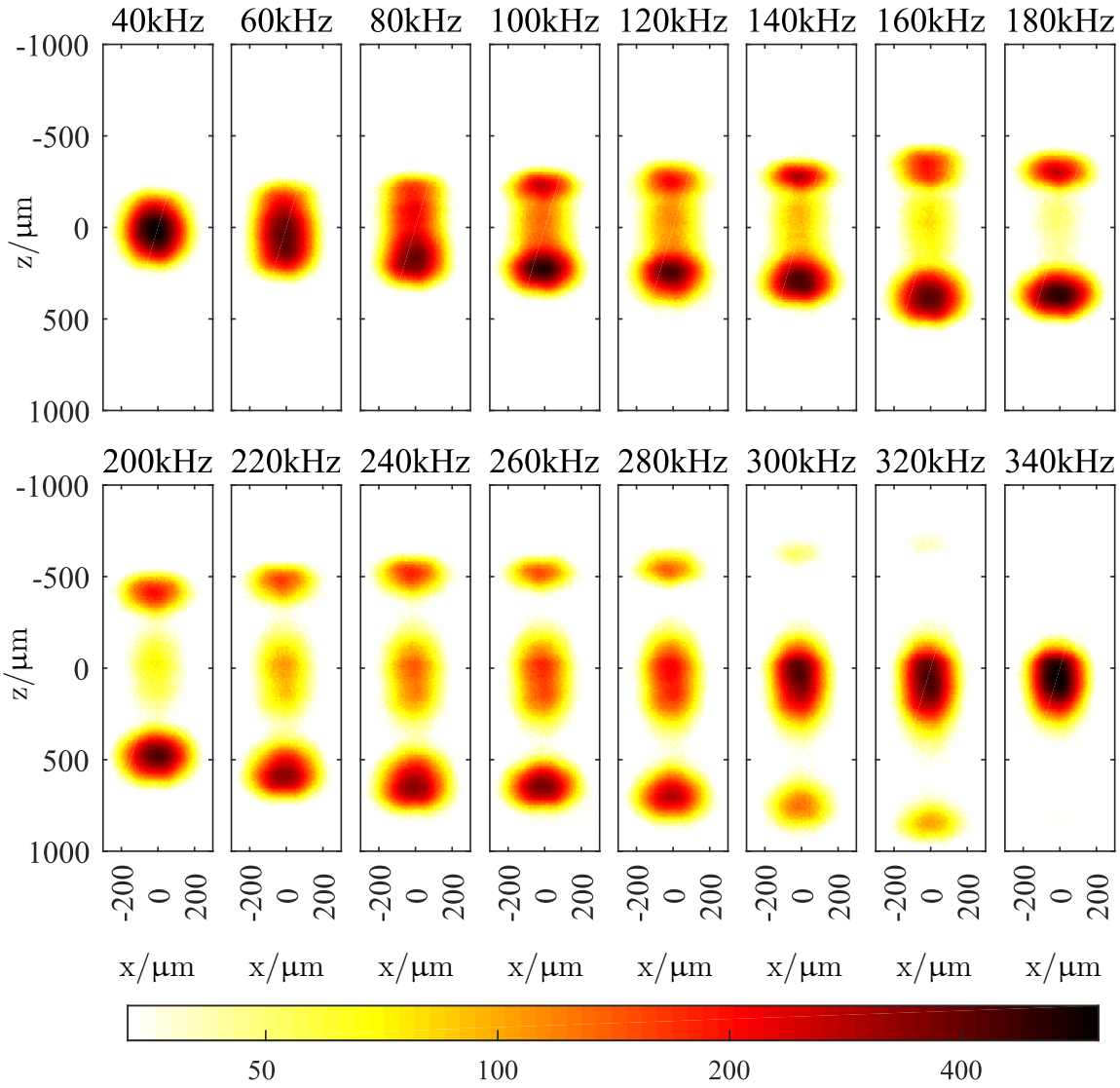

Figure B.1: One-dimensional momentum space crystals, taken with 2 ms of probe light and 5 ms of expansion time. With each 20 kHz step, the final atom distribution evolves - the velocity of the expanding sites increases with detuning, resulting in greater displacement of the position of the sites, whilst the fraction of atoms that are in the expanding sites falls until all the atoms occupy the central site. The atoms preferentially occupy the lower site relative to the upper site, due to gravity and a slight divergence in the retroreflected probe beam. The colourbar shows pixel fluorescence count. Above each image the detuning from the $5s5p\ ^3P_1\ m_J = +1$ transition is shown.

on the vertical axis pointing down, and is retroreflected. The beam is slightly diverging, so the upward beam is ∼20% less intense than the downward beam. The combination of lower intensity and the effect of gravity accelerating the atoms down result in atoms preferentially occupying the velocity class that moves downwards than upwards.

Whilst momentum-space crystals can occur in theory on broad transitions, the difference in velocities of the different sites are impractically large, and they are not practical to observe experimentally.

Appendix C

Observation of eddy currents

A significant improvement to the datataking rate of the experiment is a new oscilloscope that allows us to perform multiple Rydberg excitations within a single MOT. As discussed in Chapter 3 we can either retrap the MOT between Rydberg excitations or perform consecutive Rydberg excitations.

When performing consecutive Rydberg excitations we observe a shift in the resonance feature with excitation number. This has been observed by scanning the probe beam frequency across resonance whilst performing a two-photon excitation to the $5s37s\ ^3S_1$ state and separating the spectra by excitation number. We see the $5s5p\ ^3P_1\ m_J = -1\ (+1)$ shifting to lower (higher) frequency with excitation number. The symmetry of the shift points to this being an effect of magnetic field increasing in magnitude.

To identify the source of this shift we have performed a series of comparable experiments, varying the delay between excitation pulses, the delay between turning the quantization coil on and the first excitation, the delay between turning the MOT coil off and the first excitation, and also how long the atoms have to freefall for before beginning excitation, shown in Figure C.1. We scan the probe beam across resonance for low probe and coupling beam power, and fit the spectra, plotting the feature centre as a function of time between excitation and the freefall time t_{Freefall}, MOT coil switching time $t_{\mathrm{MOTswitch}}$ and quantization coil switching time t_{Qswitch}.

From the results, we can clearly see a correlation between the centre of the feature and how long the quantization coil has been on for. This suggests that the magnetic field experienced by the atoms continues to increase for several milliseconds after the current running through the coil has settled.

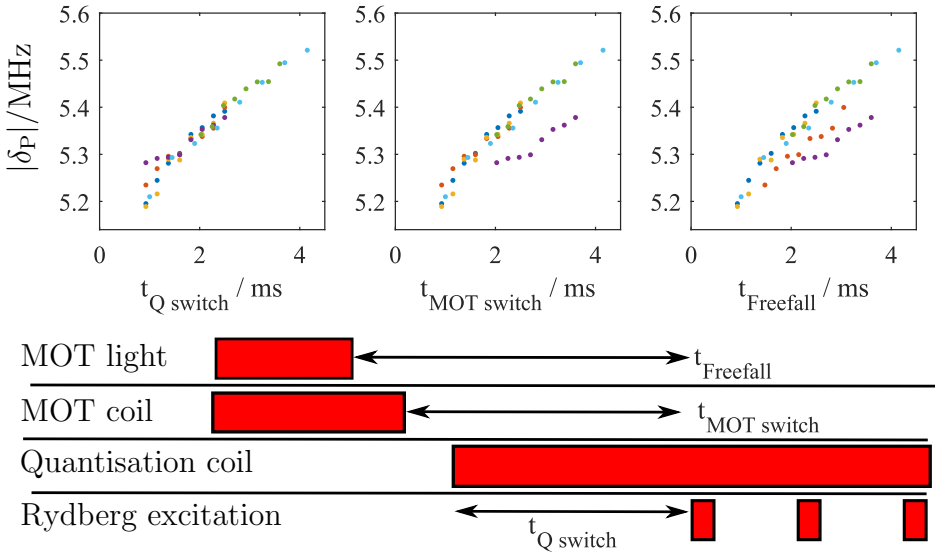

Figure C.1: By varying the delay between Rydberg excitation and the quantisation coil turning on, $t_{Qswitch}$, the MOT coil turning off, $t_{MOTswitch}$, and when the trap no longer operates, $t_{Freefall}$ (either because the MOT coil or MOT light is turned off), and measuring the resulting shift of the $5s5p\ ^3P_1\ m_J = -1$ state δ_P, we identify the shift as caused by the quantisation coil. Different colours indicate different experimental datasets.

Two different coil drivers have been used to drive current through the quantisation coil. One actively stabilises the current through the coil using a sense resistor in series with the coil and a PI feedback loop, the other applies a constant voltage to a MOSFET that sets the current flow through the coil. The effect shows no dependence on the driver.

We believe the effect is caused by eddy currents induced inside the vacuum chamber when the quantization coil turns on. Eddy currents oppose the magnetic field applied by the quantization coil, and as they die away the magnetic field at the atoms rises. The quantization coil sits ~ 3 cm beneath a 20 cm diameter copper gasket, this is the probable source of quantization coil induced eddy currents.

The effect is weak; a 300 kHz shift in 3 ms suggests a magnetic field change of around 150 mG, compared to the bare magnetic field of around 2.6 G. It is too weak to have been observed when performing singlet state Rydberg excitations via the broad $5s5p\ ^1P_1$ intermediate state. However, it is sufficient to inhibit performing multiple consecutive Rydberg excitations within a single MOT. This issue does not affect the retrapping technique, as the quantisation coil is switched off between Rydberg excitation.

Appendix D

Ion statistics

A powerful tool when studying quantum mechanics is the statistics of experimental repetitions. Statistical tools such as the correlation function ($g^{(2)}$) and the Mandel Q parameter can be used to observe correlations between signals and deviation from Poissonian statistics as indicators of interactions such as Rydberg blockade and facilitated growth. We measure the Poissonian nature of ion statistics using the Mandel Q parameter:

$$Q_X = \frac{\mathrm{Var}(X)}{\langle X \rangle} - 1 \ , \tag{D.1}$$

where the variance and mean of X are given by $\mathrm{Var}(X)$ and $\langle X \rangle$. $Q < 0$ indicates sub-Poissonian ion statistics, $Q > 0$ indicates super-Poissonian statistics.

Within this experiment we have not previously observed sub-Poissonian ion statistics. This is attributed to a combination of laser frequency noise on the 461 nm laser and the 413 nm laser used for Rydberg excitation, which can result in super-Poissonian ion statistics [85], and the low ion detection efficiency, which brings the ion statistics closer to a Poissonian statistics. By using 689 nm and 319 nm light with power broadening much greater than the observed laser frequency noise we can suppress the effect of laser noise. However, we must also consider the effect of atom number variation.

We typically trap on the order of 1 million atoms in the cloud. We typically observe standard deviations of up to 300,000 on an atom number of 1 million[a], and do not expect

[a]This is a worst-case scenario, with a poorly locked 689 nm laser due to cavity drift and a small MOT beam detuning, resulting in high sensitivity to 689 nm laser noise. Typically the atom number is more stable than this, particularly in broadband MOTs.

the atom number to follow Poissonian statistics. Expressing the fractional standard deviation in atom number ϵ_{atom} from the atom number $\langle N_{\text{atom}} \rangle$ and the standard deviation σ_{atom}:

$$\epsilon_{\text{atom}} = \frac{\sigma_{\text{atom}}}{\langle N_{\text{atom}} \rangle} \ ; \tag{D.2}$$

and noting that $\text{Var}(N_{\text{atom}}) = \sigma^2_{\text{atom}}$ we can express the Mandel Q parameter of the atom number as:

$$Q_{\text{atom}} = \frac{\sigma^2_{\text{atom}}}{\langle N_{\text{atom}} \rangle} = \epsilon^2_{\text{atom}} \times \langle N_{\text{atom}} \rangle \ . \tag{D.3}$$

If the probability of ionising an atom and detecting an atom are both Poissonian and described by $\text{P}_{\text{ionise}} \times \text{P}_{\text{detect}}$, the Mandel Q parameter of the detected ions is then given by:

$$Q_{\text{ion}} = Q_{\text{atom}} \times \text{P}_{\text{ionise}} \times \text{P}_{\text{detect}} = \epsilon^2_{\text{atom}} \times \langle N_{\text{atom}} \rangle \times \text{P}_{\text{ionise}} \times \text{P}_{\text{detect}} \ . \tag{D.4}$$

Given that the number of detected ions is given by $\langle N_{\text{ion}} \rangle = \langle N_{\text{atom}} \rangle \times \text{P}_{\text{ionise}} \times \text{P}_{\text{detect}}$ we can therefore express the expected Q parameter of the ions, assuming Poissonian Rydberg excitation and detection, as:

$$Q_{\text{ion}} = \epsilon^2_{\text{atom}} \times \langle N_{\text{ion}} \rangle \ . \tag{D.5}$$

This simple expression allows us to understand the role that atom number fluctuations play in ion statistics. The super-Poissonian atom number will give rise to super-Poissonian ion statistics and a Mandel Q parameter that is proportional to the ion number - the worst-case scenario of $\epsilon_{\text{atom}} = 0.3$ will therefore give rise to a Mandel Q parameter of $0.09 \times \langle N_{\text{ion}} \rangle$ attributable to atom number variation. Deviation from this Mandel Q parameter will indicate deviation from Poissonian Rydberg excitation and detection.

The same argument is true for ion numbers that are binned into discrete timesteps using the ion arrival times. In this case we expect:

$$Q_{\dot{\text{N}}_{\text{ion}}} = \epsilon^2_{\text{atom}} \times \langle \dot{N}_{\text{ion}} \rangle \times \Delta T \ . \tag{D.6}$$

where ΔT is the width of the discrete timestep - when considering counting statistics we must use the number of ions detected within the timestep, not the rate of ion detection. This approach to ion statistics has been verified through simple statistical modelling as part of this work.

Note that this only considers changes in atom number. The cloud width is proportional to the MOT beam detuning, so, for small MOT beam detunings, fluctuations in MOT beam frequency may cause variation in cloud size and therefore density even for constant atom number. This will not affect the Mandel Q parameter for independently excited Rydberg atoms, but may modify ion statistics if there are density dependent effects.

An ion number (detection rate) Mandel Q parameter that is greater than $\epsilon_{\mathrm{atom}}^2 \times \langle N_{\mathrm{ion}} \rangle$ ($\epsilon_{\mathrm{atom}}^2 \times \langle \dot{\mathrm{N}}_{\mathrm{ion}} \rangle \times \Delta T$) indicates super-Poissonian Rydberg excitation or ionisation. A Mandel Q parameter below this indicates either sub-Poissonian Rydberg excitation or ionisation, or saturation of the MCP. Total saturation of the MCP will allow the Mandel Q parameter to fall as low as $Q_{\mathrm{ion}} = -1$, whilst total Rydberg blockade may eliminate the effect of fluctuations in atom number but will still not allow the Mandel Q parameter to drop below the detector efficiency i.e. the lowest Mandel Q parameter that may be observed due to Rydberg blockade is $Q_{\mathrm{ion}} = -0.2$ for a detection efficiency of 20%.

With this understanding of the role of super-Poissonian atom number variation on the ion detection number and the ion detection rate, we can study the ion statistics of the ion detection rate considered in Chapter 6 and distinguish between changes in Mandel Q parameter due to atom number fluctuation, detector saturation and Rydberg excitation.

Appendix E

UV laser sidebands

During the characterisation of the UV laser we have observed very weak sidebands at ±20 MHz. We believe a very small fraction of frequency modulated 638 nm light is being frequency-summed with unmodulated light. An EOM in the frequency doubling cavity applies sidebands to the 638 nm light at ±20 MHz for PDH locking, and we have spectrospically observed very weak resonances at ±20 MHz from a strong resonance.

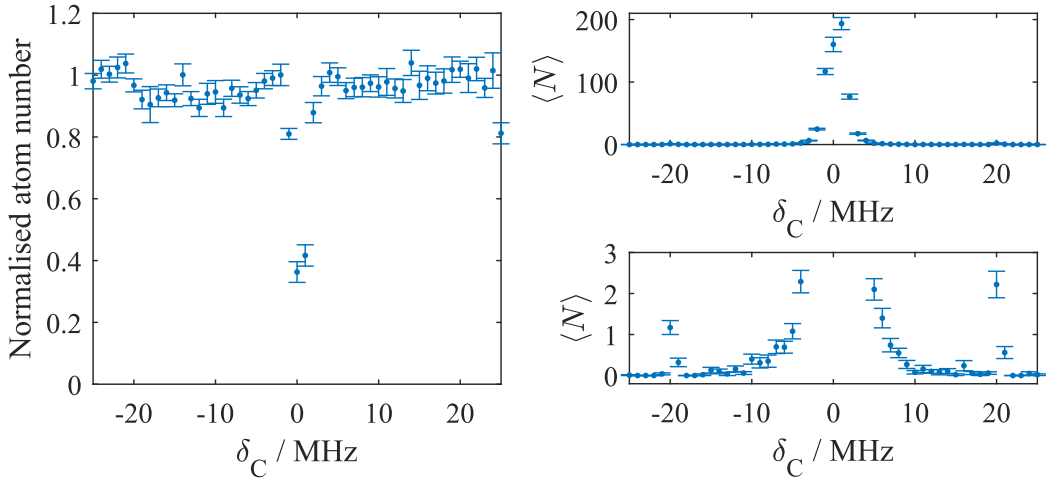

Figure E.1: Observation of weak sidebands at ±20 MHz to the main carrier frequency. On resonance we see depletion and a large ion signal that reduces with excitation number, at ±20 MHz of the main feature we also see very small ion signals that are attributed to a small fraction of frequency modulated light in the doubling cavity being doubled.

Figure E.1 shows spectroscopic observation of sidebands on the coupling beam. A coupling power of 3.5 mW was used, with 5 excitations lasting 300 us followed by a 20 us

autoionising pulse and a 5 µs electrode pulse. We retrap the cloud between Rydberg excitation and couple to the $5s37s^3S_1$ state. This is sufficient to cause significant depletion on resonance and heavily saturate the MCP, with several hundred ions detected, and a much stronger ion signal on the first excitation in the MOT. We see features two orders of magnitude smaller than the central feature at a detuning of 20 MHz either side of resonance. This two orders of magnitude estimate is very rough, as we do not have a reliable understanding of our detection efficiency for such large ion numbers, we deplete the cloud on resonance, and interaction effects on resonance may influence our atom number. However, as an order of magnitude estimate we can be confident that the intensity of this sideband light is very low compared to the main frequency.

Appendix F

MOT beam resonance with dressed states

In Chapter 5 we document the effect of coupling the MOT to the Rydberg state, with particular consideration given to the AC Stark shifted resonance condition. Initially we consider the AC Stark shift as purely dependent on the coupling beam intensity profile, the coupling beam peak Rabi frequency and the coupling beam detuning, which shows good agreement with the dressed MOT shape when using large MOT beam detunings, shown in Figures 5.5 and 5.6.

However, this approach breaks down for small MOT beam detunings and strong perturbations due to the coupling beam. In this appendix we will:

- Consider the role of coupling beam polarisation relative to local magnetic field with regards to what transitions the coupling beam can drive.
- Illustrate a simple modification to the AC Stark shifted resonance model to reflect this effect.
- Consider the validity of this approach in regimes of strong coupling by solving for the eigenvalues and eigenstates of the Hamiltonian of the coupled system and compare this to data.

The role of coupling beam polarisation relative to local magnetic field

In Section 4.4.1 we measured Rabi frequencies of Rydberg transitions with vertical coupling beam polarisation and a vertical quantisation axis, driving π transitions. In Regime I MOTs the cloud sags under gravity to the resonance curve, and predominantly experience a vertical magnetic field, allowing us to treat the coupling beam Rabi frequency as equal to that which we measured.

However, if the coupling beam polarisation is not aligned parallel to the magnetic field, we may also drive $\sigma^{\pm}$ transitions, and reduce the strength with which we drive π transitions, as illustrated in Figure 4.5(b). As we move closer to Regime II MOTs we increase the range of magnetic field directions that the cloud experiences. In the wings of the MOT atoms experience a horizontal magnetic field, whilst the coupling beam polarisation remains vertically polarised. Under these conditions, we consider the coupling beam polarisation to be a linear combination of left-hand circularly and right-hand circularly polarised light, capable of driving $\sigma^{\pm}$ transitions.

A generalised case considers the coupling beam polarisation as a combination of light that is polarised parallel to the quantisation axis $E_{\parallel}$ and light that is polarised perpendicular to the quantisation axis $E_{\perp}$ in terms of the angle θ between the vertical coupling beam polarisation and the local magnetic field:

$$\boldsymbol{E} = \begin{bmatrix} E_{\parallel} \\ E_{\perp} \end{bmatrix} = \begin{bmatrix} E_0 \cos\theta \\ E_0 \sin\theta \end{bmatrix} = \begin{bmatrix} E_0 \; 2z/\sqrt{r^2+4z^2} \\ E_0 \; r/\sqrt{r^2+4z^2} \end{bmatrix} \; . \tag{F.1}$$

Here $r^2 = x^2 + y^2$ is the position of the atom in the x-y plane and the origin is the quadrupole field centre. The factor of 2 before z reflects the stronger magnetic field in the vertical direction. This expression does not consider the coupling beam intensity profile.

We now consider what transitions the coupling beam can drive. The $E_{\parallel}$ component can drive π transitions, driving from the $5s5p\ ^3P_1\ m_J = -1$ state to the $5snl\ ^3l_1\ m_J = -1$ state. The strength with which the transition can be driven will be reduced by a factor $2z/\sqrt{r^2+4z^2}$ compared to the conditions under which the transition strength was measured i.e. with a coupling beam polarisation parallel to the quantisation axis.

The $E_{\perp}$ component, being comprised of $1/\sqrt{2}$ LHC and $1/\sqrt{2}$ RHC polarised light, can drive both σ^+ and σ^- transitions, but for $l = 1$ Rydberg states there is only the σ^+

transition to the $5snl\ ^3l_1\ m_J = 0$ transition that can be driven. The transition strength will therefore be reduced both by the factor of $r/\sqrt{r^2+4z^2}$ that reflects the component of the light that is polarised perpendicular to the quantisation axis and by a further factor of $1/\sqrt{2}$ that reflects that only part of this light can drive the transition[a]. The two Rabi frequencies Ω_π and Ω_{σ^+} of the two transitions can thus be expressed in terms of the measured Rabi frequency Ω_{meas} and horizontal and vertical position r and z:

$$\Omega_\pi = \Omega_{\text{meas}}\ 2z/\sqrt{r^2+4z^2}\ ; \tag{F.2}$$

$$\Omega_{\sigma^+} = \Omega_{\text{meas}}\ r/\sqrt{2(r^2+4z^2)}\ . \tag{F.3}$$

A modified AC Stark shift model

A rigerous analysis of the two transitions with two Rabi frequencies Ω_π and Ω_{σ^+} would consider the coherences between the states that can be driven, which are considered later. At this point we ignore these coherences, and treat the transitions as independent. We then consider the AC Stark shift of the $5s5p\ ^3P_1$ state that these couplings induce independently, and sum them. The AC Stark shift, subject to $\Omega \ll \delta$, is given by $\Omega^2/4\delta$. As the Zeeman shift of the two Rydberg states is small compared to the coupling beam detuning, we treat δ as the same for both transitions. We can therefore express the combined AC Stark shift due to the two transitions as:

$$\delta_{\text{AC}} = \frac{\Omega_\pi^2}{4\delta} + \frac{\Omega_{\sigma^+}^2}{4\delta} = \frac{\Omega_{\text{meas}}^2}{4\delta}\left[\frac{4z^2}{r^2+4z^2} + \frac{r^2/2}{r^2+4z^2}\right] = \frac{\Omega_{\text{meas}}^2}{4\delta}\left[1 - \frac{r^2/2}{r^2+4z^2}\right]\ . \tag{F.4}$$

This treatment allows us to use a simple analytical term to express the AC Stark shift that a vertically polarised uniform intensity coupling beam will introduce to the MOT, accounting for the angle between the quantisation axis of the local magnetic field and the polarisation of the coupling beam.

We now introduce the coupling beam intensity profile, described in terms of the $1/e^2$ radii ω_x and ω_z as $\exp(-2(x-x_0)^2/\omega_x^2 - 2(z-z_0)^2/\omega_z^2)$, to this term to obtain:

[a]This treatment uses the fact that all allowed transitions from the $5s5p\ ^3P_1\ m_J = -1$ state to the $5snl\ ^3l_1\ m_J$ states are equally allowed. If we couple to the $5snd\ ^3D_2$ Rydberg series we must account for the different coupling strengths between different sublevels.

$$\delta_{\mathrm{AC}} = \frac{\Omega_{\mathrm{meas}}^2}{4\delta} \exp\Big(-2\frac{(x-x_0)^2}{\omega_x^2} - 2\frac{(z-z_0)^2}{\omega_z^2}\Big)\Big[1 - \frac{r^2/2}{r^2+4z^2}\Big] \,. \tag{F.5}$$

For $z \gg r$ i.e. Regime I and III MOTs that experience predominantly vertical magnetic fields, we obtain the result shown in Equation 5.1 where we neglect the effect of quantisation axis for MOTs.

This modified expression for the AC Stark shift of the Rydberg-dressed $5s5p\ ^3P_1\ m_J = -1$ transition can then be used in Equation 5.2 to calculate a new resonance curve that accounts for the coupling beam polarisation relative to the local magnetic field. To simplify this expression we typically consider the x-z plane through the origin, by setting $y = 0$ such that $r = x$.

We compare the resonance curves generated through this approach to data in Figure 5.8, observing good agreement between the cloud shape and the resonance curves.

The effect of the changing quantisation axis is to reduce the coupling strength of the cloud where the coupling beam polarisation is not parallel to the quantisation axis. Atoms in the wings of the MOT will couple less to the $5snl\ ^3l_1\ m_J = -1$ Rydberg state and more to the $5snl\ ^3l_1\ m_J = 0$ Rydberg state. As we want to maximise the coupling strength in the position that the atoms predominantly occupy, which corresponds to a vertical magnetic field, a vertically polarised coupling beam is optimum.

If we couple to the $5snd\ ^3D_2$ Rydberg series, the different coupling strengths for different magnetic sublevel transitions result in slightly stronger coupling where the coupling beam polarisation and the magnetic field direction are orthogonal, as the strongest coupling from the $5s5p\ ^3P_1\ m_J = -1$ state occurs when coupling to the $5snd\ ^3D_2\ m_J = -2$ state, and we obtain:

$$\delta_{\mathrm{AC}} = \frac{\Omega_{\mathrm{meas}}^2}{4\delta} \exp\Big(-2\frac{(x-x_0)^2}{\omega_x^2} - 2\frac{(z-z_0)^2}{\omega_z^2}\Big)\Big[1 + \frac{r^2/6}{r^2+4z^2}\Big] \,. \tag{F.6}$$

Strong perturbations due to the coupling beam

The treatment described above assumes that we can treat the two transitions independently and sum the AC Stark shifts that result from the two transitions. It also assumes that the sublevels of the $5s5p\ ^3P_1$ states are defined purely by the local magnetic field. This treatment breaks down in some regimes. For example, under a vertical quantisation axis, and vertically polarised coupling, the $5s5p\ ^3P_1\ m_J = \pm 1$ states experience both

Zeeman shifts and AC Stark shifts, whilst the $5s5p\ ^3P_1\ m_J = 0$ state experiences neither. There can therefore be parameters (e.g. when coupling with blue-detuned coupling light) where the above treatment would predict the $5s5p\ ^3P_1\ m_J = 0$ state being lower in energy than the $5s5p\ ^3P_1\ m_J = -1$ state.

To address this we construct a Hamiltonian to describe the three sublevels of the $5s5p\ ^3P_1$ state and the three sublevels of the $5snl\ ^3l_1$ state, and the coupling between states Ω_π and Ω_σ. The full Hamiltonian is given by:

$$H = \begin{bmatrix} -B_P & 0 & 0 & \Omega_\pi/2 & \Omega_\sigma/2 & 0 \\ 0 & 0 & 0 & \Omega_\sigma/2 & 0 & \Omega_\sigma/2 \\ 0 & 0 & B_P & 0 & \Omega_\sigma/2 & \Omega_\pi/2 \\ \Omega_\pi/2 & \Omega_\sigma/2 & 0 & -B_D - \delta_C & 0 & 0 \\ \Omega_\sigma/2 & 0 & \Omega_\sigma/2 & 0 & -\delta_C & 0 \\ 0 & \Omega_\sigma/2 & \Omega_\pi/2 & 0 & 0 & B_D - \delta_C \end{bmatrix}, \tag{F.7}$$

where the Zeeman shift of the $5s5p\ ^3P_1\ m_J = \pm 1$ magnetic sublevels are given by $\pm B_P$, the Zeeman shift of the $5s36d\ ^3D_1\ m_J = \pm 1$ magnetic sublevels are given by $\pm B_D$ and the coupling beam detuning is given by δ_C. The Rabi frequencies are given by:

$$\Omega_\pi = \Omega_{\text{meas}} \exp\Big(- \frac{(x - x_0)^2}{\omega_x^2} - \frac{(z - z_0)^2}{\omega_z^2} \Big) \frac{2z}{\sqrt{r^2 + 4z^2}}\ ; \tag{F.8}$$

$$\Omega_\sigma = \Omega_{\text{meas}} \exp\Big(- \frac{(x - x_0)^2}{\omega_x^2} - \frac{(z - z_0)^2}{\omega_z^2} \Big) \frac{r}{\sqrt{2(r^2 + 4z^2)}}\ . \tag{F.9}$$

Solving this numerically for $\Omega_{\text{meas}} = 3.7$ MHz, $\delta_C = 12$ MHz, dB/dz = 8 G/cm and $y = 0$ for the x-z plane, we obtain six eigenvalues, labelled (a) to (f) from smallest to largest in Figure F.1. Far from the coupling beam three eigenvalues primarily correspond to the $5s5p\ ^3P_1$ sublevels, and the other three to the $5s36d\ ^3D_1$ sublevels. All are Zeeman shifted accordingly. We see eigenstate (d), which is largely comprised of the state $5s5p\ ^3P_1\ m_J = -1$ far from the coupling beam, rise in energy nearer the quadrupole field but then level off near the centre of the quadrupole field. By contrast, eigenstate (e), which is largely comprised of the state $5s5p\ ^3P_1\ m_J = 0$ far from the coupling beam, does not experience a Zeeman shift far from the coupling beam, but near the coupling beam is shifted to higher energy.

To understand this effect we consider eigenvectors of these eigenstates. We are primarily

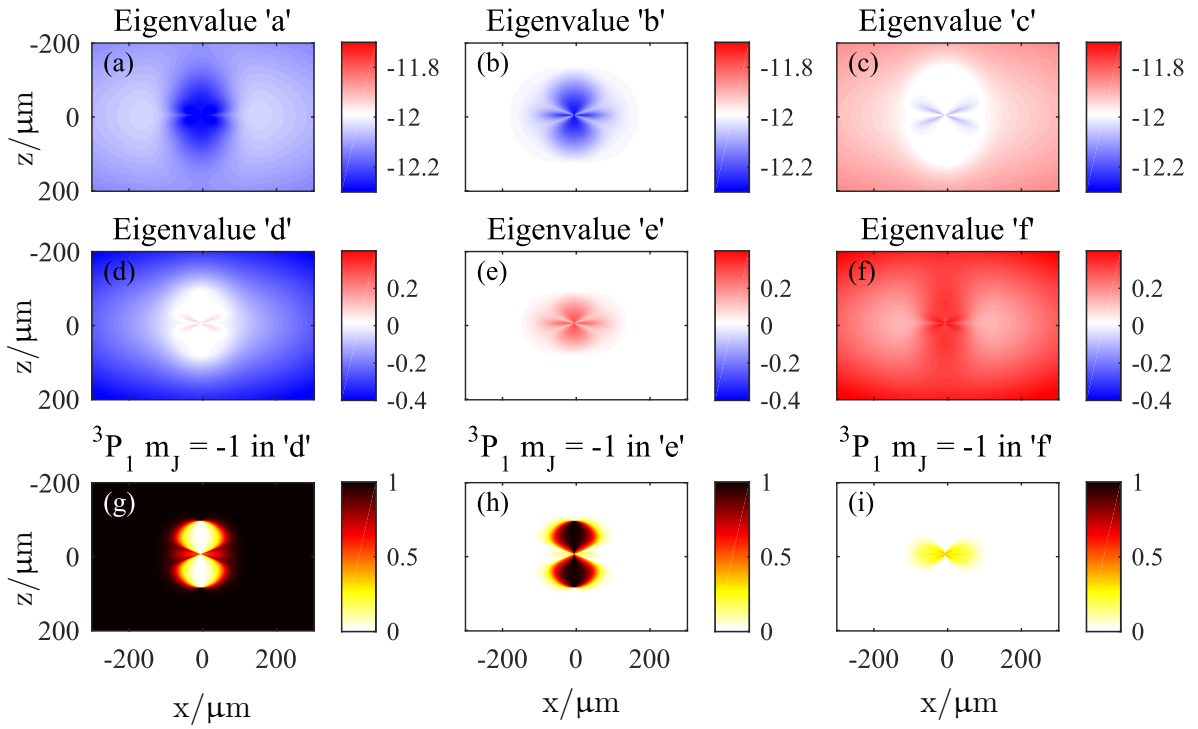

Figure F.1: Dressed MOT eigenvalues as a function of position, sorted from smallest to largest. (a) to (c) primarily correspond to the Rydberg state magnetic sublevels, (d) to (f) primarily correspond to the $5s5p\ ^3P_1$ magnetic sublevels. However, at the centre of the coupling beam we observe (d) flatten, rather than rising in energy near the quadrupole field centre, and (e), which previously was static, rising in energy near the quadrupole field centre. This is due to a change in the fraction of the $5s5p\ ^3P_1\ m_J = -1$ and $5s5p\ ^3P_1\ m_J = 0$ components of the the eigenstates, illustrated in (g-i).

interested in the $5s5p\ ^3P_1\ m_J = -1$ state as this is the state that the MOT beams drive to, we therefore show the $5s5p\ ^3P_1\ m_J = -1$ component of the three eigenstates (d-f) in Figure F.1(g-i).

Far from the coupling beam eigenstate 'd' predominantly contains the $5s5p\ ^3P_1\ m_J = -1$ state. For strong coupling, the fraction of $5s5p\ ^3P_1\ m_J = -1$ state in eigenstate 'd' falls and rises in eigenstate 'e'. This reflects the fact that there is an eigenstate that under these conditions falls in energy in response to magnetic field, but is increased in energy by the AC Stark shift by more than the Zeeman shift, rising above an eigenstate that is not sensitive to magnetic field and is not AC Stark shifted. As a result there is an eigenstate 'e' that is higher in energy than eigenstate 'd' but predominantly contains the bare state $5s5p\ ^3P_1\ m_J = -1$.

This technique allows us to map the eigenvalues and eigenvectors of the dressed MOT, avoiding the problem posed above, of the $5s5p\ ^3P_1\ m_J = 0$ state being lower in energy than the $5s5p\ ^3P_1\ m_J = -1$ state. We now consider when the MOT beams will drive these transitions.

The MOT beam polarisation is chosen such that the light can drive to the $5s5p\ ^3P_1\ m_J = -1$ as it propagates towards the quadrupole field centre, and to the $5s5p\ ^3P_1\ m_J = +1$ as it propagates from the quadrupole field centre, although this second transition is usually neglected in Regime I MOTs as the light is not resonant with this transition. We will therefore consider when is the MOT light resonant with any eigenstate, which we can see from the eigenvalues(Figure F.1(d-f)), and the $5s5p\ ^3P_1\ m_J = -1$ component of the corresponding eigenvector (Figure F.1(g-i)), which sets how strongly the MOT light can drive the transition.

As a simple treatment to understand the resonance curve of the dressed MOT we calculate a scattering from a Lorentzian for the three eigenstates (d-f) based on a MOT beam detuning of $\delta_{\mathrm{MOT}} = -140$ kHz, weight these by the $5s5p\ ^3P_1\ m_J = -1$ component of the eigenstates, and sum the three contributions of the three eigenstates. This generates the resonance curve shown in Figure F.2(a).

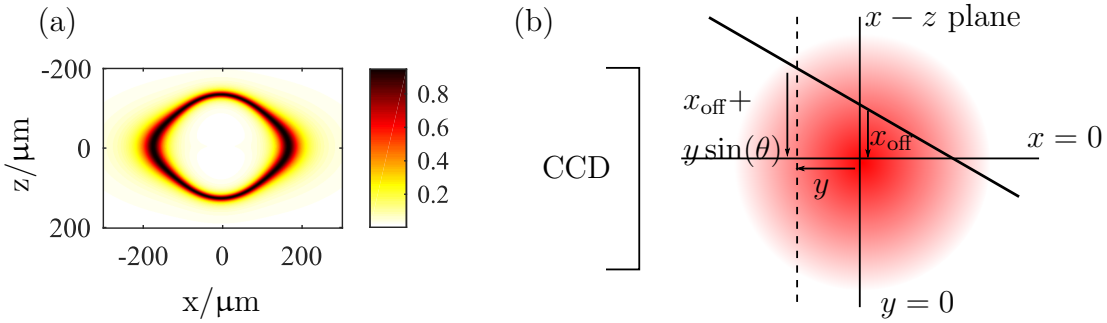

Figure F.2: (a) Normalised scattering force from the $5s5p\ ^3P_1\ m_J = -1$ fraction of the three eigenstates in Figure F.1(d-f). This is calculated for a single x-z plane, with $y = 0$. As the coupling beam propagates at an angle to the imaging axis, the effect of the coupling beam will vary across the cloud, illustrated in (b).

MOT beam resonance with the eigenstates

This technique is still a two-dimensional technique, which causes particular problems given the coupling beam angle with the imaging axis, illustrated in Figure F.2(b). For

this reason, we overlay several resonance curves, in which we vary both y (the position of the x-z plane that we consider) and $x_0 = x_{\text{off}} + y\sin(\theta)$ (the horizontal position of the coupling beam through the x-z plane). This allows us to see the relationship between the resonance curve and the position of the x-z slice. Figure F.3 shows the data from Figure 5.8 overlaid with 5 resonance curves for five values of y from -150 μm to +150 μm in steps of 75 μm, showing excellent agreement between the cloud and the resonance curves.

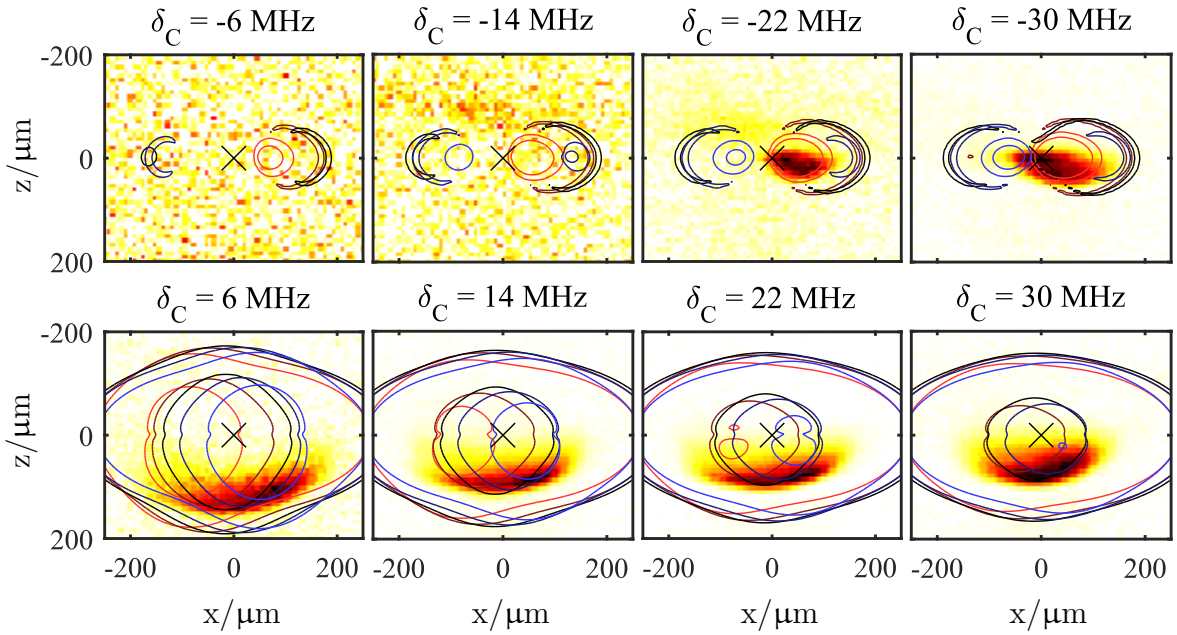

Figure F.3: Resonance curves for imaging depths from -150 μm (red) to +150 μm (blue) for six different coupling beam detunings overlaid on data. When the coupling beam is red-detuned contours represent where the force is 90% of the maximum. When blue-detuned contours indicate where the force matches gravity.

When the coupling beam is red-detuned, the resonance curve shrinks and atoms can interact with multiple MOT beams simultaneously. We therefore plot resonance curves at the 90% level, to indicate where scattering is strongest. We expect the trap to form inside the curve. If the resonance curve does not encompass the quadrupole field zero the MOT beams will not provide a trapping force in every direction, and the trap will not be sealed, causing the cloud to be lost at δ_C = -6 MHz and -14 MHz.

When the coupling beam is blue-detuned atoms predominantly interact with the vertical MOT beam, so we plot resonance contours where the scattering force matches gravity. Equilibrium occurs for the inner curves and we expect the cloud to be slightly broader than the resonance curves, as the horizontal MOT beams are weaker and thus less power

broadened, which we observe.

The agreement between the resonance curves calculated by solving the six-level Hamiltonian for multiple imaging planes and the data is very good. However, this treatment is complex, and requires numerical solution of a six-level Hamiltonian as a function of position. We would prefer to use the AC Stark shift calculation described by Equation F.5 as it offers a more intuitive understanding of the AC Stark shift on the MOT resonance condition.

Exact agreement between any model and the data is difficult due to the complexity of the theory, uncertainty in parameters (e.g. exact MOT beam detunings, quadrupole centre and coupling beam centre positions etc) and the two-dimensional nature of the imaging planes that we consider. We are therefore very satisfied with the comparisons demonstrated in Figure F.3. Typically when we consider resonance conditions for simplicity we will use the analytic expression established above, but in some regimes it may be necessary to use the full treatment established in this appendix.

Appendix G

Additional plasma seeding data

In Section 6.3 we study the seeding of the plasma that occurs during Rydberg dressing. We present data showing the effect of coupling beam detuning δ_C and ground state density on plasma formation. In this appendix we will consider the effect of coupling beam power, MOT beam power and MOT beam detuning. We also consider the Mandel Q parameter of the ion signals, and present a coupling beam power 'ramp'.

In Figure 6.4 we present ion detection rates as a function of coupling beam detuning and ground state density. In Figure G.1 we present data taken under the same conditions, but as a function of coupling beam detuning and power.

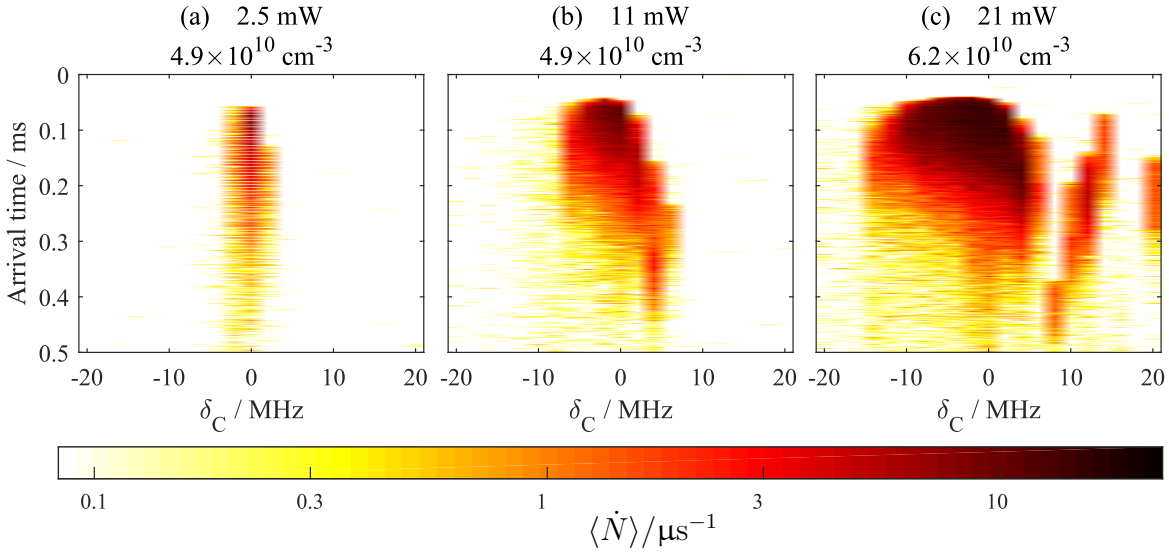

Figure G.1: Ion detection rate as a function of arrival time, coupling beam detuning and coupling beam power.

Clearly, the effect of varying the coupling beam power is not the same as varying the ground state density. We see ions predominantly on resonance at low coupling beam power, compared to ions on the red-detuned side of resonance at low ground state density. This is consistent with low coupling beam power resulting in the signal being predominantly generated through one-body processes, which suggests that the reduced power broadening of the Rydberg transition reduces the probability of off-resonantly exciting pairs of Rydberg atoms.

Increasing the coupling beam power we see the emergence of the red-detuned shifted feature first observed in Figure 6.4, although the features span a narrower range of coupling beam detunings. In Figure 6.6 the plasma seeding rate for these datasets is compared to the van der Waals interaction shift, observing good agreement apart from at low coupling beam power where one-body excitation dominates.

Average ion detection rates are not the only measurement we can make. Figure G.2 shows the Mandel Q parameter for the datasets shown in Figure 6.4 and Figure G.1.

As discussed in Appendix D we expect atom number fluctuations to result in super-Poissonian ion detection rates, but the Q parameter of the ion detection rates are too large to be explained by atom number fluctuations alone. At large ion detection rates detector saturation (discussed in Section 3.3.2) results in strongly negative Q parameters but before this occurs we clearly see super-Poissonian ion statistics for both red- and blue-detuned coupling and for a range of ground state densities.

These super-Poissonian ion detection rates are consistent with Rydberg and Coulomb anti-blockade, which enhance the Rydberg excitation rate when red- and blue-detuned. Notably, we do not see super-Poissonian ion detection rates on resonance at low coupling beam power. Taken in conjunction with the seeding rate measured in Figure 6.6(f), we can conclude that at this low coupling beam power we observe one-body Rydberg excitation but in other datasets we observe many-body Rydberg excitation.

We observe much larger Q parameters when blue-detuned than when red-detuned. The ion detection rates when blue-detuned are much more bimodal, as it is only in the experiment shots that plasma formation occurs that we see large ion detection rates.

So far we have only varied the coupling beam parameters and the ground state density. We can also vary the MOT beam parameters of MOT beam detuning, which sets the size of the MOT, and MOT beam power, which sets the excited state fraction in the MOT. Figure G.3 shows ion detection rates for a MOT taken with $\delta_{\mathrm{MOT}} = -140$ kHz,

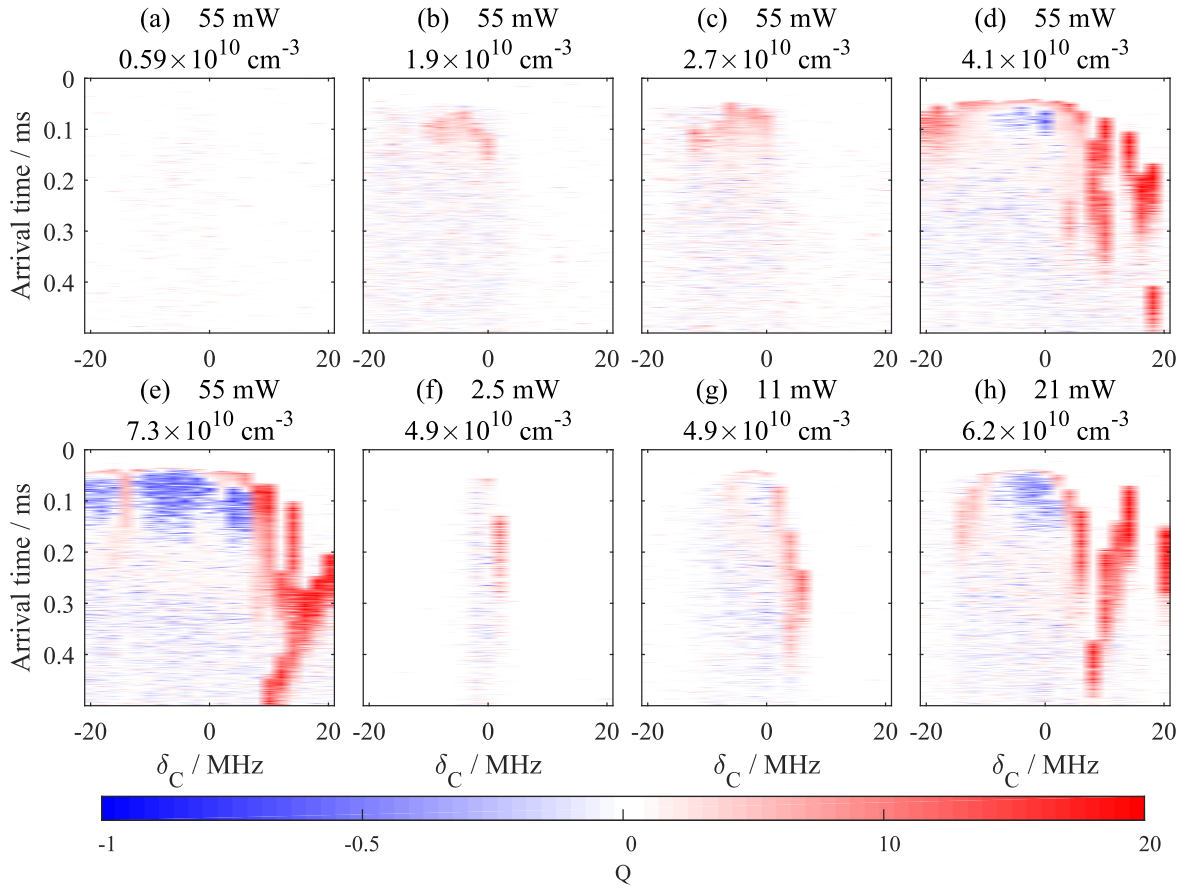

Figure G.2: Ion Mandel Q parameter as a function of arrival time, coupling beam detuning, ground state density and coupling beam power.

$P_{MOT} = 30$ μW.

The most striking observation is that the massive variation in seeding time that is observed when blue-detuned is suppressed. Whilst there is still strong variation in whether plasmas form for blue-detuned coupling, when strong ion signals are observed they will be observed within the first 100 μs.

Less visually striking but very significant is that a smaller, lower power MOT allows higher densities, roughly an order of magnitude greater, to be reached before significant ion formation occurs than for the data shown in Figure 6.4. This is true for a coupling beam that is both red- and blue-detuned. This is attributed to a combination of lower MOT beam power, reducing the fraction of atoms in the excited state, and a smaller cloud, resulting in a higher charge density being required for plasma formation. The lower excited state fraction may also reduce collisional ionisation between Rydberg atoms

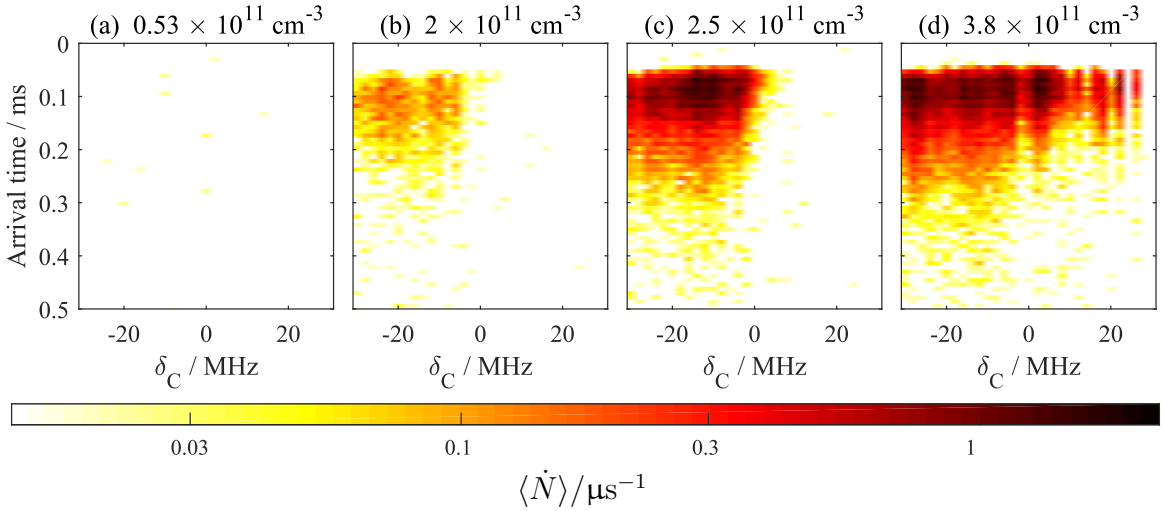

Figure G.3: Ion detection rate as a function of dressing time and coupling beam detuning for different ground state densities. The MOT beam detuning of $\delta_{\mathrm{MOT}} = -140$ kHz results in a MOT that is smaller than the coupling beam, and the MOT beam power is 30 μW.

and excited state atoms.

The final datasets we consider in this appendix smoothly increase the coupling beam power rather than using a step-change. This technique allows us to map the coupling beam power at which seeding occurs onto the ion detection rate. In addition, this technique has been used to compare data taken coupling the MOT to two Rydberg states under the same MOT conditions of $\delta_{\mathrm{MOT}} = -210$ kHz, $\mathrm{P}_{\mathrm{MOT}} = 500$ μW.

Figure G.4(a) shows a coupling beam power ramp over 1 ms, with ion detection rates taken at δ_C =-10 MHz (blue), 0 MHz (orange) and +10 MHz (yellow). When coupling to the $5s36d\ ^3D_1$ state we observe sharp ion peaks on resonance and when red-detuned (the van der Waals anti-blockade side of resonance) at low and high densities, and the emergence of sharp ion peaks at high densities when blue-detuned (the Coulomb anti-blockade side of resonance).

These sharp peaks emerge at the same density as we observe simply switching the coupling beam on in Figure 6.4 but we observe a delay that is attributed to the coupling beam power ramp. Seeding occurs only when the coupling beam power is sufficiently high for the anti-blockade effect to enhance Rydberg excitation. This is true for both van der Waals and Coulomb anti-blockade.

We can therefore identify the coupling beam Rabi frequency necessary for seeding to occur as a function of density and coupling beam detuning, shown in Figure G.5.

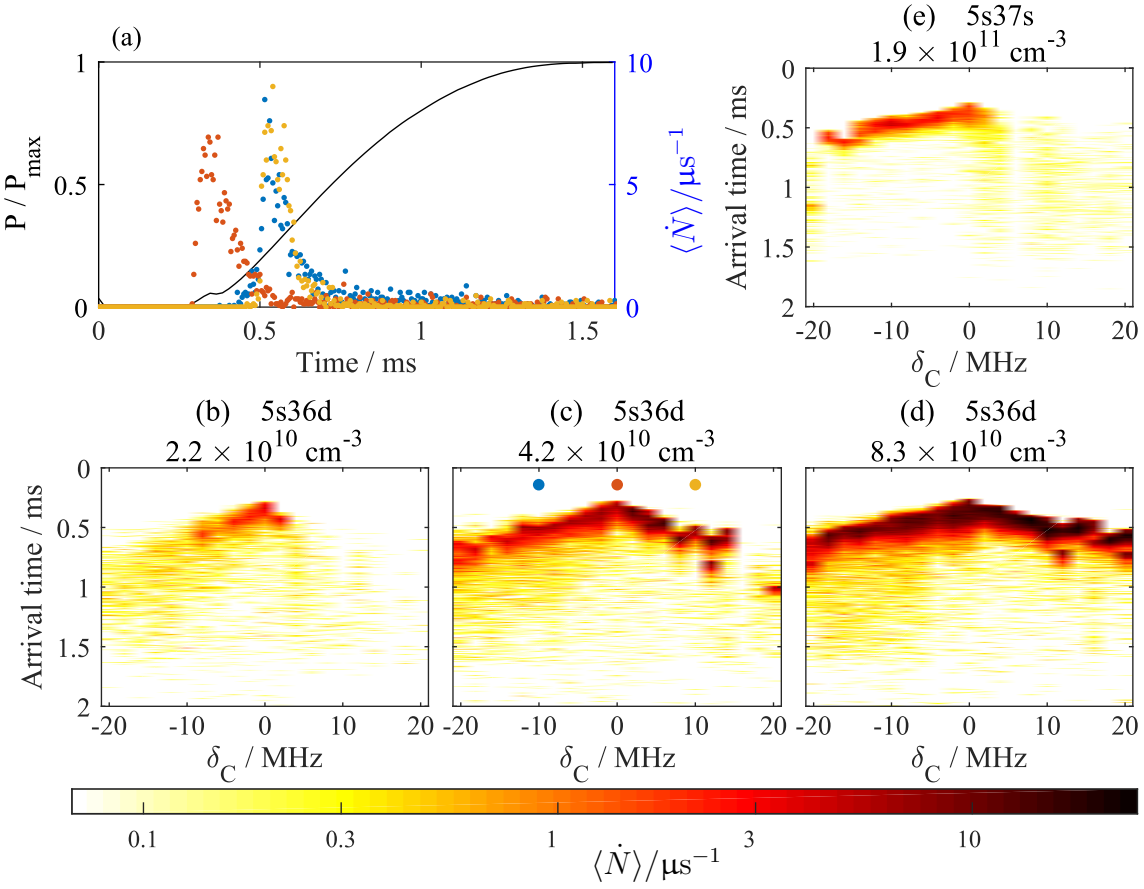

Figure G.4: Smoothly increasing the coupling beam power (a, left axis), we observe the ion detection rate for for several coupling beam detunings (right axis, indicated by the dots in (c)). From this we construct a colourmap of ion detection rates. This has been performed at three densities whilst coupling to the $5s36d\ ^3D_1$ state and one density whilst coupling to the $5s37s\ ^3S_1$ state. Different detection efficiencies were used for the different Rydberg states.

The most interesting observation from these data is from a comparison between Rydberg states. We have data from a single density whilst coupling to the $5s37s\ ^3S_1$ state, which has a positive polarisability and repulsive van der Waals interactions.

We observe the ion detection rate rise fastest on resonance, and we observe sharp ion peaks when red-detuned (the Coulomb anti-blockade side of resonance). However, we don't observe sharp ion peaks when blue-detuned (the van der Waals anti-blockade side of resonance). Whilst we achieve lower Rabi frequency coupling to the $5s37s\ ^3S_1$ state, this state has a greater C_6 coefficient than the $5s36d\ ^3D_1$ state, and the density is higher than that used when dressing the $5s36d\ ^3D_1$ state so we expect stronger van der Waals

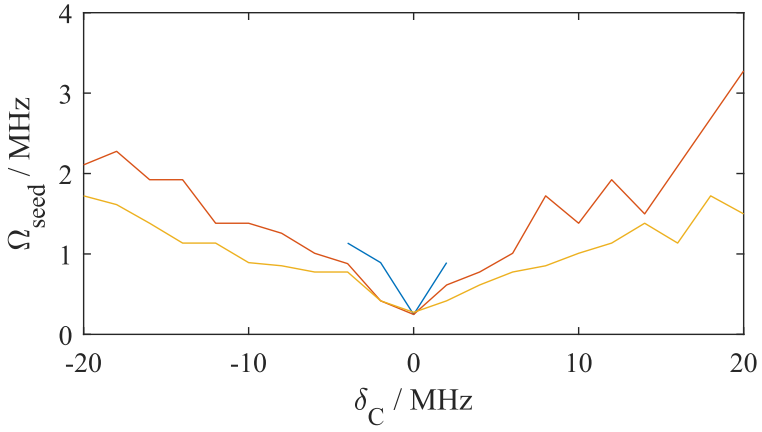

Figure G.5: The coupling beam Rabi frequency at which the plasma seeds during coupling beam power ramps, shown for a ground state density of 2.2×10^{10} cm^{-3} (blue), 4.2×10^{10} cm^{-3} (orange) and 8.3×10^{10} cm^{-3} (yellow). At higher density, the plasma seeds at lower power. Measured using the data in Figure G.4(b-d) whilst coupling to the $5s36d\ ^3D_1$ state.

enhancement of the Rydberg excitation rate.

We believe the lack of ions detected when blue-detuned from the $5s37s\ ^3S_1$ is due to a lower ionisation rate. The van der Waals interactions between $5s37s\ ^3S_1$ state pairs is repulsive, so we do not expect strong collisional ionsation between pairs of atoms. In contrast, the van der Waals interaction between pairs of $5s36d\ ^3D_1$ state atoms is attractive and can result in collisional ionisation.

Appendix H

Plasma lifetime study

In Section 6.4 we show that the charge density of the plasma results in a sufficiently large electric field to DC Stark shift the $5s36d\ ^3D_1$ state onto resonance with the blue-detuned coupling beam. We show that the lifetime of the cloud whilst the plasma is present is comparable to that which we expect due to enhanced Rydberg excitation caused by this DC Stark shift.

One surprising observation from this lifetime measurement is that the loss rate of the cloud is density dependent. In this appendix we present more data showing the lifetime dependence on density for three MOT beam powers and propose some mechanisms that may cause this.

Figure H.1 shows atom numbers and ion detection rates for three MOT beam powers and a range of initial atom numbers[a]. At the lowest MOT beam power we only observe one dataset with a high enough atom number for plasma formation to occur, but in the other two datasets we observe a rising plasma lifetime with initial atom number.

Fitting an exponential to these atom numbers we can quantify this effect. We see the plasma lifetime rise as we reduce the MOT beam power, which is consistent with a reduced Rydberg excitation rate, and we see the atom number at which plasma depletion stops rise, also consistent with a reduced Rydberg excitation rate. The ion detecton rates do not follow a purely exponential decay, the decay rate of the ion detection rate appears to rise with dressing time, which is consistent with a mechanism that inhibits Rydberg excitation at high density.

[a]The different MOT beam power datasets were taken with different oscilloscope settings, so with different ion detection efficiencies, making direct comparisons of ion numbers impossible.

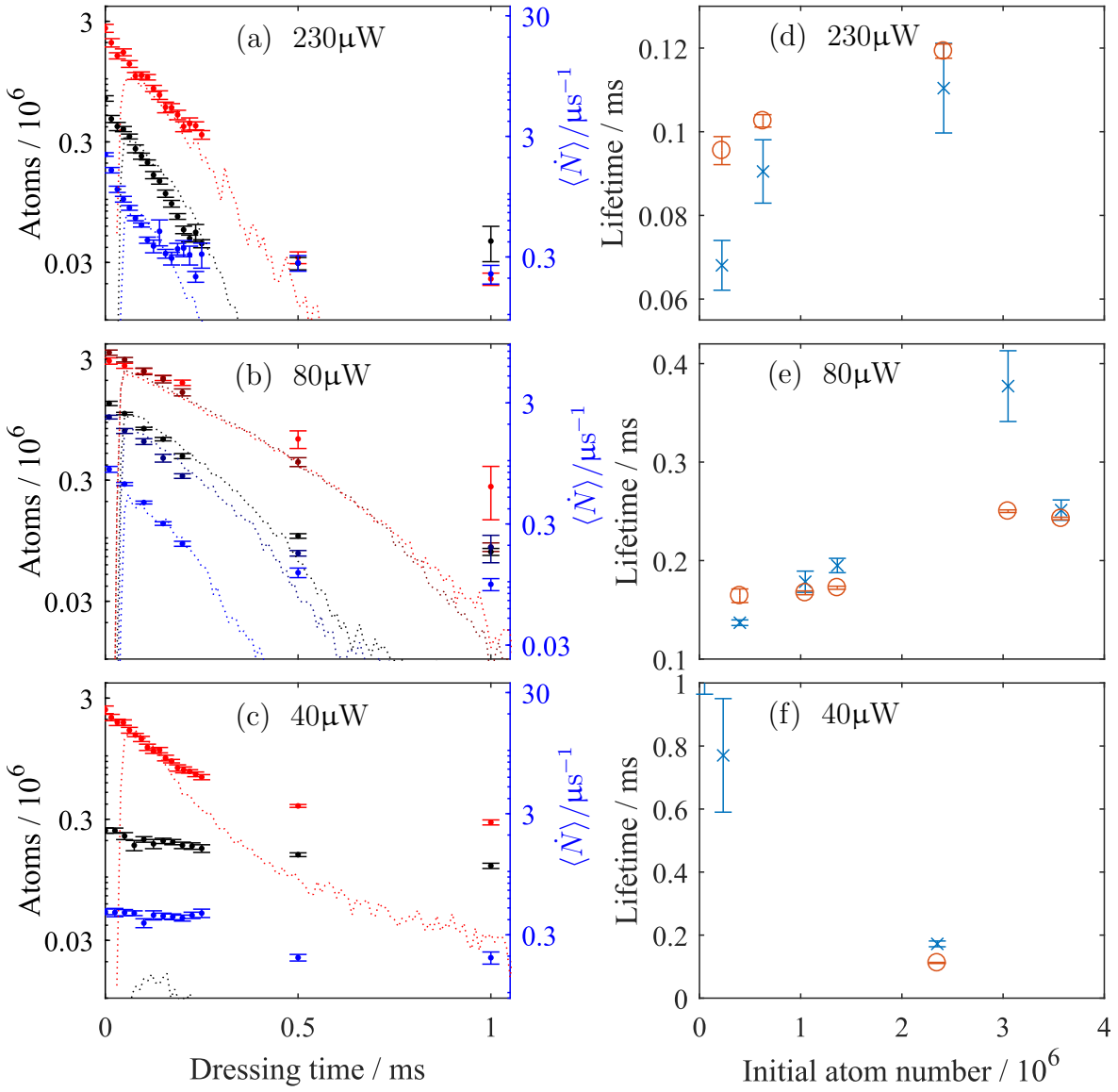

Figure H.1: Atom number (left plots, left axis) and ion detection rate (left plots, right axis) for a range of MOT beam powers and initial atom numbers, indicated by colour. We see a rapid decay in atom number corresponding to a similar rapid decay in ion detection rate. Right, fitting an exponential decay to the fall in atom number (blue crosses) and ion detection rate (orange circles), we see a lifetime that rises with initial atom number and with falling MOT beam power. At the lowest MOT beam power, we don't have strong plasma formation beyond the highest initial atom number, breaking the trend of lifetime rising with atom number.

The observation of a plasma lifetime that rises with ground state density is very surprising. We will propose some mechanisms that could result in this, but we do not have the data to draw conclusions about the mechanism that causes this effect.

The first effect we consider is Coulomb blockade. [139] proposes a feedback mechanism whereby rising ion density DC Stark shifts the Rydberg transition off resonance, limiting excitation to the rate at which ions are lost from the cloud. We are detuned to the Coulomb anti-blockade side of resonance, but at a sufficiently high charge density we may expect to pass through the Coulomb anti-blockade and reach the Coulomb blockade region. This would result in a Rydberg excitation rate limited to the rate at which ions are lost, which, for an uncoupled plasma, would result in an almost constant Rydberg density and loss rate.

In Figure 6.11 we measure the number of longlived Rydberg atoms as a function of atom number and dressing time. These measurement suggest that the charge density within the plasma is largely independent of the initial atom number and largely constant in time until the plasma depletes. These measurements are therefore consistent with such a Coulomb blockade. However, a Coulomb blockade would suggest a linear atom loss rate and a constant ion detection rate until the plasma depletes, suggesting this mechanism alone can't be responsible for the density dependence of the plasma lifetime.

We may be observing an incomplete Coulomb blockade effect, for example if the charge density varies across the cloud. Consequently, the collisional process that gives rise to longlived Rydberg atoms may be dominated by the blockaded region in the centre of the cloud, where the charge density is highest, whilst atom loss continues without Coulomb blockade in the wings of the cloud.

The nature of the Coulomb blockade may be sufficiently modified by the off-resonant nature of the coupling beam that we do not expect only a limited version of the feedback observed in [139]. Alternatively, there may be a van der Waals blockade simultaneously occuring, although we expect the Rydberg-electron collision rate to be too strong for a significant Rydberg population to develop.

Alternatively, the rate at which ions are lost from the plasma may be charge-density dependent. This is the case for strongly coupled plasmas, but the Coulomb potential energy of two ions separated by the Coulomb anti-blockade radius is a factor of thirty less than the electron kinetic energy, suggesting that we are not in the strongly coupled regime.

The plasma charge density threshold is proportional to r^{-2} where r is the size of the plasma. A higher atom number resulting in a larger ion production rate may result in more charges within the plasma, allowing a larger plasma with a lower density to form. The lower charge density may then result in a lower Rydberg excitation rate i.e. the probability of each atom being excited to the Rydberg state is reduced at higher atom numbers whilst the overall ion production rate is higher due to the higher atom number. The probability of longlived Rydberg atoms being produced due to collisions is proportional to the Rydberg population and the electron density, the probability of longlived Rydberg atoms being produced through recombination is proportional to the ion density and the square of electron density, so it is not clear what effect this would have on the longlived Rydberg population.

Charges are not only lost through plasma expansion - in [138] charge-density dependent three-body recombination in plasmas is observed to deplete the charges in the plasma. This is proportional to $N_{\text{ion}} \times N_{\text{electron}}^2$, so will be strongly dependent on the charge density. This recombination may limit the charge density within the cloud, limiting the Rydberg excitation rate within the cloud. However, this would result in the longlived Rydberg population to be strongly density dependent, whilst we observe the opposite to be true in Figure 6.11.

The rapid movement of electrons in the cloud results in large AC electric fields that allow excitation to Rydberg states other than the $5s36d\ ^3D_1$ state. Electric fields can allow coupling through transitions that are otherwise forbidden as well as DC Stark shifting Rydberg state energy levels, potentially creating a 'spaghetti' of energy levels that can be coupled to. A combination of a Coulomb blockade and excitation to different states with low ionsation probabilities may result in a density dependent loss rate.

From the data available it is not possible to conclude what the mechanism for the density dependent plasma lifetime is. The strongest candidate is an incomplete Coulomb blockade effect that limits the Rydberg excitation rate to the rate at which ions leave the cloud. A full study of this system is beyond the work of this thesis. We can, however, be confident that the high charge-density of the plasma is capable of drastically increasing the Rydberg excitation rate in a plasma when the coupling beam is detuned to the Coulomb anti-blockade side of resonance. It is an open question as to why the lifetime of the plasma rises with atom density.

Bibliography

[1] *UK National Quantum Technologies Programme*, http://uknqt.epsrc.ac.uk/, Accessed: 2017-07-30.

[2] *Hybrid Architecture for quantum Information using Rydberg ensembles and Superconductors*, http://cordis.europa.eu/project/rcn/111128_en.html, Accessed: 2017-07-30.

[3] *Quantum Europe 2017: Towards the Quantum Technology Flagship*, https://ec.europa.eu/digital-single-market/en/news/quantum-europe-2017-towards-quantum-technology-flagship, Accessed: 2017-07-30.

[4] *IBM Quantum Computing*, https://www.research.ibm.com/ibm-q/learn/what-is-ibm-q/, Accessed: 2017-07-30.

[5] *China's quantum satellite in big leap*, http://www.bbc.co.uk/news/science-environment-40294795, Accessed: 2017-07-30.

[6] Z.-K. Hu *et al.*, *Demonstration of an ultrahigh-sensitivity atom-interferometry absolute gravimeter*, Phys. Rev. A **88**, 043610 (2013).

[7] S. Abend *et al.*, *Atom-Chip Fountain Gravimeter*, Phys. Rev. Lett. **117**, 203003 (2016).

[8] S. Knappe, T. Sander, and L. Trahms, *Optically-Pumped Magnetometers for MEG* (Springer Berlin Heidelberg, 2014), pp. 993–999.

[9] R. Kleiner, D. Koelle, F. Ludwig, and J. Clarke, *Superconducting quantum interference devices: State of the art and applications*, Proceedings of the IEEE **92**, 1534 (2004).

[10] J. A. Sedlacek, A. Schwettmann, H. Kübler, and J. P. Shaffer, *Atom-Based Vector Microwave Electrometry Using Rubidium Rydberg Atoms in a Vapor Cell*, Phys. Rev. Lett. **111**, 063001 (2013).

[11] C. G. Wade *et al.*, *Real-time near-field terahertz imaging with atomic optical fluorescence*, Nat. Photonics **11**, 40 (2016).

[12] S. B. Koller *et al.*, *Transportable Optical Lattice Clock with* 7×10^{-17} *Uncertainty*, Phys. Rev. Lett. **118**, 073601 (2017).

[13] C. W. Chou, D. B. Hume, J. C. J. Koelemeij, D. J. Wineland, and T. Rosenband, *Frequency Comparison of Two High-Accuracy* Al^+ *Optical Clocks*, Phys. Rev. Lett. **104**, 070802 (2010).

[14] T. L. Nicholson *et al.*, *Comparison of Two Independent Sr Optical Clocks with* 1×10^{-17} *Stability at* 10^3 **s**, Phys. Rev. Lett. **109**, 230801 (2012).

[15] S. Blatt *et al.*, *New Limits on Coupling of Fundamental Constants to Gravity Using* ^{87}Sr *Optical Lattice Clocks*, Phys. Rev. Lett. **100**, 140801 (2008).

[16] C. W. Chou, D. B. Hume, T. Rosenband, and D. J. Wineland, *Optical Clocks and Relativity*, Science **329**, 1630 (2010).

[17] C. J. Ballance, T. P. Harty, N. M. Linke, M. A. Sepiol, and D. M. Lucas, *High-Fidelity Quantum Logic Gates Using Trapped-Ion Hyperfine Qubits*, Phys. Rev. Lett. **117**, 060504 (2016).

[18] L. Isenhower *et al.*, *Demonstration of a Neutral Atom Controlled-NOT Quantum Gate*, Phys. Rev. Lett. **104**, 010503 (2010).

[19] T. Jörg, F. Krzakala, J. Kurchan, and A. C. Maggs, *Simple Glass Models and Their Quantum Annealing*, Phys. Rev. Lett. **101**, 147204 (2008).

[20] *D Wave Systems*, `https://www.dwavesys.com/quantum-computing/`, Accessed: 2017-08-12.

[21] B. P. Lanyon *et al.*, *Experimental Demonstration of a Compiled Version of Shor's Algorithm with Quantum Entanglement*, Phys. Rev. Lett. **99**, 250505 (2007).

[22] X.-D. Cai *et al.*, *Experimental Quantum Computing to Solve Systems of Linear Equations*, Phys. Rev. Lett. **110**, 230501 (2013).

[23] G. Vallone *et al.*, *Experimental Satellite Quantum Communications*, Phys. Rev. Lett. **115**, 040502 (2015).

[24] W. Zhang *et al.*, *Quantum Secure Direct Communication with Quantum Memory*, Phys. Rev. Lett. **118**, 220501 (2017).

[25] R. Hughes and J. Nordholt, *Refining Quantum Cryptography*, Science **333**, 1584 (2011).

[26] M. Mirhosseini *et al.*, *High-dimensional quantum cryptography with twisted light*, New Journal of Physics **17**, 033033 (2015).

[27] D. Neamen, *Semiconductor Physics And Devices*, 3 ed. (McGraw-Hill, Inc., New York, NY, USA, 2003).

[28] K. F. Brennan, *Introduction to Semiconductor Devices: For Computing and Telecommunications Applications* (Cambridge University Press, 2005).

[29] L. W. Cheuk *et al.*, *Observation of spatial charge and spin correlations in the 2D Fermi-Hubbard model*, Science **353**, 1260 (2016).

[30] J. Steinhauer, *Observation of self-amplifying Hawking radiation in an analogue black-hole laser*, Nat. Phys. **10**, 764 (2014).

[31] J. I. Cirac and P. Zoller, *Goals and opportunities in quantum simulation*, Nat. Phys. **8**, 264 (2012).

[32] I. Buluta and F. Nori, *Quantum Simulators*, Science **326**, 108 (2009).

[33] K. Góral, L. Santos, and M. Lewenstein, *Quantum Phases of Dipolar Bosons in Optical Lattices*, Phys. Rev. Lett. **88**, 170406 (2002).

[34] N. Henkel, R. Nath, and T. Pohl, *Three-Dimensional Roton Excitations and Supersolid Formation in Rydberg-Excited Bose-Einstein Condensates*, Phys. Rev. Lett. **104**, 195302 (2010).

[35] V. W. Scarola and S. Das Sarma, *Quantum Phases of the Extended Bose-Hubbard Hamiltonian: Possibility of a Supersolid State of Cold Atoms in Optical Lattices*, Phys. Rev. Lett. **95**, 033003 (2005).

[36] B. DeMarco, *An Atomic View of Quantum Phase Transitions*, Science **329**, 523 (2010).

[37] J. Ghosh and B. C. Sanders, *Quantum simulation of macro and micro quantum phase transition from paramagnetism to frustrated magnetism with a superconducting circuit*, New Journal of Physics **18**, 033015 (2016).

[38] M. Greener, O. Mandel, T. Esslinger, T. W. Hansch, and I. Bloch, *Quantum phase transition from a superfluid to a Mott insulator in a gas of ultracold atoms*, Nature **415**, 39 (2002).

[39] D. Jaksch and P. Zoller, *The cold atom Hubbard toolbox*, Annals of Physics **315**, 52 (2005), Special Issue.

[40] R. Blatt and C. F. Roos, *Quantum simulations with trapped ions*, Nat. Phys. **8**, 277 (2012).

[41] L. D. Carr, D. DeMille, R. V. Krems, and J. Ye, *Cold and ultracold molecules: science, technology and applications*, New Journal of Physics **11**, 055049 (2009).

[42] J. W. Park, Z. Z. Yan, H. Loh, S. A. Will, and M. W. Zwierlein, *Second-scale nuclear spin coherence time of ultracold* $^{23}Na^{40}K$ *molecules*, Science **357**, 372 (2017).

[43] S. Fedortchenko *et al.*, *Quantum simulation of ultrastrongly coupled bosonic modes using superconducting circuits*, Phys. Rev. A **95**, 042313 (2017).

[44] J. You and F. Nori, *Superconducting circuits and quantum information*, 2005.

[45] E. Manousakis, *A Quantum-Dot Array as Model for Copper-Oxide Superconductors: A Dedicated Quantum Simulator for the Many-Fermion Problem*, Journal of Low Temperature Physics **126**, 1501 (2002).

[46] M. Lewenstein *et al.*, *Ultracold atomic gases in optical lattices: mimicking condensed matter physics and beyond*, Advances in Physics **56**, 243 (2007).

[47] C. Aron, M. Kulkarni, and H. E. Türeci, *Photon-Mediated Interactions: A Scalable Tool to Create and Sustain Entangled States of N Atoms*, Phys. Rev. X **6**, 011032 (2016).

[48] A. F. van Loo *et al.*, *Photon-Mediated Interactions Between Distant Artificial Atoms*, Science **342**, 1494 (2013).

[49] T. F. Gallagher, *Rydberg Atoms* Cambridge Monographs on Atomic, Molecular and Chemical Physics (Cambridge University Press, 1994).

[50] S. D. Hogan *et al.*, *Driving Rydberg-Rydberg Transitions from a Coplanar Microwave Waveguide*, Phys. Rev. Lett. **108**, 063004 (2012).

[51] D. Paredes-Barato and C. S. Adams, *All-Optical Quantum Information Processing Using Rydberg Gates*, Phys. Rev. Lett. **112**, 040501 (2014).

[52] H. Gorniaczyk, C. Tresp, J. Schmidt, H. Fedder, and S. Hofferberth, *Single-Photon Transistor Mediated by Interstate Rydberg Interactions*, Phys. Rev. Lett. **113**, 053601 (2014).

[53] H. Weimer, M. Müller, H. P. Büchler, and I. Lesanovsky, *Digital quantum simulation with Rydberg atoms*, Quantum Information Processing **10**, 885 (2011).

[54] H. Weimer, M. Muller, I. Lesanovsky, P. Zoller, and H. P. Buchler, *A Rydberg quantum simulator*, Nat. Phys. **6**, 382 (2010).

[55] E. Korsunsky and Y. Rozhdestvensky, *Subrecoil cooling of Rydberg atoms*, Phys. Rev. A **52**, 3027 (1995).

[56] G. Morigi, B. Zambon, N. Leinfellner, and E. Arimondo, *Scaling laws in velocity-selective coherent-population-trapping laser cooling*, Phys. Rev. A **53**, 2616 (1996).

[57] I. I. Beterov, I. I. Ryabtsev, D. B. Tretyakov, and V. M. Entin, *Quasiclassical calculations of blackbody-radiation-induced depopulation rates and effective lifetimes of Rydberg nS, nP, and nD alkali-metal atoms with $n \leq 80$*, Phys. Rev. A **79**, 052504 (2009).

[58] S. Helmrich, A. Arias, N. Pehoviak, and S. Whitlock, *Two-body interactions and decay of three-level Rydberg-dressed atoms*, Journal of Physics B: Atomic, Molecular and Optical Physics **49**, 03LT02 (2016).

[59] N. Henkel, *Rydberg-dressed Bose-Einstein condensates*, PhD thesis, Dresden University, 2012.

[60] L. I. R. Gil, R. Mukherjee, E. M. Bridge, M. P. A. Jones, and T. Pohl, *Spin Squeezing in a Rydberg Lattice Clock*, Phys. Rev. Lett. **112**, 103601 (2014).

[61] T. Keating *et al.*, *Robust quantum logic in neutral atoms via adiabatic Rydberg dressing*, Phys. Rev. A **91**, 012337 (2015).

[62] Y. Y. Jau, A. M. Hankin, T. Keating, I. H. Deutsch, and G. W. Biedermann, *Entangling atomic spins with a Rydberg-dressed spin-flip blockade*, Nat. Phys. **12**, 71 (2015).

[63] J. Zeiher *et al.*, *Many-body interferometry of a Rydberg-dressed spin lattice*, Nat. Phys. **12**, 1095 (2016).

[64] J. A. Aman *et al.*, *Trap losses induced by near-resonant Rydberg dressing of cold atomic gases*, Phys. Rev. A **93**, 043425 (2016).

[65] E. A. Goldschmidt *et al.*, *Anomalous Broadening in Driven Dissipative Rydberg Systems*, Phys. Rev. Lett. **116**, 113001 (2016).

[66] S. H. Autler and C. H. Townes, *Stark Effect in Rapidly Varying Fields*, Phys. Rev. **100**, 703 (1955).

[67] B. R. Mollow, *Pure-state analysis of resonant light scattering: Radiative damping, saturation, and multiphoton effects*, Phys. Rev. A **12**, 1919 (1975).

[68] C. Cohen-Tannoudji, J. Dupont-Roc, and G. Grynberg, *The Dressed Atom Approach* (Wiley-VCH Verlag GmbH, 2008), pp. 407–514.

[69] C. N. Cohen-Tannoudji, *The Autler-Townes Effect Revisited* (Springer New York, New York, NY, 1996), pp. 109–123.

[70] A. Browaeys and T. Lahaye, *Interacting Cold Rydberg Atoms: A Toy Many-Body System* (Springer International Publishing, Cham, 2016), pp. 177–198.

[71] J. Pritchard, *Cooperative Optical Non-linearity in a blockaded Rydberg Ensembles*, PhD thesis, Durham University, 2011.

[72] D. Tong *et al.*, *Local Blockade of Rydberg Excitation in an Ultracold Gas*, Phys. Rev. Lett. **93**, 063001 (2004).

[73] E. Urban *et al.*, *Observation of Rydberg blockade between two atoms*, Nat. Phys. **5**, 110 (2009).

[74] C. Vaillant, *Long-Range Interactions in One- and Two-Electron Rydberg Atoms*, PhD thesis, Durham University, 2014.

[75] I. Bouchoule and K. Mølmer, *Spin squeezing of atoms by the dipole interaction in virtually excited Rydberg states*, Phys. Rev. A **65**, 041803 (2002).

[76] J. E. Johnson and S. L. Rolston, *Interactions between Rydberg-dressed atoms*, Phys. Rev. A **82**, 033412 (2010).

[77] J. B. Balewski *et al.*, *Rydberg dressing: understanding of collective many-body effects and implications for experiments*, New Journal of Physics **16**, 063012 (2014).

[78] N. Henkel, F. Cinti, P. Jain, G. Pupillo, and T. Pohl, *Supersolid Vortex Crystals in Rydberg-Dressed Bose-Einstein Condensates*, Phys. Rev. Lett. **108**, 265301 (2012).

[79] T. Keating *et al.*, *Adiabatic quantum computation with Rydberg-dressed atoms*, Phys. Rev. A **87**, 052314 (2013).

[80] H. Katori, T. Ido, Y. Isoya, and M. Kuwata-Gonokami, *Magneto-Optical Trapping and Cooling of Strontium Atoms down to the Photon Recoil Temperature*, Phys. Rev. Lett. **82**, 1116 (1999).

[81] T. H. Loftus, T. Ido, M. M. Boyd, A. D. Ludlow, and J. Ye, *Narrow line cooling and momentum-space crystals*, Phys. Rev. A **70**, 063413 (2004).

[82] R. K. Hanley *et al.*, *Quantitative simulation of a magneto-optical trap operating near the photon recoil limit*, Journal of Modern Optics **0**, 1 (2017).

[83] J. Dalibard and C. Cohen-Tannoudji, *Laser cooling below the Doppler limit by polarization gradients: simple theoretical models*, J. Opt. Soc. Am. B **6**, 2023 (1989).

[84] J. Millen, *A cold strontium Rydberg gas*, PhD thesis, Durham University, 2011.

[85] G. Lochead, *Excited state spatial distributions in a cold strontium gas*, PhD thesis, Durham University, 2012.

[86] D. Boddy, *First observations of Rydberg blockade in a frozen gas of divalent atoms*, PhD thesis, Durham University, 2014.

[87] D. Sadler, *Many-body interactions in a dissipative frozen strontium Rydberg gas*, PhD thesis, Durham University, 2016.

[88] D. J. McCarron, S. A. King, and S. L. Cornish, *Modulation transfer spectroscopy in atomic rubidium*, Measurement Science and Technology **19**, 105601 (2008).

[89] R. K. Hanley *et al.*, *Probing interactions of thermal Sr Rydberg atoms using simultaneous optical and ion detection*, Journal of Physics B: Atomic, Molecular and Optical Physics **50**, 115002 (2017).

[90] E. M. Bridge, J. Millen, C. S. Adams, and M. P. A. Jones, *A vapor cell based on dispensers for laser spectroscopy*, Review of Scientific Instruments **80**, 013101 (2009).

[91] S. Stellmer, *Degenerate quantum gases of strontium*, PhD thesis, University of Innsbruck, 2013.

[92] T. Wiles, *Dynamics of bright solitary matter-waves*, PhD thesis, Durham University, 2013.

[93] K. Vogel, T. Dinneen, A. Gallagher, and J. Hall, *Narrow-line Doppler cooling of strontium to the recoil limit*, IEEE transactions on instrumentation and measurement **48**, 618 (1999).

[94] S. Stellmer, M. K. Tey, B. Huang, R. Grimm, and F. Schreck, *Bose-Einstein Condensation of Strontium*, Phys. Rev. Lett. **103**, 200401 (2009).

[95] R. Beigang and D. Schmidt, *Two-Channel MQDT Analysis of Bound 5 snd 3 D 1,3 Rydberg States of Strontium*, Physica Scripta **27**, 172 (1983).

[96] R. Beigang, K. Lcke, D. Schmidt, A. Timmermann, and P. J. West, *One-Photon Laser Spectroscopy of Rydberg Series from Metastable Levels in Calcium and Strontium*, Physica Scripta **26**, 183 (1982).

[97] C. J. Dai, *Perturbed $5snd^{1,3}D_2$ Rydberg series of Sr*, Phys. Rev. A **52**, 4416 (1995).

[98] W. R. S. Garton and K. Codling, *Ultra-violet extensions of the arc spectra of the alkaline earths: The absorption spectrum of strontium vapour*, Journal of Physics B: Atomic and Molecular Physics **1**, 106 (1968).

[99] F. Camargo *et al.*, *Lifetimes of ultra-long-range strontium Rydberg molecules*, Phys. Rev. A **93**, 022702 (2016).

[100] E. M. Bridge *et al.*, *Tunable cw UV laser with < 35 kHz absolute frequency instability for precision spectroscopy of Sr Rydberg states*, Opt. Express **24**, 2281 (2016).

[101] E. D. Black, *An introduction to Pound-Drever-Hall laser frequency stabilization*, American Journal of Physics **69**, 79 (2001).

[102] R. Kliese *et al.*, *Difference-frequency combs in cold atom physics*, The European Physical Journal Special Topics **225**, 2775 (2016).

[103] J. R. Rubbmark and S. A. Borgstrm, *Rydberg Series in Strontium Found in Absorption by Selectively Laser-Excited Atoms*, Physica Scripta **18**, 196 (1978).

[104] J. A. Armstrong, J. J. Wynne, and P. Esherick, *Bound, odd-parity $J = 1$ spectra of the alkaline earths: Ca, Sr, and Ba*, J. Opt. Soc. Am. **69**, 211 (1979).

[105] R. Beigang, K. Lucke, A. Timmermann, P. West, and D. Frlich, *Determination of absolute level energies of 5sns $^1S_0$ and 5snd $^1D_2$ Rydberg series of Sr*, Optics Communications **42**, 19 (1982).

[106] P. Esherick, *Bound, even-parity $J = 0$ and $J = 2$ spectra of Sr*, Phys. Rev. A **15**, 1920 (1977).

[107] K. J. Weatherill *et al.*, *Electromagnetically induced transparency of an interacting cold Rydberg ensemble*, Journal of Physics B: Atomic, Molecular and Optical Physics **41**, 201002 (2008).

[108] S. Mauger, J. Millen, and M. P. A. Jones, *Spectroscopy of strontium Rydberg states using electromagnetically induced transparency*, Journal of Physics B: Atomic, Molecular and Optical Physics **40**, F319 (2007).

[109] S. Sevinli *et al.*, *Quantum interference in interacting three-level Rydberg gases: coherent population trapping and electromagnetically induced transparency*, Journal of Physics B: Atomic, Molecular and Optical Physics **44**, 184018 (2011).

[110] U. Gaubatz, P. Rudecki, S. Schiemann, and K. Bergmann, *Population transfer between molecular vibrational levels by stimulated Raman scattering with partially*

overlapping laser fields. A new concept and experimental results, The Journal of Chemical Physics **92**, 5363 (1990).

[111] J. Grimmel *et al.*, *Measurement and numerical calculation of Rubidium Rydberg Stark spectra*, New Journal of Physics **17**, 053005 (2015).

[112] J. Millen, G. Lochead, G. R. Corbett, R. M. Potvliege, and M. P. A. Jones, *Spectroscopy of a cold strontium Rydberg gas*, Journal of Physics B: Atomic, Molecular and Optical Physics **44**, 184001 (2011).

[113] J. Millen, G. Lochead, and M. P. A. Jones, *Two-Electron Excitation of an Interacting Cold Rydberg Gas*, Phys. Rev. Lett. **105**, 213004 (2010).

[114] J. E. Sansonetti, *Wavelengths, Transition Probabilities, and Energy Levels for the Spectra of Strontium Ions (Sr II through Sr XXXVIII)*, Journal of Physical and Chemical Reference Data **41**, 013102 (2012).

[115] A. Guttridge *et al.*, *Direct loading of a large Yb MOT on the* $^1S_0 \leftrightarrow ^3P_1$ *transition*, Journal of Physics B: Atomic, Molecular and Optical Physics **49**, 145006 (2016).

[116] X. Xu *et al.*, *Dynamics in a two-level atom magneto-optical trap*, Phys. Rev. A **66**, 011401 (2002).

[117] K. Weatherill, *A* CO_2 *laser lattice experiment for cold atoms*, PhD thesis, Durham University, 2007.

[118] M. P. Robinson, B. L. Tolra, M. W. Noel, T. F. Gallagher, and P. Pillet, *Spontaneous Evolution of Rydberg Atoms into an Ultracold Plasma*, Phys. Rev. Lett. **85**, 4466 (2000).

[119] P. J. Tanner, J. Han, E. S. Shuman, and T. F. Gallagher, *Many-Body Ionization in a Frozen Rydberg Gas*, Phys. Rev. Lett. **100**, 043002 (2008).

[120] S. K. Dutta, D. Feldbaum, A. Walz-Flannigan, J. R. Guest, and G. Raithel, *High-Angular-Momentum States in Cold Rydberg Gases*, Phys. Rev. Lett. **86**, 3993 (2001).

[121] T. C. Killian *et al.*, *Formation of Rydberg Atoms in an Expanding Ultracold Neutral Plasma*, Phys. Rev. Lett. **86**, 3759 (2001).

[122] M. Lyon and S. L. Rolston, *Ultracold neutral plasmas*, Reports on Progress in Physics **80**, 017001 (2017).

[123] T. C. Killian, *Ultracold Neutral Plasmas*, Science **316**, 705 (2007).

[124] T. Killian, T. Pattard, T. Pohl, and J. Rost, *Ultracold neutral plasmas*, Physics Reports **449**, 77 (2007).

[125] T. C. Killian *et al.*, *Creation of an Ultracold Neutral Plasma*, Phys. Rev. Lett. **83**, 4776 (1999).

[126] W. Li *et al.*, *Evolution dynamics of a dense frozen Rydberg gas to plasma*, Phys. Rev. A **70**, 042713 (2004).

[127] T. T. Chen, *Introduction to Plasma Physics* (Springer US, 1974).

[128] S. Kulin, T. C. Killian, S. D. Bergeson, and S. L. Rolston, *Plasma Oscillations and Expansion of an Ultracold Neutral Plasma*, Phys. Rev. Lett. **85**, 318 (2000).

[129] M. S. Murillo, *Using Fermi Statistics to Create Strongly Coupled Ion Plasmas in Atom Traps*, Phys. Rev. Lett. **87**, 115003 (2001).

[130] E. A. Cummings, J. E. Daily, D. S. Durfee, and S. D. Bergeson, *Fluorescence Measurements Of Expanding Strongly Coupled Neutral Plasmas*, Phys. Rev. Lett. **95**, 235001 (2005).

[131] C. E. Simien *et al.*, *Using Absorption Imaging to Study Ion Dynamics in an Ultracold Neutral Plasma*, Phys. Rev. Lett. **92**, 143001 (2004).

[132] R. S. Fletcher, X. L. Zhang, and S. L. Rolston, *Using Three-Body Recombination to Extract Electron Temperatures of Ultracold Plasmas*, Phys. Rev. Lett. **99**, 145001 (2007).

[133] A. Walz-Flannigan, J. R. Guest, J.-H. Choi, and G. Raithel, *Cold-Rydberg-gas dynamics*, Phys. Rev. A **69**, 063405 (2004).

[134] I. I. Beterov, D. B. Tretyakov, I. I. Ryabtsev, A. Ekers, and N. N. Bezuglov, *Ionization of sodium and rubidium nS, nP, and nD Rydberg atoms by blackbody radiation*, Phys. Rev. A **75**, 052720 (2007).

[135] M. Viteau *et al.*, *Melting a frozen Rydberg gas with an attractive potential*, Phys. Rev. A **78**, 040704 (2008).

[136] T. Amthor, M. Reetz-Lamour, S. Westermann, J. Denskat, and M. Weidemüller, *Mechanical Effect of van der Waals Interactions Observed in Real Time in an Ultracold Rydberg Gas*, Phys. Rev. Lett. **98**, 023004 (2007).

[137] M. Robert-de Saint-Vincent *et al.*, *Spontaneous Avalanche Ionization of a Strongly Blockaded Rydberg Gas*, Phys. Rev. Lett. **110**, 045004 (2013).

[138] M. Siercke *et al.*, *Density dependence of the ionization avalanche in ultracold Rydberg gases*, Phys. Rev. A **89**, 022701 (2014).

[139] T. M. Weber *et al.*, *Continuous coupling of ultracold atoms to an ionic plasma via Rydberg excitation*, Phys. Rev. A **86**, 020702 (2012).

[140] S. B. Nagel *et al.*, *Magnetic trapping of metastable* $^3P_2$ *atomic strontium*, Phys. Rev. A **67**, 011401 (2003).

[141] S.-U. Haq *et al.*, *Photoionization cross section and oscillator strength distribution in the near-threshold region of strontium*, The European Physical Journal D **44**, 439 (2007).

[142] C. E. Burkhardt, J. L. Libbert, J. Xu, J. J. Leventhal, and J. D. Kelley, *Absolute measurement of photoionization cross sections of excited atoms: Application to determination of atomic beam densities*, Phys. Rev. A **38**, 5949 (1988).